Towards the Active Suppression of Disc Brake Squeal

by

Tomas Budinsky

Submitted in accordance with the requirements for the degree of

Doctor of Philosophy

The University of Leeds

School of Mechanical Engineering

September 2018

Intellectual Property and Publication Statements

The candidate confirms that the work submitted is his own, except where work which has formed part of jointly authored publications has been included. The contribution of the candidate and the other authors to this work has been explicitly indicated below. The candidate confirms that appropriate credit has been given within the thesis where reference has been made to the work of others.

The work in Chapter 5 of the thesis has appeared in publication as follows:
Budinsky T., Brooks P., Barton D., "The influence of disc geometry on the centre of pressure and squeal propensity for an automotive disc brake," Euro-Brake 2017 Conference Proceedings, FISITA, 2017, ISBN: 978-0-9572076-8-4.

The work in Chapter 5 of the thesis has appeared in publication as follows:
Budinsky T., Brooks P., Barton D., "A new analytical model of the brake pad for improved calculation of the centre of pressure and friction coefficient in a multi-piston disc brake," International Journal of Engineering and Technology, Vol. 7, No. 3.17, p. 54-63, UAE, 2018.

The candidate was responsible for majority of the work presented in these published papers, such as development of the models, undertaking experimental works, analysing and presenting the results. The co-authors contributed to the work by reviewing the publications and providing valuable advice.

Acknowledgements

I would like to thank Dr. Peter Brooks and Prof. David Barton for their assistance, source materials and constructive comments during the course of this research. Their friendly and supportive approach made my studies unforgettable. From the manufacturing workshop and laboratories, I wish to thank Anthony Wiese, David Readman, David Humpherson, Graham Brown and Steve Caddick for their advice and support. I am also grateful for help and support from Dr. Jongrae Kim especially in control systems design.

In addition, I would also thank to my parents and other family members. Their support and love made my way through the university studies possible.

In addition, I can not forget about my peer colleagues that gave me invaluable advice or simply offered a hand during some installation work in the laboratory, namely Muhammad Husman, Weibing Li and Jaffar Hussain.

Finally, I would like to whole-heartedly thank University of Leeds for awarding me their generous University Research Scholarship that enabled my studies.

Abstract

This work is concerned with disc brake squeal that is widely accepted as a friction-induced self-excited vibration of the brake assembly. The present thesis aims to investigate the possibility of active disc brake squeal suppression using a method of varying the leading and trailing piston pressures in a multi-piston opposed brake caliper.

This thesis describes the development of a new prototype four-piston brake caliper, a two-channel brake actuation system and an advanced control system, which is capable of varying the leading/trailing pressure ratio (LTPR) when squeal is detected. This causes the centre of pressure (CoP) position at the pad/disc interface to move, which leads to new dynamic parameters of the brake system and thereby to different squeal propensity. The control system maintains the overall brake torque to a constant value, so the variation of the LTPR on the brake performance is minimised.

Other novel approaches described in the thesis include a new three-dimensional analytical model of the brake pad, which was used to predict the CoP position in both circumferential and radial directions for a given LTPR. A reduced finite-element model of the current brake setup was also developed to predict positions of the CoP and unstable modes of vibration for varying LTPR.

Using low-cost piezoresistive force sensors, a new embedded brake pad sensor was designed that can determine the current position of the CoP during a braking event. The new brake pad sensor along with the new 3D analytical model served as indicators of the current CoP position during brake tests.

Experiments using the current disc brake setup showed that by varying the LTPR, thereby changing the CoP position, the squeal occurrence can be controlled. It was shown that the new squeal control system operating in an automatic mode reduced the squeal occurrence significantly for a given duty cycle.

Contents

List of Figures

List of Tables

List of Acronyms

2D Two-Dimensional

3D Three-Dimensional

ABS Anti-Lock Braking System

ASQR Automatic Squeal Reduction

CEA Complex Eigenvalue Analysis

CFD Computer Fluid Dynamics

CoP Centre of Pressure

DOF Degrees-of-Freedom

ESP Electronic Stability Program

EU European Union

FE Finite-Element

FEM Finite-Element Method

FPGA Field-Programmable Gate Array

GUI Graphical User Interface

HEPA High-Efficiency Particulate Air

IC Integrated Circuit

I/O Input/Output

LACT Los Angeles City Traffic

LTPR Leading Trailing Pressure Ratio

NI National Instruments

NVH Noise, Vibration and Harshness

OE Original Equipment

RT Real-Time

SAE Society of Automotive Engineers

SPL Sound Pressure Level

TCS Traction Control System

UoL University of Leeds

List of Symbols

α	angle (rad), real part of the eigenvalue
ϵ	strain (-)
η	efficiency of the hydraulic system (-)
λ	eigenvalue
V_T	reference negative voltage (V)
μ	friction coefficient (-)
μ_A	abutment friction coefficient (-)
μ_k	kinetic friction coefficient (-)
ω	circular frequency, disc angular speed (rad.s^{-1})
ϕ^k	approximation of k-th eigenvector of the original system
σ	stress (Pa)
σ_e	fatigue stress (Pa)
σ_{FEM}	stress (Pa)
θ'	angle (rad)
ϕ	eigenvector
$\mathbf{C}^*$	projected damping matrix to the subspace (kg)
$\mathbf{C}$	damping matrix (Nm^{-1})
$\mathbf{F_e}$	vector of excitation force (N)
$\mathbf{F_f}$	vector of friction force (N)
$\mathbf{K}^*$	projected stiffness matrix to the subspace (N.m^{-1})
$\mathbf{K}$	stiffness matrix (Nm^{-1})
$\mathbf{M}^*$	projected mass matrix to the subspace (kg)

$\mathbf{M}$	mass matrix (kg)
$\mathbf{v_s}$	vector of sliding speed (ms^{-1})
$\mathbf{X}, \dot{\mathbf{X}}, \ddot{\mathbf{X}}$	displacement (m), velocity ($m.s^{-1}$), acceleration ($m.s^{-2}$) vector
A_a	piston area (m^2)
c_{ratio}	negative damping ratio (-)
E_0	Young modulus (Pa)
e_{abs}	absolute position error (m)
e_{rel}	relative position error (-)
F	force (N)
F_f	friction force (N)
F_t	friction force (N)
F_{tA}	abutment friction force (N)
F_{tY}	Y-component of friction force (N)
F_{tZ}	Z-component of friction force (N)
i	index, imaginary unit, dimension of the system
j	dimension of the system
k	constant, coefficient (-)
k_r	specific wear rate ($m^3.Nm^{-1}$)
k_s	safety factor (-)
L	normal force (N)
L_p	sound pressure level (dB)
M_x	moment around X axis (Nm)
M_y	moment around Y axis (Nm)
M_z	moment around Z axis (Nm)
N	normal force (N)
n	constant, coefficient (-)
$n_{1,2,3,4Y}$	piston position (m)
$n_{1,2,3,4Z}$	piston position (m)

$n_{1,2}$	piston distance (m)
p	contact pressure (Pa)
p_0	minimum sound pressure defined at 1 kHz (Pa)
p_i	pressure value of i-th node (Pa)
$P_{1,2,3,4}$	piston force (N)
p_{max}	maximum sound pressure (Pa)
p_{min}	minimum sound pressure (Pa)
p_t	threshold pressure (Pa)
R	reaction force (N)
r	radius of the centre of pressure (m)
R_A	abutment reaction force (N)
r_e	effective radius (m)
r_i	inner radius of the disc rubbing area (m)
r_m	mean radius (m)
r_o	outer radius of the disc rubbing area (m)
R_{AY}	Y-component of abutment reaction force (N)
R_{AZ}	Z-component of abutment reaction force (N)
r_{pad}	vertical distance between the pad coordinate system and the rotor axis (m)
t	time (s)
t_{bp}	backplate thickness (m)
T_{brake}	brake torque (Nm)
t_{fm}	friction material thickness (m)
T_W	brake torque at wheel (Nm)
v_s	sliding speed ($m.s^{-1}$)
w_{d1}	wear displacement (m)
w_{d2}	wear displacement (m)
y_A	horizontal distance of abutment surface (m)
y_{CoP}	position of the centre of pressure (m)

y_i	position of i-th pressure node (m)
z_A	vertical distance of abutment point (m)
z_{CoP}	position of the centre of pressure (m)
z_i	position of i-th node (m)
$\dot{Q}_{airflow}$	flow rate ($m^3.s^{-1}$)

1 Introduction

"The beginning is the most important part of the work."
Plato

1.1 Background and Research Overview

Motor vehicles undoubtedly represent a significant part of a human's every-day life. There is no alternative system currently under development that could replace motor vehicles in the near future (Naunheimer, 2011). Indeed, automobiles have become one of the most important means of transport and their production and registration is still increasing (Davis et al., 2014). Despite the rising popularity, automobiles continue to have a significant impact on the environment. Besides air pollution primarily generated by combustion engines, the other important factor is noise. One system that unpredictably generates undesirable vibration and noise is the brake system (Bakar, 2012).

Brakes can typically generate noise over a range of frequencies from 100 Hz to 20 kHz, but the classic squeal occurring between 1 and 6 kHz is the most sensitive for a human ear (Day, 2014). Although brake performance is not influenced by squeal noise, it represents a comfort problem and makes passengers believe that the brake system is flawed (Hochlenert, 2006). This causes an increase in warranty claims and has a negative impact on the profit of car manufacturers. In addition, around 50% of the engineering budget of a brake pad manufacturer is spent on noise, vibration and harshness issues (Abendroth and Wernitz, 2000). Although the legislation limits are still related to the continuous sources of noise such as the engine, the ideal solution would be to manufacture silent brakes, which would also improve noise levels in some urban areas where frequent stopping of vehicles occurs (Ripin, 1995).

The first reported investigation of the brake squeal problems can be dated back to 1930's when the first attempts to clarify this phenomenon were made (Jarvis et al., 1963). Since then, brake squeal has been studied by many researchers and engineers from multiple disciplines (Chen, 2006). The main cause of brake squeal is the occurrence of friction-induced, self-excited or self-sustained vibration of the rotating disc. The requirement for squeal generation is that the frictional forces perform positive work on the system. Over the past decades, much understanding of the physical nature to this phenomenon has been achieved. The widely acknowledged hypotheses of mechanisms causing brake squeal are stick-slip, negative damping, geometric/kinematic constraints, modal coupling and hammering excitation theory (Chen, 2006). Since the early stages of

brake squeal investigation, several methods have been proposed to reduce brake squeal occurrence. These include passive countermeasures representing geometric variations of the brake components, introduction of other parts into the brake system, the application of lubricating materials or altering of the rubbing surface properties (Kinkaid et al., 2003). On the other hand, some novel approaches have introduced an element of active control of brake squeal using piezoelectric actuators (Wagner et al., 2004).

Figure 1.1 shows a typical non-uniform pressure distribution at the pad/disc interface during a braking event for a four-piston opposed caliper. This pressure distribution can be replaced by a single resultant force acting at the centre of pressure (CoP) (Day, 2014), which is a convenient method to simplify the complex pressure profile at the pad/disc interface, in particular for analytical models. On the other hand, knowing the CoP position and the resultant force does not provide full information about the shape of the pressure distribution as different pressure profiles may also result in the same CoP position. In a recent study it was observed that the position of CoP has some relation to the brake squeal onset and it was shown that by changing this position the squeal occurrence can be minimised or completely suppressed (Fieldhouse et al., 2009). This observation is a foundation stone of the current research and is investigated in greater detail in this thesis.

1.2 Overview of Disc Brake Systems

Brake systems are undoubtedly one of the most important components of modern road vehicles. Their purpose is to generate braking torque that opposes rotation of the wheels and thus retards the vehicle. The main physical principle of current disc brake systems is conversion of the kinetic energy of the moving vehicle to the heat energy by means of frictional force acting at the pad/disc interface. The generated heat needs to be effectively removed from the brake parts in order to avoid overheating of the whole system. There are currently two main types of brake systems that use friction (also termed as *foundation brakes*) to slow down the wheel assembly: disc and drum brakes.

A disc brake comprises a disc and a caliper that accommodates typically a pair of pads (Figure 1.2). Each pad presses against one side of the disc and generates a friction

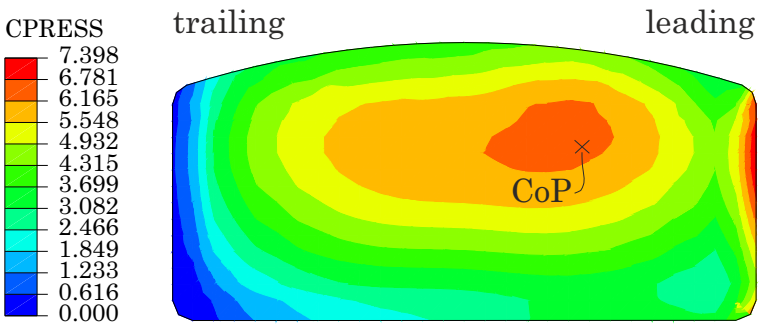

Figure 1.1: A typical non-uniform pressure distribution over the brake pad during a braking event. The contact pressure values are in MPa.

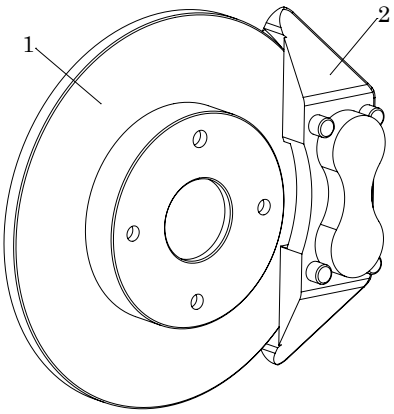

Figure 1.2: Illustration of a modern type of disc brake: 1) brake disc, 2) caliper.

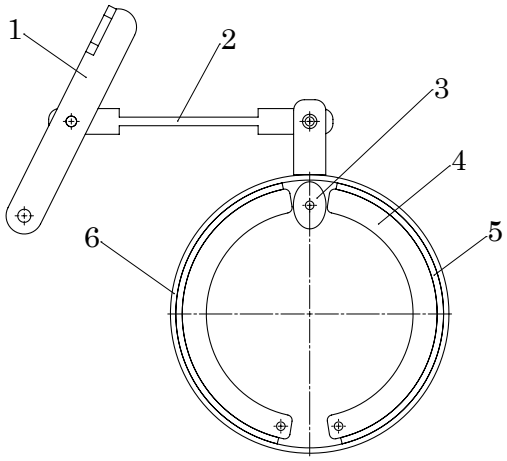

Figure 1.3: A typical drum brake with mechanical actuation: 1) brake pedal, 2) connecting rod, 3) S-cam, 4) two brake shoes, 5) brake linings, 6) brake drum.

force that opposes the disc motion. On the other hand, a drum brake uses its inner area as a rubbing surface for linings mounted on the so-called shoes (Figure 1.3).

Drum brakes still remain part of rear brake systems, mainly on small passenger cars and vans (Day, 2014). In contrast to drum brakes, disc brakes show superior behaviour in terms of fade and side-to-side balance of braking forces. Moreover, their linear relationship between braking torque and coefficient of friction at the brake pad/disc interface is also beneficial (Limpert, 2011). During a braking process, the dynamic load on the front axle is greater than on the rear axle and hence the front brakes contribute approximately 70-80% to the whole braking power. After worldwide introduction of stringent standards on vehicle braking in 1970's, disc brakes progressively replaced the drum brakes on the front axle (Kinkaid et al., 2003). Generally, no brake design can be considered to be a winner in all aspects. The drawbacks of the disc brakes are their lower brake factor (Limpert, 2011), higher maintenance costs and complication to incorporate a parking brake (Day, 2014). The lower brake factor was resolved in self-energising disc brake designs based on the wedge principle, however this design is not used in typical motor vehicles (Limpert, 2011). Other arrangements may include annular disc brakes immersed in oil and fully enclosed in a housing. These are predominantly used in heavy-duty or off-road vehicles where contamination of the rubbing surface by dust or mud would rapidly deteriorate the braking performance.

In the following text only the most typical design of the automotive disc brake will be discussed, very often referred to as an *open*, *spot* or *caliper type* of disc brake (Figure 1.2). In this design only a small part, typically 15%, of the disc area serves as a friction surface, which is in contact with the pad at any one time (Day, 2014).

1.2.1 Historical Background

Brake systems can be dated back to the invention of a wheel since an ancient wagon equipped with wheels had to be decelerated or stopped by some simple mechanism. So, the earliest brake system was probably known before 3800 B.C., as an unearthed Sumerian plaque with a depicted wheel has been dated approximately to this period (Stenberg, 1935). The first wheels were made of wood (Figure 1.4), at the beginning by cutting slices of big round tree trunks, later by fastening together wooden planks and cutting them to the circular shape. Such a wheel was equipped with two holes; one in the middle to provide axis rotation, whereas in the second hole a wooden stick from the vehicle body could be inserted which locked the wheel. Around 700 B.C., wheels began to be equipped with iron tires to prevent wear of the wheel rims (Reif, 2014). Later on, drag chains were widely used by Romans on their chariots (Stenberg, 1935). It was not until about 1850, that horse carriages began to use an iron axle and a shoe brake (Reif, 2014). Also, the first automobiles still featured shoe brakes as can be seen in a Benz car, Victoria, from the late 19th century (Figure 1.5). This technology was also employed in railway brakes (White, 1985) as shown in Figure 1.6 on an example of a historical railway car. After replacing of iron and solid rubber tires with modern air-filled tires, the era of shoe brakes was slowly fading out and band brakes or external shoe brakes were introduced in new vehicle designs (Reif, 2014).

An invention of the modern type of a spot disc brake can be dated back to 1902, when Frederick W. Lanchester patented this principle. However, this brake type did not become popular until the 1950s when, first mounted on Jaguar cars at Le Mans, its superiority over the drum brake was entirely confirmed (Day, 2014). One of the reasons why it took so long to integrate disc brakes in the road vehicles is the higher pressure of the whole system. So, first appropriate materials and components withstanding higher stresses had to be developed (Kinkaid et al., 2003). After the worldwide introduction of disc brakes in automobiles, the next milestone in brake design was a development

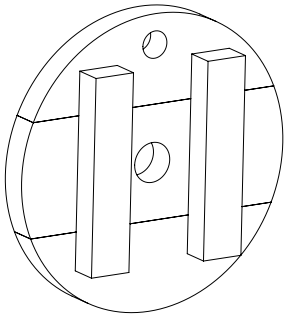

Figure 1.4: A depiction of an early wooden wheel with a hole for the parking brake (Stenberg, 1935).

Figure 1.5: Shoe brake installed in Benz's motor car Victoria (Technical Museum in Vienna).

Figure 1.6: Use of shoe brake in an early railway car (Technical Museum in Vienna).

of the electronic anti-lock braking system (ABS) in 1978 (Savaresi and Tanelli, 2010). This triggered introducing electronics as an integral part of the brake control which has since lead to a development of more sophisticated brake systems, such as traction control system (TCS) in 1986, electronic stability program (ESP) in 1995, or recently introduced electrohydraulic sensotronic brake control where the brake pedal is mechanically decoupled from the braking action (Reif, 2014).

1.3 Research Aim and Objectives

1.3.1 Scope

The present study is concerned with single-disc brake systems for automotive applications, although the outcomes can be also applicable in other areas of disc brake use, such as industrial, mining, railway, or aircraft.

1.3.2 Aim

The overall aim of this research is to investigate the possibility of active disc brake squeal reduction using a method of varying the leading and trailing piston pressures in a multi-piston opposed brake caliper.

1.3.3 Objectives

In order to realise the aim of the research, the following objectives were set up:

1. To design, manufacture and commission a disc brake test rig containing a four-piston opposed caliper that is capable of an individual control of piston pressures, and to develop an actuation and control system that enables operation of the said test rig.

2. To develop a closed-loop control system that allows the modulation of the leading/trailing pressure ratio (LTPR) of the caliper when squeal is detected by a

sound or vibration sensor. Variations of LTPR change the position of CoP at the pad/disc interface, and hence a new modified position of the friction force with respect to given geometric constraints of the brake system can lead to different squeal propensity.

3. To investigate a possible relation between the position of CoP at the pad/disc interface and squeal occurrences that would help to identify LTPR values for effective squeal suppression.

1.4 Methodology

The motivation for commencing the present work primarily stems from the encouraging previous findings on the relation of the CoP position at the pad/disc interface and tendency of the brake to squeal provided by (Fieldhouse et al., 2009). This relation could be explained by the sprag-slip theory introduced first by (Spurr, 1961), in which certain combinations of geometrical parameters of the brake (position of the friction contact with respect to the abutment points) and magnitude of the friction coefficient can give rise to squeal. The present research focuses on the practical implementation of these findings to investigate the possibility of active control of squeal noise by applying the aforementioned results. Therefore, a deep insight into the fundamental causes of the squeal generation will not be covered here.

As shown in Figure 1.7, the current work can be divided into several subsequent and parallel work packages leading to the final realisation of the aim presented above. The work can be categorised as the development of the brake test rig, the modelling work, and a testing phase. First, a new disc brake assembly is designed and manufactured, which includes development of a new four-piston opposed caliper and other peripheries. After completion of the brake assembly, development of the actuation and control system follows to build a fully functional brake test rig that can be used for development of automatic squeal reduction algorithms. Finally, development of the new brake pad sensor

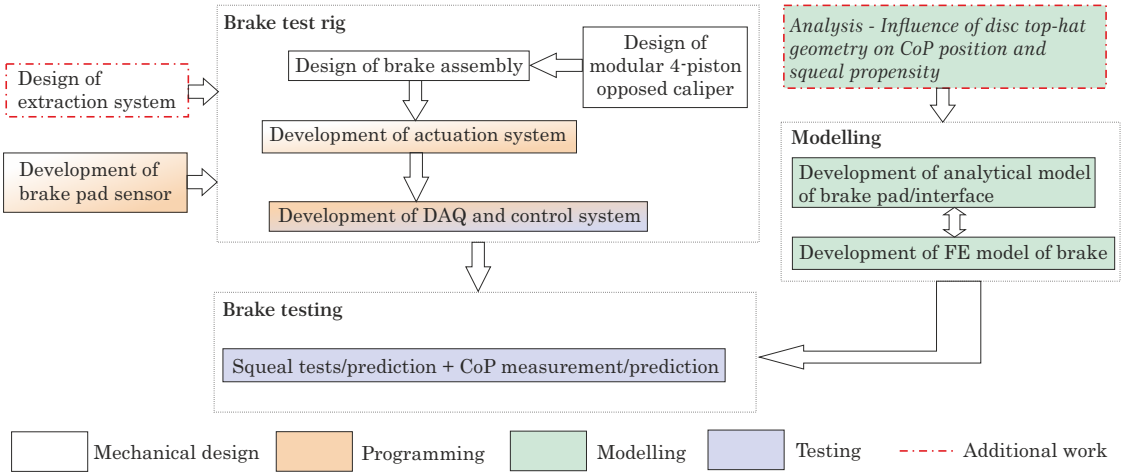

Figure 1.7: Schematic of the methodology adopted for this thesis.

and design of the extraction system complete the brake test rig work package.

A parallel modelling work package includes the CoP position investigation, where two approaches are developed and compared: a new 3D analytical model of the pad/disc interface and an equivalent finite-element (FE) model of the brake. The FE model of the brake also serves as a tool to predict unstable modes of vibration using a complex eigenvalue analysis (CEA). Despite being a small digression from the main topic, an additional analysis on the influence of the disc top-hat height on the CoP position shows how this parameter causes variation of the CoP position between the inboard and the outboard sides, as well as the effect, it has on squeal propensity.

Finally, the testing phase demonstrates the ability of the brake test rig to vary the CoP position along the pad in order to minimise or completely suppress squeal occurrences. The analytical model of the pad/disc interface as well as the brake pad sensor are used to determine the CoP position in real-time, which allows the translation of the LTPR to the CoP position and hence the identification of quiet zones on the pad.

1.5 Organisation of Thesis

This thesis consists of seven further chapters that are briefly summarised below:

Chapter 2 - Literature Review - Disc Brake Squeal
Chapter 2 introduces brake squeal and explains basic terms relevant to the present thesis to give fundamentals of the subject matter to a reader who is not familiar with the topic. Beginning with background on acoustics and brake disc vibration, the chapter further introduces some details on friction and friction pair components, as well as on other brake components, followed by a review of main theories explaining the mechanisms of brake squeal generation. The chapter also presents a review of brake squeal modelling techniques and brake squeal reduction methods. For completeness, a brief review of studies investigating brake emissions is provided. Finally, a summary and a critical review of state of art conclude the chapter.

Chapter 3 - Design and Development of Brake Test Rig
Chapter 3 presents all important steps leading to the development of the new brake test rig. It includes four main sections: design of the new brake caliper, structural analysis of the caliper assembly including brackets, development of the brake test rig enclosure, and the two development stages of the actuation system. Each section provides an overview of the work, accompanied with figures, drawings and tables. Some important topics relevant for the next chapters are covered in greater detail.

Chapter 4 - Development of DAQ and Squeal Control System
Chapter 4 concentrates on the electronic part of the new brake test rig, explaining in detail components and instruments used to control and monitor the test rig. The first section describes the connection, calibration and commision of the data acquisition instruments, whereas the second section explains the control algorithms programmed for

the controller by using illustrative schematics and diagrams. Finally, the performance of the brake test rig control system using simple testing methods is presented.

Chapter 5 - Analytical and Finite-Element Modelling of Disc Brake
Chapter 5 focuses on simulation of the new brake assembly using analytical and FE modelling approaches. The chapter includes a derivation of a new three-dimensional analytical model of the pad that can determine the CoP position in both radial and circumferential directions. Then, the development of a reduced FE model of the brake assembly is presented that serves as a prediction tool for squeal performance and CoP position.

Chapter 6 - Development of Embedded Brake Pad Sensor
Chapter 6 describes the development process of a new embedded brake pad sensor. It provides details about the main components and electronics, as well as calibration of the force sensors. The performance of the pad sensor to determine the CoP position at the pad/disc interface is evaluated during braking tests.

Chapter 7 - Experimental Brake Squeal Investigation
Chapter 7 shows results of the brake squeal experiments using the new brake test rig described in Chapters 3 to 6. The results can be used to draw conclusions about the feasibility of active brake squeal control.

Chapter 8 - Conclusions and Future Work
Chapter 8 summarises the results and important outcomes, as well as providing conclusions from the present work. This chapter further includes recommendations for future work.

2 Literature Review - Disc Brake Squeal

"The squeaky wheel gets the grease"
American Idiom

2.1 Introduction

This chapter presents a review of the literature on brake squeal with a main focus on the topics that are relevant to the current thesis. First, an overview of brake components serves to show the main building blocks of modern brake systems. Then, the basics of acoustics and principles of brake disc vibration are explained to introduce related terminology used throughout the thesis. The chapter further presents details on friction and friction pair components, followed by a review of main theories explaining the mechanisms of brake squeal generation. Also, reviews on brake system modelling techniques and brake squeal reduction methods are included. For completeness, a brief overview of studies investigating brake emissions is provided. Finally, a summary and a critical review of state of art conclude the chapter.

2.2 Overview of Brake Components

2.2.1 Brake Caliper

Brake calipers are used in disc brake systems to straddle the outside diameter of the brake disc like a C-clamp. When a brake is applied, the hydraulic pressure in the system forces pistons to move against the brake pads, which exert clamping forces on the brake disc (Erjavec, 2004). A brake caliper also transmits the reaction of brake forces to the axle housing via a mounting bracket. Currently, there are two common caliper arrangements: a fixed, and a sliding caliper.

The first type, shown in Figure 2.1(a), is often referred to as a *fixed* or an *opposed piston* type of caliper and its main advantage is even wear of the pads, a faster response due to a smaller clearance between the pad and rotor (Limpert, 2011), fewer moving components and a more even pressure distribution over the pad rubbing surface (Day, 2014). Generally, fixed calipers are more rigid, which may reduce the spongy feel on the brake pedal. Therefore, the bridge stiffness is considered to be one of the most important parameter of a caliper (Scraba, 2014). Fixed calipers usually house two or four pistons, or in special high-performance arrangements six, eight (Brembo, Stainless Steel

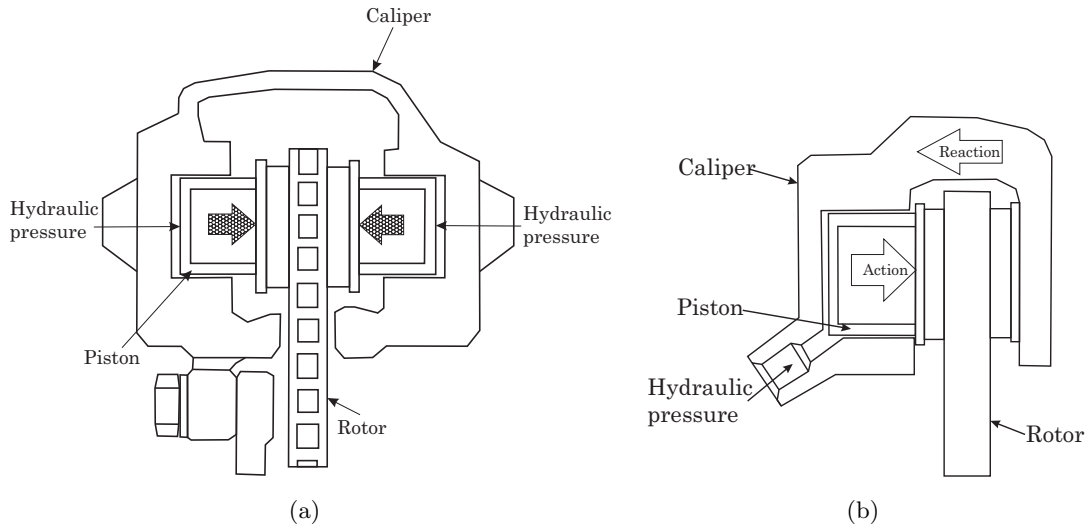

Figure 2.1: Typical caliper designs on today's passenger cars (according to (Erjavec and Thompson, 2014)): a) fixed (opposed), b) sliding (fist, floating).

Brake Corporation, Rotora), ten (Porsche) or even twelve pistons (Rotora, Brabus-Alcon). These manufacturers claim that 6- or more piston calipers improve the uniform pad/disc contact and hence the wear of the pad is significantly reduced (Rotora Brakes, 2018). On the other hand, the TBM company specialising in 4-piston calipers objects that an overall caliper performance might not be better because incorporating of a larger number of pistons, thereby decreasing the piston diameters, in a given area yields smaller overall clamping forces. Moreover, placing of additional pistons in the highly stressed area weakens the caliper body, and also the potential enlarging of the caliper body reduces the stiffness (TBM Brakes, 2018). A 2-piston caliper, in racing terms, is often called a *single* caliper, while a 4-piston caliper is referred to as a *dual* caliper (Scraba, 2014).

The second design of a disc brake caliper, illustrated in Figure 2.1(b), is often called a *sliding*, *fist* (Limpert, 2011) or *floating* (Day, 2014) type of caliper. In this arrangement, the sliding part of the caliper moves along the pins mounted on the fixed part of the caliper. It includes only one piston on the inboard side of the caliper which pushes the inboard pad directly and the reaction force of the piston moves the sliding part of the caliper backwards and thus, via a paw, pushes the outboard pad against the brake rotor. The actuation forces are equal on both sides, apart from the small difference due to the friction in the slide pins (Day, 2014). The main advantages of sliding type calipers are: easier packaging in the wheel since there is no piston on the outboard side, fewer possible leakage points, a lower risk of the brake fluid vaporisation and easier bleeding (Limpert, 2011).

Some unusual caliper designs include the three-piston opposed caliper developed by Girling, the swinging caliper produced by Lockheed and Girling, and a Girling caliper known as the Annette type (Baker, 1986).

For a caliper installation, it is important that the position of the bleeding screws allows

the bleeding of the system. There are two main caliper positions on a wheel assembly: a front position (9 o'clock) and an aft position (3 o'clock). The front arrangement has a packaging advantage for front wheel drives, but the bearing load is higher, while the aft position loads the bearing substantially less and also does not restrict cooling of the brake rotor. However, the packaging of the aft arrangement can be problematic for front wheel drives due to the steering linkage (Day, 2014), (Limpert, 2011).

The most common material for a brake caliper is cast iron. Its advantage is inexpensive mass production, small dimensions with satisfactory stiffness and a decent wear resistance on contact points, e.g. abutments. Some racing applications require, besides an excellent stiffness of the bridge, a lightweight caliper assembly to reduce the unsprung mass of the wheel assembly. This forces manufacturers to use different alloys, e.g. aluminium. Of these aluminium alloys, the forged 6061-T6 is most widely used. Interestingly, for the Formula 1 cars, special alloys have been tested, such as aluminium-beryllium, however these exotic materials for a caliper construction were banned in 1998 (Macknight, 2002) and currently only aluminium alloys can be used (Formula1, 2018). In 2018, Bugatti developed the world's first caliper manufactured by a 3D printer (Bugatti, 2018). This caliper features eight pistons and is the largest in the automotive industry. It is made of titanium with the overall weight of 2.9 kg saving over 40% of weight comparing with an aluminium predecessor. The top brake caliper manufacturers in the passenger cars category are Brembo, Baer, AP Racing, Alcon, SSBC and Wilwood. The brake calipers for commercial vehicles are manufactured by Knorr-Bremse, Wabco, ArvinMeritor, Haldex and Brembo (Fleet Parts Ltd, 2018). Formula 1 cars are supplied by AP Racing and Brembo (Macknight, 2002).

There is only a little attention devoted to the caliper structural analysis and design optimisation in the brake literature. Some studies have been made by (Tirovic and Day, 1991) and (Rajaram and Sudharsan, 2005). (Wagh, 2005) performed a FEM analysis of a Brembo 4-piston opposed caliper and designed a new modular caliper with reduced thermal stress and deformation.

2.2.2 Brake Piston and Seal

A *brake piston*, or sometimes referred to as a *brake pot* (Racecar engineering, 2018), transfers the hydraulic pressure of the brake fluid to the mechanical force acting on the backplate of a brake pad. A typical brake piston seal has usually square or rectangular cross-section and is made of a high-grade synthetic rubber, which has to withstand high temperatures and pressures over 100 bar (Baker, 1986).

Brake pistons have typically small cleareances in their bores and close running clearances betweeen pads and rotors to prevent pistons from cocking in the caliper and to minimise pushing the pistons back due to disc axial run-out or warping (Owen, 2003). In the design stage, a great emphasis must be, therefore, laid on proper choice of tolerances and surface finish. (Anwana et al., 2002) performed a parametric study for the seal groove geometry and showed which dimensions have a major influence on the proper sealing and

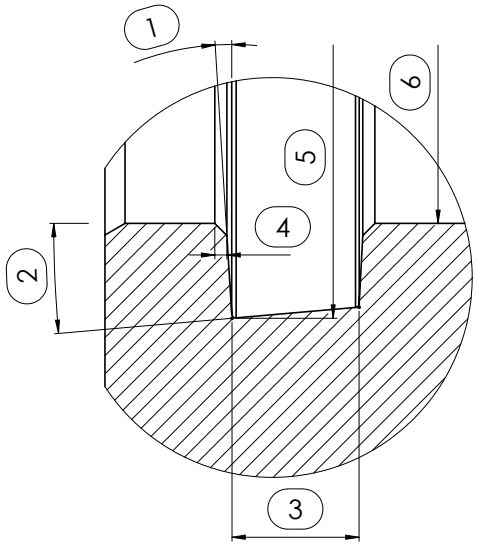

Figure 2.2: Geometry of a common piston seal groove (According to (Anwana et al., 2002)): 1) front angle, 2) bottom angle, 3) groove width, 4) chamfer, 5) groove outer diameter, 6) groove inner diameter.

piston retraction function. A typical seal groove geometry can be seen in Figure 2.2.

2.2.3 Brake Pad

Brake pads generally consist of a friction material attached to a flat metal backplate (Harding and Wintle, 1978). However, modern backplates can have a fairly complex geometry and serve multiple functions, very often acting as a frame for numerous features. Some typical shapes for an automobile brake are shown in Figure 2.3. Often, original equipment (OE) suppliers equip the backplates with adhesive (bonded) or clip-on shims to reduce vibrations (Shimizu et al., 2014). Some older pad designs comprise a pre-load spring (see the pad on the left in Figure 2.3). In order to decrease temperature of the brake fluid and piston seals, racing brake pads usually feature an insulator placed between the brake pad and the piston (Scraba, 2014). Friction materials are mostly attached to the backplates using an adhesive layer. To minimise the risk of shearing-off the friction material from the pad, backplates can additionally contain spigot holes or multiple hooks. Some other features that can be found on a backplate include pips of different shapes and sizes to attach shims or as a piston anti-twist protection, as well as a variety of holes to mount retaining springs, electric wear indicators, or bolts holding the pad in the caliper.

The friction material is often referred to as a brake lining and this term is used in the drum brakes context as well. The friction materials used today can be divided into following categories (Day, 2014):

- cast iron (brake shoes on railway vehicles)

- carbon fibre composite (aircraft and Formula 1)

Figure 2.3: Typical automobile brake pads.

- sintered metal (industrial applications and racing)
- cork- and paper-based (low duty - immersed in oil)
- resin-bonded composite (most of modern vehicles)

The resin-bonded composite friction material is the most common material used in modern disc brakes. They are further categorised as: non-asbestos organic, low steel and semi-metallic. A typical brake lining (friction material) consists of five components (Grigoratos and Martini, 2015):

- binders (bind the components together)
- fibres (mechanical strength and structure)
- fillers (thermal and noise properties)
- lubricants (wear characteristic)
- abrasives (increase friction and reduce transfer films)

The most important parameter of the friction material is its friction coefficient. The friction coefficient needs to be evaluated for a friction pair; for example, a friction material paired with cast iron can have a value of 0.4, while the same friction material mated with a stainless steel rotor can yield a friction coefficient of 0.6. The friction coefficient may vary by $\pm 10\%$ from a nominal value, so it is always recommended to carry out calculations with its upper and lower limits (Day, 2014).

Since brake pads are complex anisotropic materials, many researchers have found it difficult to accurately model the thermo-mechanical properties of brakes (Kinkaid et al., 2003). (Chen, 2006) describes in more detail how to determine mechanical properties of the friction material using an ultrasonic technique. In total, five independent constants must be specified to fully describe the mechanical properties (Mastinu, 2013). (Harding

and Wintle, 1978) studied flexural effects in disc brake pads and showed dependency of critical length, beyond which pressure is not distributed uniformly and the backplate tends to separate from the friction material, on compression modulus of the friction material relative to the stiffness of the backplate. (Kao et al., 1994) introduced a non-linear stress-strain model to improve characterisation of the compressive behaviour of the friction material. This behaviour was modelled as follows:

$$\epsilon = \frac{\sigma}{E_0} + k\frac{\sigma}{E_0}^{n}$$

where σ denotes the compressive stress, ϵ represents the compressive strain and a particular pad can be defined by parameters k, E_0 and n. Any representative values of these parameters were not given. (Kao et al., 1994) further showed a significant influence of pad modulus on the contact distribution and hot spot generation, which justified use of a non-linear stress-strain pad model.

In addition, as reported by (Malmassari et al., 2015) the dynamic stiffness of friction material also impacts on brake system noise behaviour and correlates better with squeal than static stiffness. They presented two methods of measuring dynamic modulus (ETEK and SHAKE) and also investigated the possibility of their correlation.

Damping behaviour of pads can be determined using the SAE J2598 procedure, which proposes the use of an impact hammer and an accelerometer. Another approach utilises non-contact methods, such as magnetic excitation or laser vibrometer (Mastinu, 2013).

Most brake pads require a bedding (burnishing) procedure which improves performance and wear, and reduces propensity to thermal cracking of the disc (Scraba, 2014). Also, the squeal performance depends significantly on how the friction material is bedded (Spurr, 1961). When all rubbing surfaces of the friction material come in to contact with the disc, pads are fully 100% bedded. In addition, the rubbing surface is also considered to be burnished or fully cured as a result of exposure to heat cycles (Day, 2014). A detailed description of a bedding procedure can be found in EU Regulation 90 (EU, 2010).

2.2.4 Brake Disc

Representative automobile *brake discs* (sometimes referred to as a *brake rotors*) are shown in Figure 2.4 and consist of a friction ring and a top-hat section. The rotating friction ring is swept by stationary pads from both sides, defining a rubbing or friction surface area (Day, 2014). The top-hat section connects the friction ring to the wheel hub and its role is to increase the cooling surface and the distance the heat needs to travel to reach the bearings (Kinkaid et al., 2003). Since disc brakes have smaller contact area when compared to drum brakes, the temperatures reached during the braking process are far higher. To improve cooling of the rotor, some rotors are vented (or ventilated) providing a space between the inboard and outboard cheek for vanes (Figure 2.4(b)). The two main configurations of the vented discs are: standard with an outboard friction cheek attached to the hat (Figure 2.5(a)) and a reverse ventilated with an inboard friction cheek attached to the hat or also referred as to an anti-coning brake disc (Figure 2.5(b)), (Day,

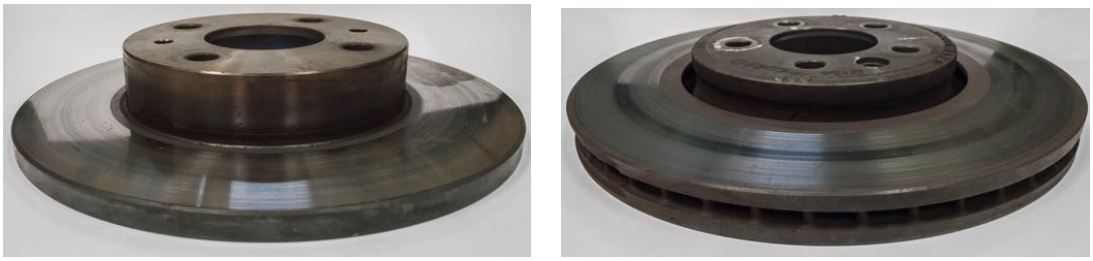

(a) (b)

Figure 2.4: Typical automobile disc designs: a) solid, b) vented.

2014). Some authors refer to these two designs as a front-vented and back-vented disc, respectively (Hassan, 2009), (Supachai et al., 2013).

The main advantage of the anti-coning disc is lower temperature difference between the inboard and outboard cheeks, which results in lower thermal stress and deformation of the disc (Supachai et al., 2013), however it has a poorer cooling performance due to restriction of the air flow from the wheel assembly, which was partly enhanced by including piercing in the wheel carrier (Day, 2014). Combining the two designs results in a concept with better heat dissipation since the air flow can be provided from both inboard and outboard sides of the rotor (Lee, 2007). This two-sided ventilation is often used in shaft braking discs for rail vehicle disc brakes (Wirth, 1987), (Reibenschuh et al., 2009).

As previously stated, a brake disc is a part of the friction pair, so the size and material of the disc needs to be carefully chosen to dissipate the heat from the friction surface (Day,

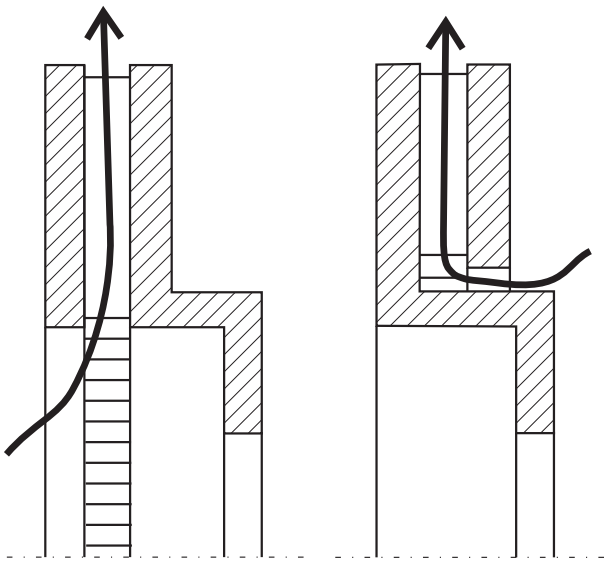

(a) (b)

Figure 2.5: Illustration of two main vented disc designs: a) standard, b) reverse-ventilated (anti-coning).

2014). The most common material for brake discs is grey cast iron that is characterised by good friction, thermal properties (Alnaqi, 2014), relatively low production costs (Kinkaid et al., 2003), good machinability and very good vibration damping properties (Day, 2014).

In the motorcycle sector, stainless steel has become popular mainly because of cosmetic reasons (Day, 2014). The major drawback of the stainless steel disc is a significant decrease of the friction coefficient in wet conditions (sometimes by factor of 3) and manufacturers must incorporate drillings or grooves to the disc design to enable removal of the water film (Day, 2014). Some motorcycles feature floating discs on front wheels to improve the thermal and mechanical stresses that arise in the disc (Stan, 2005). In a floating disc, the friction ring is mounted to an aluminium carrier by means of pins that enable a certain play between the ring and carrier. The floating discs are also often used in student racing formulas to improve the braking performance and prevent the warping of the disc when subjected to excessive heat.

In order to improve fuel consumption and limit emissions, intensive studies have been recently made on investigation of lightweight brake rotors. The most encouraging material is an aluminium alloy because of its low density and high thermal conductivity along with high specific heat capacity. However, the main disadvantages of aluminium alloys are low maximum working temperatures and poor wear resistance. Therefore many researchers endeavour to improve the surface properties of aluminium by anodising or thermal spraying (Alnaqi, 2014). Other rotor materials include reinforced carbon-carbon or ceramic matrix composites (Grigoratos and Martini, 2015).

2.3 Background on Brake Noise

2.3.1 Basic Terminology

Some physical definitions of sound state that it can be referred to as a *mechanical vibration* or *mechanical wave propagation* in an elastic medium (Blauert, 2008). The medium can be a fluid, such as air or water, or a solid material, e.g. steel. When a sound source oscillates, it creates small pressure fluctuations in the surrounding air which are transmitted to the human's ear and perceived as a sound (Moeser, 2009). Both vibration and waves can be mathematically defined in form of differential equations; ordinary differential equations are used for vibration, while waves, due to dependency on space and time, must be described by partial differential equations (Blauert, 2008). In order to describe and analyse sound fields *sound pressure* is the most important quantity used (Moeser, 2009). According to (Blauert, 2008) the maximum sound pressure at the level of discomfort for humans is defined as follows:

$$p_{max} \approx 10^2\,\mathrm{N/m^2} = 100\,\mathrm{Pa}$$

Similarly, the minimum pressure at the threshold of human hearing at 1 kHz is:

$$p_{min} \approx 2.10^{-5}\,\mathrm{N/m^2} = 20\,\mu\mathrm{Pa}$$

As it can be seen, the range of the pressures (approximately $1 : 10^7$) that needs to be covered in acoustics is quite large for comfortable calculating. Therefore, a logarithmic measure called *level* was adopted. In addition, the Weber-Fechner law describing the relation between a physical stimulus and a sensory organ can be approximated by a logarithmic function (Blauert, 2008). These reasons lead to definition of new quantities to describe sound, of which the most widely used is the *sound pressure level (SPL)* defined as following:

$$L_p = 20 \log \frac{p}{p_0} \,[\mathrm{dB}] \quad \text{with} \quad p_0 \approx 2.10^{-5} \mathrm{N/m^2} = 20\,\mu\mathrm{Pa}$$

Hearing levels cannot by defined precisely, but the range 16 Hz - 16 kHz is a typical value for a healthy, around 20-year-old, human being. With ageing, there is a usual decrease of 1 kHz per decade for the upper limit of the range (Moeser, 2009). Generally, the sound frequency ranges can be divided as follows (Blauert, 2008):

- Audible sound $\approx$ 16 Hz - 16 kHz
- Ultrasound >16 kHz
- Infrasound <16 Hz
- Hypersound >1 GHz

The human ear is especially sensitive for the frequency range 3 to 4 kHz, within which a lower sound pressure level is necessary to create the same feeling as for lower or higher frequencies (Morello et al., 2011). Due to this specific relation, arithmetic A-, B-, and C- weighting filters were developed to enable quantification of the intensity as perceived by the human ear (Hedge, 2016). The most common is the A-weighting filter (Bao and Panahi, 2013) (see graph in Figure 2.6) and is also used in the brake squeal monitoring, although this filter is presumably correct to use only for relatively low sound levels ($\approx$40 dB) and for pure tones (Hedge, 2016).

In turn, noise is a subjective perception of sound, but generally it can be defined as a sound that is unacceptable or even harmful for a human (Barron, 2003). There are three fundamental components of a general noise system: the source of the sound, the travelled

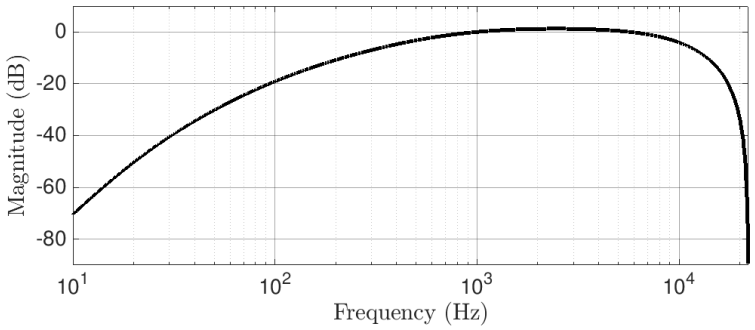

Figure 2.6: A graph of the A-weighting filter across the frequency range.

path of the sound and the receiver of the sound (Barron, 2003). Naturally, the number of each component can vary; there can be several sources, different paths through which the sound travels and also various number of receivers. The main objective is to reduce the sound level at the receiver, which can be accomplished by modifying the sound source, altering of the transmission path, or noise control at the receiver. The source of the noise is a vibrating surface, and changes at this component are considered to be the best possible way to solve the noise problem (Barron, 2003). Modifications in the transmission path in the brake squeal context by placing a wall or barrier between the source and receiver (the human ear) is provided partly by the car body, however it does not solve the problem of emitting the sound to the environment. The brake squeal is considered to be an intermittent phenomenon, modifications at the receiver, e.g. by limiting time the passengers are exposed to squeal or by using hearing protectors, would not be acceptable.

The automotive brake noise is typically categorised to numerous groups according to their frequency such as grunt, hum, groan, moan and the whole family of squeals (Akay, 2002). Figure 2.7 depicts the main categories of brake noise ordered by frequency. Automotive brake squeal can be classified as a high frequency noise, ranging from the frequency 1 kHz up to the higher audible limit 16 kHz (Papinniemi et al., 2002), whereas, for example, aircraft brakes tend to squeal at lower frequency range 100 Hz - 1 kHz (Akay, 2002). The frequency spectrum of automotive brake noise is usually divided as follows:

- **Low-frequency noise**, from 100 Hz to 1 kHz, generally includes grunt, grind, groan and moan. The generation of these types of noise are often associated with the friction material excitation at the pad/disc interface and the transmitted vibration couples with other chassis components (Dunlap et al., 1999a).

- **Low-frequency squeal**, from 1 to 5 kHz, takes place usually up to the first circumferential (in-plane) mode of the disc (Dunlap et al., 1999a). This type of squeal is usually characterised by 1, 2, 3 or 4 nodal diameters, which means that the

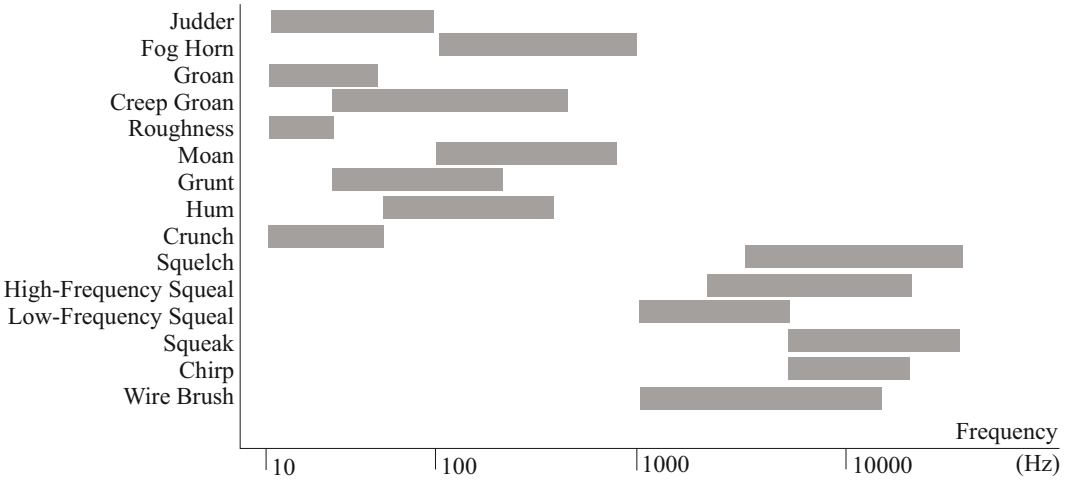

Figure 2.7: Brake noise categories and their approximate frequency spectrum (According to (Akay, 2002)).

distance between the nodes is larger than the pad length (Akay, 2002). Therefore, besides the pad and disc also other components such as caliper, anchor bracket, knuckle and suspension contribute to the squeal generation (Tirovic et al., 2018).

- **High-frequency squeal**, above 5 kHz, is often characterised by the presence of a circumferential mode of the disc, usually accompanied by coupling of the circumferential and out-of-plane mode, or a circumferential mode of the disc and a vibration mode of another brake component. In most cases, the high-frequency squeal closely matches with the resonance circumferential frequency of the disc (Dunlap et al., 1999a). This type of squeal involves 5 to 10 nodal diameters (Akay, 2002) and its generation is mostly due to the pad and disc only (Tirovic et al., 2018).

Some authors shift the boundary between the low- and high-frequency squeal to 3 kHz (Mastinu, 2013) or 7 to 8 kHz (Triches et al., 2004).

Figure 2.8 shows a general breakdown of brake noise categories according to their relative occurrence. It can be seen that brake squeal still represents a significant part of the brake noise, vibration and harshness (NVH) problems, however due to number of thermal instabilities experienced in high performance cars the judder problem is currently more prevalent (Fieldhouse et al., 2009). Since the low-frequency brake squeal coincides with the frequency bandwith in which a human ear is most sensitive, this type of brake noise is considered to be the most annoying (Triches et al., 2004).

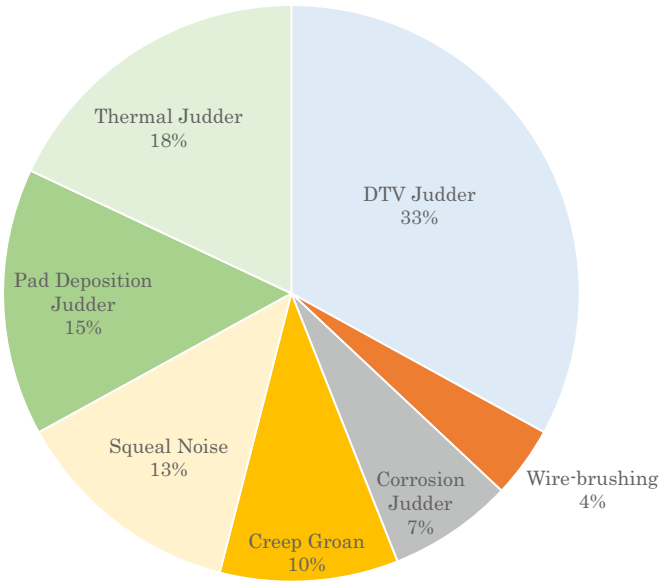

Figure 2.8: Relative occurrence of various types of brake system instabilities (According to (Fieldhouse et al., 2009)). DTV=Disc Thickness Variation.

2.3.2 Brake Disc Vibration

The current consensus among brake researchers is that squeal is a self-excited vibration induced by a dynamic instability of the brake due to the friction forces at the pad/disc interface (Wagner et al., 2004). The disc vibrates during squeal in a complex manner, therefore an analytical or numerical approach is usually adopted to model the real disc vibration. The vibration mode may contain out-of-plane (also called bending or normal) or in-plane modes, or a combination of both (Mastinu, 2013). The out-of-plane modes can be determined by a partial differential equation that describes a free vibration of a circular plate (Yang et al., 2003), (Chen, 2006). The out-of-plane mode can be represented by three typical mode shapes: diametric, twisting and umbrella mode (Yang et al., 2003). Each of these modes can be defined by a simple code (m, n), where m is the number of circumferential lines and n represents the number of diametric lines. The circumferential nodal lines represent *singlet* modes, while the diametric nodal lines are referred to as *doublet* modes (Mastinu, 2013). The singlet modes result from eigenvalues that are isolated roots of a characteristic equation, and do not depend on the angular coordinate, whereas the doublet modes have double roots of a characteristic equation (Chen, 2006) and occur in pairs with the same natural frequency distinguished by a relative spatial phase shift (Kim et al., 2000).

The in-plane modes can be also studied analytically using a partial differential equation describing in-plane vibrations of a circular plate (Yang et al., 2003). The in-plane vibration is represented by radial and circumferential (also called longitudinal or tangential) modes. These two can be termed by codes IPR(r) and IPC(c) where r and c represent the number of in-plane radial and circumferential mode shapes, respectively.

Due to geometrical complexity of real disc rotors, the pure out-of-plane and in-plane modes do not exist and are difficult to be predicted using the analytical approach (Yang et al., 2003). Therefore, FE modelling is typically used to include other geometrical features of rotors, for example a hat section or vanes. However, for high-frequency vibration, such as squeal, the disc modes of disc rotors are similar to those of a circular plate (Yang et al., 2003).

2.3.3 Noise Testing Procedures

Over the years, measurement of brake squeal on a brake noise test dynamometer has become standard in many research laboratories. There are typically two main designs of dynamometer for brake research: a shaft-type, and a chassis dynamometer. In a shaft-type dynamometer the brake rotor is bolted to the shaft that is driven by motor, usually via a transmission. The new internationally recognised brake noise procedure SAE J2521 includes both drag and regular stop test procedures, so dynamometers without additional mounted inertia are outdated and cannot be fully used for this type of noise testing procedure (Chen, 2006).

The brake squeal measurements typically includes collecting of a large amount of data, which requires use of a high-performance data acquisition (DAQ) system. For some

testing procedures a single microphone is sufficient for noise data collection, but other testing methods require more than one microphone deployed around a brake assembly, or sometimes other sensors are installed, such as accelerometers, laser Doppler vibrometers and optical holography systems. An air flow around the brake assembly is in some test rigs provided to represent cooling of the brakes, which is significant especially at higher speeds. Typical physical quantities recorded during a noise testing procedure are brake pressure, temperature, speed, sound pressure levels and vibration amplitudes (Chen, 2006). The most important test procedures for brake noise investigation are:

- AK Noise Procedure

The AK noise test procedure evaluates the propensity of brakes to generate squeal using a matrix of testing procedures. This procedure was developed by a working group in Germany and is not a published standard, therefore many different versions can be also found. One of the known limitations of this procedure is that it does not include enough deceleration stops. During testing, the triangular pressure profiles are used to incorporate all possible pressure values so it is assured that noise occurrences at some specific pressure values are not missed. The whole procedure contains 1409 stops including some reverse stops to also evaluate this possibility (Chen, 2006).

- SAE J2521 Procedure

The SAE J2521 procedure was first suggested by (Blaschke and Rumold, 1999) and further developed by the US Working Group on Brake NVH. In contrast to the AK noise procedure, the SAE J2521 includes more deceleration stops, so it better represents the real vehicle operation, and also evaluates the characterisation of friction coefficient after each test segment. Furthermore, noise is recorded through all sections of the test matrix. Due to incorporating more deceleration stops and friction characterisation, the SAE procedure shows significant differences in results when compared with the AK procedure. In these sections of the SAE procedure, surprisingly, the highest noise occurrences have been found (Thompson and Fudge, 2002). Some researchers point out that including tests at 90% humidity and close to freezing temperatures, to simulate brake "morning sickness", would improve this noise test procedure even more (Chen, 2006).

- LACT Test Procedure

The Los Angeles City Traffic (LACT) test is used in the United States to demonstrate brake noise performance in real driving situations, usually as a final brake noise evaluation during the vehicle development. This test is known to produce significant brake squeal in some vehicles. The drawback of this test might be its length, usually 2-3 weeks, which can be difficult to incorporate in an early development stage. By comparing the SAE J2521 and the LACT test, it has been shown over the years that the SAE J2521 is usually a more severe procedure capable to uncover noise that might not be observed during the LACT test (Chen, 2006).

2.4 Pad/Disc Interface

2.4.1 Contact Pressure Distribution

A conventional disc brake analysis assumes that the pressure at the pad/disc interface is either constant or inversely proportional to the radius. The latter is used to compensate the varying sliding speed and to achieve a constant specific loading over the pad surface. This requires that the radial pressure distribution must follow the hyperbolic curve, which can be mathematically expressed as (Tumbrink, 1989):

$$p_i r_i = const. \tag{2.1}$$

where p_i is a pressure, and r_i an effective radius component.

However, in real braking situations the interface pressure distribution is not ideal and varies with time. According to (Kao et al., 1994), three main mechanisms contribute to the non-uniformity of pressure distribution:

1. Heat generated at the contact area causes the thermal distortion.
2. Actuation forces have impact on the mechanical distortion.
3. Wear of the friction material.

All studies about the contact pressure distribution can be divided to three main categories: static and dynamic pressure distribution measurements, and numerical modelling.

The static pressure distribution has been experimentally monitored by a ball pressure method (Tumbrink, 1989) and via pressure sensitive films, e.g. Fuji film, or Pressurex Super Low pressure indicating film (Bakar, 2012), (Samie and Sheridan, 1990), (Park et al., 2016). Other methods not used in braking systems include PET (Polyethyleneterephtalate) films, transferred oil films and an ultrasound reflection (Bakar, 2012).

On the other hand, methods for measuring the dynamic pressure distribution did not exist until the 2000's. Probably the first researchers were (Degenstein and Winner, 2006) who used four Kistler force sensors, each integrated in one of the pad corners, to measure forces acting in the contact surface. Although this method did not allow monitoring of the pressure distribution, it was possible to calculate position of the centre of pressure (CoP). (Fieldhouse et al., 2009) and (Ashraf, 2013) used a pressure sensitive film integrated in a specially adjusted brake pad. This method allowed observation of the pressure distribution at the brake pad/disc interface during braking. (Kim et al., 2015) used a capacitive pressure sensor (PPS, Inc.) embedded between the friction material and backplate to monitor the dynamic pressure distribution at the pad/disc interface. Today, PPS Inc. offers a complete system featuring a brake pad equipped with embedded sensors to measure the pressure distribution during braking (PPS Inc., 2017). Also, one of the functionalities of the new ITT Smart pad presented at EuroBrake 2017 is its ability to measure the CoP position (The Brake Report, 2017).

Numerical modelling of the pressure distribution became popular recently, mainly because of advances on contact interpretation made in finite-element (FE) softwares. From earlier works, (Samie and Sheridan, 1990) developed an FE model of a brake with a two-piston sliding caliper to investigate pressure distributions at the inboard and outboard pad/disc interfaces. They used complementarity equations for a gap between adjacent nodes to define the contact interfaces and developed an iteration scheme to calculate the nonlinear system of equations for each contact problem. Finally, the FE model was validated by measuring the pad/disc static pressure distribution using a pressure sensitive paper. They found a good correlation between the measured and computed results.

(Tirovic and Day, 1991) used multiple three-dimensional (3D) FE models of various complexity to study effects of friction material compressibility, backplate stiffness, friction coefficient, caliper flexure, piston/caliper bore contact, caliper position, and disc stiffness on the pressure distribution. The results confirmed previous two-dimensional (2D) numerical studies and experimental work, demonstrating that the friction material compressibility and backplate stiffness contribute significantly to the uniform pressure distribution. Also, an application of forces spread over the pad, such as in the outboard pad of a sliding caliper, should be favoured to a single piston position acting at the centre of the pad. Adding dynamic friction forces showed that the peak of the pressure distribution shifted to the leading side of the pad. It is suggested that spragging leading to higher noise propensity might occur depending on the position of the friction forces with respect to the abutment points. Further it was shown that the caliper tends to open under actuation forces, which can change the interface pressure distribution depending on the caliper constraints. It was also noted that the disc deflection from the mechanical load is significantly smaller than the deformation caused by the thermal load, therefore the heat effects should be included in the analysis to reflect better the reality.

Further numerical models to study pressure distribution at the pad/disc interface were developed by (Bakar, 2012), (Hassan, 2009), or (Ashraf, 2013).

2.4.2 Friction Models

To generate brake torque, a friction brake uses the principle of dry friction between two surfaces (Tirovic et al., 2018). Friction acts as a resistance to relative motion between two sliding surfaces and its existence is independent on the magnitude of the relative motion. The two major processes developing at the contact area are: the energy is transmitted from one surface to the other and the energy of relative motion is dissipated (Akay, 2002). Friction and wear are caused by three main mechanisms: adhesion, abrasion and deformation (Day, 2014).

Most of the friction models, used in the brake system context, are based on the classical friction model. The reason for this is that the brake models are so complex that the acquired benefit from inclusion of detailed friction models is not worth the additional computational costs. Therefore, a simple friction model, with adequate correlation to experiments, can be used to predict squealing (Bakar, 2012). The classical friction model

is based on the Amontons' laws (Kinkaid et al., 2003):

$$\mathbf{F}_f = F_f \mathbf{t} = -\mu N \frac{\mathbf{v}_s}{\|\mathbf{v}_s\|}, \tag{2.2}$$

where F_f is the friction force, μ represents the friction coefficient, N is the normal force and $\mathbf{v}_s$ is a vector of sliding speed according to $\mathbf{v}_s = v_s \mathbf{t}$. Later, Coulomb also suggested that the friction coefficient μ may depend on the sliding speed v_s. However, this relation is explained by some authors to be only apparent due to normal displacement between contact bodies (Kinkaid et al., 2003). Therefore, in many models it is assumed that μ is constant.

More advanced models are represented by state-dependent friction laws (Mastinu, 2013), for instance the Dahl or the LuGre models.

2.4.3 Wear Effects

Numerous studies have been made on the effect of wear on brake squeal occurrence. It has been shown that wear has a great influence on triggering and removal of the squeal, but it is still not known how to implement this effect in squeal prediction (Tirovic et al., 2018). The condition of the pad surface is therefore intensively studied in the research community either experimentally or by modelling. Most of the simulations are based on the adjustments of the nodal positions calculated by a wear formula. For instance, (Bakar, 2012) determined the wear displacement w_d by including the disc sliding time t as following:

$$w_d = k_r p r_m \omega t \qquad \text{(m)} \tag{2.3}$$

where k_r is the specific wear rate, p is the contact pressure, r_m is the mean radius, and ω is the disc angular speed. (Bakar, 2012) used the specific wear rate k_r=1.78x10^{-13} m^3/Nm determined by (Jang et al., 2004) for a friction material with steel fibers sliding on a cast iron disc. Depending on the complexity, other effects can be also added to the wear formula, such as hardness of the softer material at the pad/disc interface (Kinkaid et al., 2003).

(Kao et al., 1994) noted that wear is proportional to load and inversely proportional to the hardness of the friction material. Moreover, wear increases with temperature, usually due to decrease in hardness of the material being worn. They included wear in the formulation of a newly developed finite element as a function of pressure and temperature in each node.

(Tirovic and Day, 1991) also pointed out the influence of the pressure and temperature on pad wear, causing the regions with higher pressure and temperature to wear faster. In disc brakes, a higher thermal expansion in the centre of the pad increases the local contact pressure, causing this part of the pad to wear faster which can eventually lead to an edge contact after cooling, an effect known in a drum brake as toe and heel contact.

As shown in Figure 1.1, during braking the uneven pressure distribution at the pad/disc interface is slightly offset to the leading side causing the pad to develop a

tangential tapered wear (Yue and Zhang, 2009). The wear also causes the pad to lose some of its mass and thickness, which forces the pistons to move out further from the caliper bores (Millner, 1978). This contributes to a change of geometrical constraints and material parameters of the brake system and potential squeal propensity.

2.5 Brake Squeal Theories

Brake squeal can be annoyingly elusive (Spurr, 1961). Not every braking action triggers brake squeal, and it is rather evident that this phenomenon is intermittent or probably even random (Kinkaid et al., 2003). Therefore, it has been very difficult for many investigators over the past decades to understand brake squeal. The current research community is in agreement that the brake system dynamic instability is the fundamental cause of the brake squeal generation (Tirovic et al., 2018). Five main hypotheses on brake squeal mechanisms can be categorised: stick-slip, negative damping, sprag-slip, modal coupling, and hammering excitation theory (Chen, 2006).

2.5.1 Stick-Slip Theory

The stick-slip theory or sometimes used interchangeably with negative $\mu - v$ characteristic, or $\frac{d\mu}{dv_s} < 0$ theory was first examined by (Mills, 1938), who studied various combinations of brake lining materials and noted that a necessary condition for a brake to squeal is the presence of the coefficient of friction μ that decreases with increasing sliding speed v_s (Kinkaid et al., 2003). The necessary condition can be also described as a difference between the static and dynamic coefficients of friction (Chen, 2006). The stick-slip theory was popular in the early stages of brake squeal research, but now there is a little attention devoted to this mechanism, mostly due to later experiments that found no correlation between the negative slope of friction coefficient and squeal occurrence. Moreover, this theory cannot explain why squeal behaviour is different when the same friction pair is mounted in different brake systems (Dihua and Dongying, 1998). Despite this, the stick-slip theory can still explain some other brake noise categories in the lower frequency spectrum, such as *groan* (Day, 2014).

2.5.2 Negative Damping Theory

According to the negative damping theory, the negative damping accumulates the vibration energy to increase the proneness to squeal, whereas the positive damping dissipates the vibration energy (Chen, 2006). The negative damping often emerges due to the negative slope of the friction force with respect to the velocity vector. This can result in a system matrix with positive real parts, which indicates an unstable system (Abdelhamid, 1995). The system damping is also influenced by damping of pads, rotor and a caliper. The pad damping is often represented by viscoelastic material damping, Coulomb friction damping and isolation mechanism (Chen, 2006). These are in practice usually achieved by adding insulators to the pad. Since brake squeal is often described

as a phenomenon of non-linear dynamic instability, the commonly used linear methods do not characterise the real behaviour of the system during squeal occurrence. The non-linearity in a brake system arises from the friction interface (friction and normal forces) and contact stiffness. A non-linear representation of a brake system can have the following form (Chen, 2006):

$$\mathbf{M}\ddot{\mathbf{X}} + \mathbf{C}\dot{\mathbf{X}} + \mathbf{K}\mathbf{X} = \mathbf{F}_f(\mathbf{X}, \dot{\mathbf{X}}) + \mathbf{F}_e(t) \tag{2.4}$$

where $\mathbf{M}$ denotes the mass matrix, $\mathbf{C}$ and $\mathbf{K}$ are the damping and stiffness matrices, respectively. $\mathbf{F}_f$ represents the non-linear damping and restoration forces, and $\mathbf{F}_e(t)$ is an external excitation.

2.5.3 Sprag-Slip Theory

The sprag-slip theory is often referred to as a *kinematic constraint* or a *geometrically induced vibration* (Kinkaid et al., 2003). According to the sprag-slip theory, brake squeal is dependent on the magnitude of the friction coefficient and position of the friction force with respect to the abutment points (Spurr, 1961) and can be generated even with a constant friction coefficient μ (Dihua and Dongying, 1998). Figure 2.9 shows a cantilever experiment as it was originally proposed by Spurr (Fieldhouse et al., 2009). The rigid

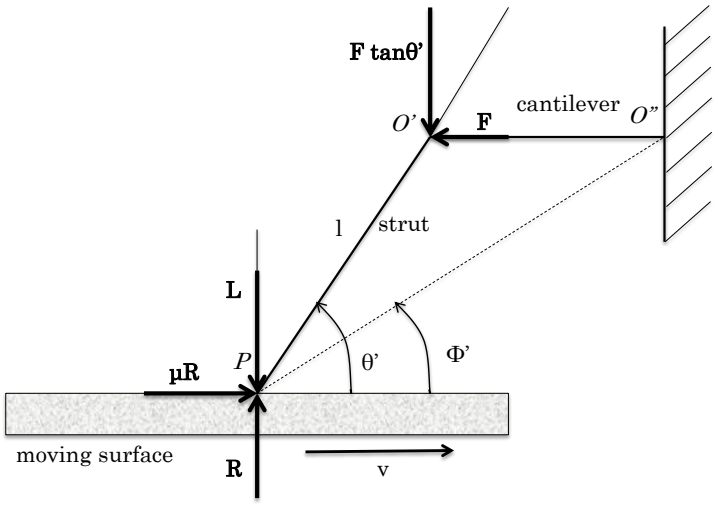

Figure 2.9: Sprag-slip model as suggested by Spurr (According to (Fieldhouse et al., 2009))

lever $O'P$ touches the rotating disc in point P and is loaded with a normal force L. A second cantilever $O''O'$ introduces the flexibility in the system so that the point O' can move under load. Resolving the vertical forces and moment equilibrium about O' gives:

$$\mathrm{F} = \frac{\mu \mathrm{L}}{(1 - \mu \tan \theta')} \tag{2.5}$$

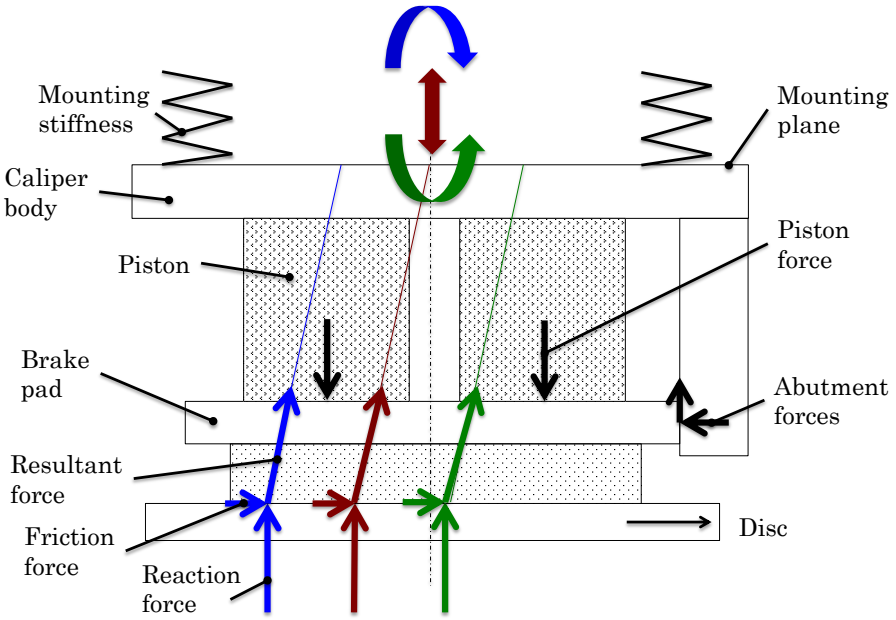

Figure 2.10: Forces at the pad-disc interface explaining the sprag theory (According to (Fieldhouse et al., 2009))

It can be seen that if μ approaches $\cot\theta'$, F tends towards infinity, which can eventually trigger the spragging and the onset of squeal (Day, 2014). This would last until the sprag angle is reduced by flexibility of the second cantilever (Fieldhouse et al., 2009).

The sprag-slip theory was further elaborated in other studies, for example, the position of the point O' can be associated with the caliper mounting as illustrated in Figure 2.10. In this case, noise could be triggered by the resultant force that is intersecting the mounting points symmetry line with the caliper mounting plane. For instance, the red resultant force crosses the symmetry line, causing only a vertical motion of the caliper body. When the resultant force has some offset (blue and green), the caliper body performs a rotational motion. (Fieldhouse et al., 2009) were experimenting with the position of the resultant force by changing the piston pressures in a multi piston opposed caliper. The results suggest that if the resultant force periodically moves between the two extremes (red and either blue or green case), it causes the rise of the normal reaction and friction force at the pad/disc interface, which could be a potential source of vibration.

2.5.4 Modal Coupling Theory

The modal coupling theory has been studied since 1994, first mostly on pin-on-disc or beam-on-disc models. This theory states that when two aligned modes of a brake system are coupled with each other, the system becomes unstable and this can cause squeal. The coupled modes are either modes within one component, e.g. out-of-plane and in-plane modes of a brake disc, or modes between other brake components, e.g. between the disc and the pad. Figure 2.11 illustrates potential coupling of an in-plane and out-of-plane mode in a brake disc. Whether two aligned modes become coupled or not, depends on proper vibration-phase relationship induced by the friction force or interface condition. A

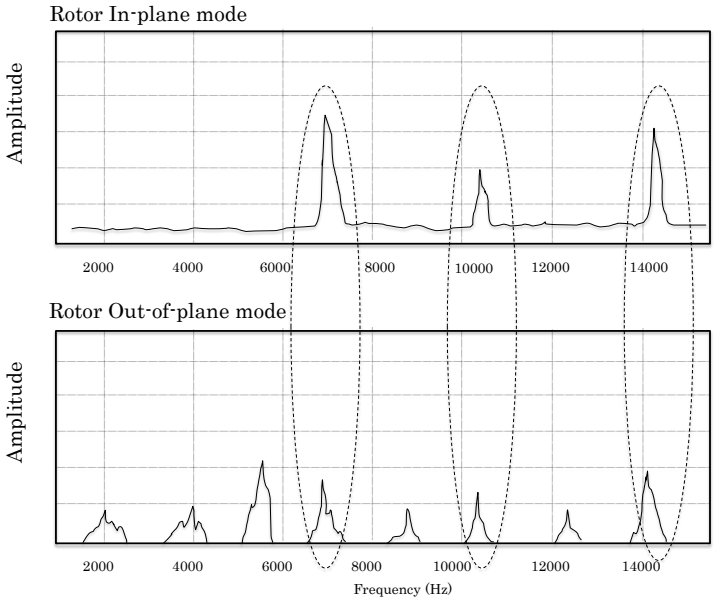

Figure 2.11: Illustration of potential coupled pairs of an in-plane and out-of-plane mode in a brake disc (According to (Chen, 2006)).

certain critical value of the contact forces can cause coupling of the two modes and the system becomes unstable (Abdelhamid, 1995). The modal coupling can be achieved, for example, by presence of close split modes from the doublet of the rotor or by aligning the in-plane and out-of-plane modes of a rotor. In recent studies it has been shown that a deliberate disc mode separation contributed to the reduction of squeal propensity (Chen, 2006).

2.5.5 Hammering Excitation Theory

The hammering theory is based on the observation that brake squeal frequency is similar to the natural frequencies of brake components, which led to the development of a mechanical impact model called *hammering* to describe the onset of brake noise (Kinkaid et al., 2003). The theory was first proposed by (Rhee et al., 1989) who also suggested several hammering mechanisms, such as disc imperfections and spragging. The first can be explained by a relative sliding motion of the pad over the disc surface having macroscopic waviness as a result of a thermal or mechanical distortion. The rocking motion of the pad might trigger the hammering of the disc or caliper and gradually other system components, which can eventually excite some of these elements into natural modes of vibration. The spragging and resulting unstable interactions between the components may cause the hammering excitation leading to squeal (Kinkaid et al., 2003).

2.5.6 Other Brake Squeal Theories

There can be found a variety of other theories in the literature explaining the onset of brake squeal. For example, the stick-slip theory can be combined with the sprag-slip

theory and used as a model to determine the instabilities in a brake system (Mastinu, 2013). In 1972, the term flutter instability as a possible theory of brake squeal occurrence was coined (North, 1972). Other theories include bifurcation and thermo-elastic dynamic instability (Mastinu, 2013).

2.6 Experimental Methods of Squeal Determination

Brake noise is a result of vibration of the brake components, therefore the majority of experimental methods are focused on its monitoring. The most common techniques to measure the vibration of brake systems are as follows (Mastinu, 2013):

- Measuring of displacements and velocities
- Double pulse holographic interferometry
- Electronic speckle pattern interferometry
- Laser vibrometer
- Scanning laser vibrometer

Important outcomes from the number of brake noise experiments found in literature are summarised below (Mastinu, 2013), (Kinkaid et al., 2003):

- A brake system can squeal at several distinct frequencies.
- Amplitudes during squealing can achieve an order of 0.1 mm.
- Standing and travelling waves can rotate around the disc.
- Brake noise propensity is usually influenced by disc velocity, brake pressure and the pad/disc friction coefficient.
- The natural frequencies of the disc are slightly higher than the squealing frequencies.
- The higher the coefficient of friction, the higher the propensity for squeal.
- It is not known which component contributes the most to squeal.
- It was not demonstrated that knowledge about stationary uncoupled modes of the disc, pads or caliper is sufficient to predict squeal frequencies. However, it was observed that the squeal frequency is close to one of the disc natural frequencies.

A number of classical experiments are reviewed by (Kinkaid et al., 2003). One of the first investigators in this field was (Mills, 1938) who performed a series of experiments in an attempt to show a relation of squeal to the decreasing coefficient of friction with increasing sliding velocity; however he did not draw any definitive conclusion. (Fosberry and Holubecki, 1959) could not confirm a complete correlation of brake squeal occurrence with decreasing $\mu(v_s)$ function. They also found that during squeal pads vibrate with

similar amplitude as the brake disc whereas the caliper oscillates with a smaller amplitude and in a more complex way. Other classical experiments were carried out by (Spurr, 1961) who demonstrated his sprag/slip theory on a modified pad that contacted the rotor only on a narrow strip located towards the leading end of the pad. He observed that only this position of the friction contact could generate the squeal. (North, 1972) was the first researcher who correlated a brake model with experiments, reporting a very good prediction of the model. He used accelerometers to measure the vibrations of the pads and the caliper, and a vibration meter to determine the oscillations of the disc.

Later, (Felske et al., 1978), (Murakami et al., 1984), and (Nishiwaki et al., 1989) began to use double pulse holographic interferometry to investigate brake systems during squealing. This method gave more insight into the disc mode shapes during squeal, especially the existence of diametral nodes. They all concluded that the whole brake assembly vibrated during squealing. (Fieldhouse and Newcomb, 1993) also observed diametral nodes during squeal, and in addition they found travelling waves rotating around the disc. The rate of the wave rotation coincided with the squeal frequency divided by the diametral mode order.

Other research studies include (Matsuzaki and Izumihara, 1993), who demonstrated that the audible squeal has a better agreement with an longitudinal (in-plane) disc vibration rather than bending (out-of-plane) modes. Later, (Dunlap et al., 1999b) confirmed the existence of the in-plane vibration during high frequency squeal, and (Chen et al., 2002) demonstrated that a coupling between the in-plane and out-of-plane modes can trigger squeal.

From more recent studies it is worth mentioning the work from (Shimizu et al., 2014) who performed a range of SAE J2521 noise tests to study the influence of shims and grease on brake squeal generation. They found that adding shims on the backplates could eliminate the high-frequency squeal (pad bending mode) by increasing damping between the backplate and the shim. On the other hand, it was possible to suppress the low-frequency squeal (pad rigid mode) by adding grease between the shim and the piston or caliper fingers. It is explained that application of grease allows the backplates to abut in the caliper body, which increases the stiffness of the system. Furthermore, it was demonstrated that the adhesive shim was a more effective way to eliminate squeal than the clip-on shim.

(Blaschke et al., 2015) compared several approaches of Experimental Modal Analysis (EMA): disc in free-free condition, pad in free-free and grounded condition, pad/disc and pad/disc/piston assembly with weak and high clamping forces. They successfully extracted mode shapes up to 6 kHz for all configurations and concluded that mounting and different clamping forces influenced the modal frequencies.

(Ostermeyer et al., 2015) carried out several experiments on a full- and reduced-scale dynamometer to find correlation between squeal and friction coefficient. They concluded that a clear correlation was not observed and that the friction is a necessary but not the only parameter important for squealing.

(Jarnestrom et al., 2015) compared two different shim designs and their effectiveness

to reduce squeal. They found that in contrast to the bonded shim, the floating style is more effective in squeal reduction for a frequency range 1 - 4 kHz. Further, it was observed that use of a PTFE-coated (Polytetrafluoroethylene) shim gives better results than a floating shim with grease. This is probably due to some deterioration of the grease over time.

An interesting investigation was made by (Stegmann et al., 2015) who performed an experimental modal analysis (EMA) using an integrated piezoelectric actuator in the brake piston and the system response was measured with acceleration sensors. Two approaches to analyse resonance frequencies were used, namely frequency-response-function (FRF) and complex mode indicator function (CMIF). In addition, a new concept of friction force measurement was presented in which a piezoelectric force sensor was attached to an abutment of the caliper and used to measure the tangential part of the friction force. In their future work, the possibility of inclusion of radial part of the friction force will be investigated.

(Yue and Zhang, 2009) developed an analytical and a CAE model, and performed tests on a dynamometer and vehicle to demonstrate the influence of the friction properties of the secondary contact interfaces on squeal propensity. They found that the low-frequency squeal propensity as well as the tangential taper wear can be minimised by reducing the friction coefficient at the pad/piston and pad/caliper finger. This is in accordance with the findings from (Shimizu et al., 2014) who observed reduction of the squeal when they reduced the friction coefficient at these interfaces by applying grease.

2.6.1 Monitoring of Pressure Distribution at Pad/Disc Interface

Recent studies have shown that there is an evident relation between the position of the centre of pressure (CoP) at the brake pad/disc interface and the brake propensity to generate squeal. (Fieldhouse et al., 2009) and (Ashraf, 2013)) used a 12-piston opposed caliper actuated by a series of hand valves to control the position of the CoP. The piston chambers were connected in such manner that they allowed the CoP to move in both circumferential and radial direction. To determine the instantaneous position of the CoP during a braking event, they developed an embedded brake pad sensor, which featured a pressure sensitive film inserted between the backplate and a friction material plug. A series of noise tests showed that speed had little effect on the CoP position while an increase of pressure invoked moving of the CoP towards the trailing edge. A light pressure setting and a uniform distribution of the piston forces demonstrated that the CoP tends to be leading which generated loud squeal. It was observed that a quiet brake would be obtained with a central or trailing CoP and radially displaced outwards from the centre of the pad. In turn, the area of maximum instability is when the CoP is at the leading edge and radially close to the centreline of the pad (Figure 2.12). This area was related to a CoP position where spragging is likely to occur which could be why such brakes tend to squeal. Furthermore, it was observed that the inboard pad appears to be loaded more than the outboard one. To reduce the brake propensity to noise generation, it was

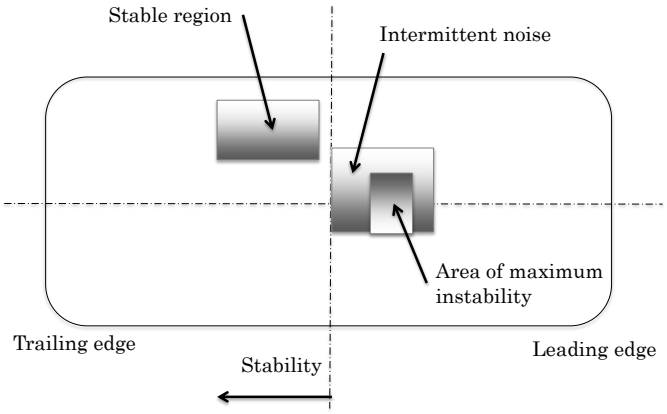

Figure 2.12: Illustration of potential stable and instable regions of the CoP on the brake pad (According to (Fieldhouse et al., 2009)).

suggested to design the caliper mounting with a permanent trailing offset of the CoP. (Fieldhouse et al., 2009) noted that his future research will be aimed at these possible caliper mounting arrangements along with the geometry of the abutments.

In contrast to the pressure sensitive films, (Degenstein and Winner, 2006) used SlimLine piezoelectric quartz Kistler sensors which were integrated in the brake pad, allowing determination of the point of application and magnitude of the resultant clamping force. This method, however, does not show the pressure distribution at the pad/disc interface. To keep temperature of the sensors within limits (below 120° C), an air cooling system was provided at the test bench. The results showed that during braking the point of application of the load moved towards the leading edge and increasing the line pressure from 10 to 60 bar caused a significant movement radially outwards. This justifies the allowance of 10% error when calculating the pad/disc friction coefficient if assuming a constant effective radius.

(Kim et al., 2015) used a dynamic capacitive pressure sensor developed by PPS, Inc. inserted between the friction material and backplate to measure pressure distribution at the inboard and outboard pad for a variety of driving conditions. They attributed the variations of the CoP positions for the inboard and outboard pad to the different geometry of the caliper finger and piston side. By analysing the influence of chamfer size on pressure distribution, they found that larger chamfers resulted in more even pressure distribution. On the other hand, the number of slots did not show any correlation with uniformity of the pressure distribution. The measured dynamic pressure distributions were used to improve an FE model of the brake. It was found that the updated model showed a better ability to predict squeal.

From more recent studies, (Park et al., 2016) designed a four-piston opposed laboratory caliper, which is capable of independent pressure setting in each piston, to study the influence of the leading and trailing offset on squeal occurrence. It was observed that squeal was readily generated with a higher pressure value at the leading side resulting in a leading offset. The study does not include monitoring of the CoP position. Corresponding

CEA and transient analysis models were created to replicate the measured tests, whereby it was found that the transient analysis better correlates to the real tests.

2.7 Analytical Modelling Techniques

Since 1963 when Mills introduced his first detailed analysis on disc brake squeal, numerous analytical models of a brake system have been developed featuring different numbers of degrees-of-freedom (DOF), various contact definitions and disc model complexity (Kinkaid et al., 2003). These models are sometimes referred to as *lumped-parameter* (Mastinu, 2013), *distributed-parameter* (Flint and Hulten, 2002), *theoretical* or *minimal* models.

Reviews on analytical modelling of brake systems have been made by (Kinkaid et al., 2003), (Wagner et al., 2007), and Cantoni et al. (in (Mastinu, 2013)). A chronological survey of some important analytical models is presented below:

- The analytical model of (Jarvis et al., 1963) showing that the disc vibration consists of at least two vibrations of the same order and with different phases. Moreover, they found that the existence of the disc vibration is due to the geometric configuration of the coupling between the disc and the pad, rather than due to the variation of friction coefficient. This finding had a significant influence on following researchers (Flint and Hulten, 2002).
- The binary-flutter models of (North, 1972). For the first time, brake squeal was considered to be a self-excited vibration induced by a friction force with a constant friction coefficient.
- The four-DOF pin-on-disc model of (Earles, 1977) demonstrating the essential characteristics of the squeal found in a disc brake. It showed that the squeal generated using this model resulted from instabilities induced either geometrically or by kinematic constraints.
- A five-DOF model developed by (Millner, 1978) including a fixed caliper allowing variations of the mass and stiffness parameters, as well as modification of the pad/piston position.
- A seven-DOF model developed by (Murakami et al., 1984) consisting of a disc, a pair of pads, piston and a sliding caliper. This detailed model allowed for variations of numerous parameters to study squeal mechanism.
- A simple three-DOF model developed by (Matsui et al., 1992), which comprised a caliper, a pad and a rotor allowing the modelling of a self-excited mechanism with a feedback system.
- A complex twelve-DOF model developed by (Brooks et al., 1993) was used to investigate squeal onset using an eigenvalue sensitivity analysis.
- A minimal two-DOF model (Figure 2.13) by (Hoffmann et al., 2002) to clarify the modal coupling instability.
- A minimal model by (Shin et al., 2002) to explain self-excited vibrations using the stick-slip and negative $\mu - v$ theory.

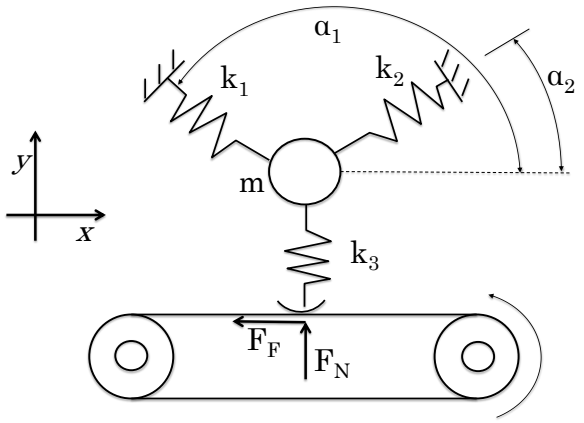

Figure 2.13: A minimal two DOF model developed by Hoffmann (According to (Hoffmann et al., 2002)).

- A multi-DOF model of a brake assembly developed by (Flint and Hulten, 2002), in which the disc and pads are modelled as continuous elements and pistons and caliper body as rigid bodies. The contact between the disc and pads is represented by an infinite number of spring elements.
- A twelve-DOF non-linear model presented by (Wagner et al., 2004) with a disc modelled as a flexible rotating plate.
- A four-DOF model by (Kinkaid et al., 2005), which was used to propose a new mechanism of disc brake squeal. Although being similar to the friction-induced origin of brake squeal, the new mechanism included the transient analysis of the braking event.
- A new model, which contains a wobbling disc (Kirchoff plate) and two pads with a point contact, developed by (Wagner et al., 2007).
- A two-DOF model developed by (Chu et al., 2018) is based on the CEA results from a FE model. As a representative system an unstable mode with seven nodal diameters is used as an example. The response surface method was employed to determine the kinematic parameters, resulting in a parameter-optimised model. Then, a transient analysis was conducted to study the influence of braking velocity on stability of the brake system.

Low-frequency squeal can be modelled using models with rigid pads, for instance, the model of North, Millner, Brooks or Rudolp and Popp as the disc nodal distance during this type of squeal is larger than the pad length, whereas in the high-frequency squeal the pad bending becomes important so it is suggested to use a sprag/slip model such as the Earles's pin-on-disc model (Kinkaid et al., 2003).

2.8 Numerical Modelling Techniques

Numerical modelling techniques can be dated back to 1989, when (Liles, 1989) developed a 3D finite-element (FE) model of a disc brake (Bakar, 2012), which was validated using an experimental modal analysis (EMA), (Kinkaid et al., 2003). Later, (Nack, 1999) derived a non-linear analysis of brake noise using a FE model. The first researchers in this field struggled with the contact area definition, therefore many models featured only point contact between the disc and pads and the disc was stationary (Mastinu, 2013). Since then, software such as ABAQUS® or ANSYS® have improved in terms of the contact interactions or inclusion of thermal phenomena, and now allow a variety of different techniques to be used in the brake modelling. However, the duration of the simulations and computational memory load are still immense. Therefore many researchers reduce the complexity of their models via neglecting some physical phenomena in brake systems, e.g. use of isothermal models, assuming perfect surface contact between the disc and the pad, no wear, etc.

2.8.1 Complex Eigenvalue Analysis

The complex eigenvalue analysis (CEA) computes complex eigenvalues of the brake model that are used to determine the unstable modes of vibration and their frequencies. The eigenvalue problem of a FE model can be formulated as (Abaqus-2, 2018):

$$(\lambda^2 M^{ij} + \lambda C^{ij} + K^{ij})\phi^j = 0 \tag{2.6}$$

where M is the mass matrix, C is the damping matrix, K is the stiffness matrix, λ is the eigenvalue, and ϕ is the eigenvector representing the mode of vibration. i and j are the dimensions of the system. A general solution of this system would include complex eigenvalues and eigenvectors. In ABAQUS®, this procedure is based on the subspace projection technique, hence natural frequencies (eigenvalues) must be extracted prior the complex eigenvalue step.

Eigenvalue Extraction

The eigenvalue extraction step requires the system to be symmetrised, which is achieved by assuming that K is symmetric and by neglecting C (Abaqus-2, 2018). Then, the new system has only real squared eigenvalues λ^2 and real eigenvectors ϕ. By further assuming that K is positive semidefinite, λ can be expressed as $\lambda = i\omega$, where ω denotes the circular frequency. Then, the original Eq. 2.6 can be written using matrix notation as:

$$(-\omega^2[M] + [K])\{\phi\} = 0 \tag{2.7}$$

For the contact problems, the Lagrange multipliers are included in the system of equations and the stiffness matrix K becomes indefinite. However, the Lagrange multipliers are equal to zero and the system of equations can be still represented by Eq. 2.7. This

procedure can be solved by defining the step `*FREQUENCY,` in the ABAQUS® input file.

Complex Eigenvalue Extraction

In the complex eigenvalue extraction step, the subspace projection technique is used to solve the complex eigenvalues as defined in the original system by Eq. 2.6. The original system is projected to the subspace that is created during the eigenvalue extraction. This requires definition of the mass, stiffness and damping matrices as follows:

$$[M^*] = [\phi_1, ..., \phi_N]^T [M][\phi_1, ..., \phi_N] \tag{2.8}$$

$$[C^*] = [\phi_1, ..., \phi_N]^T [C][\phi_1, ..., \phi_N] \tag{2.9}$$

$$[K^*] = [\phi_1, ..., \phi_N]^T [K][\phi_1, ..., \phi_N] \tag{2.10}$$

Then, Eq. 2.6 can be written as:

$$(\lambda^2[M^*] + \lambda[C^*] + [K^*])\{\phi^*\} = 0 \tag{2.11}$$

The eigenvectors can be extracted from:

$$\phi^k = [\phi_1, ..., \phi_N]\{\phi^*\}^k \tag{2.12}$$

where $\{\phi\}^k$ is the approximation of k-th right eigenvector of the original system.
The complex eigenvalue extraction explained above can be performed by defining the complex eigenvalue step `*COMPLEX FREQUENCY,` that follows the eigenfrequency extraction step. By including the option `*COMPLEX FREQUENCY, FRICTION DAMPING=YES` in the input file, software automatically detects the slipping nodes due to velocity differences at the contact interface and implements friction damping contributions to the damping matrix (Abaqus, 2012). ABAQUS® specifies two main types of friction damping effect. Whereas the first effect uses the friction forces to stabilise the vibrations in the perpendicular direction to the slip direction, the second effect can cause a destabilising effect known as negative damping if a velocity-dependent friction coefficient is defined.

The effects of motion are included in the complex eigenvalue step, if they are defined in a preceding general step by one of these keywords `*MOTION, ROTATION` or `TRANSLATION`. Similarly, the applied loads can be propagated to the complex eigenvalue step, if the non-linear geometric effects `*STEP(,NLGEOM)` are included in the step defining the loads. The same boundary conditions as defined in the step preceding the natural frequency analysis are included in the complex eigenvalue step.

The complex eigenvalue extraction allows the extraction of the real α and imaginary ω part of the eigenvalues, as well as the frequencies (cycles/time) and the damping ratio. These values can be automatically written to the output .dat and .odb file. To determine potential unstable modes of vibration, the real part of the complex eigenvalue α can be used to predict the unstability of the system. The system becomes unstable, if the real

part of the complex eigenvalue α is positive, while the magnitude of the real part typically indicates the level of the system instability. Alternatively, the negative damping ratio $c_{ratio} = -2\frac{Re(\lambda)}{Im(\lambda)}$ can be used as a precursor for an unstable mode.

2.8.2 Isothermal Models

Isothermal models of brake systems are typically developed to investigate pressure distributions at the pad/disc interface, or to carry out complex eigenvalue analysis (CEA) in the frequency domain or transient analysis in the time domain. Assuming that the phenomenon is periodic, the transient time domain results can be converted to the frequency domain using fast Fourier transformation (Mastinu, 2013). An alternative approach can include evaluation of the Routh-Hurwitz criterion that determines the stability of the system. However this method does not provide information on how the system should be modified to remove the instability (Liles, 1989).

The transient analysis includes the non-linear behaviour of the brakes compared to the CEA analysis in which the equations are linearised and solved at quasi-static conditions. On the other hand, CEA analysis can find all unstable eigenvalues and modes in one run and the computational cost is relatively low.

Using a FE model, (Mahajan et al., 1999) compared three different methods for prediction of squeal frequencies: non-linear transient analysis, component modal nodes using modal locking theory, and CEA. He found that the non-linear transient analysis provided good agreement with the experimental data, while the normal modes method represents a cost efficient way to implement changes during the design. The limitations of each method need to be recognised and several methods must be used in conjunction to reduce the squeal propensity.

(Soh and Yoo, 2010) studied possibility of reducing the squeal propensity by changing caliper designs. They carried out several parametric simulations with a sliding caliper and found that an optimal design is a caliper with asymmetric finger shapes. This configuration reduced dynamic instability by about 22%.

(Bakar, 2012) used a real surface topography in his FE model. He found that this improved the correlation with the experimental results at the contact level. The use of a perfect contact interface model showed a significant difference in static contact pressure distribution between the model and the experiment. In terms of the real surface topography, the surface was measured at the specific nodal positions using a linear gauge. He used three stages of the correlation to validate the model: the component level, the assembly level, and through the contact analysis. A simplified wear formula was implemented in his model and it was found that the predicted unstable frequencies seemed to appear and disappear through the wearing process, which was considered to be one of the reasons why squeal is so fugitive. He developed his FE model in ABAQUS® and proposed several useful contact interface settings: the surface-to-surface contact interface gives more accurate prediction of contact pressure, the small sliding compared to the finite sliding contact saves computational time without affecting the results, the penalty

method is faster than the use of Lagrange multipliers and the results remain identical. Bakar developed a high-quality FE model and showed interesting results of the brake squeal behaviour, however his model lacked several details which could influence the squeal prediction: 1) his model was isothermal, 2) the validation at the component level was made only for the disc, 3) he used spring-to-spring contact between other elements, the use of surface-to-surface contact might be a better solution 4) and he used only a simple wear formula.

(Ashraf, 2013) developed a FE model of a brake system in ANSYS containing a disc and brake pads. This model was validated using modal analysis on the component level. Furthermore, the pad/disc contact surface was correlated by means of experimental data acquired from pressure sensors. He performed a CEA to determine natural frequencies and modal shapes of the brake system, followed by a stability analysis to predict unstable modes. Finally, he carried out parametric studies to better understand the squeal behaviour of the brake system.

(Elguezabal et al., 2015) developed a simplified squeal prediction model and compared different mesh elements during a CEA. He found that the best mesh element, that represents a good compromise between the results accuracy and computation cost, was an incompatible mode linear brick element of size 5 mm. Furthermore, he studied an influence of material properties, friction coefficient and friction damping on the squeal prediction using CEA. After implementation of more accurate methods to define material properties (ASTM and SAE standards), he discovered that the brake disc material did not change results significantly, however the friction material properties had great impact on the squeal prediction. Introducing a contact pressure and slip-rate dependent friction coefficient did not influence the results. In turn, a friction damping included in the model showed reducing of some frequencies above 10 kHz and modes with a small positive part.

(Vermot des Roches et al., 2015) introduced damping in their FE model of a railway disc brake and suggested several methods to improve the brake stability estimation.

References to other models can be found in works from (Bakar, 2012), (Kinkaid et al., 2003) and Cantoni et al. (in (Mastinu, 2013)).

2.8.3 Thermal Models

As previously stated, the kinetic energy of the rotating disc during braking is converted into thermal energy via friction at the disc/pad contact surface. The generated heat, often in repeated braking applications, needs to be rapidly dissipated into the environment since high temperatures in the brake components can lead to excessive thermal stress and degradation of the rubbing surface. Pads and discs can normally operate at temperatures up to 800°C (Kao et al., 1994). There are three modes of heat transfer: conduction, convection and radiation. For most road vehicles convection is the most important mode of heat dissipation (Day, 2014). To provide preliminary thermal calculations of a brake, analytical methods can be sufficient, however they often cannot be applied to the real component geometry, material properties or boundary conditions. Therefore, most of the

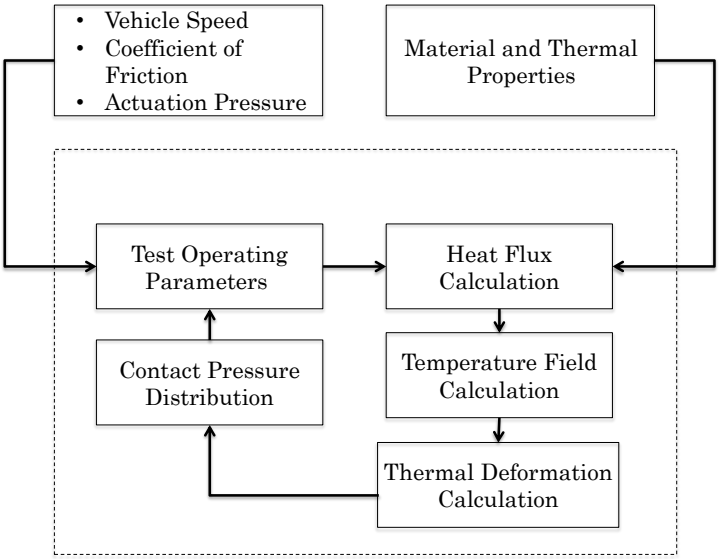

Figure 2.14: Procedure of a coupled thermo-mechanical simulation (According to (Hassan, 2009))

today's brake thermal analyses are carried out using FE modelling. The FE modelling including heat effects can be divided into following types (Hassan, 2009):

- heat transfer analysis
- thermal stress analysis
- coupled thermo-mechanical analysis

Heat transfer and thermal stress have been intensively studied by many researchers and various numerical models have been developed. References to large number of works can be found in (Hassan, 2009) and (Alnaqi, 2014).

A coupled thermo-mechanical analysis predicts the temperatures in brake components and derives a new contact pressure distribution at the pad/disc interface for each time step (Hassan, 2009). The inputs for the heat flux calculation can include the actuation pressure, the friction coefficient, the disc rotational speed, material and thermal properties. A typical simulation procedure is shown in Figure 2.14. The coupled thermo-mechanical analysis have recently gained in popularity since the correlation with the experimental tests gives a good agreement.

(Kao et al., 1994) provided a thermo-mechanical investigation of hot-spot formation in a disc brake using an axisymmetric model with a newly developed finite element for the pad/disc interface. The model also featured non-linear behaviour of materials and a wear formula was included in the new element formulation. In spite of the two-dimensional simplification of the real brake assembly, the results showed a very good correlation with the experimental data.

(Hassan, 2009) developed and validated a fully coupled thermo-mechanical model of the Rover 75 front disc brake assembly, and then performed a CEA to identify possible squealing modes. The model was validated on the component level using a technique called free-free modal analysis. He also showed, that with an introduction of heat effects, the contact pressure distribution evolves with time. Hassan found a good correlation of the squeal frequencies acquired from the numerical modelling with the experimental results carried out using the standard braking test procedure SAE J2521. A parametric study concluded the work which demonstrated that geometry and material properties are important factors that change the propensity for squeal. He noted that an increase in disc cheek thickness and vane number improved the system stability, and also lower values of Young modulus for the disc and the friction material had the same effect. His model showed for the first time the effect of the heat on the brake system stability, however his model lacked inclusion of the whole caliper and the wheel hub, of wear, of real pad surface geometry and also of damping material behaviour.

(Belhocine and Bouchetara, 2012) performed a fully coupled thermo-mechanical analysis of a disc brake rotor during a stop-braking mode. A computational fluid dynamics (CFD) analysis was first used to determine the time evolution of the heat transfer coefficients on the particular surfaces, and the coefficients were subsequently used in the fully coupled simulation. They compared solid and vented discs, different disc materials, and also influence of braking modes on the temperature distribution in the disc. However, they did not carry out any experiments to validate the simulation results.

(Tirovic et al., 2018) developed a complex approach to design new brake assemblies with improved squeal characteristics at early development stage. The methodology contains four clearly defined stages that can improve the data flow and communication between each sector of the brake development and production chain. The first stage is concerned with the free-free modal analysis of the components and characterisation of their material properties. In the second stage, a full FE model of the brake corner is developed using the real geometries of individual components. This stage also includes validation of mechanical analyses provided on the assembly level. The third stage deals with development of a fully coupled thermo-mechanical model of the whole brake system, and in the fourth stage the CEA is conducted. The model was validated through experiments on a brake dynamometer. The results from the CEA and the dynamometer tests correlated very well, showing occurrences of the predicted squeal frequencies of 3 and 6 kHz. It was pointed out that inclusion of the thermal effects in the FE model is important to predict squeal as the squeal propensity can evolve over time due to the thermal loads and changes of the pressure distribution at the pad/disc interface, as well as changes of the friction coefficient and material properties.

2.9 Overview of Brake Squeal Reduction Methods

2.9.1 Geometrical, Properties and Damping Modifications

A very strong excitation mechanism can cause vibration of the system, even if the system exhibits low sensitivity or less modal coupling. In contrast, when the system shows strong coupling, a little excitation force may cause brakes to squeal. Accordingly, there are two main approaches to eliminate the squeal propensity by reducing: 1) the excitation mechanism, and 2) the system sensitivity (Chen, 2006). Some of the methods below listed may belong to both categories:

- **Reduction of the impulsive excitation**
  - Brake pads often contain shims mounted on the backplates to reduce the vibration (Shimizu et al., 2014). To improve damping, some shim designs may have more layers (Kinkaid et al., 2003). Sufficient pad damping reduces impulsive excitation to the sensitive frequencies of the brake system (Chen, 2006).
  - Application of an anti-squeal product on the backplate of the pad assembly increases the viscous damping of the brake system (Kinkaid et al., 2003).
  - Use of a grease between the backplate and pistons affects damping of the system (Kinkaid et al., 2003), and stiffness of the brake assembly (Shimizu et al., 2014).
  - Chamfering of the pads results in a more even pressure distribution at the pad/disc interface and CoP moves from the leading end to the more stable central area of the pad. Moreover, reducing the angular extent of contact has influence on modal coupling between the pad and a disc (Kim et al., 2015).
  - Slotting of the pads (Kinkaid et al., 2003), (Day, 2014).
  - Sanding or re-machining of the brake rotor surfaces removes hot-spots and a potential source of hammering (Kinkaid et al., 2003), (Day, 2014).
  - Application of a lubricant to the pins connecting a sliding caliper with its mounting bracket (Day, 2014).
  - Use of pads with a lower friction coefficient (Liles, 1989).
  - Ensuring of a uniform contact pressure distribution, e.g. by including more pistons. (Chen, 2006)

- **Reduction of the system sensitivity**
  - Decoupling of the caliper and pad modes. In addition, it is recommended to decouple the caliper and the pad modes with the modes of the rotor (Chen, 2006).
  - Decoupling of the rotor in-plane and out-of-plane modes. The ideal case would be placing the in-plane modes in the middle of the out-of-plane modes (Chen, 2006).
  - Splitting the pair modes of the disc to prevent development of the binary

flutter mechanism leading to squeal (Tirovic et al., 2018).
- Increasing of the rotor stiffness (Chen, 2006).
- (Akay, 2002) described methods that relate to adjustments of the brake disc geometry. Radial slits in the disc prevent developing of the circumferential waves, thereby reduce peak amplitudes of the sound. He observed that using longer slits decreased the amplitude and insertion of a metal piece in the slit smoothed the peaks. The bending modes of the rotor were almost completely eliminated using ring dampers around the circumference of the rotor. This is due to the friction induced between the ring and the rotor that eliminated the vibration.

Other approaches may include moving of unstable modes out of audible frequency range, e.g. via coupling of the rotor modes with the modes of other components at higher frequencies (Chen, 2006).

2.9.2 Active Suppression of Brake Squeal

During the past two decades there has been a certain endeavour to tackle brake squeal by adding an actuator or series of actuators to the brake system that would act either against the vibration of the components or would modify geometrical constraints of the brake system.

(Cunefare et al., 2001) used a dither open-loop control to actively eliminate the brake squeal. A piezoelectric stack actuator was placed in the piston where it introduced, during a squeal occurrence, high-frequency (non-audible) disturbance signal into the brake system, and thereby stabilised the non-linear self-oscillations. The system was successful to actively suppress squeal for certain duty cycles.

On the other hand, a closed loop control system to actively suppress brake noise and vibration was investigated by (Hashemi-Dehkordi et al., 2008). He used a lumped model suggested by (Hoffmann et al., 2002) that consisted of a brake pad and a conveyor belt representing a rotating brake disc, and provided a computer simulation to analyse the functionality. The results demonstrated that a pure PID controller reduced, but not completely eliminated the vibration. The combination of an Active Force Control + PID controller technique was also tested and this approach largely reduced the vibration and noise after introducing a disturbance to the system. However, an experiment which would verify the theoretical concept was not provided.

A piezoelectric actuator was also used by (Wagner et al., 2004) and (Hochlenert, 2006) from TU Darmstadt who used "smart pads" with integrated piezoelectric actuators to suppress squeal. They also developed a new minimal model of a brake, consisting of a rotating Kirchhoff plate and two simplified pads touching the plate in one point, that was used as a basis for a more advanced twelve-degree-of-freedom model containing a caliper and a mounting bracket. This model was used to study controllability using various active control methods. It was shown that by applying two control forces to both pads, the system can be controlled. As the control force, the high-frequency piezo-ceramic

actuators and sensors were attached on the backplates. Three control strategies have been tested, namely the Kalman-Bucy filter, the output feedback and the maximal dissipation control. All the control methods successfully, within half a second, suppressed squeal during braking. The maximal dissipation method appeared to be the most appropriate because the approximate squeal frequency alone was enough to extract relevant phase information. Since the squeal frequency is in the range of kHz, the controllers had to be of lower order to enable a real-time closed loop control.

Further studies that can be related to the active control of brake squeal, although in their stage of design developed only for manual control, have already been covered in Section 2.6.1.

2.10 Overview of Studies on Brake Emissions

A comprehensive review on brake particle emissions is provided by (Grigoratos and Martini, 2015) where the commonly used materials of the friction pairs are firstly introduced, followed by an extensive list of research studies on the mass and distribution of the particles. Then research works on the chemical characterization of the brake particles are listed, and the review is concluded with the studies on possible adverse effects of brake particle emissions on human health. The major conclusions of this review can be summarised as follows:

1. Studies that link the adverse effects of the brake particle emissions to human health are still missing, some of the existing works on animals or in-vitro experiments are difficult to extrapolate to humans.
2. Brake particle emissions contribute between 11-21 % to the total traffic-related PM_{10} emissions.
3. Approximately half of the brake particle emissions are airborne PM_{10}, while the rest are left on the traffic road or with an unknown destiny.
4. The most important chemical elements present in the brake wear are Fe, Cu, Ba and Pb, whereas the organic materials have been studied only little.
5. Owing to the diversity of existing brake particle measurement techniques and sampling methodologies, it is difficult to compare the results directly.

Another extensive review on non-exhaust emissions is elaborated by (Thorpe and Harrison, 2008), focusing on physical and chemical properties of the particles and their source tracing. The major difficulty of particle source identification lies in their possible resuspension on the road surface. A reliable tracer of brake particles in the urban environment seems to be presence of Cu and Sb with ratio Cu:Sb of around 5:1.

Some newer research with emphasis on particles assessment and a new testing method development is reported by (Gramstat et al., 2017) who performed brake particle sampling tests using a new enclosure around the brake to avoid particle losses in the test chamber. When using an enclosure, a constant particle concentration was observed during a specific

cycle, which favors use of an enclosure if precise measurements are to be undertaken. Due to thermal radiation from the enclosure surfaces, a temperature difference in the brake lining of 20 K was observed in contrast to the setup without the enclosure, which can be considered as negligible. Direct comparison of different air flow rates also revealed that the lower flow rate lead to a higher measured temperature in the pad, and thus the flow rate has clear impact on the cooling behaviour of the brake. A comparison of different mass inertias showed that a larger comparable vehicle mass emitted higher total particle concentrations. Since a different wheel size and thus cooling behaviour for larger vehicles were not included in this study, it cannot be generally inferred that large vehicles emit more particle emissions.

(Augsburg et al., 2017) used standard test cycles, and a constant volume sampling system to evaluate brake particle concentration number and chemical element analysis. More than half of the emitted particles were smaller than 100 nm and their concentration number was dependent on the setup and whether new brake discs and pads were used or not. It was also shown that the particle sampling efficiency and uniformity is dependent upon the air flow velocity, direction of the rotor rotation and the sampling location.

(Perricone et al., 2016) used a new test stand with an inlet air cleanness control and over-pressurised chamber to ensure that all captured particles originate from the brake materials. The comparison of results with and without clean air supply showed the importance of pumping a clean air to the chamber as otherwise some particle concentrations between stops for specific test conditions could not be discerned. The new test stand was suggested to be used as a standard design to evaluate particle emissions in future regulations. Perricone et al. used a test cycle from (Alemani et al., 2014) and modified it such that it included an interval of 5 minutes between each braking block to clean the chamber from generated particles during a single braking section.

(Agudelo et al., 2017) performed extensive brake emission tests to compare low-metalic and NAO brake pad material formulations, as well as isokinetic and near brake sampling methods, using six different test cycles to show their influence on each setup. It was found that the isokinetic sampling method is more repeatable for different caliper-disc combinations, the low-metallic friction formulations tend to generate more brake emissions and that a threshold temperature in the range 125 to 175° C exists above which brake emissions are increased significantly.

The brake emission monitoring can be linked to studies on brake noise via the brake wear, which as an important factor for brake noise generation. For example, it was shown that a taper pad wear strongly influenced the propensity of the brake to create moan noise by exciting some of the suspension members (Xie et al., 2014). It is worth mentioning that NAO pads with maximum weight content 10% of Cu and Cu alloys can be characterised by relatively low wear and noise propensity when compared with low-steel and semi-metallic pads (Alemani, 2017).

2.11 Review of State of Art

2.11.1 Summary of State of Art

The numerous published research studies on brake noise have shown that this research area is truly interdisciplinary and countless researchers, over decades, have been interested in finding causes, mechanisms and reduction methods of brake noise.

The following points summarise the most important outcomes from the above complex review that may be relevant for the present thesis:

1. Brake squeal remains one of the most frequently occuring brake noise problems. The aim from the scientific community is to develop methodology on how to predict squeal performance of a brake system at an early stage of development to reduce costs linked to potential customer warranty claims.

2. The most annoying type of brake noise is considered to be low-frequency brake squeal (up to 5 kHz) as it coincides with the frequency range in which the human ear is the most sensitive. In addition, during low-frequency squeal more energy is transmitted to the vibrational mode. This leads to special attention from brake engineers to eliminate this type of brake noise in the first place.

3. Brake squeal is very elusive, which represents difficulties to readily generate a squeal event or to repeat results for given operational parameters.

4. The current agreement in the brake community is that squeal is a friction-induced vibration generated from the dynamic instabilities in the system. The brake squeal does not impair the brake performance, it is a comfort-related problem for vehicle occupants and a noise burden for the environment.

5. Generally, the squeal frequency spectrum contains one or two single frequencies, which can be accompanied by one, two, or three harmonics.

6. The brake disc can oscillate in an out-of-plane or a coupled out-of-plane and in-plane mode, whereby the magnitude of the amplitude can reach 0.1 mm. During squeal all brake elements vibrate with the same frequency.

7. Generally, changes at the source of the noise are considered to be the way to solve the noise problem.

8. The SAE J2521 test procedure seems to be so far the most representative out of existing squeal test procedures.

9. The squeal performance changes throughout the pad lifetime and strongly depends on how the brake pad is bedded.

10. In the last two decades, several researchers have managed to monitor dynamic pressure distribution at the pad/disc interface by embedding a pressure sensor

between the backplate and the friction material. Some commercial brake pad instruments already exist or are currently under development.

11. Due to complex geometry of the brake components, as well as numerous friction interfaces and associated boundary conditions, FE modelling techniques seem to better represent the complexity of the real systems and lead to better squeal prediction tools than analytical models.

12. FE models validated on multiple levels show better agreement with experimental data. Typical validating steps include modal analysis on component level, various analyses on assembly level, and heat transfer effects validation.

13. Numerical studies on pressure distribution at the pad/disc interface have become increasingly popular, showing that the friction material compressability and the backplate stiffness have impact on the uniformity of the pressure distribution. During braking the CoP position is shifted to the leading side of the pad due to the existence of the abutment reaction forces and resulting turning moment. This can cause an uneven wear (tapered) and a higher propensity to squeal.

14. The thermal distortion of the disc can be more significant than the mechanical deformation resulting from the actuation forces, which means that in order to improve correlation of an FE model with experiments thermal effects should be included. Good correlation of squeal prediction FE models with experiments are achieved with fully coupled thermo-mechanical FE models.

15. Inclusion of the real surface topography in an FE model improves the squeal prediction. The pad wear has been simulated by many researchers and resulted in better correlation with experimental data. Also, a correct characterisation of friction material properties influences the prediction of unstable modes. Some recent studies also propose the use of damping in the FE models.

16. Multiple theories have been proposed explaining the brake squeal mechanism, of which the most popular are the sprag/slip and the coupling modes theory. The stick/slip theory seems to be outdated as a direct correlation between the negative slope of the friction coefficient and sliding speed and the onset of the squeal was not confirmed. Moreover, this theory cannot explain the variability of squeal performance when the same friction pair is installed in other brake systems.

17. Disc velocity, brake pressure and pad/disc friction coefficient are the main operating parameters that influence the squeal propensity of the brake.

18. Numerous experiments on brake dynamometers have shown that the pressure distribution at the pad/disc interface, and particularly the position of CoP, influences the squeal characteristic of the brake system. A small leading offset of the CoP readily generates squeal.

19. Active suppression of squeal was successfully demonstrated by using a piezoelectric actuator integrated in the pad.

20. There is no standard procedure yet developed to collect and monitor brake particle emissions. Each research laboratory uses their own methods and particle extraction systems. Monitoring the particles can improve the characterisation of the pad wear, which was shown to be an important factor for brake noise generation.

2.11.2 Critical Review of State of Art

Recent experimental studies have shown that the position of the CoP at the pad/disc interface in a disc brake system has an influence on the squeal generation (Fieldhouse et al., 2009), (Park et al., 2016). Fieldhouse et al. and Park et al. varied the brake line pressures and monitored squeal to investigate the relation between the CoP and noise propensity. Although they found that certain CoP positions are more likely to generate squeal, they did not use the actuation systems to automatically change the CoP based on the squeal occurrence. Moreover, the piston bores were integrated in the calipers, so changes of the number or positions of the pistons would require replacement of the whole caliper.

(Fieldhouse and Steel, 2003) also used simple co-planar 2D analytical models of the pad/disc interface to determine the position of the CoP for various types of abutments. Although, the models are helpful to calculate the CoP offset as well as to investigate the influence of pad geometry and friction coefficients at the contacts on potential stability of the brake, the models do not allow determination of the CoP position in the radial direction, which might unveil new areas of pad CoP leading to quieter brake.

(Degenstein and Winner, 2006) used force sensors built into the pad to determine the CoP, whereas (Fieldhouse et al., 2009) and (Kim et al., 2015) used thin-film pressure sensitive sensors integrated between the lining and the backplate, which also allowed visualisation of the pressure distribution. However, the latter can be generally more expensive as a complete pressure mapping system often requires a dedicated DAQ device and software. In addition, the limited space between the lining and backplate might require a specially tailored sensor area.

The active suppression of brake squeal using a dither control was investigated by (Wagner et al., 2004), (Hochlenert, 2006) and (Cunefare et al., 2001). Although it was shown that squeal could be suppressed by introducing an ultrasonic disturbance signal of a certain amplitude, the main disadvantage of such a system is the necessity to implement additional components into the brake system. The large dimensions of the actuators and dither control hardware, connecting cables to the pads as well as the limited space with harsh operating conditions between the lining and backplate could represent difficulties to design a robust system not prone to failure. In addition, it was shown that the dither signal can reduce the effective braking torque by 3 - 5% (Badertscher and Cunefare, 2003), whereas a theoretical model predicted as much as 10% (Hess and Soom, 1991), which could be a serious obstacle to implement this system on a real vehicle. Since the

magnitude of the brake torque drop depends on the amplitude of the dither signal, the maximum acceptable amplitude threshold would have to be determined.

2.11.3 The Need for a New Approach

As discussed above the current state of art lacks a research study on active brake squeal control using the method of leading and trailing pressure variation in order to reduce or completely suppress squeal. Therefore, the aim of this thesis is to investigate, develop and test such a system.

In order to attain a high level of flexibility to refine the system during experiments, the design of the new caliper, as presented below, is characterised by a high level of modularity that has not been found elsewhere in brake literature. It is a four-piston opposed caliper, in which the pistons are controlled independently, allowing change of the position of the CoP at the pad/disc interface. The pistons are located in a separate module that can be replaced by a module with a different number of pistons. Also, the abutments and split caliper bodies are able to accommodate a variety of disc and pad components. Since the dither squeal control suffers from a brake torque drop when activated, the new system, as shown below, includes a control architecture that maintains the brake torque while a differential pressure is set at the leading and trailing pistons. In addition, the novel automatic squeal reduction (ASQR) system is designed to use a minimum number of additional features that are not already available on a real vehicle.

The 2D analytical model of the pad/disc interface with a trailing abutment, as discussed above, cannot predict the CoP offset in the radial direction. Therefore, a new 3D analytical model of the pad/disc interface was developed to determine the acting point of the normal and friction force in the radial as well as in the longitudinal direction. Furthermore, a new FE model of the corresponding brake is used to compare the computed CoP positions as well as serving as a prediction tool for squeal propensity.

As was shown above, all existing pad sensors are characterised by some design-specific drawbacks, so the new approach presented further represents a new design that includes five high-temperature piezoresistive force sensors deployed between the lining and backplate allowing to determine the resultant normal force and its acting point (CoP). These sensors are chosen so they are not dependent on specific hardware and software, and allow the development of a bespoke DAQ system. Therefore this solution is highly adaptable and not costly.

3 Design and Development of Brake Test Rig

"A journey of a thousand miles must begin with a single step"
Lao-Tze

3.1 Introduction

This chapter includes four main sections: design of the new brake caliper, structural analysis of the caliper assembly including brackets, development of the brake test rig enclosure, and design of two development stages of the actuation system. Each section provides an overview of the work that has been carried out towards the test rig completion, and also explains some important topics relevant for the next chapters in greater detail.

The first section provides an overview of existing brake caliper designs and basic terminology, followed by design requirements for a new brake caliper. Further, an ordered list of designed assemblies, sub-assemblies and components is accompanied with relevant figures. Finally, this section concludes with comments on the caliper design, and recommended commissioning and maintenance techniques.

In the second section, a finite-element (FE) analysis of the caliper assembly is used to investigate the maximum stress and deformations of the parts subjected to brake forces, limited here only to the most important results and figures.

Next, an overview of the design work that was conducted on the extraction system of the brake test rig is presented, beginning with a brief description of the whole system, followed by the actual design and commission of the brake test rig enclosure. Also here, numerous figures and diagrams accompany the written text to illustrate the design process.

Finally, the last section presents the two development stages of the test rig actuation system. This section begins with calculation of volumetric losses in a closed hydraulic brake system, which is used to determine the size of the master cylinder. Next, the section introduces the main components of the actuation system Stage I, and explains the operation of the system during testing. Finally, the design process of the actuation system Stage II as well as description of all components and their basic data are presented.

3.2 Brake Dynamometer

The research brake dynamometer currently used in the University of Leeds (UoL) is a shaft-type dynamometer (Figure 3.1(a)). The shaft is driven by a Lorey Somer

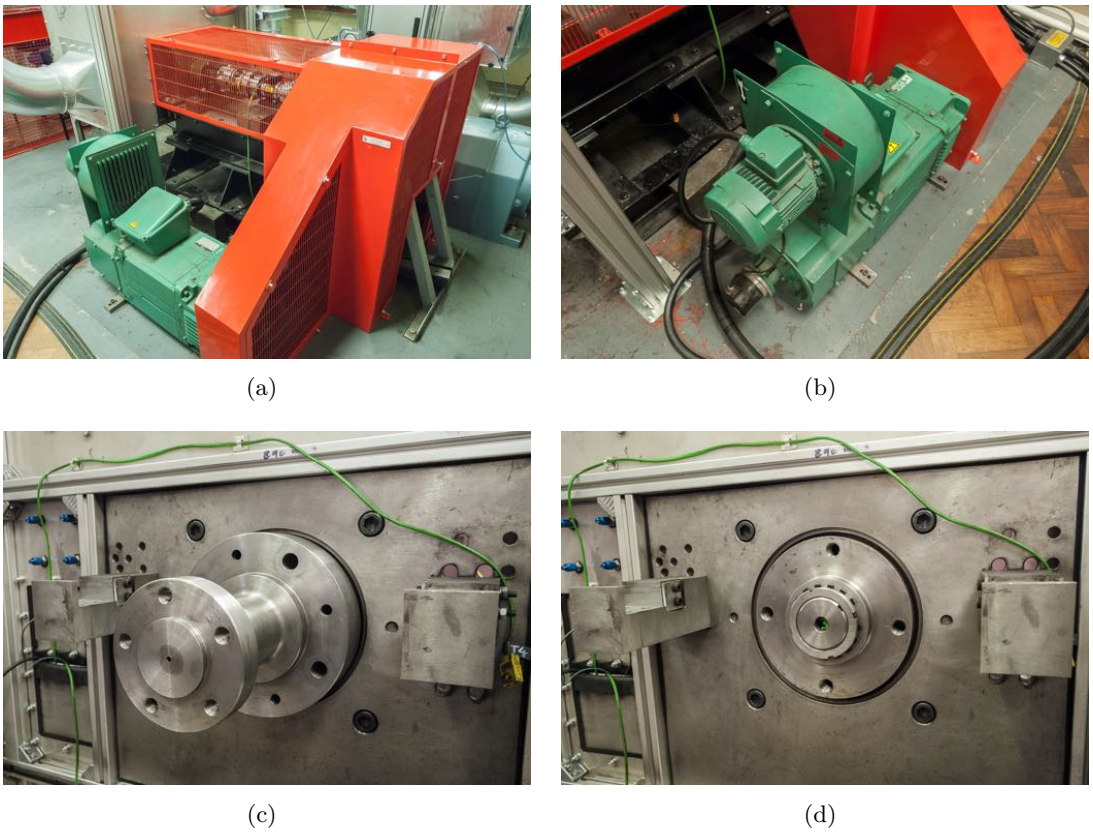

(a) (b)

(c) (d)

Figure 3.1: UoL brake dynamometer: (a) side-view, (b) electric motor unit, (c) shaft adaptor, (d) dynamometer flange and mounting plate.

LSK1604M04 45 kW DC electric motor (Hassan, 2009) shown in Figure 3.1(b). The major limitation of this dynamometer is that it can be used only for drag brake tests because the current design does not include a shaft decoupling mechanism and inertia masses required for full-stop brake tests. The torque transducer built in the shaft limits the maximum braking torque to 500 Nm and the minimum and maximum rotational speed of the shaft is 30 and 1500 rpm, respectively. A shaft adaptor shown in Figure 3.1(c) is used to compensate the mounting distance for different brake discs. Different caliper types and sizes are compensated via shims and brackets mounted to a steel plate of the dynamometer structure (see Figure 3.1(d)).

3.3 Design of Prototype Brake Caliper

3.3.1 Design Requirements

The main requirement for the new caliper design is the implementation of independent inlet hydraulic channels to all pistons. This allows individual control of each piston, and thereby arbitrary positioning of the centre of pressure (CoP) between the pistons. To enable separate control of the pistons, the caliper has to be of a fixed (opposed) type. Since its use is intended for a variety of disc types and dimensions, it is advantageous

to split the caliper in two opposite inboard and outboard part, which gives it versatility to straddle discs of different thicknesses by inserting shims between them. Allowing replaceable abutments and piston modules enables further flexibility of the caliper use.

Table 3.1 summarises all design requirements for the new prototype caliper and shows their relative importance.

3.3.2 Overview of Brake Assembly Components

The new brake assembly was developed in SOLIDWORKS® and went through several design stages while adhering to the above requirements. The final CAD model is illustrated in Figure 3.2 and includes a caliper assembly, bracketry and a brake disc. To accommodate a variety of disc thicknesses, the caliper was split to an inboard and outboard part allowing adjustments of its overall width. The main components of the caliper are illustrated in Figure 3.3 and include:

- Inboard and outboard caliper body
- Pistons
- Brake pads
- Piston module
- Abutments
- Fasteners and fittings
- Pad pre-load assembly

Caliper Body

The caliper body forms a structure to which other components such as the piston module, abutments and the pre-load assembly are bolted. This ensures a unique modularity

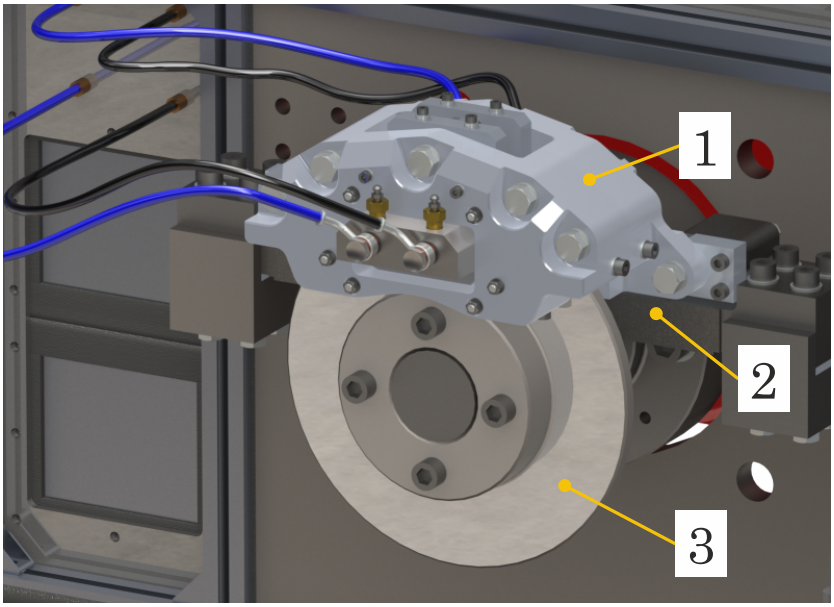

Figure 3.2: CAD model of a new brake assembly consisting of: 1) caliper assembly, 2) bracketry, 3) brake disc.

Table 3.1: Design requirements for the new prototype brake caliper and their relative importance.

Design Requirement	Essential	Desired
A fixed type of caliper that allows independent piston control.	X	
A modular design of the caliper that ensures flexibility to accommodate a variety of discs, abutments, piston modules, and other accessories.		X
An aluminium caliper body to facilitate fabrication by using machining tools available in the UoL workshop.	X	
The mounting position of the caliper to be at the twelve o'clock position with respect to the disc.	X	
Accommodation of brake discs with a diameter from 240 mm (Fiat Punto) to 290 mm (aluminium split disc) and a width ranging from 11 mm (Fiat Punto) to 25 mm (aluminium split disc).	X	
Use of Wilwood pistons (diameter 28.3 mm) along with the appropriate Wilwood seals.		X
Hydraulic pressure design value of 120 bar for a typical passenger car (Day, 2014).		X
Inclusion of removable steel abutments to allow their geometry modification and studying of other aspects, for instance different pad/abutment contact areas.		X
Mounting of the pistons in a part of the similar material (steel), so the risk of leakages resulting from different thermal expansion coefficients is minimised.		X
A removable piston module, which would allow its replacement with a similar module consisting of a different number of pistons.		X
Bleeding points designed at the highest position of the brake fluid chamber to avoid air bubbles to be trapped in otherwise inaccessible pockets.	X	
Minimising of the threads in the aluminium parts due to their expected frequent assembling/disassembling.		X
An easy access to the pads from the top or bottom side of the caliper.		X
Inclusion of an adjustable brake pad spring pre-load assembly.		X
The maximum outward caliper deflection at the maximum design pressure less than 0.4 mm.		X
Adjustable mounting brackets in the X, Y, and Z direction.		X

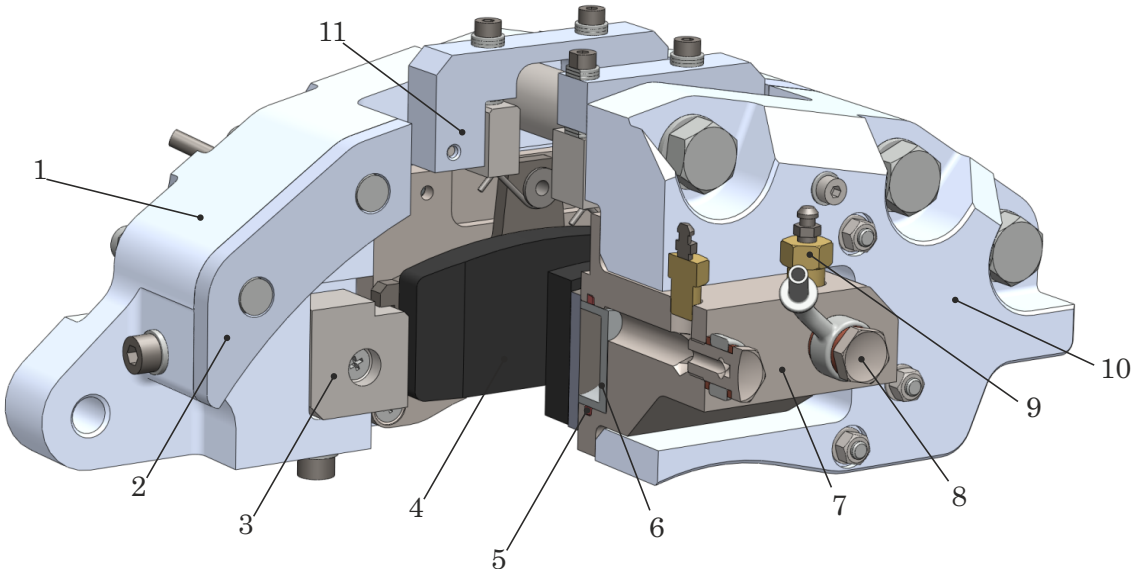

Figure 3.3: Main components of the caliper assembly: 1) inboard caliper, 2) shim, 3) abutment, 4) brake pad, 5) piston seal, 6) piston, 7) piston module, 8) banjo bolt fitting, 9) bleeding valve, 10) outboard caliper, 11) brake pad pre-load assembly.

of the caliper. To facilitate machining and maintain good strength performance at high temperatures, aluminium alloy 7075-T651 was chosen as the material for the caliper body. This aluminium alloy is characterised by a very good fatigue stress at higher temperatures (see Table 3.2), as well as better machineabilty in contrast to the more widely used aluminium 6061-T6. However, this material is more expensive and has a slightly lower corrosion resistance. Since only one caliper was fabricated and exposed to the laboratory low-corrosive environment, both drawbacks are acceptable. The lower corrosion resistance was in fact observed after the fabrication of the caliper, when the caliper was exposed to highly corrosive machining liquids, which created stains on some of its surfaces. A similar problem was reported in a study on machining of aluminium aeronautic components (Faria et al., 2013). To enhance the caliper appearance, its surface can be electrochemically coated.

Brake Pistons

The new prototype caliper uses the Wilwood stainless steel brake piston with diameter of 28 mm (Part No. 200-5089) as shown in Figure 3.4(a). The piston suits the PS-1 lightweight caliper (Part No. 120-8373/4) and matches with a particular Wilwood square cross-sectional seal (Part No. 130-2579) (see Figure 3.4(b)). This piston is not equipped

Table 3.2: Aluminium 7075-T651 fatigue stress at elevated temperature of 205°C (400°F)(Kaufman, 2008).

Aluminium 7075-T651 (Rolled rod and shapes) 205°C						
Cycles	10^4	10^5	10^6	10^7	10^8	5×10^8
Fatigue stress [MPa]	305	230	150	115	85	75

with a dust boot to keep the dirt and moisture out of the piston bore.

(a) (b)

Figure 3.4: Brake components of the new caliper assembly: (a) Wilwood piston with diameter of 28 mm, (b) Wilwood square cross-sectional seal (internal diameter of 28 mm).

Brake Pads

A Mintex MDB 1189 brake pad as shown in Figure 3.5(a) was chosen for the new prototype caliper. This pad can be fitted with the Fiat Punto, Rover and coated aluminium brake disc. The backplate includes a pre-load spring, and its side abutment faces are flat, which allows easier modelling of the backplate/abutment interface. However, the backplate contains small technological spigot holes interfering with the piston positions, thereby preventing a full interface contact of the piston with the backplate (see Figure 3.5(b)). This could cause a small deviation from the CoP position predicted during braking.

(a) (b)

Figure 3.5: Brake Pad Mintex MDB 1189: (a) front view, (b) rear view: 1) spigot hole, 2) piston contact area.

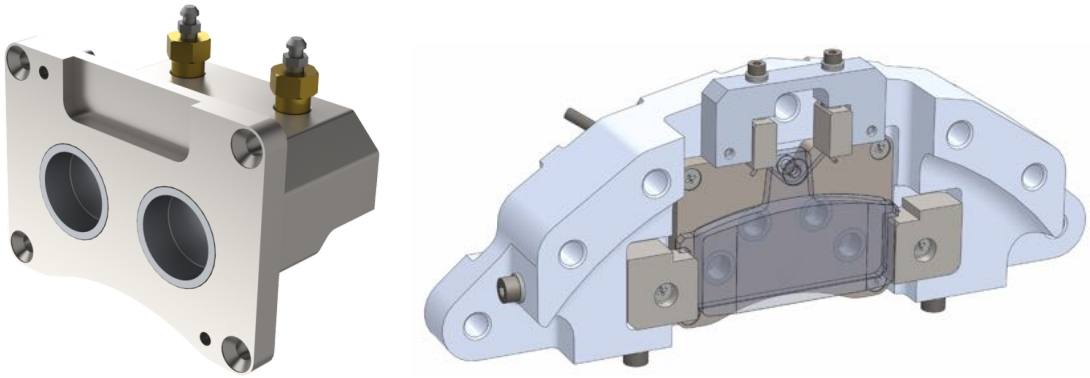

(a) (b)

Figure 3.6: CAD model of piston module: (a) with two pistons, (b) with four pistons - in assembled position.

Piston Module

The piston module represents one of the most innovative features of the caliper as it encapsulates the whole hydraulics in a replaceable module including piston bores, outlets

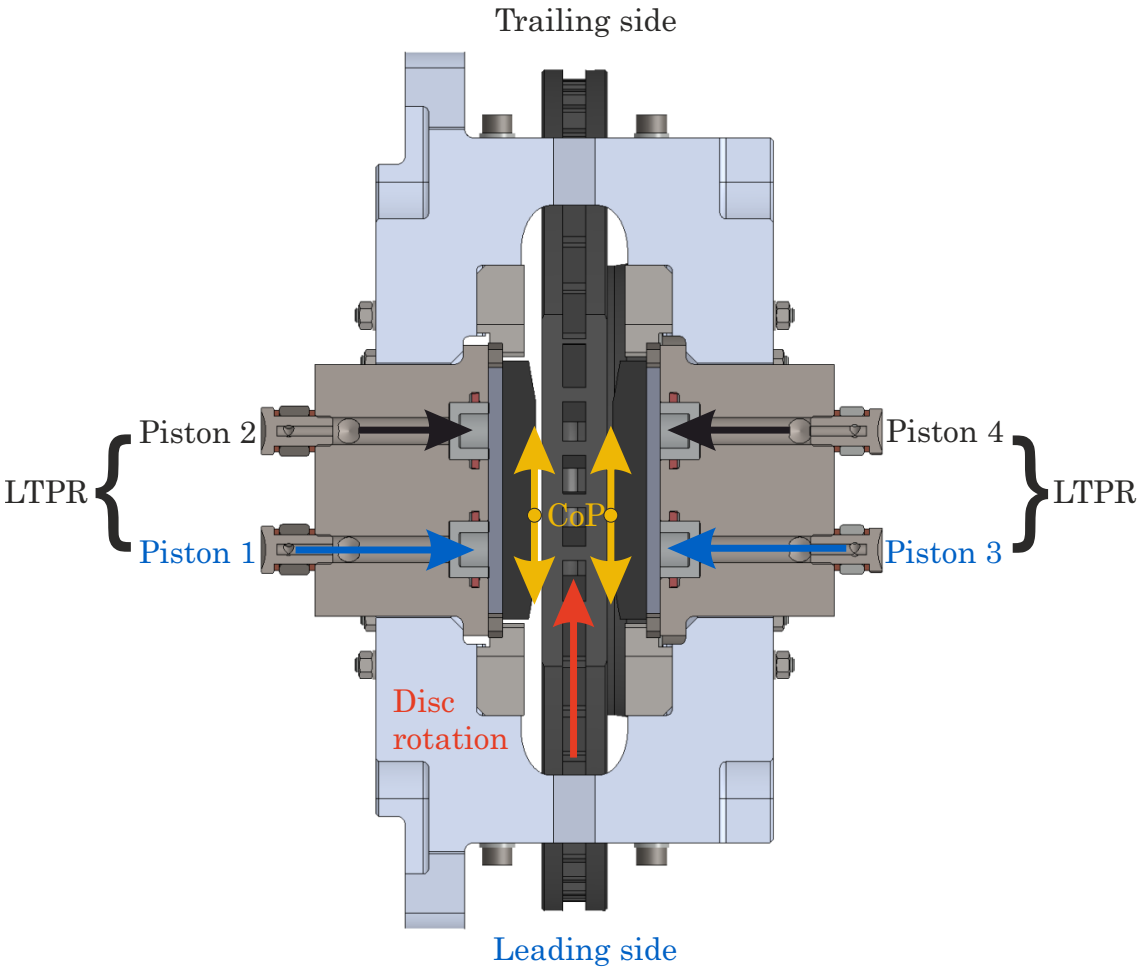

Figure 3.7: A section view through the piston hole.

Figure 3.8: Replica of the caliper piston hole using high-resolution Microset replication material.

Figure 3.9: Nikon projector V-16D. The projection of the seal groove is highlighted.

and bleeding ports (Figure 3.6(a)). The position of the module with respect to the caliper body is determined by two diagonally placed stepped dowel pins. The module is machined from a stainless steel 316 block, which improves the brake fluid tightness due to similar thermal expansion coefficient as the piston material. As all fitting threads are drilled in the steel body, their wear is smaller than it would be in an aluminium alloy, and the overal lifetime of the component can be increased. The bleeding outlet is positioned at the highest point of the channel which ensures removing of the air pockets when bleeding the brake (see Figure 3.3). Some manufacturers use clear plastics facsimiles to determine the position of air pockets (Baker, 1986), however this technique was not used here. A drawing used for manufacturing of the two-piston module can be seen in Figure A-2 in Appendix A.

The current piston module containing two piston chambers can be replaced for a module with a different number of pistons. Figure 3.6(b) shows a representative design concept featuring four piston bores.

The main function of the new prototype caliper is to enable independent control of each piston pressure. Therefore, the piston hydraulic channels are not connected at the caliper level but leave this possibility open for the actuation system. Since only two actuation channels are available, each of the leading and trailing pair of pistons are hydraulically coupled. This allows control of the leading trailing pressure ratio (LTPR). A working principle of the LTPR control is explained in the section view of the assembly through the piston axis in Figure 3.7. Assuming the direction of disc rotation, the leading and trailing side can be assigned to the caliper. By hydraulic coupling of the piston 1 and piston 3, the leading side of the caliper can be actuated. Similarly, hydraulic coupling of the piston 2 and piston 4 enables actuation of the trailing side. By changing the LTPR, the CoP position can be moved along the pad. For each value of the LTPR (assuming a constant μ), a specific position of CoP can be attributed (see Chapter 6).

The parameters of the seal groove for the new prototype caliper were determined

Figure 3.10: A single-purpose tool for seal groove machining.

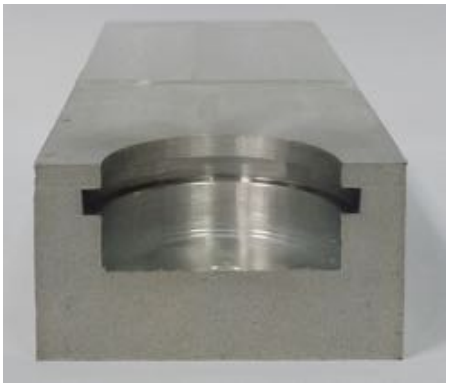

Figure 3.11: Prototype of the seal groove in an aluminium block.

by creating a replica of the piston hole and a section cut of the original Wilwood PS-1 caliper (Figure 3.8). The replica was created using the Microset high-resolution material and measured by the Nikon profile projector V-16D shown in Figure 3.9. The design specifications of the seal groove used for its machining are illustrated in Figure A-1.

Due to the complex geometry of the seal groove, a dedicated machining tool as shown in Figure 3.10 had to be used for its fabrication. The stainless steel piston module was manufactured after a series of aluminium prototypes were machined (Figure 3.11) that served to adjust the path of the machining tool to meet the design tolerances.

One of the properties indicating a proper function of the seal inside the groove is the piston retraction - an ability to return the piston back to the initial position after releasing the brake pressure. In order to determine the retraction of the piston, a simple test jig was constructed allowing measurement of the gap between the piston and a steel plate using a feeler gauge as shown in Figure 3.12. The actual retraction distance was

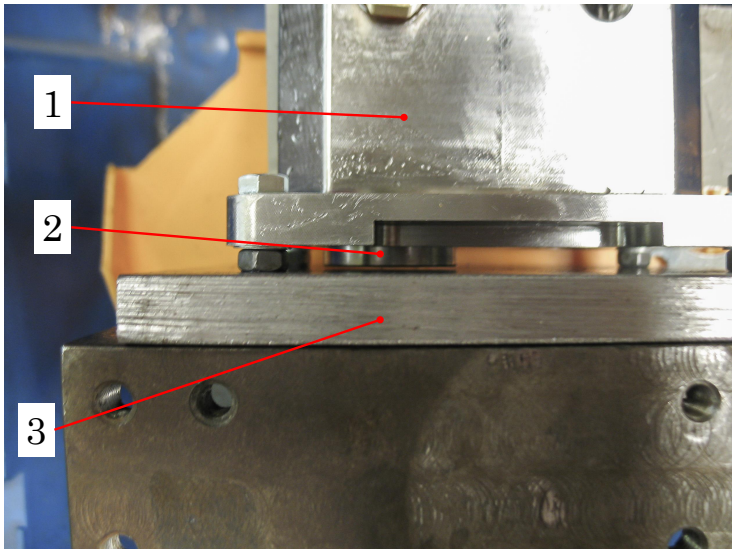

Figure 3.12: A simple test jig to measure retraction of the piston: 1) piston module, 2) piston, 3) steel plate.

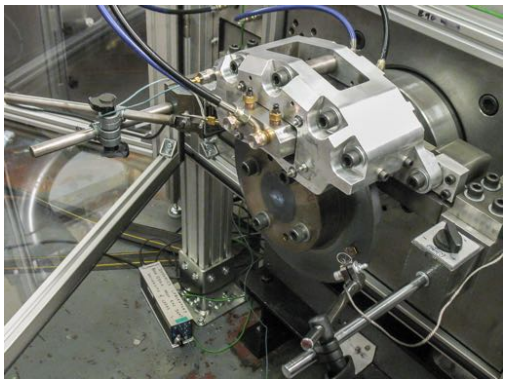

(a)

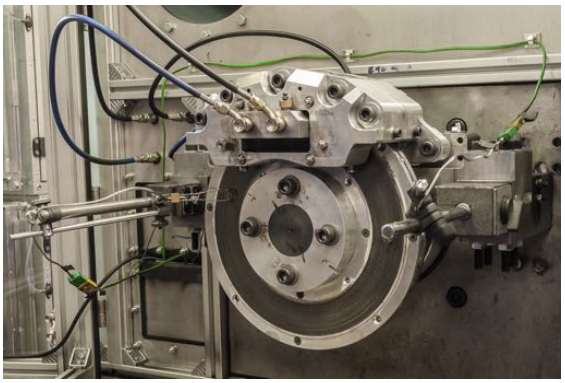

(b)

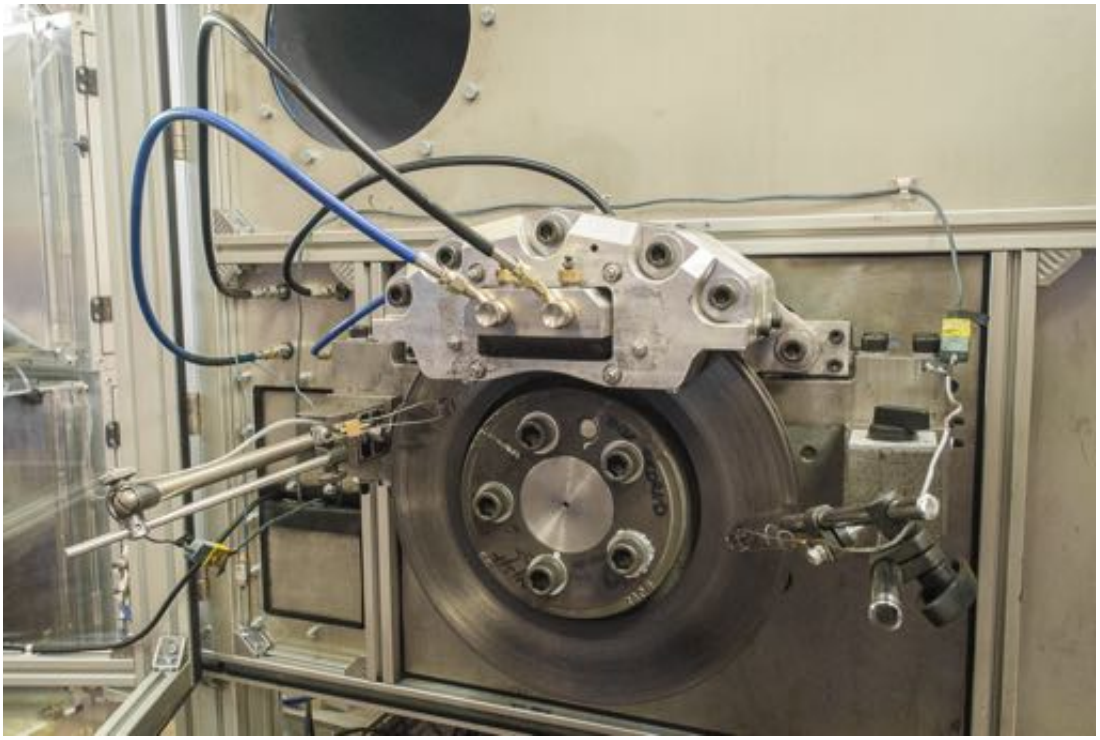

(c)

Figure 3.13: Flexibility of the rig to accommodate a variety of disc sizes and types: (a) Fiat Punto disc, (b) coated aluminium rotor, (c) Rover 75 disc.

determined for a variety of pressures up to 50 bar, giving values in the range of 0.35 - 0.40 mm. This value seemed to be sufficient as the maximum runout that was measured on the discs was 0.3 mm. Following examination of the sealing function did not reveal any leakages around the piston, therefore modifications of the dimensions and tolerances of the piston hole and seal groove were not necessary.

Brake Discs

In total, three different brake discs have been so far used with the new caliper assembly: a Fiat Punto solid brake disc (Figure 3.13(a)), a vented coated aluminium disc (Figure

Figure 3.14: Axial runout measurement using a dial test indicator.

3.13(b)), and a Rover 75 anti-coning disc (Figure 3.13(c)). The nominal dimensions of the Fiat Punto and Rover 75 discs are shown in Appendix A in Figure A-3 and Figure A-4, respectively. Since the coated aluminium disc was not used primarily for this thesis, its drawing is not included here.

The discs are mounted to a shaft adaptor that is further bolted to the brake dynamometer flange. The Fiat Punto and coated aluminium disc share the same shaft adaptor (see Figure A-5 in Appendix A), while the Rover 75, due to different wheel bolt number and size, required a fabrication of a new adaptor (see Figure A-6 in Appendix A).

When manufacturing brake discs, it is important to maintain tight geometrical tolerances of the friction ring. The most important parameters are disc thickness variation and axial runout of the disc. The latter was measured with a dial test indicator for the Fiat Punto and Rover disc when assembled on the shaft adaptor (Figure 3.14), yielding values of 0.3 and 0.2 mm, respectively. These values are quite significant as compared to the maximum disc runout of 0.05 mm given by SAE J2521. A large runout can cause the pistons to be pushed back during a single rotation of the disc when the brake is applied. As a result, the piston pressure and brake torque could vary during braking.

As the Rover disc has a smaller runout and can easier generate low-frequency squeal, this setup was used for the remaining work. The still significant runout of this disc was not possible to minimise during this work, as the problem is probably at the brake dynamometer main flange, where the average runout was about 0.15 mm. A large runout can change a continuous type of squeal to an intermittent one, however this is considered acceptable for the following work as both types of squeal commonly occur in real braking situations. Moreover, an active squeal reduction system developed for an intermittent type of squeal can be readily applied for a continuous squeal, but this might not be possible vice versa.

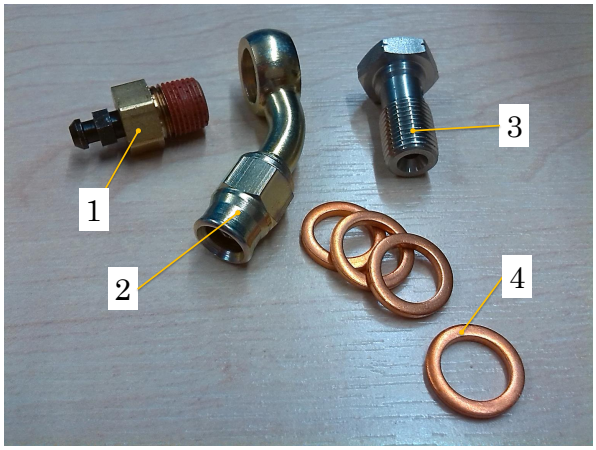

Figure 3.15: Fitting and standard parts used in the prototype caliper: 1) Wilwood bleed screw (Part No. 220-4269), 2) Goodridge banjo inlet fitting 45°, 3) Goodridge banjo bolt M10x1, 4) Goodridge crush washer 10 mm.

3.3.3 Additional Comments on Caliper Design after its Commission

1. The prototype caliper and bracketry were fabricated in the UoL workshop and then installed on the brake dynamometer. All fittings and standard parts were ordered from local dealers (Figure 3.15): Goodridge extended neck 45° banjo fitting, Wilwood bleed screws (Part No. 220-4269), Goodridge banjo bolt M10x1, Goodridge crush washer 10 mm.
2. The manufacturing tolerances specified in the drawings were thoroughly fulfilled and the actual assembling of the caliper and the framework assembly did not represent any difficulties. To maintain long lifetime and ensure proper functioning of the caliper assembly, the assembling instructions and maintanence recommendations listed in Section A.2 in Appendix A should be followed.
3. The preload assembly ((11) in Figure 3.3) did not noticably affect the brake vibration, therefore it was not mounted during the current research work.
4. The original 8.8 grade bolts and nuts used to tighten up the inboard and outboard caliper half were replaced with high tensile bolts (grade 12.9) and nuts (grade 10.9) as they were severely damaged after overloading them during tightening, therefore special care needs to be taken to not exceed the prescribed torque of 40 Nm.
5. To the author's knowledge, the idea of removable piston modules (containing one or more pistons) mounted in the caliper body to independently control pistons, has not yet been used. Some modular concepts of brake calipers can be seen in the literature (Wagh, 2005), (Twiflex Ltd, 2018), but the current design comprising of a removable piston module, which would enable use of a various number of pistons, seems to be unique.
6. The prototype caliper is not intended to be used on a real vehicle, therefore the caliper volume and mass was not optimised to meet packaging and unsprung mass criteria in a wheel assembly.
7. The test rig brackets were designed to allow testing other disc/caliper combinations.

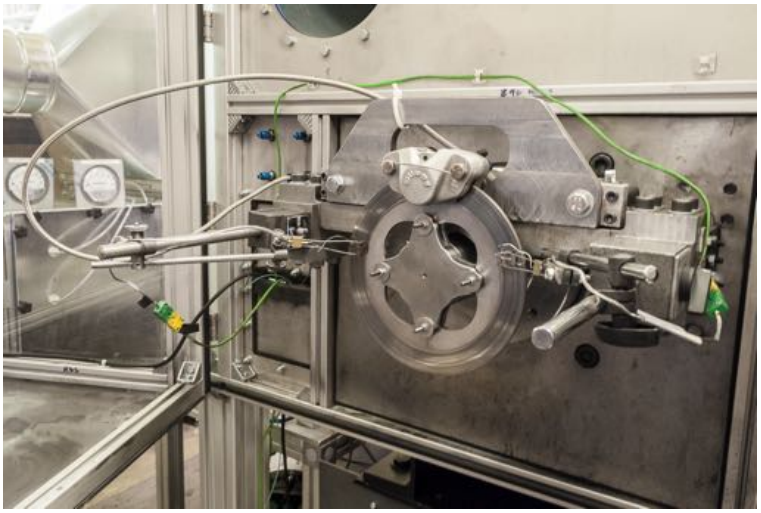

Figure 3.16: Brake setup to study thermal stresses of a floating stainless steel disc.

Figure 3.16 shows for instance an arrangement consisting of a racing caliper and a stainless steel floating disc.

3.4 Structural Analysis of Caliper Assembly

A finite element (FE) analysis using ABAQUS® was performed to examine maximum stress concentrations and deformations of the bracketry and caliper subassembly during braking. The braking application was considered as a quasi-static loading, therefore the methods of static analysis were employed to determine maximum von Mises stress and deformation. The calculated von Mises stress was compared with the tensile yield strength to evaluate the safety factor.

3.4.1 Structural Analysis of Bracketry

The bracketry shown in Figure 3.2 gives flexibility to position the caliper depending on the disc size, but also has to withstand loads that exist during braking. The reduced FE simulation model shown in Figure 3.17 contains a left and a right bracket, a central bridge part, a mounting plate and shims. The brackets are attached to the mounting plate using *Tie* constraints. A surface-to-surface contact is applied to the faces of the central bridge and both right and left bracket. When braking, the central bridge is subject to reaction forces acting in the caliper mounting points. The mounting point was loaded with a horizontal force of 10 kN that was calculated using *CalBrakes* as a maximum abutment reaction force for a brake line pressure of 120 bar. As it is not known which mounting point is active during braking, the same force was applied to both mounting points. Due to symmetry, only one direction of braking was examined. The pre-load of the bolts was simulated through the force application on the particular faces under the fasteners and its value is 28 kN at each bolt position. The central bridge and right and left brackets are made of mild carbon steel with a typical value of the yield strength $\sigma_e = 370\,\text{MPa}$. The

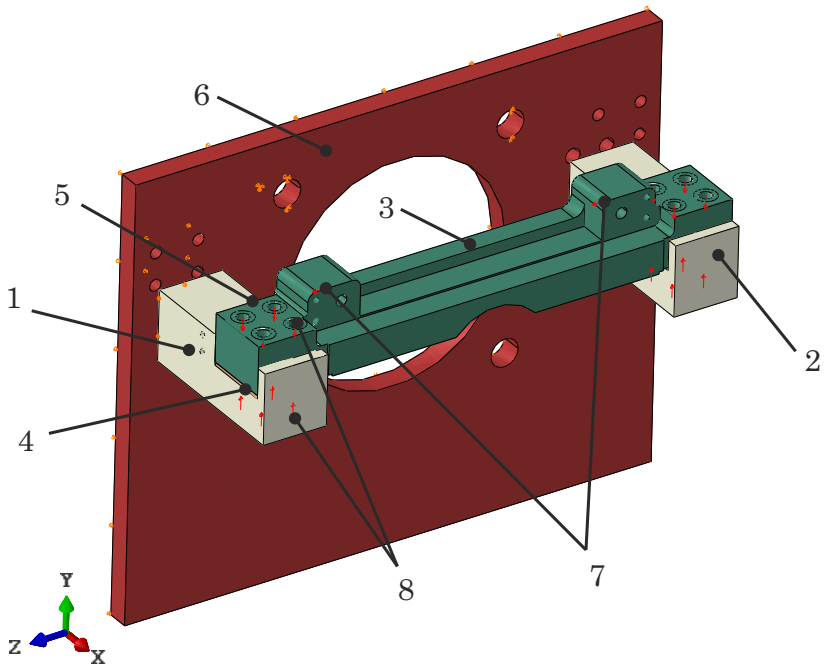

Figure 3.17: FE model of bracketry: 1) left bracket, 2) right bracket, 3) central bridge, 4) shim Y direction, 5) shim Z direction, 6) mounting plate, 7) brake (reaction) force, 8) bolt pre-load.

Young's modulus and Poisson's ratio used in the simulation for components made of steel are 205 GPa and 0.29, respectively. For aluminium shims, these values are 68.9 GPa and 0.33, respectively.

An overview of the type and number of the mesh element used in the simulation is given in Table 3.3, where C3D4 is a 4-node linear tetrahedron and C3D8R represents an 8-node linear brick with reduced integration.

Table 3.3: Type and number of the elements used in the FEM simulation.

Part	FEM element type	Number of elements
Mounting plate	C3D4 (Tet)	45 872
Right bracket	C3D4 (Tet)	68 701
Left bracket	C3D4 (Tet)	66 687
Central bridge part	C3D4 (Tet)	271 318
	C3D8R (Hex)	2 760
Shim Z	C3D4 (Tet)	10 588
Shim Y	C3D4 (Tet)	3 514

To verify the quality of the mesh, a mesh sensitivity analysis was provided as shown in Table 3.4. The central bridge, left and right bracket and mounting plate were meshed again with a coarse and a finer mesh. The von Mises stress was compared on a selected element set resulting in differences of the stress values $< 2\%$, which is well within acceptable limits. Further refinement of the current mesh improved the stress value only by 0.8% and almost doubled the calculation time.

Table 3.4: Mesh sensitivity analysis of the bracketry provided for a coarse, medium and fine mesh. The highlighted mesh was chosen for strength analysis. Rel.Diff. = Relative difference.

Mesh (Number of Elements)	Coarse (191551)	Medium (480028)	Rel. Diff.	Fine (1125252)	Rel. Diff.
Von Mises Stress (MPa)	40.1	40.8	+1.5%	41.1	+0.8%
Calculation time (mm:ss)	01:05	04:46	+340%	08:25	+76.6%

The results from the FE simulation are shown in Figures 3.18(a) - 3.18(b). The

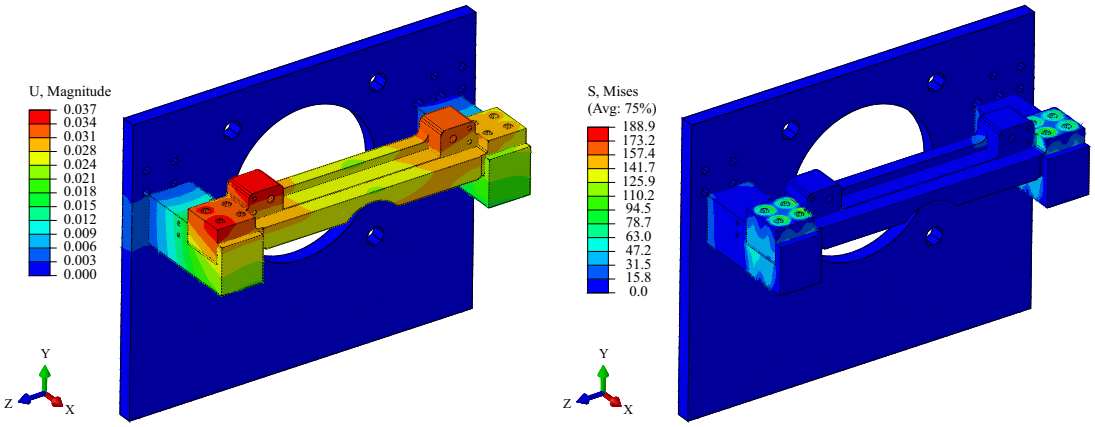

(a) (b)

Figure 3.18: FE analysis of the bracketry: (a) displacements (mm), (b) von Mises stress (MPa).

maximum von Mises stress determined by simulation is $\sigma_{FEM} = 188.9\,\text{MPa}$ and therefore the safety factor k_s can be calculated as:

$$k_s = \frac{\sigma_e}{\sigma_{FEM}} = \frac{370\,\text{MPa}}{188.9\,\text{MPa}} = 1.96$$

Furthermore, the maximum displacement resulting from the FE simulation is 0.037 mm (Figure 3.18(a)), which is well within acceptable limits.

3.4.2 Structural Analysis of Caliper Assembly

The reduced caliper assembly used for the structural analysis is shown in Figure 3.19 and comprises of the inboard and outboard caliper, piston modules, bolts and a spacer. These parts are assembled using surface-to-surface interactions and tie constraints.

During braking the caliper is typically subject to a combination of loads and an increased temperature (estimated to be about 200°C). The latter is considered in the simulation by using the Young's modulus determined at the higher temperature. For the 7075 aluminium family, the Young's modulus at a temperature of 205°C (400°F) is approximately 65.5 GPa (Hill and K.D., 1961). All material properties used in the simulation are displayed in Table 3.5.

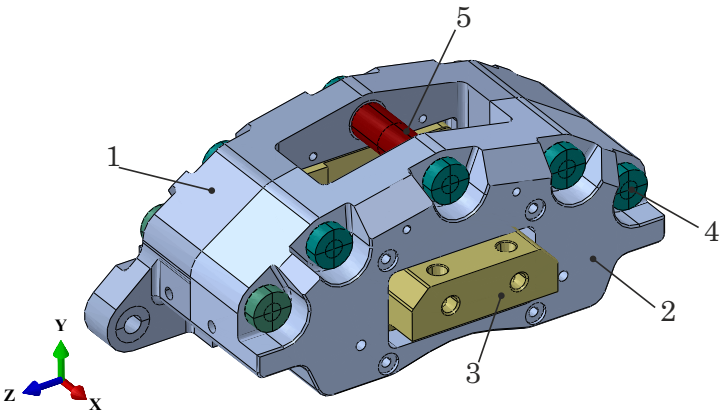

Figure 3.19: FE model of reduced caliper assembly: 1) inboard caliper, 2) outboard caliper, 3) piston module, 4) bolt, 5) spacer.

Table 3.6 summarizes the type and number of the mesh elements used in the simulation, where C3D4 is a 4-node linear tetrahedron, C3D8R represents an 8-node linear brick with reduced integration, and C3D6 is a 6-node linear triangular prism.

Figure 3.20 shows loads and boundary conditions applied in the model. The simulation is divided into three steps:

1. pre-load of the bolts
2. pre-load of the bolts + brake line pressure in the piston module
3. pre-load of the bolts + brake line pressure in the piston module + tangential force acting on the caliper abutments

First, the bolts are tightened to 40 Nm, which creates for M10 bolts approximately 20 kN of axial force applied to the middle of each bolt. In the second step, each piston hole is pressurised to 120 bar. Finally, a tangential load of 10 kN is applied to both trailing abutments. The calculated results of the von Mises stress are displayed in Figures

Table 3.5: Material properties used in the FE simulation.

Material	Young's Modulus at 205°C (GPa)	Poisson's Ratio (-)
Aluminium 7075-T651	65.5	0.33
Steel	190	0.3

Table 3.6: Type and number of the elements used in the FE simulation.

Part	Finite-element type	Number of elements
Inboard caliper	C3D4 (Tet)	206 719
	C3D8R (Hex)	9 728
Outboard caliper	C3D4 (Tet)	176 865
	C3D8R (Hex)	7 936
Bolt	C3D8R (Hex)	192
	C3D6 (Wedge)	672
Piston module	C3D4 (Tet)	27 700

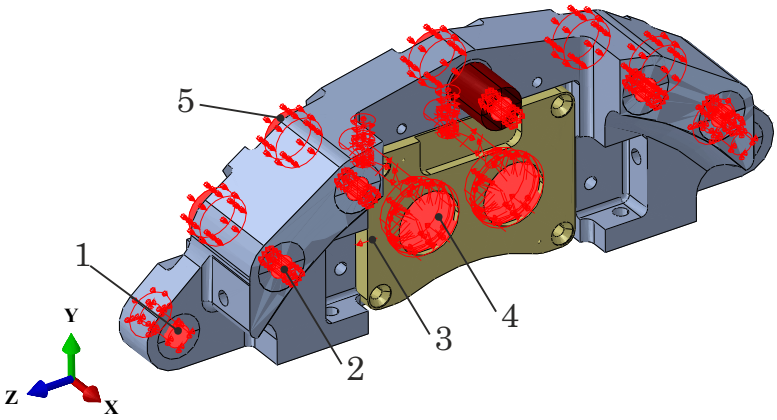

Figure 3.20: A view of caliper loads and boundary conditions: 1) boundary condition to restrict caliper motion, 2) bolt pre-load, 3) tangential abutment force, 4) brake line pressure, 5) bolt boundary condition to restrict its rotation.

3.21(a)-3.21(c).

The maximum von Mises stress calculated in the caliper body is 151.1 MPa. Then, assuming the yield strength of 505 MPa for this aluminium type (Shackelford et al., 2016), the safety factor k_s can be determined as:

$$k_s = \frac{\sigma_e}{\sigma_{FEM}} = \frac{505\,\text{MPa}}{151.1\,\text{MPa}} = 3.34$$

which is well within satisfactory limits allowing a safety zone for the initial assumption of braking forces as a quasi-static loading case. Figure 3.21(d) shows the caliper displacement in X direction giving the maximum value of 0.18 mm, which is an acceptable result. For a comparison, (Rajaram and Sudharsan, 2005) measured a deflection of 0.41 mm on a commercial sliding caliper with one piston loaded to a pressure of 300 bar. Figure 3.22 shows von Mises stress for the piston modules, with maximum stress of 147.0 MPa. The yield strength for the piston module made of 316 stainless steel is 310 MPa (Shackelford et al., 2016), resulting in the safety factor of 2.11.

3.5 Design of Brake Test Rig Enclosure

3.5.1 Introduction

As presented in Chapter 2, a research brake laboratory can be a health-hazardous environment where specific measures need to be provided to avoid exposure of the personnel to the potentially noxious substances generated during brake experiments. An increased endeavour within the brakes community to commence regulation of the brake particle emissions on road vehicles is a motivation to develop standardised measurement methods. In order to extract and monitor the brake emissions at UoL brake testing laboratory, it was decided to equip the brake dynamometer with a new ventilation system.

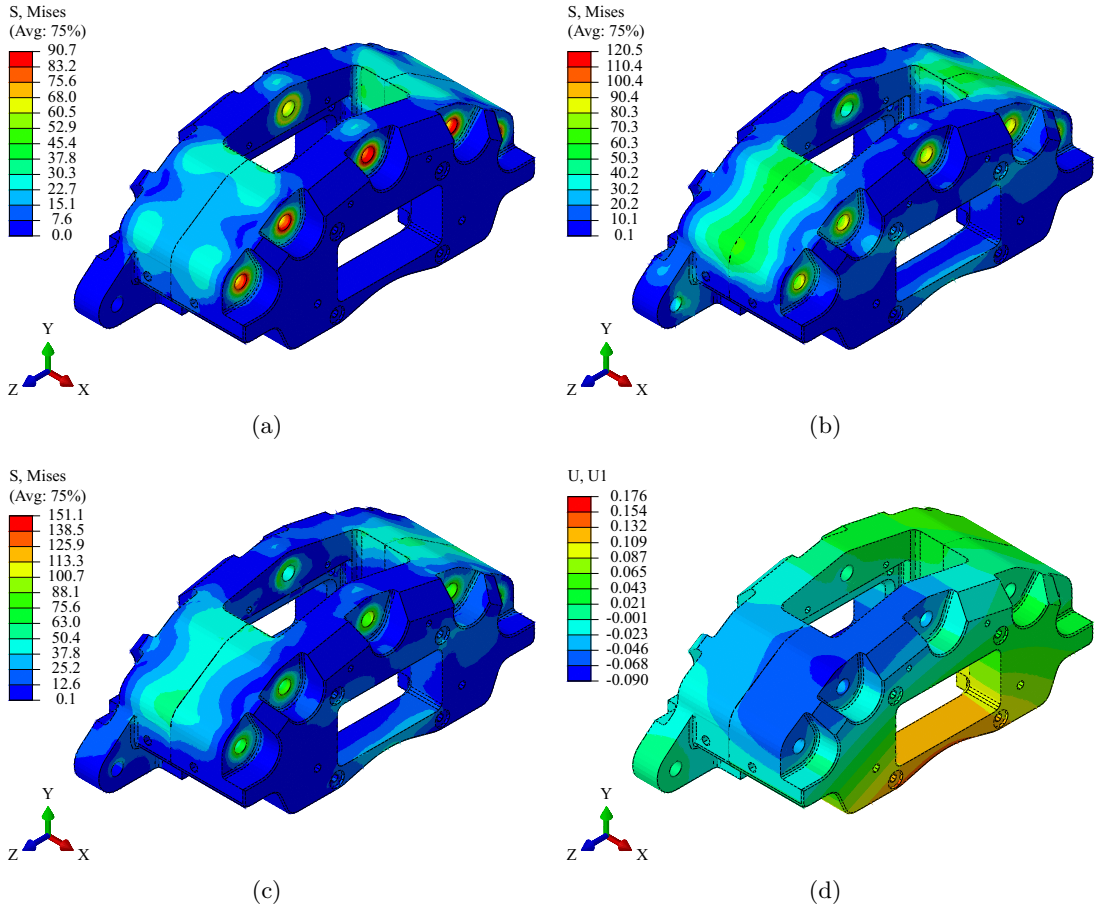

Figure 3.21: FE analysis of the caliper: (a) von Mises stress (MPa): pre-load of the bolts, (b) von Mises stress (MPa): pre-load of the bolts + brake line pressure, (c) von Mises stress (MPa): pre-load of the bolts + brake line pressure + abutment load, (d) inboard and outboard caliper displacement in X direction (mm).

This can extract the potentially harmful brake emissions outside of the testing room and monitor the particle composition by connecting an appropriate sampling system to the existing duct. In the following, a brief overview of the suggested extraction system is presented, followed by the actual design and commission work done on the new test rig enclosure.

3.5.2 Design and Fabrication of Brake Test Rig Enclosure

Figure 3.23 shows a schematic diagram of the new extraction system, consisting of inlet high-efficiency particulate air (HEPA) filters, a test rig enclosure, a sample collection tube, an outlet HEPA and a carbon filter, and an outlet duct leading to the roof of the building, where a fan unit is installed. This system includes two separate design work packages: a) a brake test rig enclosure b) the actual extraction system including the fan and filters. The test rig enclosure was designed and assembled by UoL, whereas the rest of the system was designed and commissioned by the company Glen Wilson Ltd. The

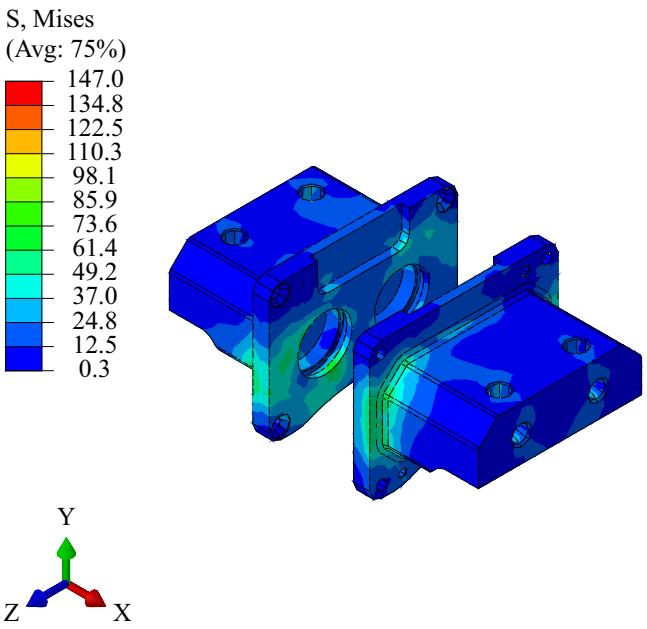

Figure 3.22: Von Mises stress (MPa) simulation results of the piston modules for pre-load of the bolts + brake line pressure + abutment load.

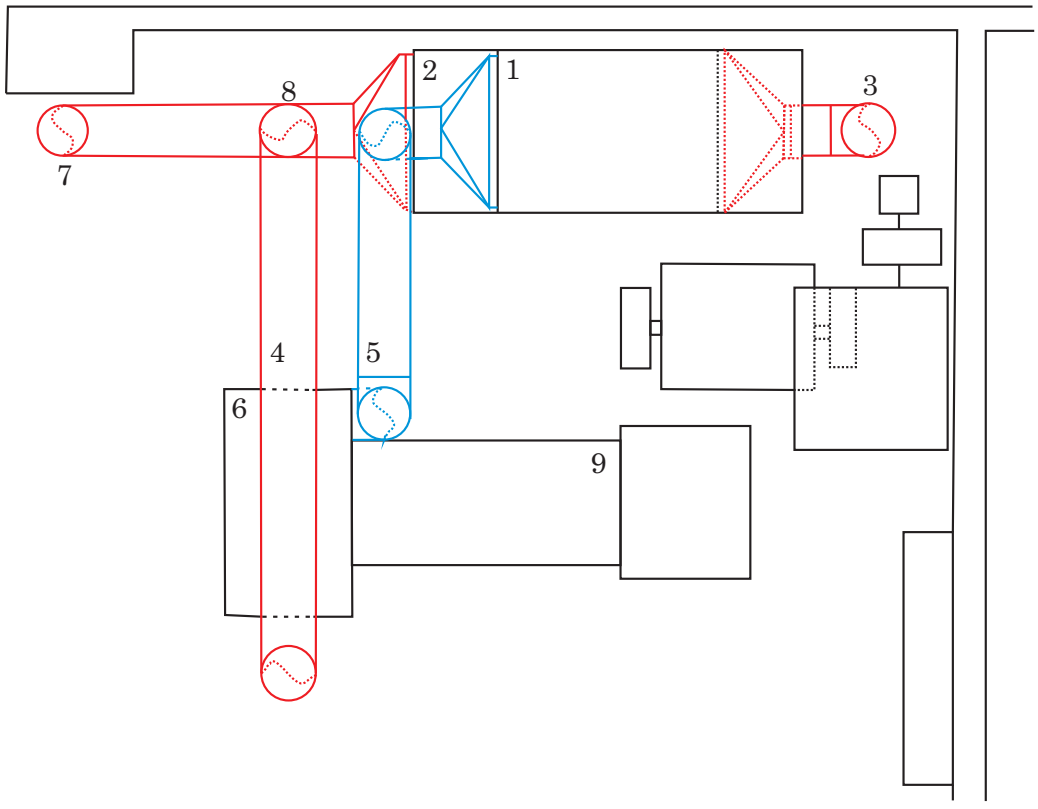

Figure 3.23: Schematic of the new extraction system installed in the UoL (provided by Glen Wilson Ltd): 1) air inlet filter 2) air outlet filter 3) duct exit to the roof 4) outlet from enclosure 5) air inlet to enclosure 6) enclosure 7) extraction branch duct 8) sample collection tube 9) brake dynamometer.

dimensions of the enclosure were determined to accommodate all possible variants of the brake assembly with all instrumentation, such as sliding thermocouples and microphone. The latter increased the height of the enclosure significantly as the SAE J2521 standard recommends the position of the noise transducer for squeal tests to be 500 mm above the rotor axis. The flow rate required to capture the brake particles was calculated using a preliminary sectional area of the enclosure and multiplied by an aproppriate velocity as follows (determined by Glen Wilson Ltd):

$$\dot{Q}_{airflow} = \text{Height} \times \text{Width} \times \text{Air Velocity} = 0.75\,\text{m} \times 0.45\,\text{m} \times 1.5\,\text{ms}^{-1} = 0.501\,\text{m}^3\text{s}^{-1} \tag{3.1}$$

Based on Eq. 3.1, the size of the ductwork, the fan unit and an appropriate motor was selected. The galvanised smooth clipped ductwork has an inner diameter of 225 mm and is supplied by Truduct. The fan unit includes a direct drive centrifugal fan driven by a 4 kW 3-phase electric motor.

Overall, the design and function requirements for the new extraction system are summarised in Table 3.7:

Table 3.7: Design requirements for the new extraction system and their relative importance.

Design Requirement	Essential	Desired
Extraction of the noxious gases and airborne particles resulting from braking experiments in the laboratory to the outer environment.	X	
Filtering of the extracted air via a set of filters to minimise polluting of the UoL environment.	X	
The air entering the enclosure should be filtered to ensure that all particles originate from the friction braking.	X	
The outlet should be at the same height as the rotor axis.		X
The enclosure should permit a comfortable access to the brake assembly.	X	
A proper sealing of the enclosure to prevent any air flow to and from the enclosure.	X	
A major part of the enclosure should be transparent to allow visual control of processes around the brake assembly.	X	
The enclosure should be modular and easily assembled allowing future design modifications.		X
Possibility of leading cables and brake lines to and from the enclosure while maintaining a good sealing function.		X
Possibility of the flow control and measurement.		X

During the design process, it turned out that it is difficult to achieve a decent access to the brake assembly and simultaneously maintain a perfect sealing function. Since most of the brake tests are not aimed at particles sampling, having a comfortable access to the brake assembly was of paramount importance. From numerous concept designs of enclosures, the one in Figures 3.24 - 3.25 was eventually chosen as the currently installed design. It contains a fixed rear and side stainless steel panel to firmly attach the ductwork,

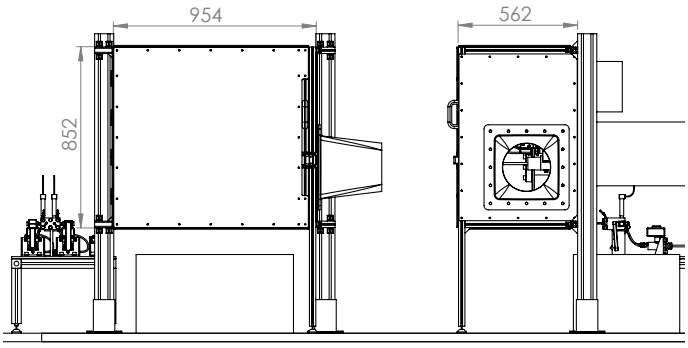

Figure 3.24: Basic dimensions (mm) of the enclosure.

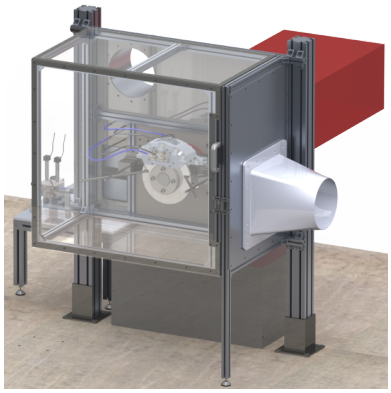

Figure 3.25: A CAD model of the enclosure.

and a door of a box shape, mounted on hinges allowing easy access to the brake assembly. For the main framework, the Bosch Rexroth system was used to maintain modularity and simple assembly. The transparent panels mounted on the door are made of polycarbonate plastics with thickness of 6 mm which allow the personnel to visually monitor the brake environment. However, polycarbonate materials are not transparent to infrared light so this setup cannot be used for thermovisual monitoring of the brakes using a standard thermocamera. The position of the outlet from the enclosure was carefully chosen to allow mounting of a relatively long duct where the turbulent flow can be moderated.

A realistic view of the complete extraction system can be seen in Figure 3.26. The sample collection tube with outlet fittings allows attachment of a particle measurement instrumentation.

It was observed that not all particle emissions can be extracted from the enclosure during brake tests and some remain deposited on the bottom panel as can be seen in Figure 3.27. To remove the brake dust from the enclosure and brake assembly a Numatic HZ200-2 vacuum cleaner is used. This industrial vacuum cleaner contains a HEPA filter to minimise the contamination of the lab environment.

3.5.3 Summary of Brake Test Rig Enclosure

The new extraction system described above was installed and commissioned in the UoL brake laboratory, which eliminated the earlier problems with the brake emissions odour in the laboratory area and more extensive brake tests could then be carried out. The door of the enclosure enables personnel to reach easily all components of the brake assembly, which facilitates changing of brake setup. Since a concept with the door of box shape was used, it was not possible to completely avoid formation of gaps in the door sealing, especially in the corners, through which the air flow can be contaminated by the substances present in the laboratory. For more precise particle emission measurements, it is recommended to seal the door and openings for cables by closing the gaps with an isolation tape. Furthermore, there is a possibility of some adhesion of the particles on the transparent polycarbonate panels due to formation of static charge between the particles

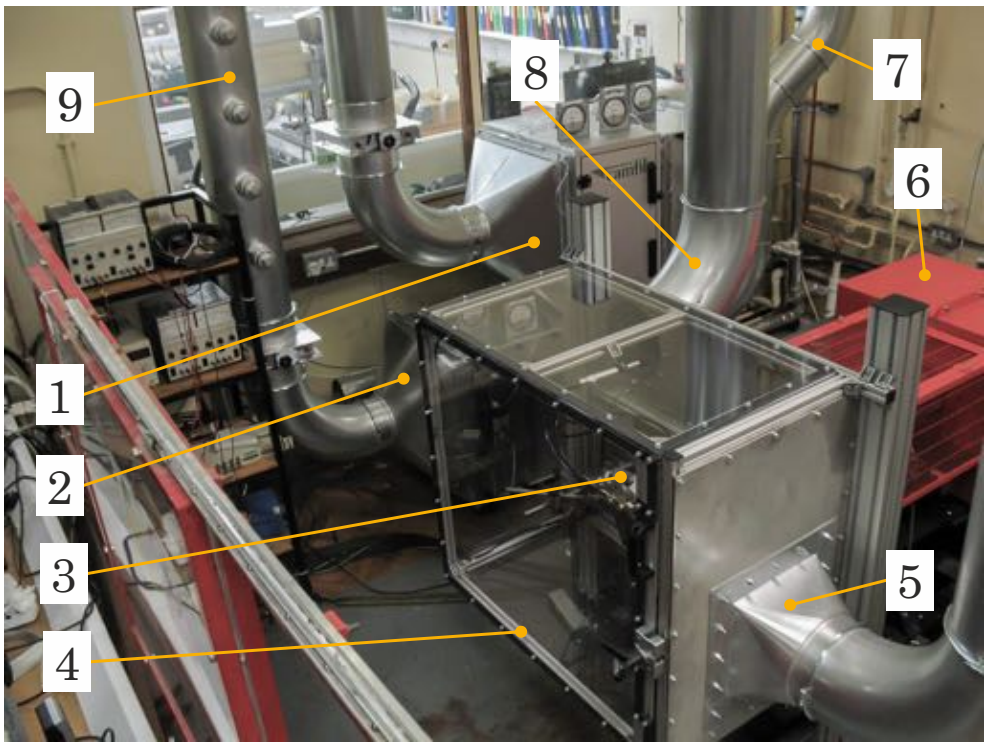

Figure 3.26: Extraction system after installation: 1) set of inlet HEPA filters 2) set of outlet HEPA filters 3) brake assembly 4) enclosure 5) outlet duct from enclosure 6) brake dynamometer 7) outlet duct to environment 8) inlet duct to enclosure 9) sample collection tube.

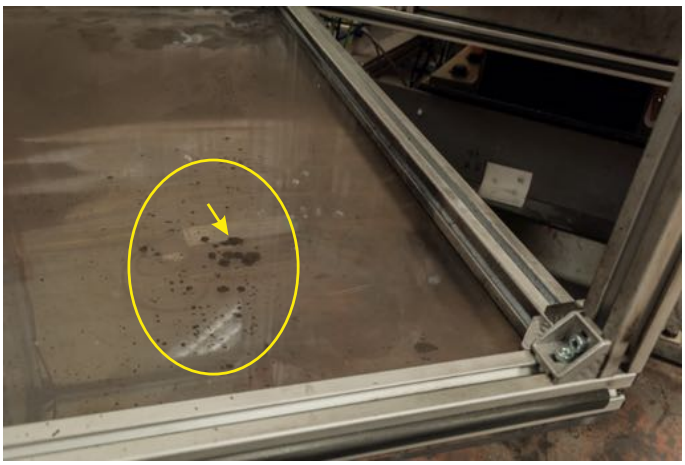

Figure 3.27: Dust deposition in the enclosure after brake testing.

and the panels.

3.6 Development of Actuation System

3.6.1 Introduction

This section presents the development stages of the new actuation system for the brake test rig described above. For present thesis, the new prototype caliper requires a two

channel hydraulic actuation system to enable control of the LTPR. The first prototype (Stage I) contains a hand-brake system to confirm the functionality of the caliper to change the CoP position when a different pressure setting for the leading and trailing piston pair is set. However, the further objective to reduce the squeal as and when it occurs requires electronic control of the LTPR. Therefore a second system is developed (Stage II) that enables full electronic control of the pressure in both leading and trailing channels.

3.6.2 Hydraulic System of Disc Brake

Brake Fluid Volume Analysis

Disc brakes use two main principles of hydraulics: the force applied at the pushrod of the master cylinder is multiplied to a higher force at the caliper piston (Owen, 2003), and the principle of equal pressure in the entire brake system (Limpert, 2011). To determine the appropriate size of a master cylinder for a particular brake, common practice includes calculation of brake fluid volumetric losses in the brake system (Limpert, 2011), (Day, 2014). The particular volumetric losses are typically calculated for the pressure required to generate a deceleration of 1 g (Day, 2014), however for this work the maximum brake system pressure of 50 bar is used. This value approximately corresponds to the maximum torque limit of 500 Nm for the UoL brake dynamometer. All brake fluid volumetric loss contributions used in the calculation are summarised below (according to (Limpert, 2011)):

- **Pad/Rotor Clearance**

$$V_{Clearance} = A_{tot} \times R_c \tag{3.2}$$

where A_{tot} is the total piston area, and R_c is the running clearance.

- **Brake Hose Expansion**

$$V_{HoseExp} = k_H \times l_H \times p_L \tag{3.3}$$

where k_H is the brake hose expansion coefficient, l_H is the brake hose length, and p_L is the brake line pressure.

- **Master Cylinder Losses**

$$V_{MasterCyl} = k_{MC} \times p_L \tag{3.4}$$

where k_{MC} is the specific master cylinder volume loss, and p_L is the brake line pressure.

- **Caliper Deformation**

$$V_{CaliperDef} = k_C \times p_L + V_r \tag{3.5}$$

where p_L is the brake line pressure, V_r is the residual air volume, and k_C can be estimated by

$$k_C = 482 \times 10^{-6} d_P - 1632 \times 10^{-6} \tag{3.6}$$

where d_P is the caliper piston diameter.

- **Brake Pad Compression**

$$V_{PadComp} = A_{tot} \times C_S \times p_L \tag{3.7}$$

where A_{tot} is the total caliper piston area, C_S is the brake pad compressibility, and p_L is the brake line pressure.

- **Brake Fluid Compression**

$$V_{FluidComp} = V_A \times C_{FL} \times p_L \tag{3.8}$$

where C_{FL} is the brake fluid compressibility factor, p_L is the brake line pressure, and V_A is the active volume of the brake system which can be determined as follows

$$V_A = V_0 + A_{tot} \times w \tag{3.9}$$

where V_0 is the brake fluid volume with new pads, A_{tot} is the total caliper piston area, and w is the wear travel of pads.

- **Air or Gas in the Brake System**

$$V_{AirGas} = \frac{V_G T}{T_0[1 - p_0/(p_L + p_0)]} \tag{3.10}$$

where T_0 is the absolute temperature at initial conditions, T is the absolute temperature at operating conditions, p_0 is the atmospheric pressure, p_L is the brake line pressure, and V_G is enclosed gas volume at ambient temperature which can be approximated as

$$V_G = 0.03 \times V_A \tag{3.11}$$

where V_A is the active volume of the brake system (see Eq. 3.9).

Then, the minimum displacement of the master cylinder V_{min} is

$$V_{min} \geqslant k(V_{Clearance} + V_{HoseExp} + V_{MasterCyl} + \cdots + V_{CaliperDef} + V_{PadComp} + V_{FluidComp} + V_{AirGas}) \quad (3.12)$$

where k denotes the fluid reserve coefficient and its value is typically in the range 1 to 2.

Table 3.8 shows the values that were used to calculate the brake fluid volumetric losses of the current brake system. Resolving Eqs. 3.2 - 3.11 and substituting into Eq. 3.12 yields the minimum displacement of the master cylinder V_{min}

$$V_{min} \geqslant 9.5\,\mathrm{cm}^3 \quad (3.13)$$

Brake Fluid

Today, the most commonly used brake fluid types in automotive applications are DOT 3, DOT 4 and DOT 5.1, all being based on polyglycolether (Limpert, 2011). Other types, not very common in passenger cars, are based on mineral oils (DOT 5) or silicon. Currently, in the UoL brake research laboratory, only the DOT 4 brake fluid is used. Since the brakes are frequently bled before each testing and the brake fluid reservoir is every time refilled with a new brake fluid, the fluid change intervals are very short when compared to a passenger car brakes where recommended intervals are usually 24 months or 30 000 miles (Gilles, 2016). This ensures that the hydraulic system of the laboratory brake remains relatively clean and airless, which can prolong lifetime of the brake system components.

Table 3.8: Calculation data for the brake fluid volume analysis.

Brake line pressure p_L (bar)	50
Brake fluid volume with new pads V_0 (cm^3)	100
Specific master cylinder volumetric loss k_{MC} ($\mathrm{cm}^3/(\mathrm{N/cm}^2)$)	190×10^{-6}
Pad wear travel w (mm)	5
Brake fluid compressibility factor C_{FL} ($\mathrm{cm}^3/(\mathrm{N/cm}^2)$)	10×10^{-6}
Brake hose length l_H (mm)	2000
Caliper piston diameter d_P (mm)	28.4
Brake hose expansion coefficient k_H ($\mathrm{cm}^3/(\mathrm{N/cm}^2)$cm)	4.39×10^{-6}
Brake pad compressibility C_S (cm/(N/cm^2))	33×10^{-6}
Running clearance R_c (mm)	0.35
Absolute temperature at initial conditions T_0 (K)	294
Absolute temperature at operating conditions T (K)	394
Atmospheric pressure p_0 ($\mathrm{N/cm}^2$)	10
Residual air volume V_r (cm^3)	0.4
Fluid reserve coefficient k (-)	1.2

3.6.3 Development of Actuation System Stage I

The first actuation system (Stage I) that was developed to control the LTPR is shown in Figure 3.28. Each actuation channel consists of an OBPHB003L lockable vertical handbrake with an integrated master cylinder that is connected via a brake hose to the caliper. The first master cylinder purchased for the actuation (designated as OBPMC03) had a bore diameter of 3/4 in (19.05 mm). The first tests showed that the actuation of this cylinder to pressures larger than 20 bar requires a big effort, therefore an OBPMC01 master cylinder with 5/8 in (15.875 mm) bore diameter was purchased for the second channel. The smaller bore diameter gave a softer feel at the handle, therefore this master cylinder was used to set a higher pressure in the split leading/trailing mode. To monitor the pressure value, each channel includes an analog pressure gauge. Both master cylinders have a stroke of 11/8 in (34.925 mm) resulting in the brake fluid displacement of 10.0 and 6.9 cm^3 for the 3/4 and 5/8 in master cylinder, respectively. Only the larger master cylinder fulfills the minimum displacement requirement evaluated in Eq. 3.13, however this was evaluated for the worst case scenario when one master cylinder actuates all four pistons. Hence, the master cylinder with the smaller diameter was used only when the split leading/trailing configuration was tested.

The actuation system Stage I enabled testing of the caliper function to independently control leading and trailing pair of pistons in the early stage of the test rig development. It also successfully verified the caliper ability to control squeal occurrence during first trial tests. In addition, this system served for standard brake tests when one handbrake actuated all four pistons by appropriate reconnecting the brake lines. Since the actuation system Stage I is dependent on human intervention, it is not possible to use it for a closed loop control system.

(a) (b)

Figure 3.28: Actuation system Stage I: (a) side-view, (b) front-view.

3.6.4 Development of Actuation System Stage II

To enable a closed loop electronic control of the output pressure and brake torque, a new actuation system Stage II containing air pressure regulators was developed. This system can be used to electronically control the LTPR of the new prototype caliper. Table 3.9 summarises main design requirements that were stated for the actuation system Stage II.

Table 3.9: Design requirements for the actuation system Stage II and their relative importance.

Design Requirement	Essential	Desired
A two-channel hydraulic system capable to control the pressure of the leading and trailing brake lines independently.	X	
Possibility to bleed and refill the hydraulic system with a new brake fluid.	X	
Electronic control of the hydraulic pressure with a feedback loop.	X	
The maximum output hydraulic pressure should be < 50 bar to prevent exceeding of the maximum torque capacity of the brake dynamometer.	X	
Electro-pneumatic control of the actuation system and use of the laboratory air pressure supply of 7 bar as a system input.		X
Easy and quick change of the system between split (two leading and two trailing pressure outputs) and uniform mode (four identical pressure outputs).		X

The final design of the two-channel actuation system is shown in Figure 3.29. Each channel consists of an electro-pneumatic pressure regulator, an air-pressure hose, a single-acting pneumatic cylinder with connecting rod and clevis, an adapter, a master cylinder, a hydraulic manifold, output fittings, and an electronic pressure sensor.

The Stage II actuation system was developed using off-the-shelf components by selecting appropriate parts combination to meet the output hydraulic pressure requirements. Table 3.10 shows calculatated output hydraulic pressure values using data available from master and pneumatic cylinder manufacturers. From possible combinations, the highlighted hydraulic pressure value of 46.4 bar was chosen. This output pressure can be designed by combining the 7/8 in (22.225 mm) master cylinder with a 63 mm pneumatic cylinder.

Figure 3.30 shows the Stage II actuation system after its commission. The components are mounted to a table assembled using the Bosch Rexroth aluminium profile system. This table allows mounting of other peripheries such as a CompactRIO controller and a dummy disc to test the system functionality with the new prototype caliper.

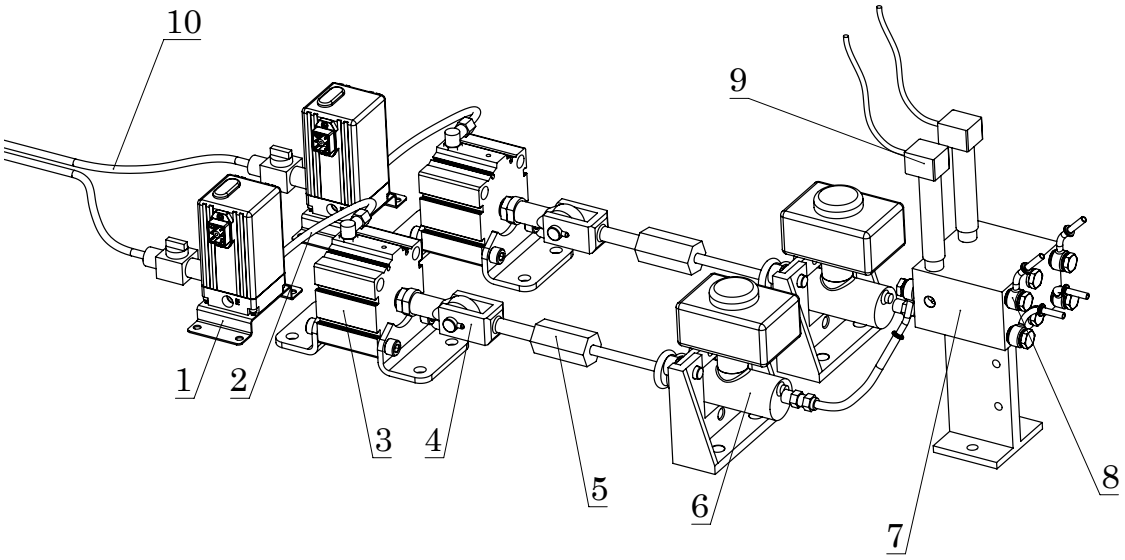

Figure 3.29: Basic layout of the components of the actuation system Stage II: 1) electro-pneumatic pressure regulator, 2) air-pressure hose, 3) single-acting pneumatic cylinder, 4) clevis, 5) adapter, 6) master cylinder, 7) hydraulic manifold, 8) output fittings, 9) electronic sensor, 10) inlet air pressure.

Table 3.10: Calculation of the output hydraulic pressure using manufacturer's data for master (Wilwood) and pneumatic cylinders (FESTO). The highlighted pressure of 46.4 bar represents an appropriate combination of the components that was chosen for the Stage II actuation system.

Master cylinder	Bore diameter (in)	5/8	3/4	13/16	7/8	1	1 1/4
	Cylinder area (mm^2)	198	285	332	388	507	792
Pneumatic cylinder diameter (mm)	Theoretical cylinder force at 6 bar (N)	Output hydraulic pressure (bar)					
25	270	13.6	9.5	8.1	7.0	5.3	3.4
32	450	22.7	15.8	13.5	11.6	8.9	5.7
40	700	35.4	24.6	21.1	18.0	13.8	8.8
50	1120	56.6	39.3	33.7	28.9	22.1	14.1
63	1800	90.9	63.1	54.1	46.4	35.5	22.7

- Electro-Pneumatic Pressure Regulator

The laboratory air pressure supply of 7 bar is used as an input for an electro-pneumatic pressure regulator which regulates the output air pressure based on the command signal from an external controller. The pressure regulator purchased for this application is manufactured by the Proportion-Air company and its type code is QB1XANEEZP7BRG-BR. It is a single loop controller giving an output pressure proportional to an electrical command signal input. The working principle is based on the control of two solenoid valves, one being an inlet, the other an exhaust. An internal pressure transducer provides a feedback signal to the built-in electronics, where the signal is compared with the command signal input. Their difference causes opening of one of the solenoid valves resulting in

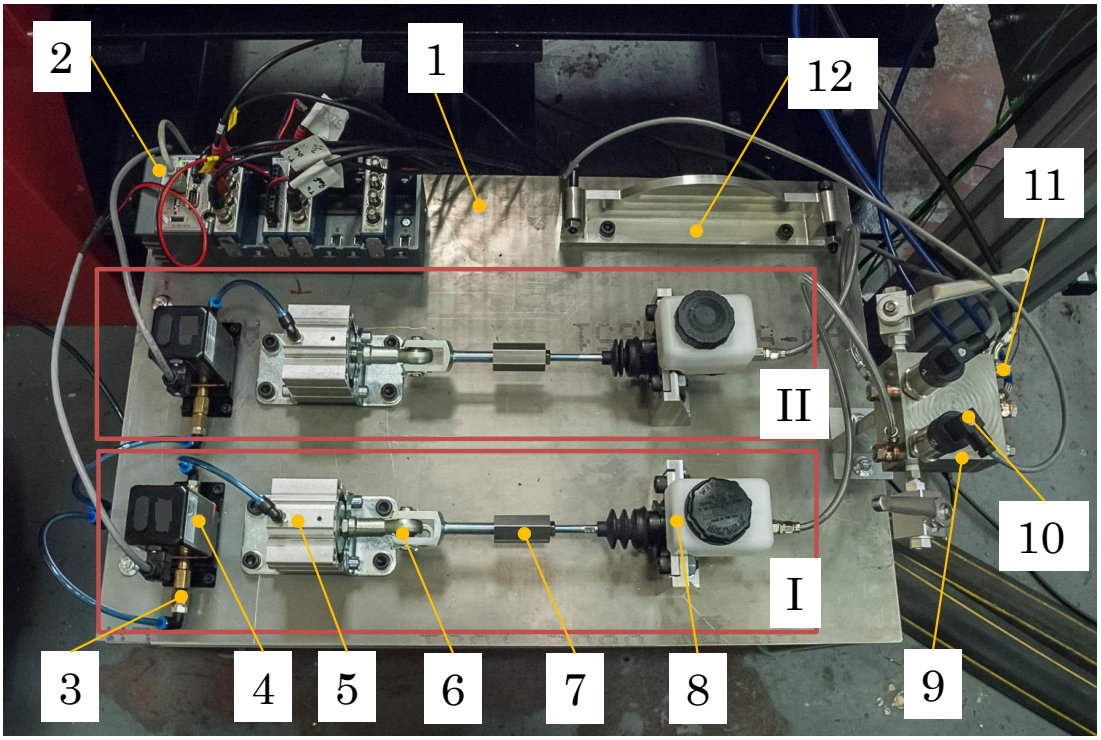

Figure 3.30: Stage II actuation system after commission: I) leading channel, II) trailing channel, 1) table, 2) CompactRIO controller, 3) input air pressure 4) electro-pneumatic pressure regulator, 5) pneumatic cylinder, 6) rod eye and clevis, 7) adaptor, 8) master cylinder, 9) hydraulic manifold, 10) pressure sensor, 11) output fitting, 12) dummy disc stand.

increase or decrease of the pressure. Both input and output signals are in the range 0 - 10 V.

- Pneumatic Cylinder

The pneumatic cylinder that is used to convert the air pressure to a mechanical linear force is a short-stroke single-acting pneumatic cylinder purchased from the FESTO company. The reverse motion of the single-acting cylinders is provided by a built-in spring, therefore the cylinder features only one input. Referring to the manufacturer's data, the cylinder diameter is 63 mm, yielding a theoretical force of 1800 N at 6 bar. This cylinder is designated as AEVC-63-25-A-P and its accessories include the foot mounting HNC-63, the rod clevis SGA-M12X1.25, and the rod eye SGS-M12X1.25.

- Adaptor

To bridge the pneumatic cylinder rod clevis with the master cylinder, a special adaptor was fabricated. The thread at the side of the rod clevis is M12x1.25, whereas the master cylinder rod has a 5/16-24 in thread. The material used for the adaptor is a mild steel.

- Master Cylinder

The role of the master cylinder in the new actuation system is to convert the mechanical force from the pneumatic cylinder to the hydraulic pressure of the brake fluid at the output. To utilize the full length of 25 mm of the pneumatic cylinder stroke, a master cylinder with a stroke of 28.4 mm was chosen. This type of master cylinder is manufactured by the Wilwood company and can be delivered as a kit including a non-integral brake fluid reservoir. As calculated in Table 3.10, the master cylinder bore size is 7/8 in, giving a cylinder area of 388 mm^2. Multiplying this value with the pneumatic cylinder stroke yields the maximum brake fluid displacement of 9.7 cm^3. This fulfills the requirement of the minimum master cylinder displacement calculated in Eq. 3.13. The part number for this type of master cylinder is 260-10374 and it was ordered from a Wilwood dealer.

- Hydraulic Manifold

A tailored hydraulic manifold was designed to facilitate connection of the brake lines. The manifold allows a distribution of the brake fluid from two inputs to two independent outputs (e.g. LTPR control), or one input to up to four outputs (e.g. single-input brake calipers, or multi-piston brake calipers with uniform pressure setting). In addition, the manifold can accommodate pressure sensors and drain valves. The material of the manifold is the 316 stainless steel to prevent corrosion and thread damage due to frequent change of the fittings. The manufacturing process of the internal channels required a more challenging oblique drilling which was completed satisfactorily by the UoL workshop.

- Pressure Sensor

The pressure sensor is mounted to the hydraulic manifold where it monitors the brake fluid pressure and sends the pressure value to the controller. The model of the pressure transmitter is WIKA S-20 with measuring range 0 to 60 bar giving an output signal 0 to 10 V. The sensor kit was ordered from Fluid Controls Ltd and it included a calibration certificate.

3.7 Summary

This chapter has presented thoroughly all steps of the new brake test rig design. The largest section was devoted to the design of the prototype brake assembly, followed by explaining the development process of the new extraction and actuation system.

The new 4-piston brake caliper met all design requirements that had been originally stated. It has been effectively used for numerous braking tests of different disc and pad friction pairs, and demonstrated comfortable assembling process and overall maintanence. The caliper can be used to control the leading/trailing pressure ratio (LTPR), as well as for standard braking tests with uniform piston pressure setting.

An FE analysis performed on the caliper and brake brackets showed that maximum deformations and stresses of the brake under testing loads are well within acceptable

limits.

Also covered in this chapter is the design and commission of a new air extraction system that was installed in the UoL brake laboratory. The extraction system effectively removed the gaseous emissions and their odour out from the laboratory environment during brake testing. The particle emissions are filtered through sets of HEPA filters to prevent contamination of the environment. The design of the enclosure complies with the required space for the recommended position of the noise microphone given in the SAE J2521 standard for next squeal tests.

Finally, the development of the new electronic actuation systems Stage I and Stage II has been presented. The actuation system Stage I containing handbrakes successfully confirmed all functionalities of the new brake prototype and early tests demonstrated the potential to control squeal occurrence by modifying the LTPR. To control the brake line pressure electronically, the actuation system Stage II featuring electro-pneumatic pressure regulators was developed. This system has been used successfully for numerous braking tests.

4 Development of DAQ and Squeal Control System

"I couldn't find the sports car of my dreams, so I built it myself."
Ferdinand Porsche

4.1 Introduction

This chapter presents the development of the data acquisition (DAQ) and squeal control system for the actuation system Stage II described in the previous chapter. First, an overview of the brake test rig control signals and DAQ architecture is given, followed by introducing the DAQ hardware and software. A more detailed section is devoted to the main controller and its topology. Also, the architecture of a newly developed control program is explained and accompanied by numerous illustrations. Next, all the main test rig sensors are presented in greater detail, explaining their primary function and operation, position on the brake and connected accessories. The main calibration procedure and results are also included. In the following section, the pressure and torque tracking operational modes of the brake test rig are described, and the architecture and the principle of operation of the new automatic squeal reduction (ASQR) system is presented. The functionality of the operational modes is demonstrated using simple testing procedures. Finally, important outcomes from this chapter are given in the conclusions.

4.2 Control System and DAQ Architecture

Today, brake dynamometers are equipped with numerous electronic sensors that require a fairly complex DAQ system. The data to be monitored often include disc rotational speed, brake torque, temperature or temperature field of brake components, brake line pressure, sound and/or accelerometer data files. The University of Leeds (UoL) brake dynamometer is controlled from an operation stand positioned outside of the brake dynamometer area and protected by a safety cage as shown in Figure 4.1. All monitored data and command signals are electronic, hence a desktop computer (Figure 4.2) is used to control test rig processes, as well as to visualise and store data. An overview of the energy and signal flow between the components of the brake test rig is illustrated in Figure 4.3. It is obvious that DAQ and processing of all electronic signals requires a controller capable of a rapid multi-channel control with the ability to manage and store

Figure 4.1: Protecting cage in the UoL brake test area.

Figure 4.2: Computer control of the brake test rig.

large sound and/or accelerometer data. At UoL, such systems are currently provided by National Instruments (NI) Corporation that offers complex hardware and software solutions for DAQ and test application development.

4.2.1 Control System Hardware

NI offers a wide range of cards and chassis that can interface with the desktop computer as shown in Figure 4.2. There are three NI DAQ systems currently used in the UoL brake laboratory: NI 6225 M Series DAQ card connected to NI BNC 2090 chassis (Figure 4.4(a)), NI CompactRIO 9024 controller (Figure 4.4(b)), and NI USB 6003 DAQ device (Figure 4.4(c)).

The NI 6225 DAQ system is installed on the desktop computer and connected to the BNC 2090 chassis that enables easy connecting to peripheries via BNC connectors. This existing system was used to log data from all sensors for the majority of previous brake tests and also for the actuation system Stage I.

The NI CompactRIO 9024 controller is employed for the new actuation system Stage II presented in Chapter 3 to control the output hydraulic pressure or brake torque depending on the operational mode. Furthermore, it also enables the processing of large quantities of data from the microphone or accelerometer in real-time. CompactRIO controllers feature a real-time controller, reconfigurable input/output (I/O) modules, and a field-programmable gate array (FPGA). The controller body is mounted to an 8-slot cRIO-9114 chassis, allowing the attachment of a variety of I/O C-series modules. For the current application, one NI 9263 and two NI 9215 modules are used. The NI 9263 is a 4-channel 10 V voltage output module, allowing the user to update analog signal simultaneously up to 100 kS/s/ch. It has a 10-position screw terminal. The NI 9215 is a 4-channel 10 V voltage input module with BNC connectors. It provides 100 kS/s/ch sampling rate in 16-bit resolution. The controller communicates with the host computer via an ethernet cable.

For other applications that require portability, the NI USB 6003 DAQ device is used. It allows connection of up to 8 analog inputs in single-ended or 4 in differential connection, 2 analog outputs and 13 digital I/O ports. Furthermore, it features one 5 V power output,

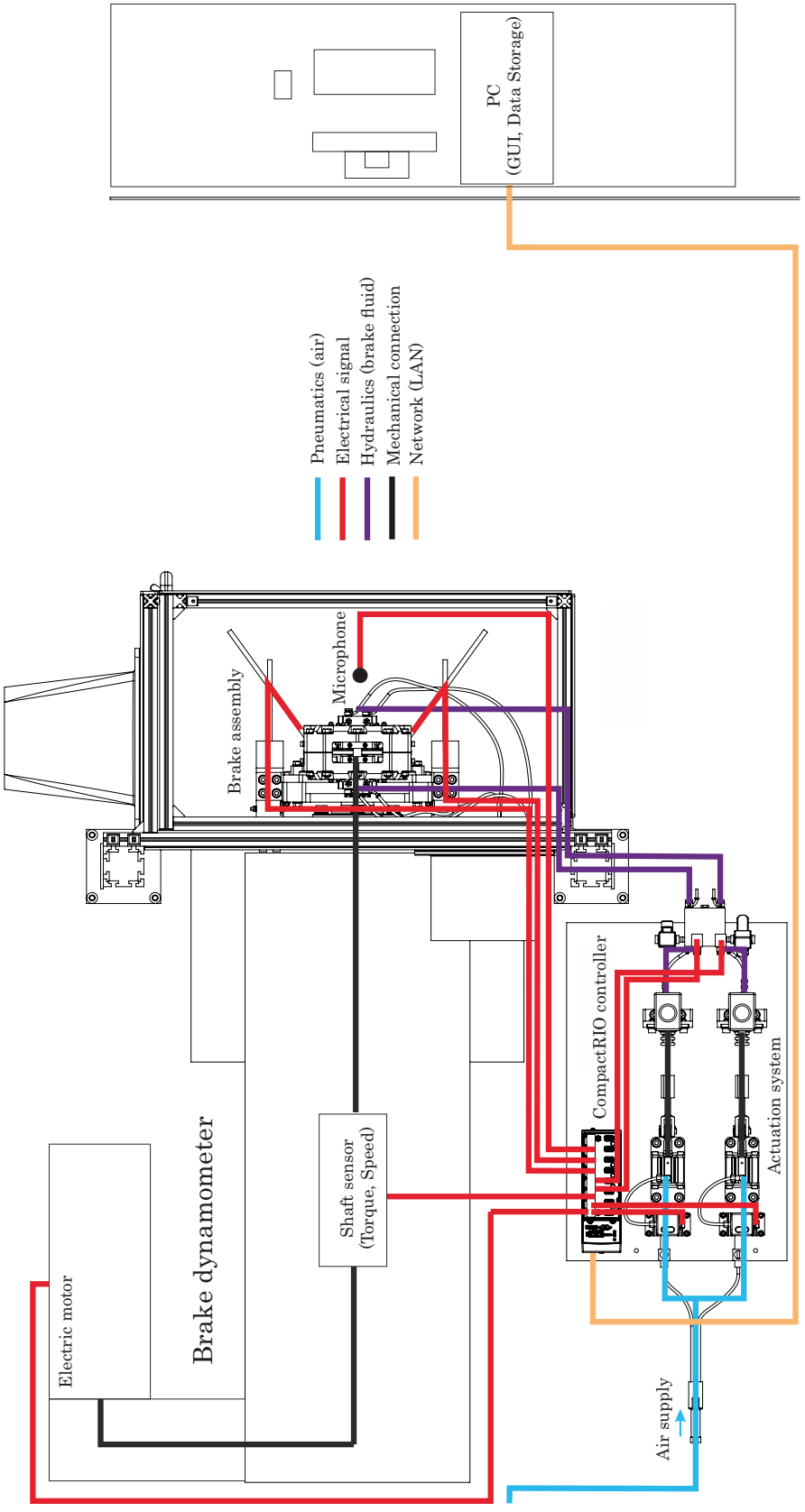

Figure 4.3: Top view of UOL brake dynamometer showing energy and signal flow.

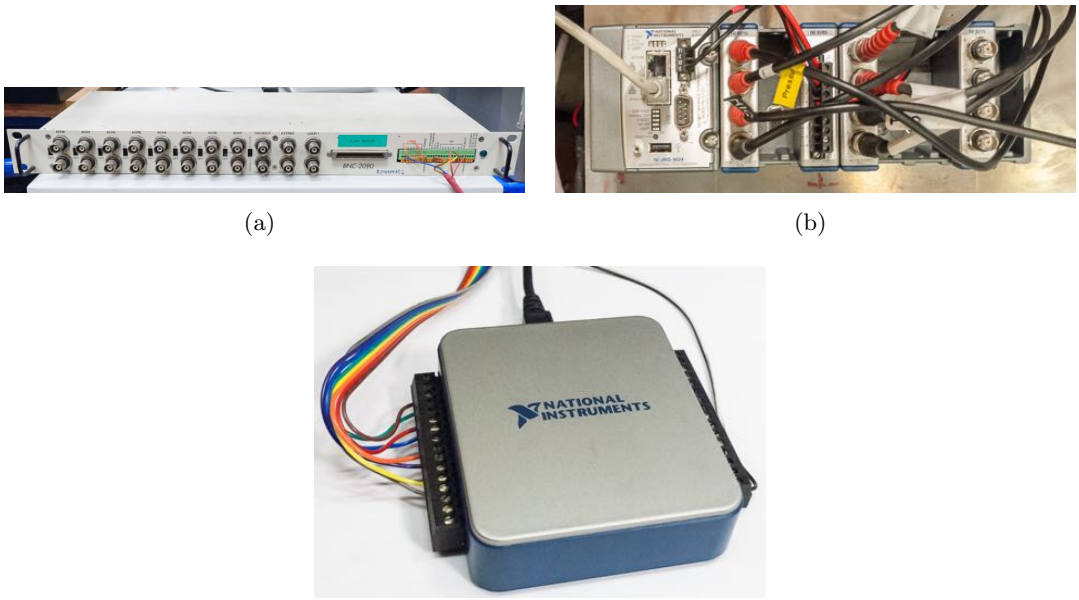

(a) (b)

(c)

Figure 4.4: NI DAQ and controller systems: a) BNC 2050 chassis, b) CompactRio 9024 controller, c) USB 6003 DAQ device.

as well as trigger and counter functions. The digital-to-analog converter resolution is 16-bit. The main advantage of this lightweight device is its portability and connectivity to a computer via USB port. In this work it is used to calibrate and acquire signals from the pad sensor presented in Chapter 6.

In the remaining part of this chapter, the CompactRIO control system is presented in greater detail.

4.2.2 Control System Software

NI provides a Laboratory Virtual Instrument Engineering Workbench (LabVIEW), which is a system design platform and development environment for control and DAQ applications. LabVIEW uses a graphical programming language called "G" that helps the user to visualise the dataflow of large applications. LabVIEW applications consist of a front panel, a connector panel, and a block diagram. Typically, a programmer develops an application in a block diagram by dragging and connecting pre-programmed virtual instruments named VIs. Also, there is a possibility to create the user's own subVIs. Most applications include some of the well-known design architectures that enable easier and faster implementation of communication and data exchange techniques between the DAQ hardware, a user and a computer. The most common architectures are:

- State machine
- Event-driven user interface
- Master-slave

- Producer-consumer

- Queued state machine with event-driven producer-consumer

For large applications, very often a combination of the above techniques is used. A general LabVIEW program architecture for the CompactRIO controllers is shown in Figure 4.5. The top level Windows PC VI communicates via the network with a normal priority VI at the CompactRIO system. The normal priority VI can interact with time-critical loops using interthread communication (termed as Real-Time (RT)). These can exchange data with the lowest FPGA level via a dedicated interface. The LabVIEW FPGA VI can access I/O modules and can provide time-critical operations. However, a limiting factor of the FPGA is usually the memory size, so only simple algorithms can be here implemented.

The FPGA contains an array of programmable logic blocks, programmable interconnect and I/O blocks as shown in Figure 4.6. These can be configured to implement complex digital computations and are, unlike processors, truly parallel in nature. They offer very fast I/O response times, usually exceed the computing power of digital signal processors and enable flexibility of fast prototyping and verification in contrast to an application specific integrated circuit design. Figure 4.7 illustrates an example of calculation of a simple mathematical expression (A+B)xCxD. It can be seen how certain processes can run in parallel as they do not have to compete for the same resources.

To implement the general program architecture shown in Figure 4.5, a sample project *LabVIEW FPGA Control on CompactRIO* was adopted and modified to meet the requirements of the actuation system Stage II. The template for this project is accessible from LabVIEW software. It provides a deterministic, hardware-based control of a plant and contains three main levels: user interface on the host desktop computer, Real-Time (RT) controller, and loops running on the FPGA. The basic principle of the communication between the levels can be explained using the example of setting a new pressure value (Figure 4.8) as follows:

1. In the first step a new pressure value of 10 bar is set for the leading pressure channel.

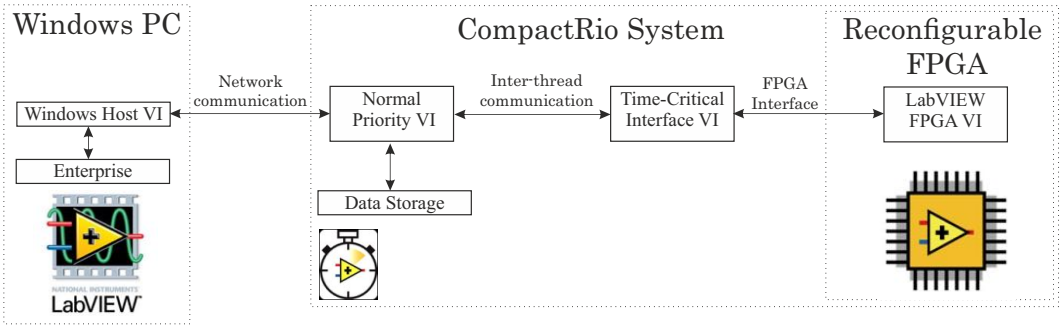

Figure 4.5: Typical communication topology of a system that uses an FPGA module.

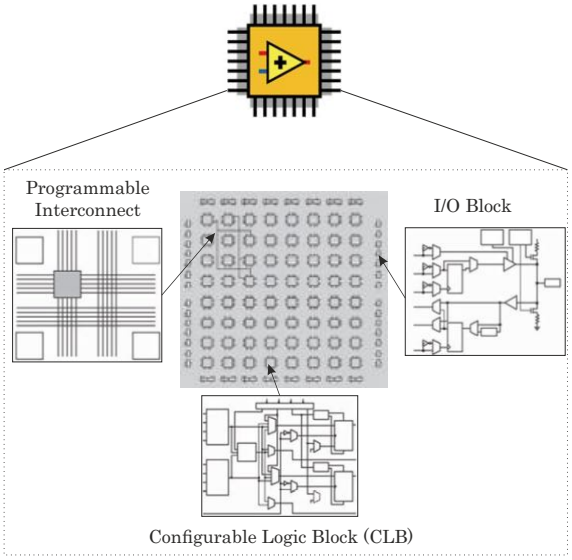

Figure 4.6: FPGA chip containing a configurable logic block (CLB), programmable interconnect and input/output (I/O) blocks.

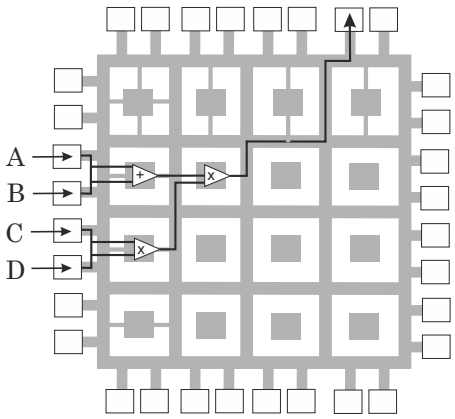

Figure 4.7: Example of calculation (A+B)xCxD on FPGA.

2. The Event Handling Loop registers an event and creates and send the Update Setpoints message, including the changed value, to the message queue.

3. The message is dequeued in the UI Message Handling Loop followed by an execution of a corresponding message diagram.

4. The code of the message diagram executes writing the Update Setpoints message and data to a network stream.

5. On the RT controller, the UI Commands loop reads the message and the data from the network stream.

6. The message including data are sent to the RT Message Handling Loop.

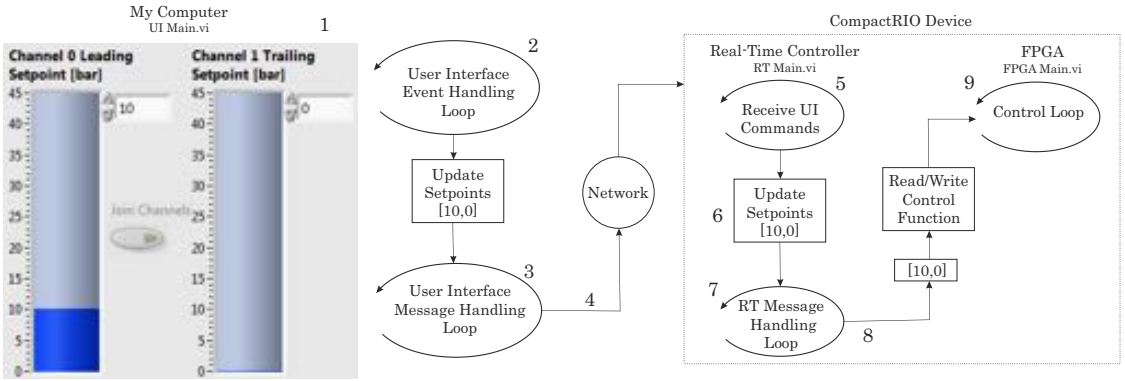

Figure 4.8: Illustration of the program flow showing the sequence of steps when setting a new pressure value.

7. The message is dequeued in the RT Message Handling Loop followed by an execution of a corresponding message diagram.

8. The code of the message diagram executes writing the data to the front panel of the FPGA VI with Read/Write Control function.

9. On the FPGA, the Control Loop updates the new pressure value.

Figure B-2 in Appendix B shows a complete CompactRIO project structure including the host computer level, RT level, and FPGA level.

The front panel of the UI Main.vi is displayed in Figure B-3. It contains the following functionalities: setting the operational parameters of the brake test rig (Area 1), test cycles management (Area 2), time plots of the main operational parameters (Area 3), and squeal, CoP and LTPR indicators (Area 4). Activating the UI Main.vi in the project tree runs by default an additional UI panel shown in Figure B-1 that allows the user to observe plots and values of the main brake operating parameters on a second computer screen. The parameters include the pressure of the leading and trailing channel, temperature T1 and T4, speed, and brake torque. On the test cycle panel (Area 2 in Figure B-3), a .csv or .dat file with test parameters can be loaded to track the dyno speed and either leading and trailing pressure values in the pressure mode or torque values in the torque mode. The input test file for the pressure tracking is in a three-column format (leading and trailing pressure, and speed), whereas the file for the torque tracking is formatted in a two-column file (torque, and speed). In addition, the cycle can be repeated for a range of temperatures by activating the *SAE J2521* button. The default setting complies with the temperatures recommended for the drag brake procedure of the SAE J2521 standard (from 50 to 300°C and down to 50°C with 25°C increments). The temperatures can be modified in the block diagram before running the program.

Besides the loops governing the communication between the host computer and FPGA, the RT level contains a squeal control and a microphone signal processing loop. The front panel of the RT Main.vi is shown in Figure B-6 and allows the user to set the parameters of the squeal filter (Area 1) and ASQR control algorithm (Area 2).

The front panel of the FPGA level is shown in Figure B-7 and allows the user to set all parameters of the low-level control functions.

4.2.3 Sound and Vibration

As explained in Section 2.3, sound is a mechanical vibration or a mechanical wave propagation that is transmitted in an elastic medium. The former can be monitored with an accelerometer mounted on a vibrating surface, while the latter is commonly observed using a microphone. In this work both methods were examined and on the hardware side prepared for future work as can be seen in Figures 4.9 - 4.10. However as explained above, due to the limited size of the code that is possible to compile on the current FPGA level, only one method can be used at a time during brake testing. Since the SAE J2521

Figure 4.9: Behringer ECM8000 microphone.

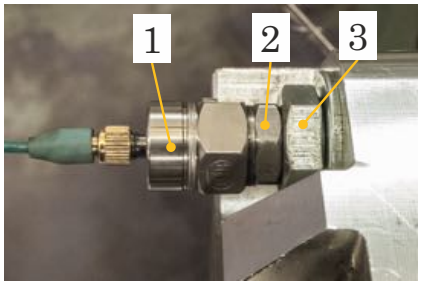

Figure 4.10: Accelerometer assembly containing: 1) DJB A20T accelerometer, 2) adapter 3) M10 bolt with tapped hole.

standard requires a microphone to be used for noise measurements, this method was also chosen for squeal detection in this work.

The accelerometer shown in Figure 4.10 is a 1-axis DJB A20T accelerometer that is connected via a signal amplifier (Figure 4.11(a)) to an analog input port of the CompactRIO. The power source for the amplifier is displayed in Figure 4.11(b). To enable attachment of the accelerometer to the main caliper clamping bolts, a bolt mounting adapter (Figure 4.11(c)) was fabricated. Similarly, a nut adapter (Figure 4.11(d)) permits mounting of the accelerometer to an abutment fastener.

The microphone employed in this work is a Behringer ECM8000 ultra-linear measurement condenser microphone that features an evenly weighted true omnidirectional polar pattern and exceptionally flat frequency response in the range 20 Hz - 20 kHz. It is mounted to the enclosure above the brake assembly as shown in Figure 4.12(a), complying with the recommended position included in the SAE J2521 standard concerning the location of the sound transducer for squeal measurements (Figure 4.12(b)). The microphone requires a phantom power from 15 to 48 V which is provided by the pre-amplifier shown in Figure 4.12(c). This is a Pulse MPRE DUAL 48 V phantom power dual channel microphone pre-amplifier with individual gain controls and LED peak indicators for each channel. It was modified to be powered from a power source (see the left part of Figure 4.15) instead of a 9 V battery. The output of the pre-amplifier is connected with an analog input port of the CompactRIO via a 3-pin XLR to BNC conversion cable. The conversion constant of 304 mV/dB was calculated by measuring the voltage output for 94 and 104 dB reference 1 kHz sound generated with the calibrator shown in Figure 4.12(d). The dB reference is set to $20\text{x}10^{-6}$ Pa.

Due to memory limitations of the FPGA, it was not possible to implement squeal detection at the FPGA target. The microphone signal is, therefore, buffered from the FPGA target to the RT host, where the available memory is much larger as well as more advanced block functions to process the sound signal can be applied here. The sound signal between the FPGA and the RT is transferred with a direct memory access (DMA) method that contains two buffers, one at each side. The code at FPGA writes data to the buffer, while the code at the RT reads the data from the buffer, so the

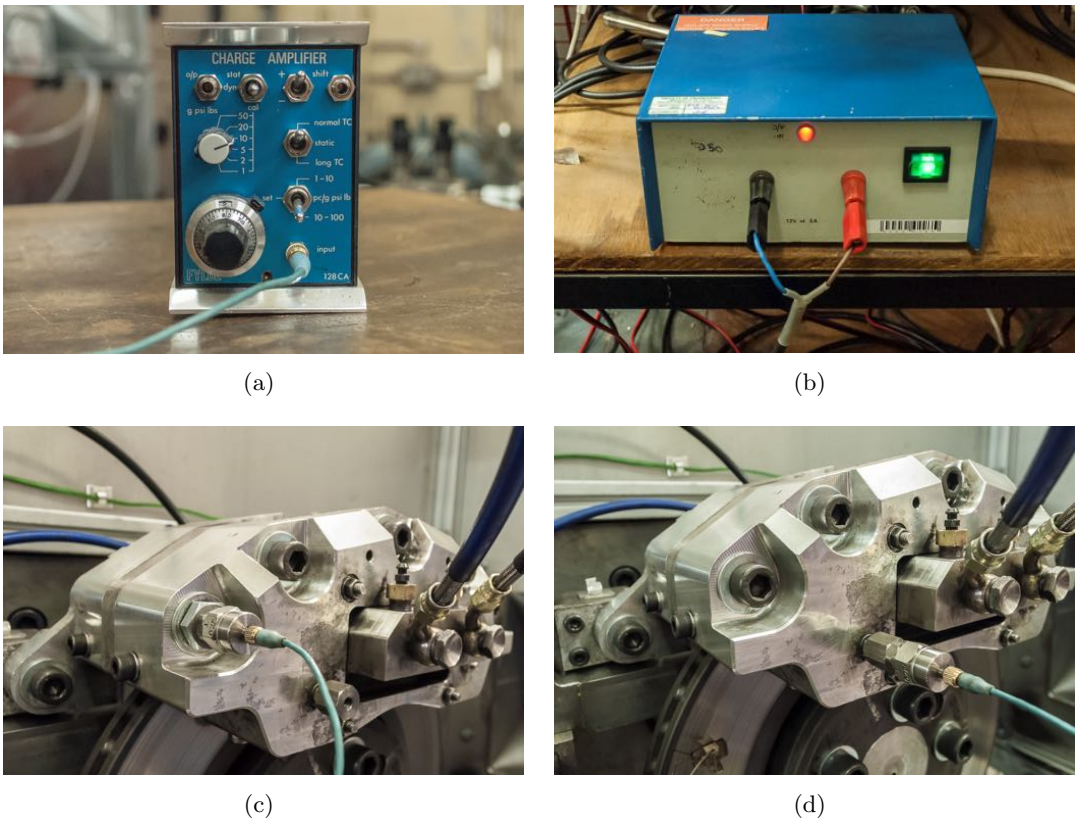

(a) (b)

(c) (d)

Figure 4.11: Accelerometer: a) amplifier, b) power source for the amplifier, c) mounting position on the main caliper clamping bolt, d) mounting position on the abutment nut.

method is strictly unidirectional. The DMA method is based on the first-in, first-out (FIFO) access policy, which holds the order of the data array in the same order as they are received. It is the fastest available method between the FPGA and the host as the host processor is not involved and can perform other data calculations during the data transfer. In addition, it reduces the number of the front panel controls or indicators. The current NI CompactRIO can contain up to three DMA FIFO channels, so in theory both accelerometer and microphone signals could be transferred at the same time, however due to the limited size of the code on the FPGA, this was not possible. Another option is to interleave one DMA FIFO for two signals on the FPGA and then to decimate them on the host. However, it was found that occassionally the signals were swapped on the host, so this possibility was not used due to lack of robustness.

After receiving the microphone signal at the RT, it is post-processed to identify the squeal occurrences as outlined in the flowchart in Figure 4.13. First, the buffered data array is converted to a waveform and then from voltage to decibels. Then, the scaled microphone signal is used to compute the power spectrum density using a fast Fourier transformation, where the resulting frequency band of interest can be set by the user. The next operation includes searching for amplitude peaks occuring above a certain amplitude threshold defined by the user. Finally, a weighting function applies the A-filtering to the

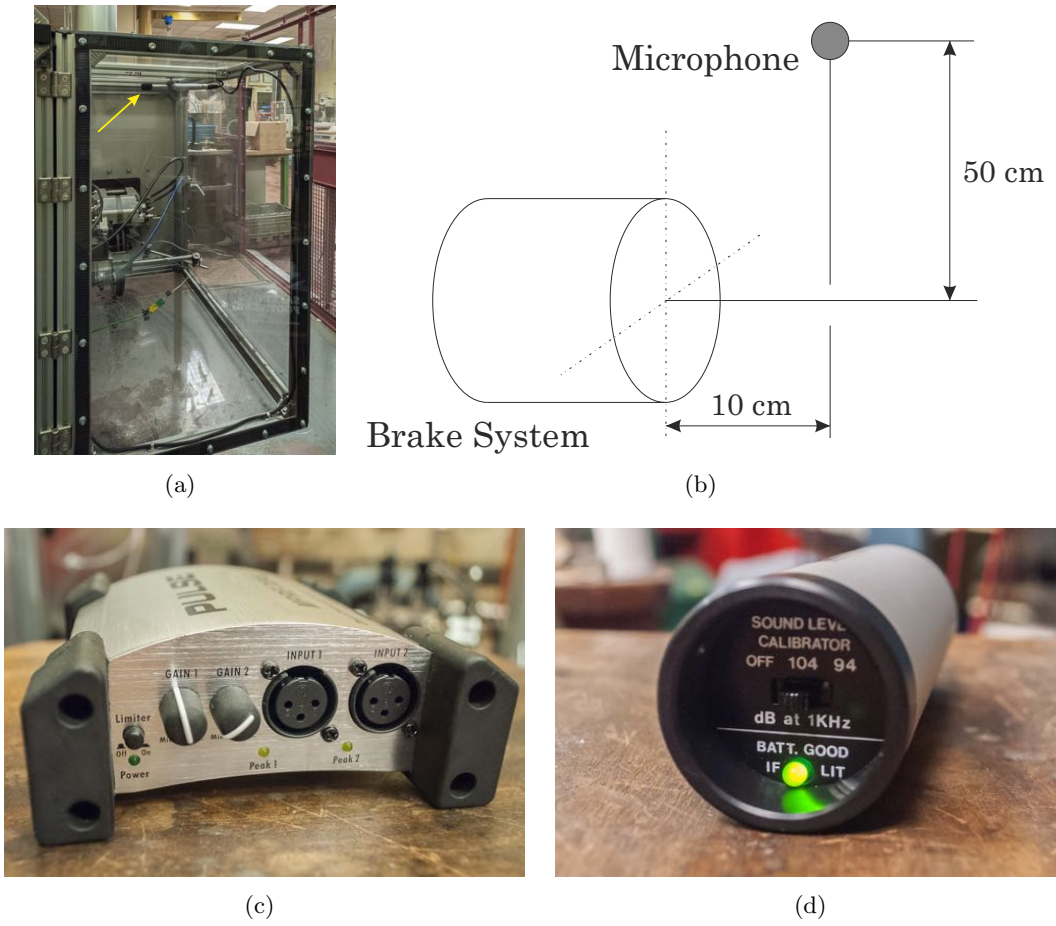

Figure 4.12: Microphone: a) recommended position according to the SAE J2521 standard, b) position after installation, c) Pulse MPRE DUAL microphone pre-amplifier, d) sound level calibrator.

peak amplitude values. If squeal occurs in a frequency bandwith of interest and above a certain amplitude threshold set by the user, the signal is evaluated as a squeal occurrence and the boolean squeal trigger is changed from 0 to 1. This trigger can be subsequently employed in the ASQR control loop. Due to a possible different timing of the ASQR control loop, the squeal hold functionality was programmed, which allows the user to set the duration of the detected squeal occurrence. These sequences are programmed using specialised VIs from the Sound and Vibration Toolkit as shown in the block diagram in Figure B-8.

Figure 4.14 shows the same squeal event for the two most common types of magnitude/frequency/time plots: 2D spectrogram (Figure 4.14(a)) and 3D waterfall plot (Figure 4.14(b)). These are mainly used to identify squeal occurrences and their frequencies from long duration recordings of the microphone signal.

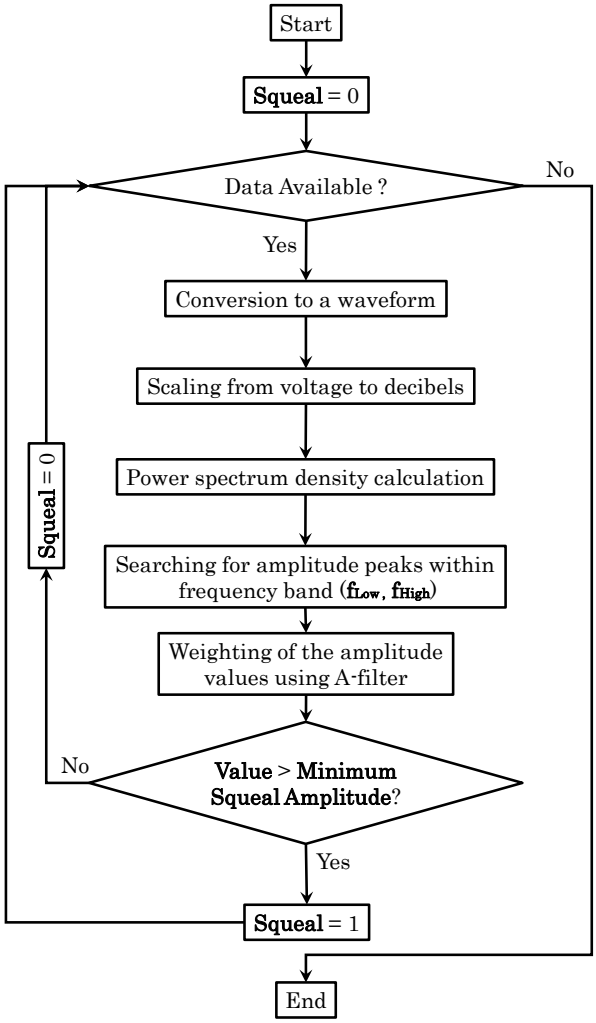

Figure 4.13: Flowchart describing the process of the squeal detection.

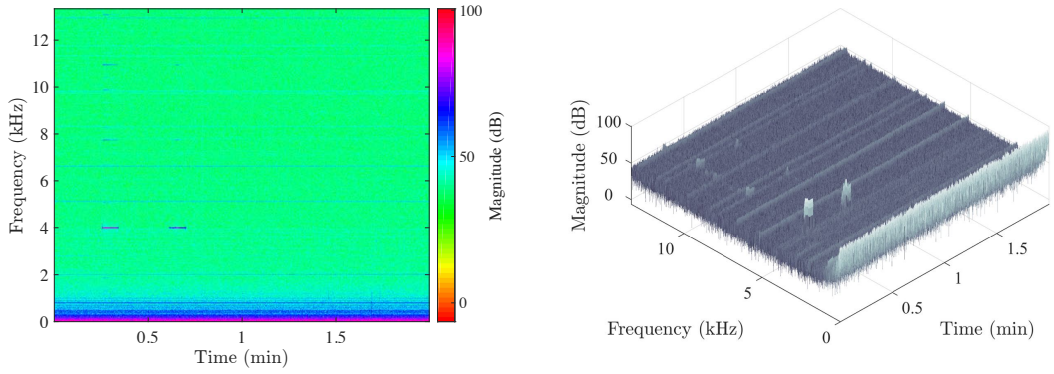

(a) (b)

Figure 4.14: Two most common types of squeal magnitude/frequency/time plots used for squeal investigation: a) 2D spectrogram, b) 3D waterfall plot.

4.2.4 Brake Fluid Pressure

The brake fluid pressure is monitored with a pressure sensor as shown in Figure 3.30. The input voltage of the sensor is in the range 12 - 35 V and is provided by the left voltage channel of the power source on the right side of Figure 4.15. As mentioned

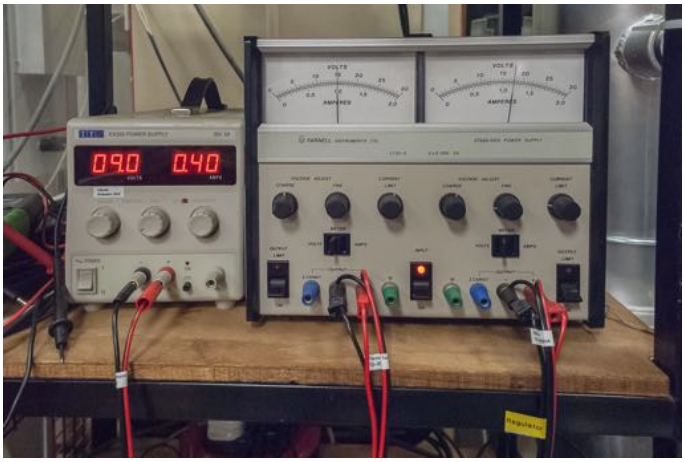

Figure 4.15: Power source for the microphone pre-amplifier (left), and pressure transducer and air pressure regulator (right).

in Chapter 3, the pressure sensor was delivered with a calibration certificate, so the calibration procedure was not necessary. The data from the calibration certificate were used to determine the coefficients of linear regression as shown in Figure 4.16. These

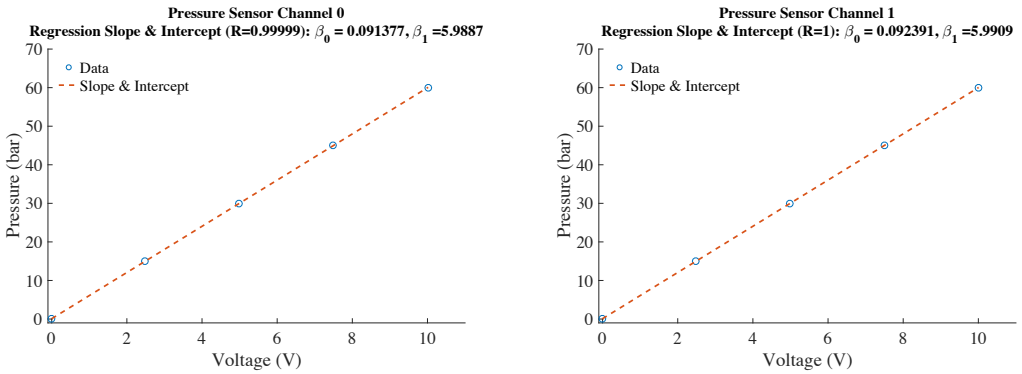

(a) Channel 0

(b) Channel 1

Figure 4.16: Pressure transducer linear regression curves to determine the coefficients for LabVIEW control program.

coefficients are used in the UI Main.vi to convert the voltage signal to pressure values, and vice versa.

4.2.5 Temperature

The temperature at the disc rubbing surface is monitored using two sliding thermocouples (labelled T1 and T4) as shown in Figure 4.17. These thermocouples are TC Ltd

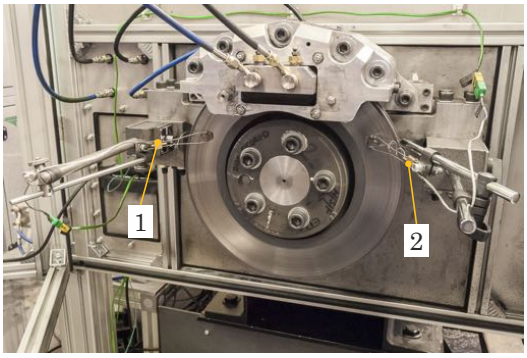

Figure 4.17: Positions of the sliding thermocouples on the disc rubbing surface: 1) T1 thermocouple 2) T4 thermocouple

Figure 4.18: Thermocouple amplifier equipped with four inputs.

Type 30 brake disc rubbing thermocouples containing a fast response miniature mineral insulated thermocouple sensor which is microwelded to a floating stainless steel shoe. The position of the shoe is fully adjustable via a screw and nut on the main sensor body that is bolted to an arm of a magnetic base attached to the rig brackets. The thermocouple is of the K type allowing the system to monitor the brake disc temperature up to 850°C. The current version is of robust style where the sensor is wrapped around the frame for extra support. The output voltage from the sensor is enhanced with the amplifier shown in Figure 4.18. The amplifier is powered by a 9 V battery, allowing it to connect in total up to four thermocouples. The signal from the amplifier is connected to an input port of the CompactRIO.

To calibrate a thermocouple, the sensor output voltage needs to be determined for at least two reference temperatures. In the calibration setup shown in Figure 4.19, the first reference point represents the mixture of melting ice and water that maintains a temperature of 0°C until all the ice cubes melt. The second reference point is boiling water which maintains a temperature of 100°C. A reference digital thermometer is used to identify the equilibrium state for actual measurements. The sensor output voltage is read for both points using a simple LabVIEW code and a linear interpolation is provided to generate a trendline as can be seen in Figures 4.20(a) - 4.20(b).

4.2.6 Torque and Speed

The brake dynamometer shaft shown in Figure 4.21 features a torque transducer that allows the system to measure the brake torque as well as the rotational speed of the shaft. The torque transducer is a Vibro-Meter TORQUEMASTER TM 213 with a maximum torque rating of 500 Nm. It is supported by the frame and connected via a double-element coupling to the shaft on the gearbox and brake disc side. The torque sensing of this particular device is based on the principle of measuring the induction

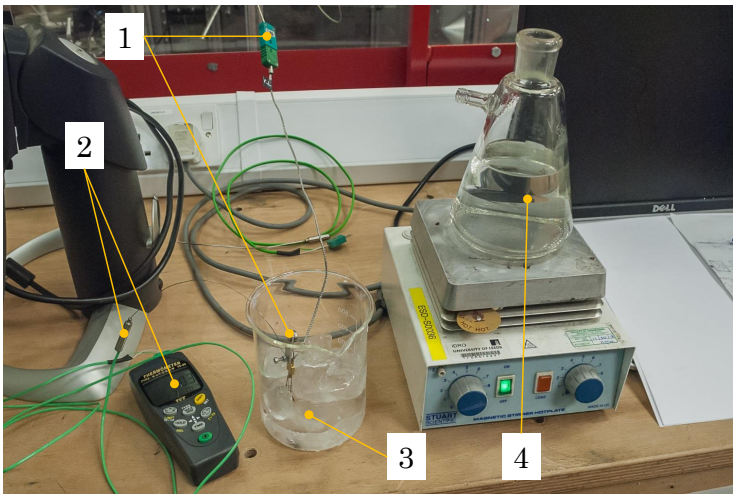

Figure 4.19: Calibration procedure of the thermocouple: 1) calibrated thermocouple, 2) reference thermometer, 3) a beaker containing ice bath, 4) a flask with boiling water.

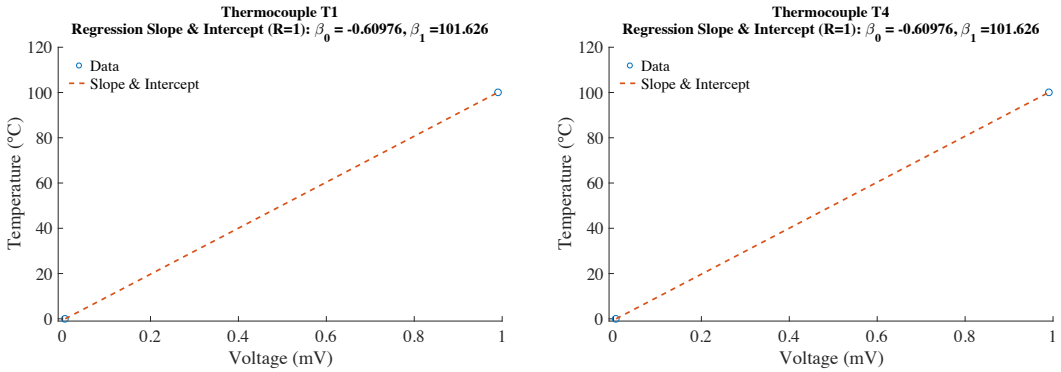

(a) (b)

Figure 4.20: Calibration curves: a) Thermocouple T1, b) Thermocouple T4.

Figure 4.21: Torque and speed transducer.

Figure 4.22: Power source for the torque and speed transducer electronic unit (5V and 25V).

between two transformer coils, each of them connected to one side of a deformation shaft. An applied torque causes the shaft to deform, which results in an increased overlap of the coils and hence an increased induction. Since the primary coil is excited by a sinusoidal voltage signal, the secondary coil generates a voltage signal, the magnitude of which is dependent on the applied torque. Then, the voltage signal is processed in an electronic unit giving an output voltage of $\pm$ 10 V which is connected to an input port of the CompactRIO. The torque transducer and the electronic unit use 5 V and 25 V supplied by a power source as shown in Figure 4.22. The calibration conversion coefficient of 0.1 V/Nm is applied in the main LabVIEW DAQ program to give torque values in Nm. It should be noted that all calculations that use the brake torque value should be reduced by the torque drag losses which can be determined by running the shaft without applied pressure.

To measure the rotational speed of the shaft, the torque sensor is equipped with a speed transducer that faces a toothed gear wheel mounted on the shaft and detects generated analog pulses. The number of pulses is 30 per each revolution. As for the torque signal, the speed signal is processed with an electronic unit, and connected to an input channel of the CompactRIO. To obtain a rotational speed in rpm, it is necessary to use a counter function. This was programmed on the FPGA level as can be seen in the block diagram at the top of Figure B-4. It uses a function detecting the signal crossing between the specified minimum and maximum threshold, followed by numerical operations to get values of the speed in rpm. This value is equal to the brake disc rotational speed as the disc is directly mounted on the same shaft. The minimum speed of the shaft that can be measured is 20 rpm.

The steps required for putting the brake dynamometer and extraction system into operation are explained in Section B.1 and B.2, respectively.

4.3 Brake Test Rig Control System

The CompactRIO controller presented above is used to provide a real-time reduction of brake squeal, as well as a control of two main operational modes of the brake test rig: pressure and torque tracking. The squeal controller is located on the RT level due to a complex microphone and/or accelerometer signal processing as described above, and its control is based on the state-machine controlling method. On the other hand, the control algorithms for piston pressure and brake torque tracking are due to their relative simplicity located on the FPGA level, which has an advantage of fast response times. The torque and pressure tracking methods utilise a PID controller and apply a simple negative feedback principle in their control loops.

4.3.1 Speed Control

The speed of the brake dynamometer shaft is set by sending a signal command to the controller of the dynamometer electric motor. The command is represented by a voltage

value in the range 0 - 10 V, where a step of 1 V is approximately 155 rpm. As the actual speed is regulated by the dynamometer controller, the control program does not require an additional feedback loop, and outputs only a desired target value as shown in the bottom loop in Figure B-4.

4.3.2 Pressure Control

A basic schematic of the control loop applied for the control of the hydraulic pressure is presented in Figure 4.23, in which each channel can be categorised as a single-input single-output system (SISO) with a negative feedback loop. Therefore, the process error

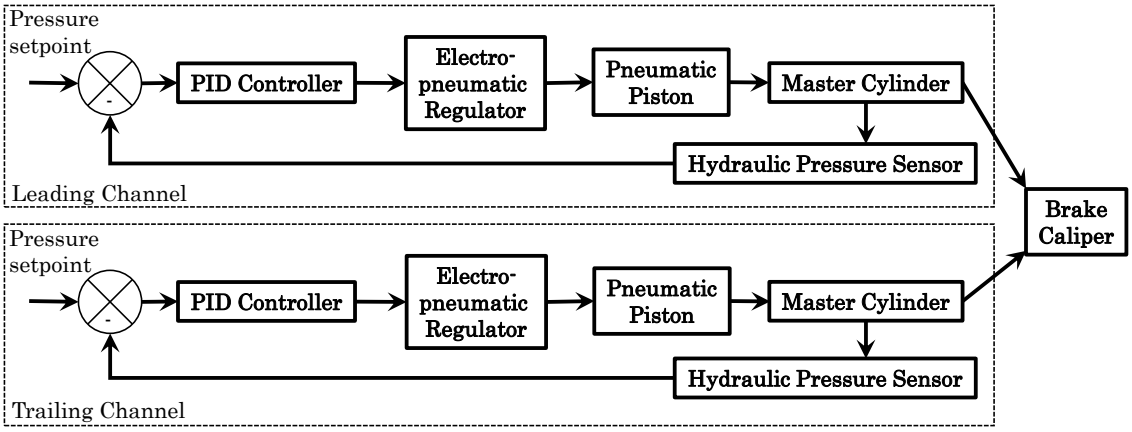

Figure 4.23: Schematic of the control loop to regulate the hydraulic pressure in the pressure tracking mode.

is computed as a difference of the negative value of the process variable and the set point. The process error is routed to a PID controller that outputs a command signal to the air pressure regulator to minimise the error. The gains for the controller were determined using an empirical tuning method that is briefly explained as follows:

1. Set all gains to 0.
2. Increase the P gain until the response to a step starts to oscillate.
3. Increase the D gain until the oscillations disappear.
4. Repeat the steps 2 and 3 until the response starts to chatter.
5. Set P and D gains to the last stable values.
6. Increase the I gain to achieve the desired steady state error and number of oscillations.

Using this method, it was desired to achieve a critically damped or a stable underdamped pressure response with a minimum overshoot and zero steady state error. A small overshoot ($< 5\%$) and maximum two oscillations were tolerated as a compensation for

Table 4.1: PID gains for the leading and trailing channel.

	Proportional gain K_c	Integral gain $K_c \times T_s/T_i$	Derivative gain $K_c \times T_d/T_s$
Channel 0 (Leading)	1.15	8E-5	1700
Channel 1 (Trailing)	1.2	7E-5	1800

minimising the settling time and zero steady state error. Resulted PID gains for both leading and trailing channels are shown in Table 4.1.

The system response curves to a step command (5, 10, 15, and 20 bar) and a pressure ramp (sequence from a modified SAE J2521) are shown for both channels in Figures 4.24 - 4.25, respectively. The settling time of the pressure response to the step command is within 1.5 - 2 s.

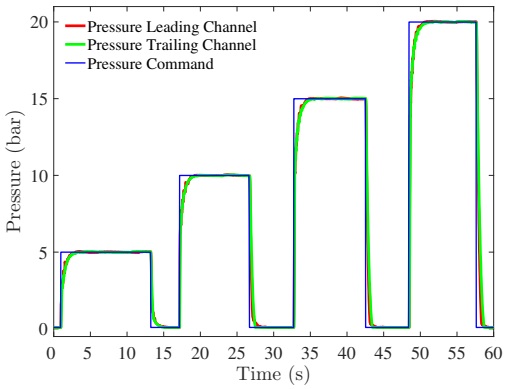

Figure 4.24: Step response.

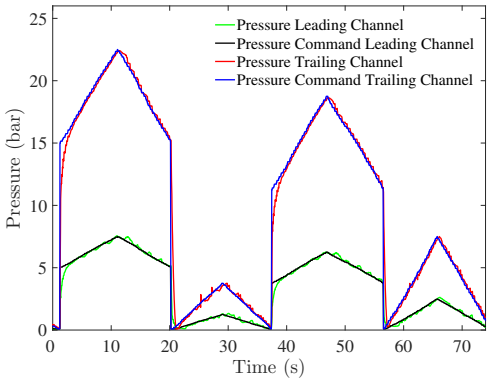

Figure 4.25: Pressure tracking.

4.3.3 Torque Control

In contrast to the pressure control mode, in which a SISO system for each channel is employed, the torque control mode uses a single-input two-outputs (SITO) system, having in its standard mode, an equal control signal for the leading and trailing channel (LTPR=1) as shown in Figure 4.26. Analogously to the pressure mode, the process error is computed as the departure of the torque measured by the transducer from the setpoint value, and is routed to a PID controller that outputs a command value to the air pressure regulator to minimise the error. Again here, the PID controller gains were determined using the empirical method described above. The resulting proportional, integral and derivative gains are 1, 5E-5 and 3000, respectively. The torque step (50, 250, and 400 Nm) and ramp (75, 150, 125, and 100 Nm) response curves are shown in Figures 4.27 - 4.28, respectively. The settling time of the brake torque response to the step command is 2.5 - 3 s. It should be noted that the evident oscillation is presumably due to a large axial runout and/or disc thickness variation of the brake setup (Mastinu, 2013), as the frequency of the peak values correlates with the rotational speed of the disc, and is,

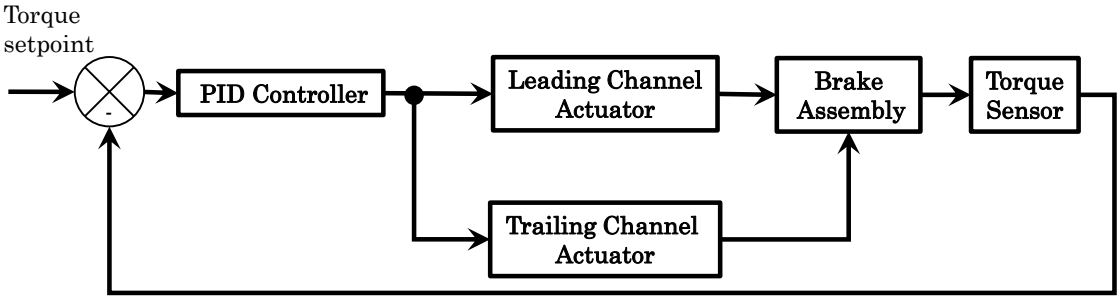

Figure 4.26: Schematic of the control loop to regulate the brake torque in the torque tracking mode.

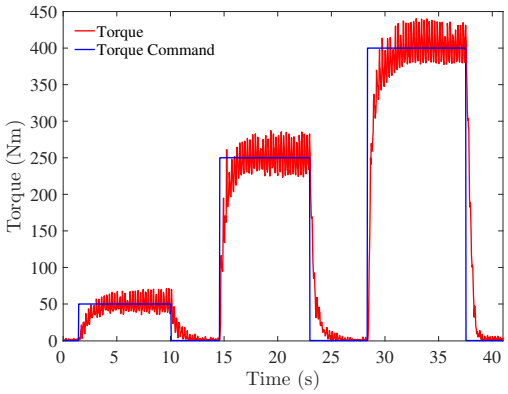

Figure 4.27: Step response.

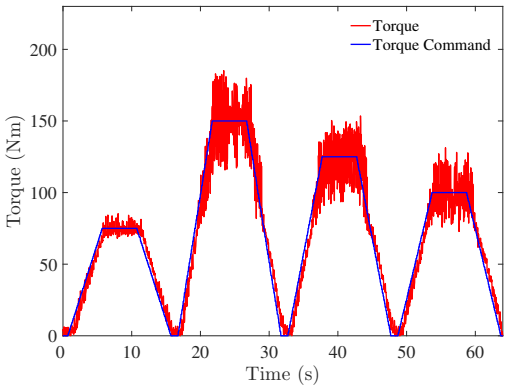

Figure 4.28: Torque tracking.

therefore, not caused by the signal noise.

Besides the ability to track the brake torque, the torque mode allows the user to change LTPR by altering the ratio of the two-outputs in the SITO control scheme as illustrated in Figure 4.29. This way, the LTPR ratio can be controlled by a user and

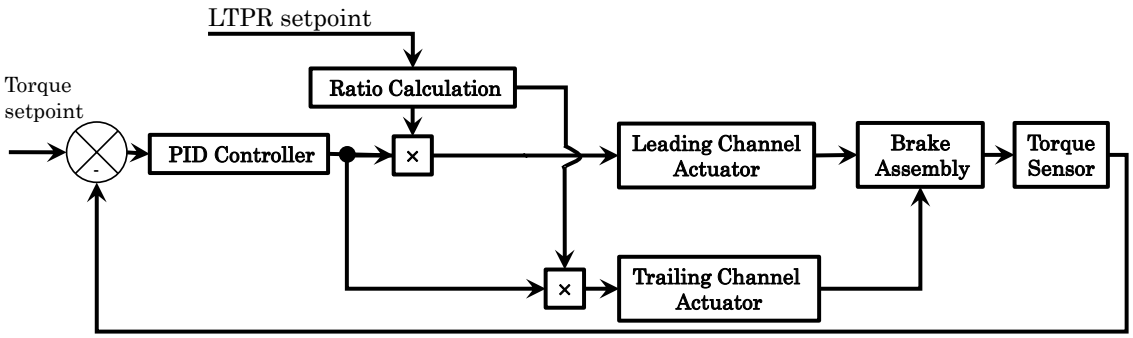

Figure 4.29: Schematic of the control loop to regulate the brake torque and LTPR in the torque tracking mode.

the brake torque can still be maintained. A main disadvantage of the current SITO control scheme is that an exact ratio between the two outputs is not closed-loop controlled and basically relies on the hardware setting. The non-feedback control of the LTPR is

acceptable for this prototype, in particular due to reduction in complexity, but solutions will be sought in future work to further improve this, e.g. by adding another control loop. Furthermore, it was found that a scaling constant is needed for the LTPR command to achieve a desired LTPR calculated from the pressure values given by both leading and trailing pressure transducers for LTPR $\neq 1$. This can be explained by the fact that the signal sent from the PID controller to the air pressure regulator is generally different from the signal monitored by the hydraulic pressure transducer. For instance, getting a real LTPR of 4 requires the user to set the command LTPR = 2.7, whereby the scaling factor can be calculated as $\frac{4}{2.7} = 1.48$. Since the scaling factor can be easily calculated from the real LTPR and any given LTPR command, this drawback can be readily eliminated.

It is obvious that by changing LTPR the torque undergoes a certain fluctuation. To investigate the torque response to the LTPR variation, five different LTPR step input commands from 1 to 2.5 with a step time interval of 0, 1, 2, 3, and 4 s (Test 1 to 5) were designed as shown in Figure 4.30. The results from Test 1 to 5 are shown in Figures

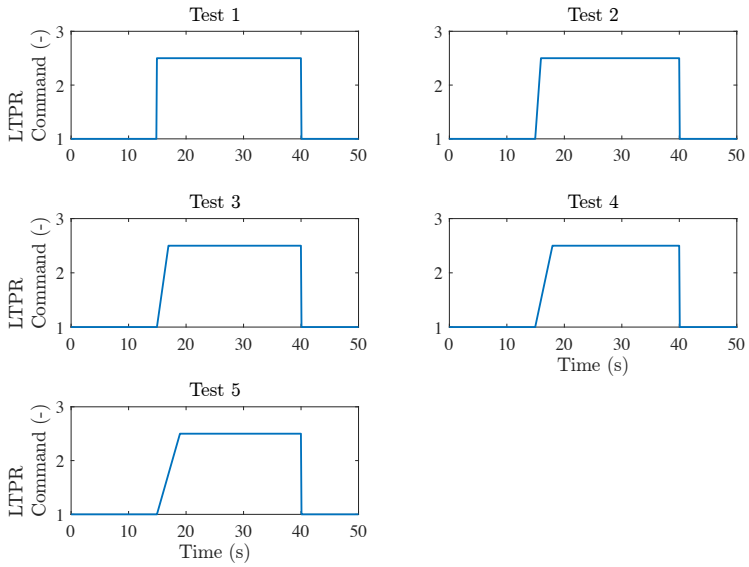

Figure 4.30: Test 1 - 5 representing five different LTPR step commands to examine the torque response to the LTPR variation.

4.31(a) - 4.31(e), respectively. It can be seen that larger gradients of the LTPR command as in Tests 1 to 3 induce a small variation of the mean brake torque (black line), whereas for Test 4 and 5 the torque variation is less obvious. Faster changes of the LTPR cause larger variations of the brake torque due to a controller response time that was tested as explained above.

A block diagram of the FPGA program showing the torque control mode is presented in Figure B-13.

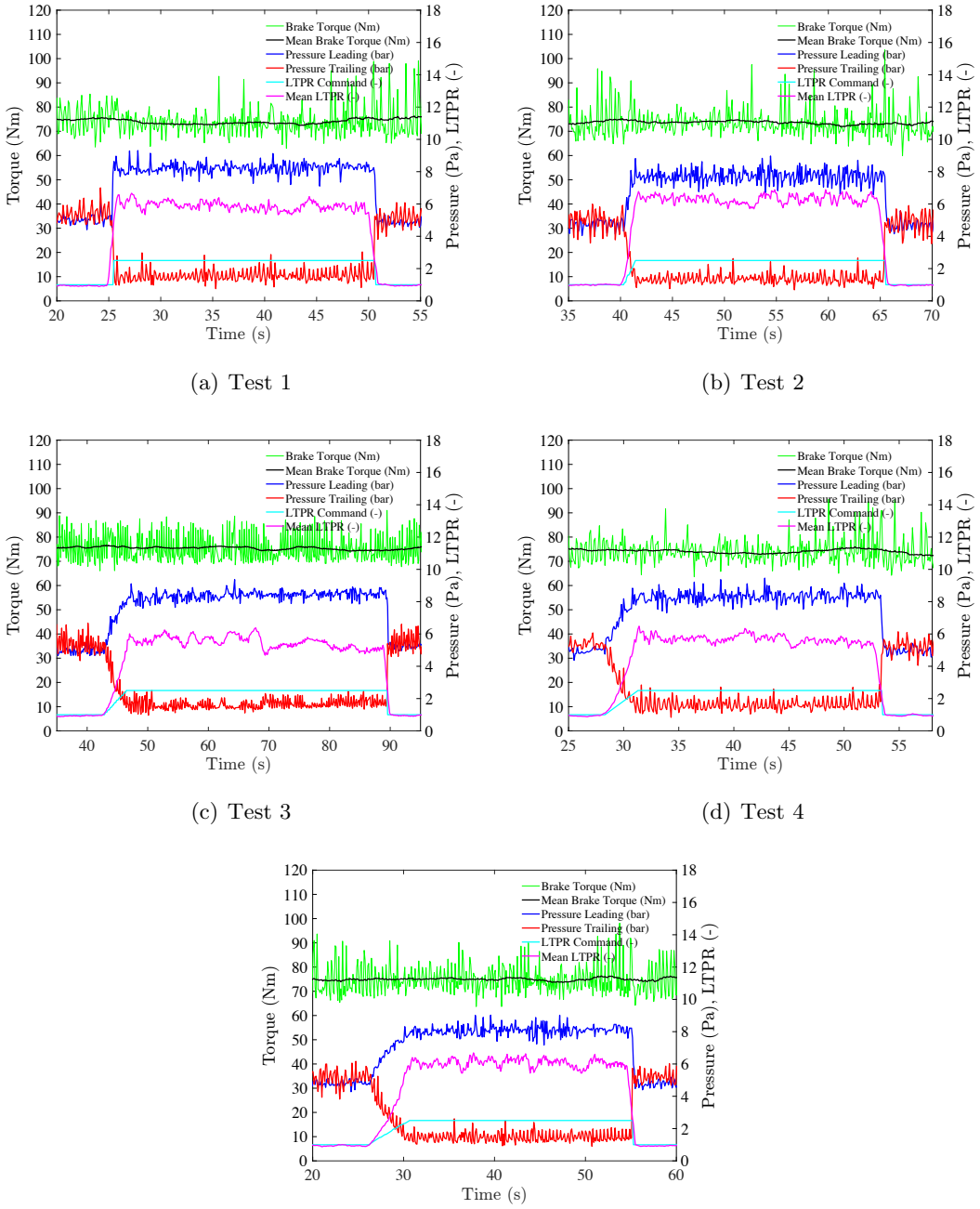

(a) Test 1

(b) Test 2

(c) Test 3

(d) Test 4

(e) Test 5

Figure 4.31: Plots displaying the time variation of brake torque and pressure as a response to five different LTPR step commands (Test 1 - 5). The LTPR step is induced by altering the LTPR command value (cyan). The monitored values include the unfiltered brake torque value (green), mean brake torque (black), leading pressure (blue), trailing pressure (red), and the actual LTPR value (magenta).

4.3.4 Automatic Squeal Reduction System

Modern electronic brake systems mostly use variables other than hydraulic pressure as a process value to control the magnitude of braking. These variables can include

rotational speed, slip, acceleration, brake torque etc. Therefore, the torque control loop presented above serves as a basis for the development of an automatic squeal reduction (ASQR) system to show that an additional parameter can be maintained during squeal control. A basic principle of squeal control can be explained by the flowchart in Figure 4.32. First, sound from a microphone and/or vibrational signal from an accelerometer is processed to create a frequency spectrum of the signal, which allows the system to find squeal within the required frequency interval and of certain sound pressure level. If a squeal occurrence is detected, a control algorithm modifies the CoP position at the pad/disc interface using an electronic actuation system while maintaining the value of the process variable. Optionally, the CoP position can be monitored via an embedded pad sensor. In the following the CoP position will be governed by the LTPR value. By connecting an additional controller and squeal detection algorithm to the torque control loop in Figure 4.29, the schematic of the ASQR control system can be illustrated as in Figure 4.33.

Since only an intermittent squeal could be readily generated with the Rover disc setup, the ASQR control is based on an on/off control using a simple state-machine to change between particular cases. Figure 4.34 shows a flowchart of the simple squeal control algorithm that was developed and later tested as described in Chapter 7. The

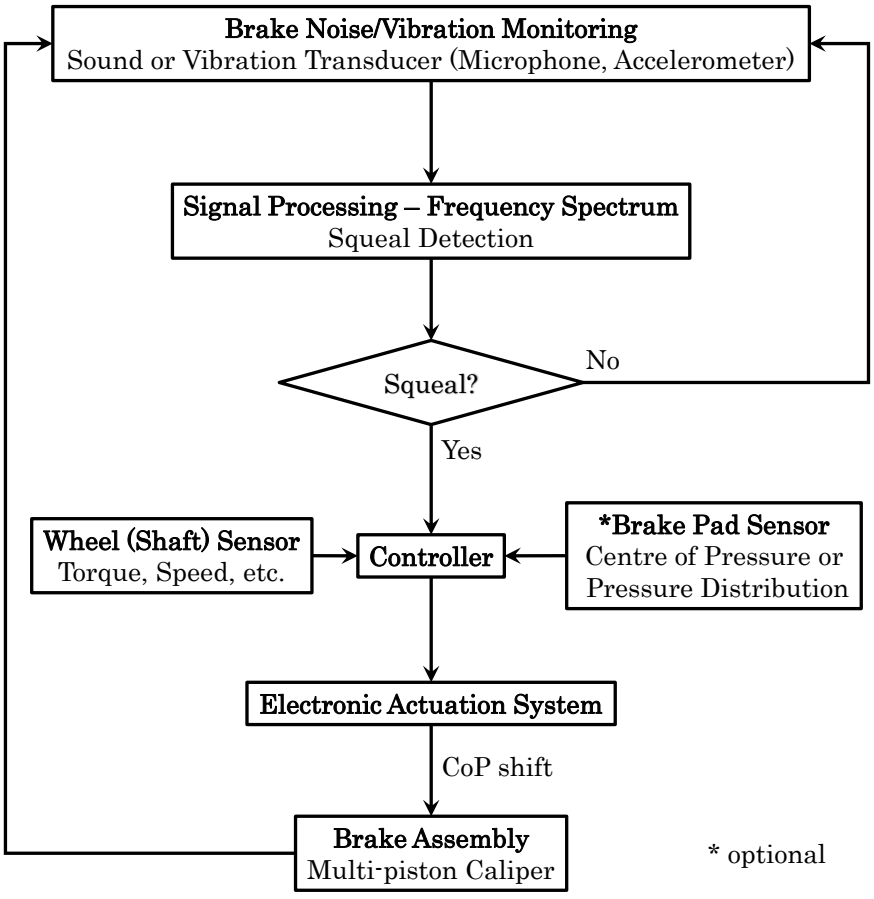

Figure 4.32: Flowchart showing a basic principle of squeal control.

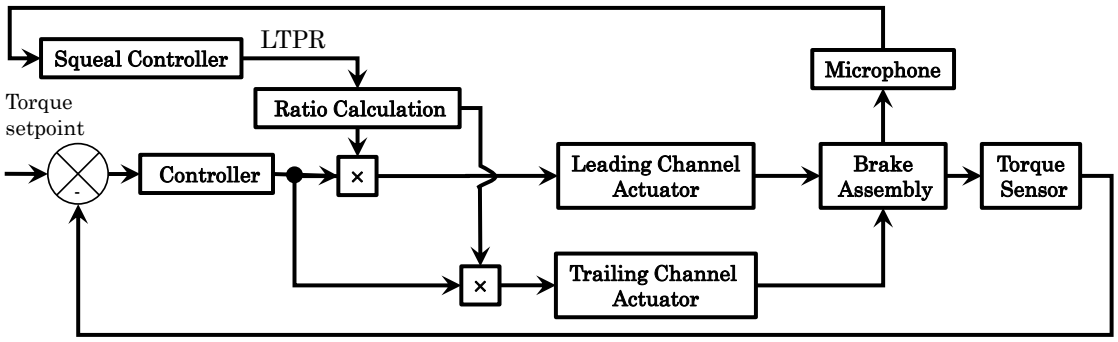

Figure 4.33: Schematic illustrating the main principle of automatic squeal reduction (ASQR) mode.

sequence of the program is as follows: while the brake torque has a non-zero value, the squeal detection algorithm monitors squeal occurrences, or else terminates the brake application and resets LTPR back to 1. If a squeal event is detected, LTPR is changed to a pre-defined value, for instance $LTPR\_1 = 4$, otherwise LTPR remains equal to 1. Providing that the LTPR variation did not suppress the squeal, LTPR is changed to a second pre-defined value, for example $LTPR\_2 = 1/4$. If this eliminates the squeal, the LTPR value is maintained until the end of the brake torque application. Tests showed that usually only two pre-defined values were required to successfully eliminate the squeal providing a proper squeal filter setup was applied. The time interval between detected squeal occurrences can be relatively short. To allow the system to provide the CoP change without interuption, a process delay is included between the CoP change and listening to the next squeal.

A block diagram of the squeal control algorithm exposing the cases for the CoP change towards the leading side is shown in Figure B-14.

4.4 Discussion

Generally, due to a more precise control over the test parameters, a pressure tracking mode is often used in the brake research community to test brakes. The torque control mode described above represents an attempt to approach real automotive applications where the brake torque or slip is regulated to control the complex vehicle dynamics during braking. The ASQR system could be integrated in an automotive brake system as shown in the system layout in Figure 4.35. It is obvious that the brake system would have to allow an independent control of the leading and trailing piston pressure, which would require a dedicated caliper and the number of brake lines as well as channels of the electro-hydraulic actuation unit would have to be multiplied. An electro-hydraulic actuation is usually integrated in today's ABS modules. In addition, the calipers would need to be equipped with accelerometers to monitor the vibrations. Alternatively, a microphone could be installed in the wheel area or inside the cabin to monitor the sound. It is worth mentioning that cabin microphones can be already included in an in-car voice

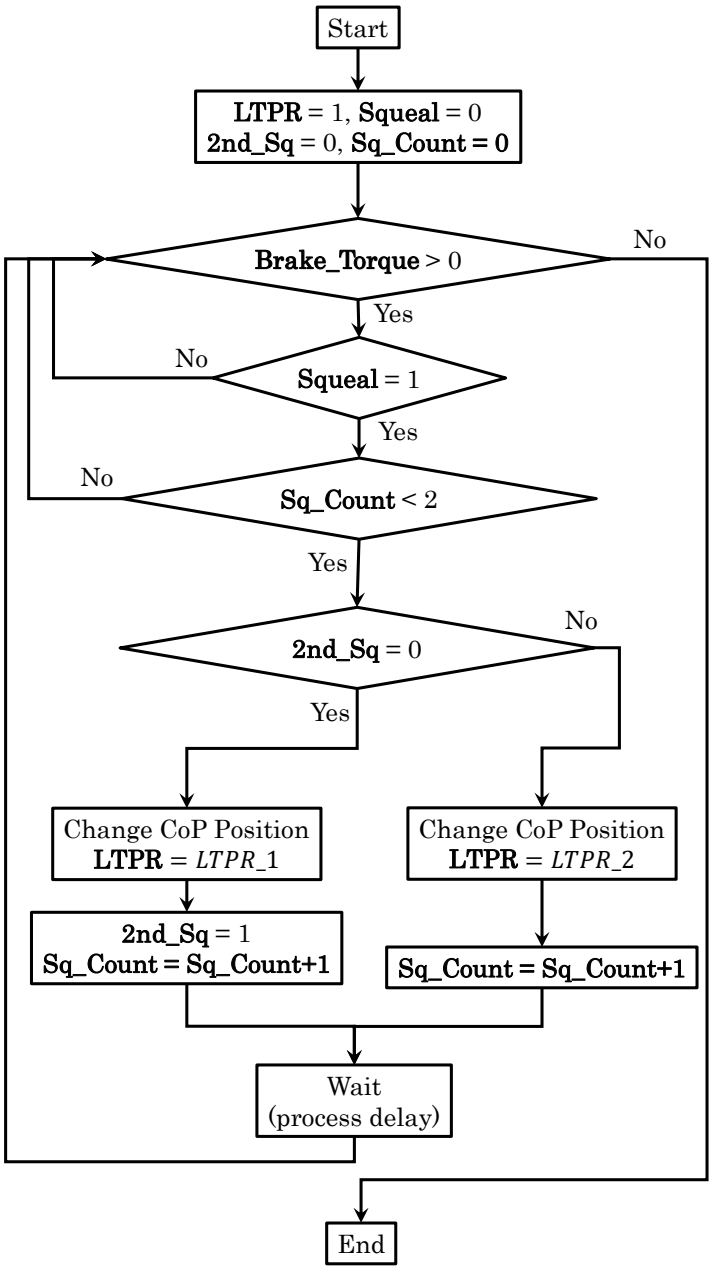

Figure 4.34: Flowchart illustrating the main algorithm of the squeal controller.

control system (Whittington et al., 2010). The proposed ASQR system including the squeal detection algorithm can be programmed for the CPU controlling brake assistance systems such as ABS, ESP or TCS.

It should be discussed whether a continuous or discontinuous control of the squeal should be employed in the ASQR algorithm. Preliminary squeal tests did not show a continuous relation between the LTPR and squeal sound pressure level, and often the squeal within the frequency bandwith of interest rapidly appears and disappears when LTPR is slightly changed. This implies that for a specific frequency bandwith, the boundaries for the CoP positions between the quiet and loud zones over the pad

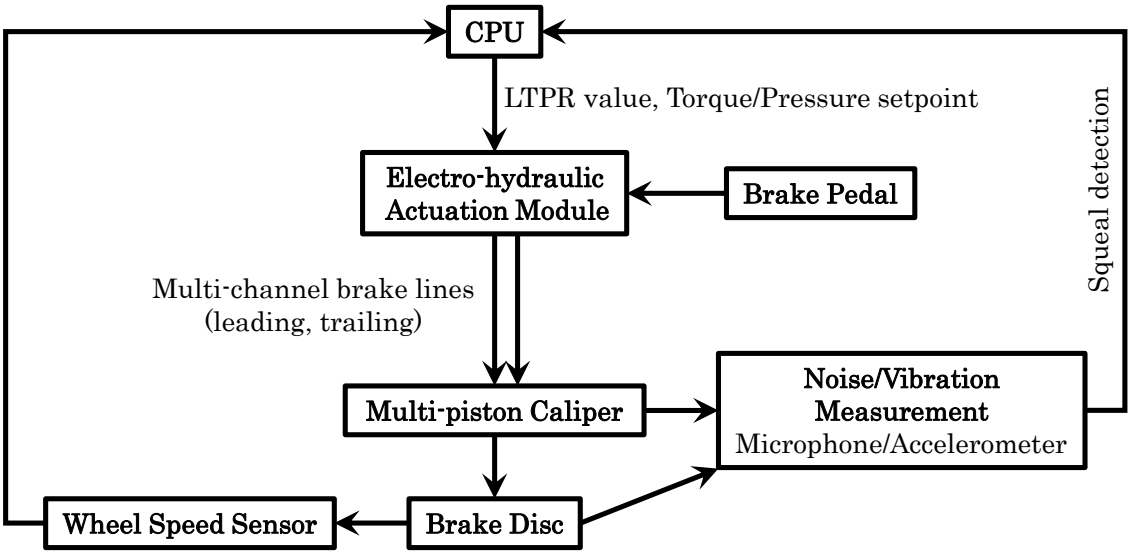

Figure 4.35: Schematic of a potential inclusion of the ASQR system in a vehicle brake system.

area can be confined by sharp boundaries rather than smooth transitions. This could be explained by the squeal generation mechanism of the sprag/slip theory in which the system instability can be triggered when a specific geometric condition of the assembly is formed, and this either exists or it does not. Therefore, the currently used discontinuous control of the squeal seems to be appropriate.

The current test rig setup generates only an intermittent squeal of short durations, which is limiting in developing other control strategies. However, the proposed strategy should also work for continuous squeal as the intermittent squeal can be considered as a worse case scenario due to its short existence and resulting difficult detection. In future, a brake setup that can readily generate continuous squeal events will be sought to examine behaviour of the ASQR system for this scenario.

4.5 Summary

This chapter has outlined the development of the control system for the new brake test rig featuring the Stage II actuation system. The test rig uses a CompactRIO controller to acquire data from all sensors including a sound microphone as well as to provide a stable and highly responsive control of the actuation units. The controller includes an FPGA module, which enables the incorporation of parallel and independently timed DAQ and control loops in the program code. The FPGA code currently includes the pressure and the torque control loop, as well as DAQ loops such as the temperature and microphone sound DAQ loop. However due to limited memory size of the current FPGA, a loop to acquire the accelerometer data along with the microphone sound data could not be used. Also, the sound is processed at the RT level to use the selection of, at this level available, standard sound processing functions.

This chapter has also described two control modes to operate the test rig. The system adopted for the pressure control mode is a SISO control system and uses a simple negative feedback loop of the process variable to calculate the process error. Each channel has its own PID controller whose parameters were determined empirically to achieve a fast and stable feedback system. On the other hand, the torque control loop represents a SITO control system, which allows the setting of a ratio between the two outputs. Also here, the PID controller was tuned empirically to obtain a stable and fast response curve. The main disadvantage of the simple SITO control system is that it does not allow a feedback control of the ratio between the two outputs. Also, due to complexity of the current actuation system, the LTPR set as a command for the brake is different from the real LTPR calculated from the hydraulic pressure values by a certain gain. Despite these drawbacks, it was demonstrated that the SITO control system can be used as a first prototype version for the ASQR system. The performance of both pressure and torque tracking mode was demonstrated using a pre-defined test input signal and is considered as satisfactory for the current research.

Finally, the chapter has presented the working principles of the squeal control algorithm. The proposed ASQR system uses a simple state-machine control that monitors sound from the microphone. When squeal is detected, the program activates change of the LTPR to pre-defined values that were evaluated via squeal experiments as quiet zones as reported in Chapter 7.

5 Analytical and Finite-Element Modelling of Disc Brake

"Essentially, all models are wrong, but some are useful."
George E. P. Box

5.1 Introduction

In this chapter two different modelling approaches to determine the centre of pressure (CoP) position in a multi-piston caliper are presented. The first analytical method uses a rigid body model where the CoP can be calculated by solving algebraic equations. Using this principle both two dimensional (2D) and three-dimensional (3D) models were derived. The second approach is represented by a reduced finite-element (FE) model of a 8-piston brake that is used to compare the CoP predictions from the two approaches. Then, a new approach to the pad/disc friction coefficient calculation using the new analytical 3D model is presented, followed by a study on the influence of the disc top-hat geometry on the CoP position and squeal propensity. Finally, a reduced FE model of the Rover disc brake assembly is developed to predict the CoP positions, as well as to determine unstable modes of vibration using complex eigenvalue analysis (CEA).

In the following analyses two coordinate systems X'Y'Z' and XYZ are used to evaluate CoP positions (Figure 5.1). The X'Y'Z' coordinate system is located on the disc rotational axis, whereas the XYZ lies in the same X'Z' plane and is radially shifted to the centroid of the brake pad. This coordinate system facilitates comparison of the CoP positions for different leading/trailing pressure ratios (LTPR). The radial distance between the XYZ and X'Y'Z' coordinate system r_{pad} depends on the employed brake disc as shown in Table 5.1.

5.2 Calculation of Centre of Pressure Using Analytical Modelling Approaches

A simple rigid body model of a brake pad can be used to investigate the position of CoP without any need for excessive modelling effort. Analytical models mostly neglect elasticity of the brake pad, temperature effects, wear, and replace complicated surface interactions with individual forces acting at a single point. Therefore, the calculation time of such models is relatively short, which gives the possibility to use them in real-time

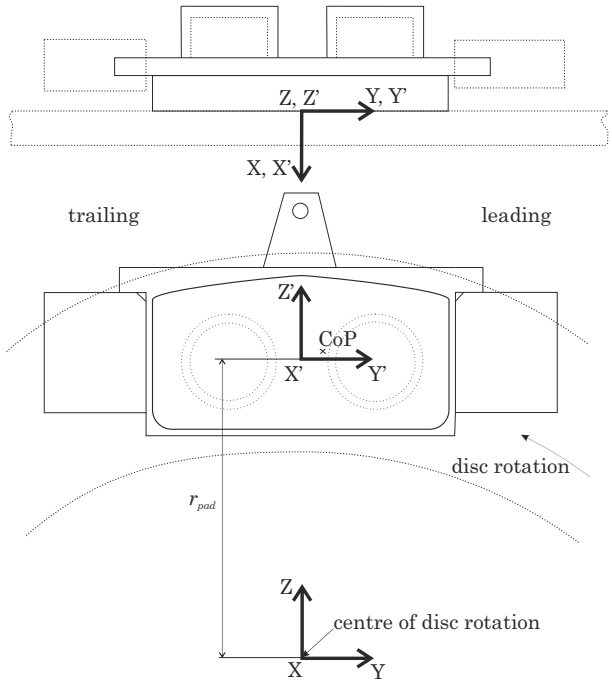

Figure 5.1: Axis systems employed in the analyses.

Table 5.1: Radial distance between the axis system XYZ and X'Y'Z' for different brake assemblies.

Brake assembly	Fiat Punto disc	Rover disc	Aluminium disc
r_{pad} (mm)	98	118	110

applications. On the other hand, FE models can show what additional effects arise at the brake pad/disc interface, providing a potential for further development of analytical models.

The following analytical models include only one brake pad, allowing the engineer to model the inboard and outboard side of a disc brake individually. For the sake of simplicity it is assumed that both sides are identical. All assumptions and justifications for the development of analytical models are summarised in Table 5.2.

5.2.1 2D Rigid Body Model

A two-dimensional (2D) analytical model of the brake pad for calculation of the CoP position has already been developed in the literature (Fieldhouse et al., 2006). A similar model for a four-piston opposed caliper with a trailing abutment is derived below. A 2D analytical modelling approach assumes that all forces are co-planar and the friction forces at the backplate/piston interface are neglected. Figure 5.2 shows the relevant free body diagram of the brake pad with a trailing abutment for a four-piston opposed caliper.

The sum of the forces for static equilibrium can be written as follows:

$$\text{X:} \qquad P_1 + P_2 - F_{tA} - R = 0 \tag{5.1}$$

Table 5.2: Assumptions being made for development of analytical models of the brake pad interface.

Assumption	Justification
The brake pad and surrounding components are modelled as perfectly rigid bodies.	The deformations of the components are small and contribute insignificantly to the change of CoP position when compared to its change due to actuation forces. Therefore, the elastic behaviour of the pad can be neglected, which permits mathematical modelling with simple algebraic equations and contributes to a main simplification of the problem.
The friction at the pad/disc interface is modelled as a point contact (at the CoP), where the friction force is expressed as $F_t = R\mu$.	The surface-to-surface contact at the pad/disc interface can be replaced with a single resultant force R acting at the CoP. This contributes to loss of information about the pressure distribution, but for mere calculation of the CoP position this is acceptable.
The heat effects at the pad/disc interface are neglected.	Neglecting heat effects permits a great simplification of the model.
The wear of the components is neglected.	The wear of the pad can be partly assumed in adjustment of the friction material thickness but can be only applied to the whole friction surface.

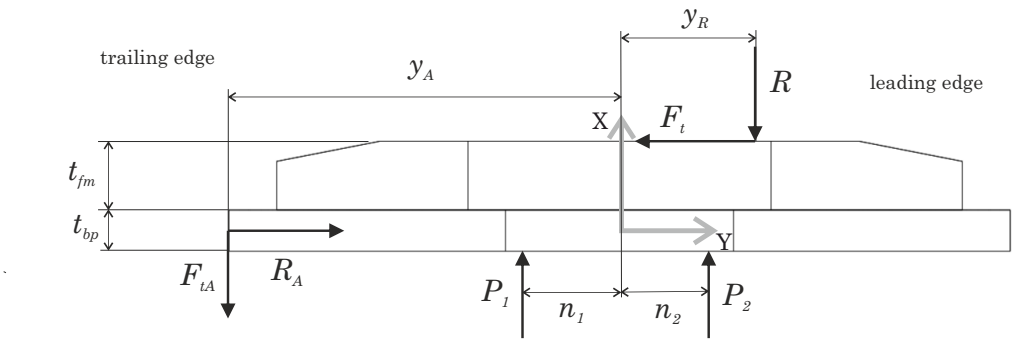

Figure 5.2: Simple 2D model of the brake pad for calculation of the CoP position at the pad/disc interface.

$$\text{Y:} \qquad R_A - F_t = 0 \tag{5.2}$$

and for moment equilibrium with respect to the z axis:

$$Ry_R - F_t\left(t_{fm} + \frac{t_{bp}}{2}\right) + P_1 n_1 - P_2 n_2 - F_{tA} y_A = 0 \tag{5.3}$$

Substituting Eq. 5.1 into Eq. 5.3 and since

$$F_t = R\mu \quad F_{tA} = R_A\mu_A \quad F_t = R_A \tag{5.4}$$

the position of CoP can be derived as:

$$y_R = \mu\mu_A y_A + \mu\left(t_{fm} + \frac{t_{bp}}{2}\right) + \frac{(-P_1 n_1 + P_2 n_2)(1 + \mu\mu_A)}{P_1 + P_2} \tag{5.5}$$

where μ is the friction coefficient at the pad/disc interface, μ_A denotes friction coefficient at the backplate/abutment surface, y_A represents distance of the pad center to the abutment surface, P_1 and P_2 are piston forces, F_t and R are friction force and reaction force (clamp force) at the rubbing surface respectively, F_{tA} and R_A are friction force and reaction force at the abutment surface respectively, n_1 and n_2 represent distances of the pistons from the center of the pad, and t_{fm} and t_{bp} are thicknesses of the friction material and the backplate respectively.

5.2.2 3D Rigid Body Model of 4-Piston Opposed Caliper

A new three-dimensional (3D) analytical model of the brake pad for the calculation of the CoP position was derived, which allows determination of the CoP position in the circumferential as well as in the radial direction. Figure 5.3 shows the relevant 3D free body diagram of the brake pad model, assuming an XYZ coordinate system placed at a distance r_{pad} from the disc axis and located in the middle of the backplate. In the Y-Z plane, the pad was modelled as a binary member, i.e. the trailing abutment reaction is represented by a single force acting at the trailing edge interface which is always collinear with the friction force acting at the CoP. The contact between the backplate and the trailing abutment was assumed to be in compression and was modelled as a sliding friction contact, whereas the potential contact forces at the leading abutment as well as the friction forces at the piston/backplate interface were neglected. These assumptions facilitated mathematical representation of the model and allowed the problem to be solved.

Again, μ and μ_A represent friction coefficients at the pad/disc and pad/abutment interface respectively, y_A is the horizontal distance from the pad center to the abutment point, z_A is the vertical distance from the pad center to the abutment point, P_1 and P_2 are piston forces, F_{tY}, F_{tZ} and R are friction forces and reaction force (clamp force) at the rubbing surface respectively, F_{tA}, R_{AY} and R_{AZ} are friction force and reaction forces at the abutment surface respectively, n_1 and n_2 are distances of the pistons from the center of the pad, t_{fm} and t_{bp} are thicknesses of the friction material and the backplate, respectively. Furthermore, r_{pad} is the vertical distance of the pad coordinate system to the rotor axis, r is the instantaneous distance of the CoP to the rotor center (effective radius), and α is the angle between the line intersecting the CoP with the rotor axis and the Z-axis of the coordinate system.

The sum of the forces for static equilibrium can be written as follows:

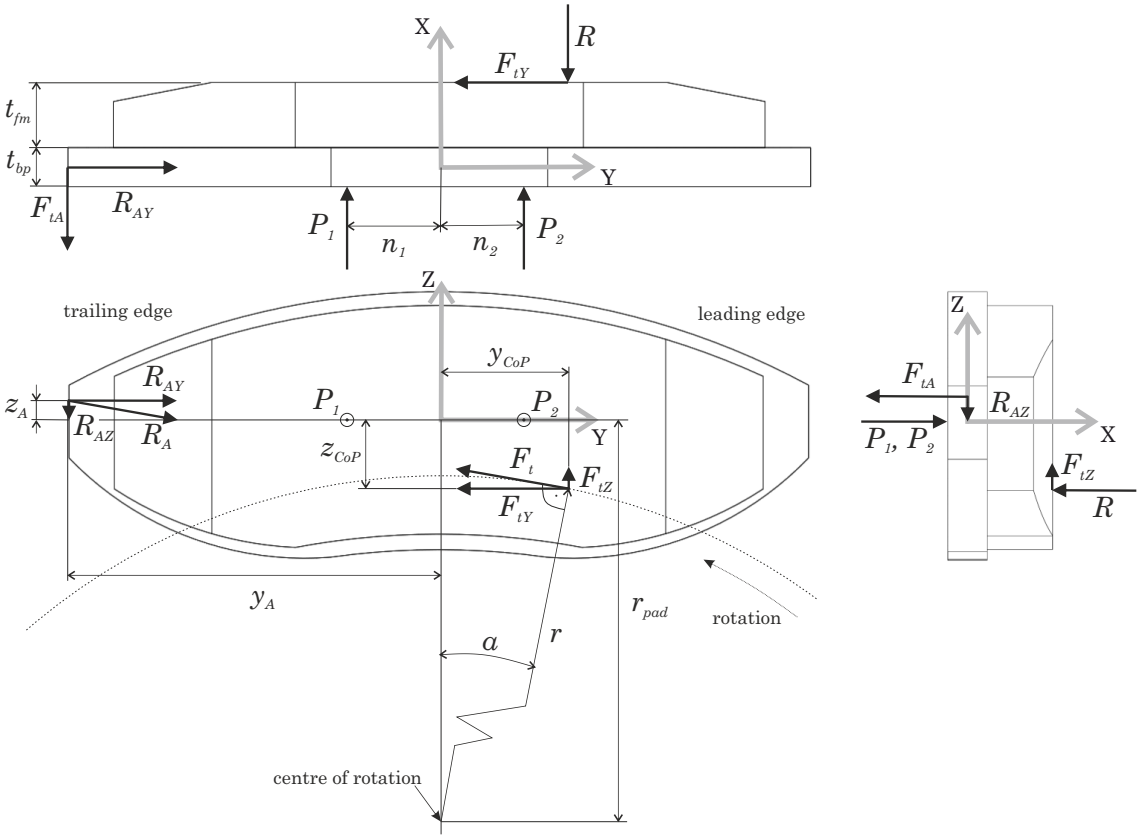

Figure 5.3: Free body diagram of the new 3D brake pad analytical model for calculation of the CoP position at the pad/disc interface. In this model, two pistons represented by P_1 and P_2 are acting on the backplate of the brake pad.

$$\text{X:} \qquad P_1 + P_2 - F_{tA} - R = 0 \tag{5.6}$$

$$\text{Y:} \qquad R_{AY} - F_{tY} = 0 \tag{5.7}$$

$$\text{Z:} \qquad F_{tZ} - R_{AZ} = 0 \tag{5.8}$$

The equations of moment equilibrium with respect to the axis system XYZ are:

$$\text{M}_x\text{:} \qquad -R_{AZ}y_A + R_{AY}z_A + F_{tY}(r_{pad} - r\cos\alpha) - F_{tZ}r\sin\alpha = 0 \tag{5.9}$$

$$\text{M}_y\text{:} \qquad F_{tA}z_A - R(r_{pad} - r\cos\alpha) + F_{tZ}\left(t_{fm} + \frac{t_{bp}}{2}\right) = 0 \tag{5.10}$$

$$\text{M}_z\text{:} \qquad Rr\sin\alpha - F_{tY}\left(t_{fm} + \frac{t_{bp}}{2}\right) + P_1n_1 - P_2n_2 - F_{tA}y_A = 0 \tag{5.11}$$

Substituting the following expressions into Eq. 5.6 - Eq. 5.11

$$F_t = R\mu \tag{5.12}$$

$$F_{tA} = R_{AY}\mu_A \quad F_{tY} = F_t\cos\alpha \quad F_{tZ} = F_t\sin\alpha \tag{5.13}$$

and since

$$z_A = (y_A + r\sin\alpha)\tan\alpha + r\cos\alpha - r_{pad} \tag{5.14}$$

$$R_{AY} = F_{tY} \quad F_{tZ} = R_{AZ} \tag{5.15}$$

the system of equations can be written as follows:

$$R = \frac{P_1 + P_2}{1 + \mu\mu_A\cos\alpha} \tag{5.16}$$

$$r = \frac{-\mu\mu_A\cos\alpha(-r_{pad} + y_A\tan\alpha) + r_{pad} - \mu\sin\alpha\left(t_{fm} + \frac{t_{bp}}{2}\right)}{\mu\mu_A + \cos\alpha} \tag{5.17}$$

Substituting Eq. 5.12 and Eq. 5.15 into Eq. 5.11 yields:

$$R\left(r\sin\alpha - \mu\cos\alpha\left(t_{fm} + \frac{t_{bp}}{2}\right) - y_A\mu\mu_A\cos\alpha\right) + P_1n_1 - P_2n_2 = 0 \tag{5.18}$$

Finally, substituting Eq. 5.16 and Eq. 5.17 into Eq. 5.18, and rearranging gives:

$$\frac{P_1 + P_2}{1 + \mu\mu_A\cos\alpha}\left(\frac{-\mu\mu_A\cos\alpha(-r_{pad} + y_A\tan\alpha) + r_{pad} - \mu\sin\alpha\left(t_{fm} + \frac{t_{bp}}{2}\right)}{\mu\mu_A + \cos\alpha}\sin\alpha + \ldots\right.$$
$$\left. - \mu\cos\alpha\left(t_{fm} + \frac{t_{bp}}{2}\right) - y_A\mu\mu_A\cos\alpha\right) + P_1n_1 - P_2n_2 = 0 \tag{5.19}$$

Eq. 5.19 is a non-linear trigonometric equation that includes the unknown angle α. This can be solved numerically in MATLAB® using some of the built-in mathematical functions based on a combination of bisection, secant, and inverse quadratic interpolation methods. Due to the nature of trigonometric equations having a repeated periodical solutions, a possible solution of Eq. 5.19 needs to be limited to a small interval to obtain a meaningful solution for α. To determine the CoP position over the pad area as illustrated in Figure 5.3, α can be only an acute angle with small values, typically defined over the interval -25° $< \alpha <$ 25° (or -0.4 rad $< \alpha <$ 0.4 rad). There is only one solution for α in this interval as shown in the plot of Eq. 5.19 in Figure 5.4. After α is determined, the radius r on which the resultant friction force is acting can be calculated by substituting α into Eq. 5.19. Finally, the CoP position can be obtained from:

$$z_{CoP} = -(r_{pad} - r\cos\alpha) \tag{5.20}$$

Table 5.3: Example data for calculation of the CoP position. The piston forces P_1 and P_2 are calculated for pressure 30 bar.

P_1 (N)	P_2 (N)	d_{piston} (mm)	n_1 (mm)	n_2 (mm)	r_{pad} (mm)	μ (1)	μ_A (1)	t_{fm} (mm)	t_{bp} (mm)	y_A (mm)
1900.4	1900.4	28.4	20	20	98	0.4	0.15	11.3	4.7	45

$$y_{CoP} = r \sin \alpha \tag{5.21}$$

By substituting α into Eq. 5.16, then resolving Eq. 5.12 and assuming two rubbing surfaces, the overall brake torque is

$$T_{Brake} = 2F_t r \tag{5.22}$$

For a disc brake with the data given in Table 5.3, α can be calculated as follows:

$$\begin{aligned}
&\frac{1900.4 + 1900.4}{1 + 0.4 \times 0.15 \cos \alpha} \left(\frac{-0.4 \times 0.15 \cos \alpha (-0.098 + 0.045 \tan \alpha)}{0.4 \times 0.15 + \cos \alpha} \sin \alpha + \dots \right. \\
&\qquad + \frac{0.098 - 0.4 \sin \alpha \left(0.0113 + \frac{0.0047}{2}\right)}{0.4 \times 0.15 + \cos \alpha} \sin \alpha + \dots \\
&\qquad \left. - 0.4 \cos \alpha \left(0.0113 + \frac{0.0047}{2} \right) - 0.045 \times 0.4 \times 0.15 \cos \alpha \right) + \dots \\
&\qquad + 1900.4 \times 0.020 - 1900.4 \times 0.020 = 0
\end{aligned} \tag{5.23}$$

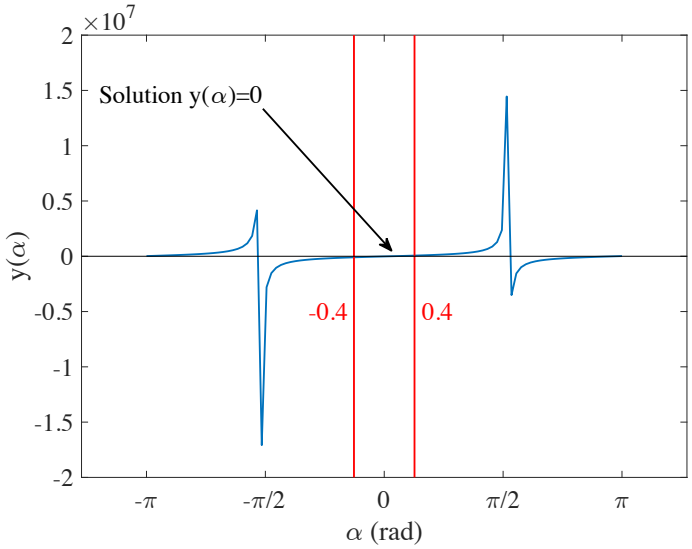

Figure 5.4: A plot of the trigonometric equation Eq. 5.19 over the interval (-π,π) rad. The angle α is assumed to be acute, hence the possible solution is limited to a small interval -0.4 < α < 0.4.

The numerical solution of Eq. 5.23 gives:

$$\alpha = 0.0834\,\text{rad} = 4.77^{\circ} \tag{5.24}$$

Substituting into Eq. 5.17 yields the radial distance of CoP:

$$r = 97.66\,\text{mm} \tag{5.25}$$

and the brake torque assuming two rubbing areas is:

$$T_{Brake} = 2 \times 1434.6 \times 0.09766 = 280.2\,\text{Nm} \tag{5.26}$$

5.2.3 Three-Dimensional Rigid Body Model of 8-Piston Opposed Caliper

Analogously to the four-piston opposed caliper, the equations can be also derived for a caliper containing a different number of pistons. Figure 5.5 illustrates a free body diagram of the brake pad featuring eight opposed pistons (four at each side). Without derivation, the resultant equations corresponding to Eqs. 5.16 - 5.17 for an eight-piston opposed caliper are:

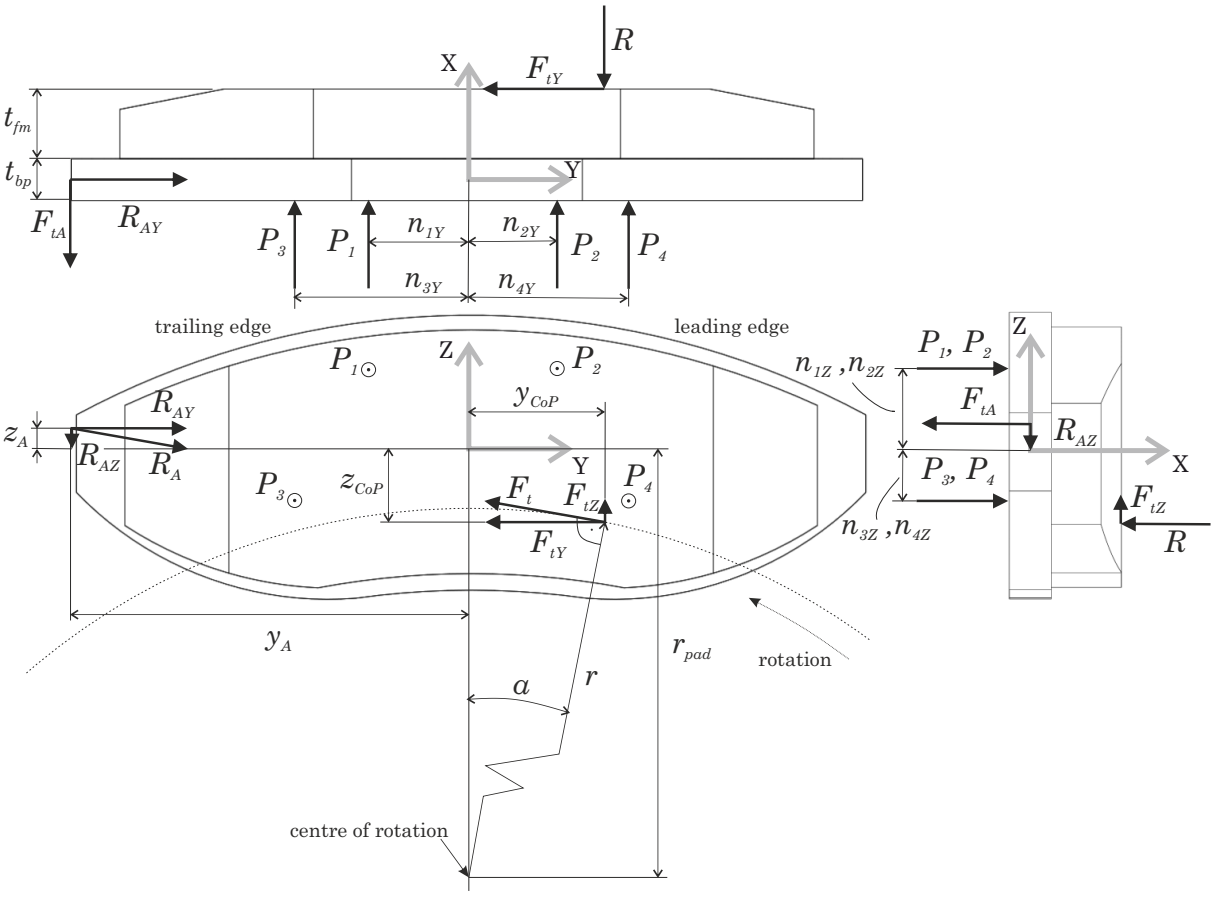

Figure 5.5: A free body diagram of the 3D brake pad model with four pistons acting on the backplate.

$$R = \frac{P_1 + P_2 + P_3 + P_4}{1 + \mu\mu_A \cos\alpha} \tag{5.27}$$

$$r = \frac{-\mu\mu_A \cos\alpha(-r_{pad} + y_A \tan\alpha) + r_{pad} - \mu \sin\alpha\left(t_{fm} + \frac{t_{bp}}{2}\right)}{\mu\mu_A + \cos\alpha} + \ldots$$
$$+ \frac{P_1 n_{1Z} + P_2 n_{2Z} + P_3 n_{3Z} + P_4 n_{4Z}}{R(\mu\mu_A + \cos\alpha)} \tag{5.28}$$

Finally, analogously to Eq. 5.19, the resultant equation is:

$$\frac{P_1 + P_2 + P_3 + P_4}{1 + \mu\mu_A \cos\alpha}\left(\frac{-\mu\mu_A \cos\alpha(-r_{pad} + y_A \tan\alpha) + r_{pad} - \mu \sin\alpha\left(t_{fm} + \frac{t_{bp}}{2}\right)}{\mu\mu_A + \cos\alpha}\sin\alpha + \ldots\right.$$
$$\left. + \frac{P_1 n_{1Z} + P_2 n_{2Z} + P_3 n_{3Z} + P_4 n_{4Z}}{R(\mu\mu_A + \cos\alpha)}\sin\alpha - \mu\cos\alpha\left(t_{fm} + \frac{t_{bp}}{2}\right) - y_A\mu\mu_A\cos\alpha\right) + \ldots$$
$$- P_1 n_{1Y} - P_2 n_{2Y} - P_3 n_{3Y} - P_4 n_{4Y} = 0 \tag{5.29}$$

Here, the positions of the piston forces n_{1Y}, n_{1Z}, n_{2Y}, n_{2Z}, n_{3Y}, n_{3Z} and n_{4Y}, n_{4Z} are expressed as Y, Z coordinates, for example n_{1Y} = -30 mm and n_{1Z} = 7.5 mm.

5.2.4 Computer Application of Analytical and Numerical Models

The 2D and 3D analytical models of the brake pad were implemented in a new MATLAB® program *CalBrakes* shown in Figure 5.6. Its front panel consists of five main panels, allowing the user to set the type of intended calculation and a variety of input data, as well as providing a visualisation of the results from the analytical and FE calculations.

CalBrakes also enables the user to set up a numerical calculation of the FE models developed in ABAQUS® by accessing their input and output files. A basic schematic of the programmatic connection between *CalBrakes* and ABAQUS® is displayed in Figure 5.7. In the first step, a model of a brake assembly is developed in the usual fashion in the ABAQUS® graphical environment (.cae), followed by writing the input files (.inp) describing the geometry and simulation parameters. To facilitate modification of the brake geometry, the original input file can be divided into a main input file that contains the material data, interactions, simulation steps and parameters, and a second input file containing the nodal description of the brake geometry. This is advantageous for minor geometrical changes of the brake assembly, for example, mesh density or dimension values, when only the nodal input file has to be replaced. The nodal input file can be called by adding the following code in the heading of the main input file (Abaqus, 2012):

```
*INCLUDE, INPUT=FileName_e.inp
```

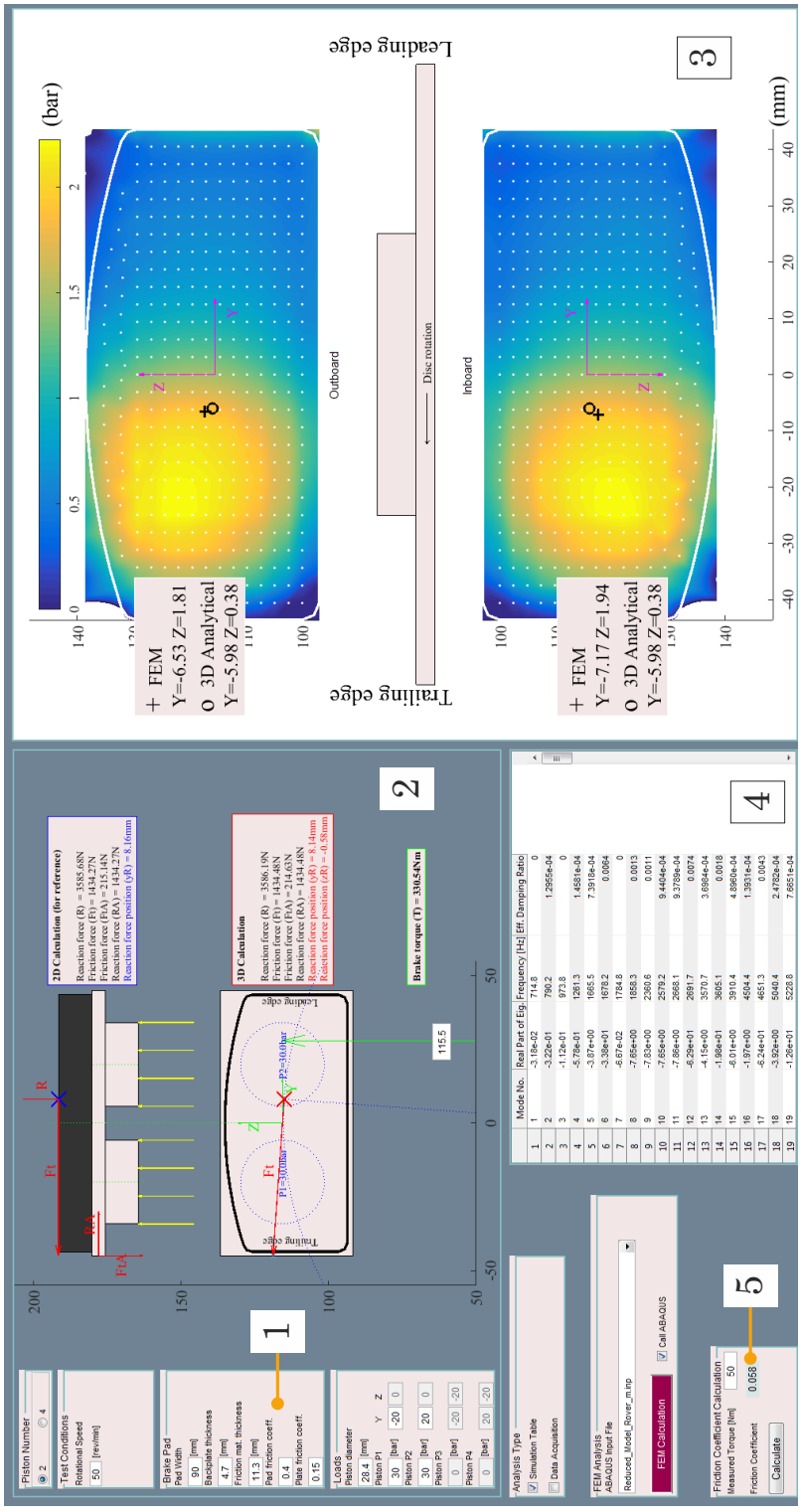

Figure 5.6: Graphical user interface of the MATLAB® program *CalBrakes*: 1) input parameters, 2) analytical CoP calculation, 3) numerical CoP calculation, 4) complex eigenvalue analysis (CEA), 5) friction coefficient calculation.

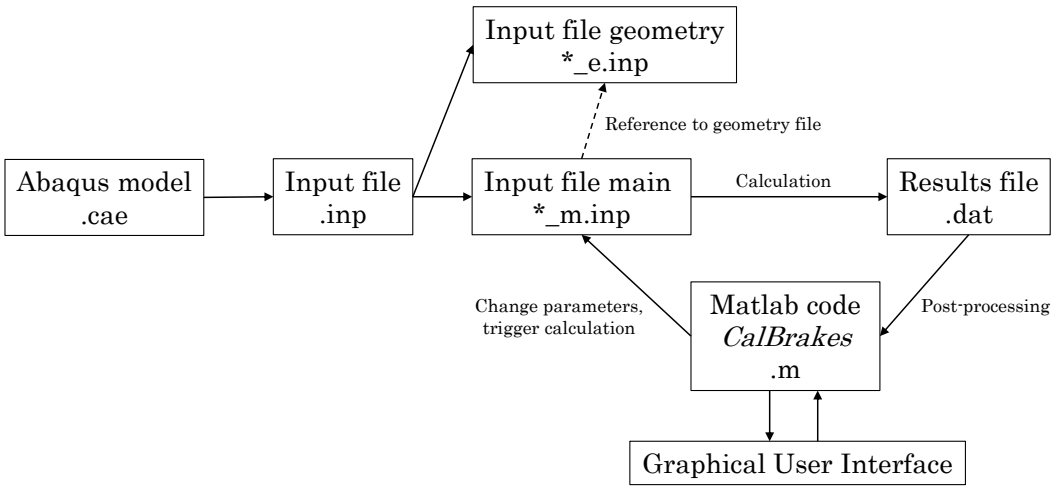

Figure 5.7: Schematic of the programmatic connection between *CalBrakes* and ABAQUS environment.

This approach also enables *CalBrakes* to access and make modifications in a relatively small main input file that is independent of the model geometry. To change piston loads, friction coefficients or disc rotational speed, *CalBrakes* searches for the particular part of the code in the main input file and modifies the values. *CalBrakes* then calls the ABAQUS® solver to start simulation. After completing the simulation, relevant data from the results file (.dat) are extracted and displayed in the *CalBrakes* front panel.

For parameter studies, the sequence change parameters→ calculation→ post-processing from Figure 5.7 can be automatically repeated in the batch mode for a variety of models and test parameters. Figure 5.8 shows the front panel of the batch mode which allows the user to select the input files and define the varying test parameters.

	Abaqus Input File Name	Piston 1 [bar]	Piston 2 [bar]	Piston 3 [bar]	Piston 4 [bar]	Piston 5 [bar]	Piston 6 [bar]	Piston 7 [bar]	Piston 8 [bar]	Rotati...	Pad/Di...	Pad/A...
1	CEA_parametric_0_sym_pistons_m.inp	10	10	0	0	10	10	0	0	30	0.5000	0.2000
2	CEA_parametric_0_offset_pistons_m.inp	10	10	0	0	10	10	0	0	30	0.5000	0.2000
3	CEA_parametric_1_pistons_m.inp	10	10	0	0	10	10	0	0	30	0.5000	0.2000
4	CEA_parametric_2_pistons_m.inp	10	10	0	0	10	10	0	0	30	0.5000	0.2000
5	CEA_parametric_3_pistons_m.inp	10	10	0	0	10	10	0	0	30	0.5000	0.2000
6	CEA_parametric_0_sym_pistons_m.inp	5	5	0	0	5	5	0	0	30	0.5000	0.2000
7	CEA_parametric_0_offset_pistons_m.inp	5	5	0	0	5	5	0	0	30	0.5000	0.2000
8	CEA_parametric_1_pistons_m.inp	5	5	0	0	5	5	0	0	30	0.5000	0.2000
9	CEA_parametric_2_pistons_m.inp	5	5	0	0	5	5	0	0	30	0.5000	0.2000
10	CEA_parametric_3_pistons_m.inp	5	5	0	0	5	5	0	0	30	0.5000	0.2000
11	CEA_parametric_0_sym_pistons_m.inp	5	5	0	0	5	5	0	0	50	0.5000	0.2000
12	CEA_parametric_0_offset_pistons_m.inp	5	5	0	0	5	5	0	0	50	0.5000	0.2000
13	CEA_parametric_1_pistons_m.inp	5	5	0	0	5	5	0	0	50	0.5000	0.2000
14	CEA_parametric_2_pistons_m.inp	5	5	0	0	5	5	0	0	50	0.5000	0.2000
15	CEA_parametric_3_pistons_m.inp	5	5	0	0	5	5	0	0	50	0.5000	0.2000
16	Select Abaqus Input File	0	0	0	0	0	0	0	0	30	0.5000	0.2000
17	Select Abaqus Input File	0	0	0	0	0	0	0	0	30	0.5000	0.2000
18	Select Abaqus Input File	0	0	0	0	0	0	0	0	30	0.5000	0.2000
19	Select Abaqus Input File	0	0	0	0	0	0	0	0	30	0.5000	0.2000
20	Select Abaqus Input File	0	0	0	0	0	0	0	0	30	0.5000	0.2000
21	Select Abaqus Input File	0	0	0	0	0	0	0	0	30	0.5000	0.2000
22	Select Abaqus Input File	0	0	0	0	0	0	0	0	30	0.5000	0.2000
23	Select Abaqus Input File	0	0	0	0	0	0	0	0	30	0.5000	0.2000
24	Select Abaqus Input File	0	0	0	0	0	0	0	0	30	0.5000	0.2000
25	Select Abaqus Input File	0	0	0	0	0	0	0	0	30	0.5000	0.2000

Figure 5.8: *CalBrakes* front panel of the batch mode: 1) input files, 2) varying test parameters.

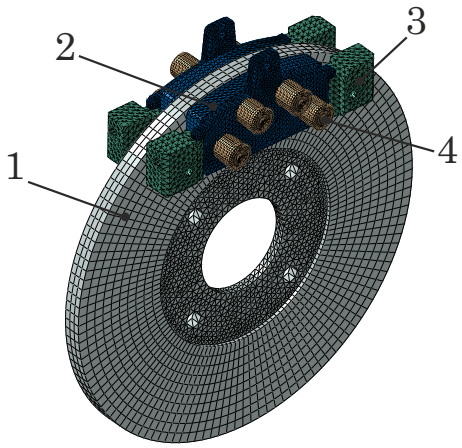

Figure 5.9: FE model of an 8-piston brake assembly: 1) brake disc, 2) brake pad, 3) abutment, 4) piston.

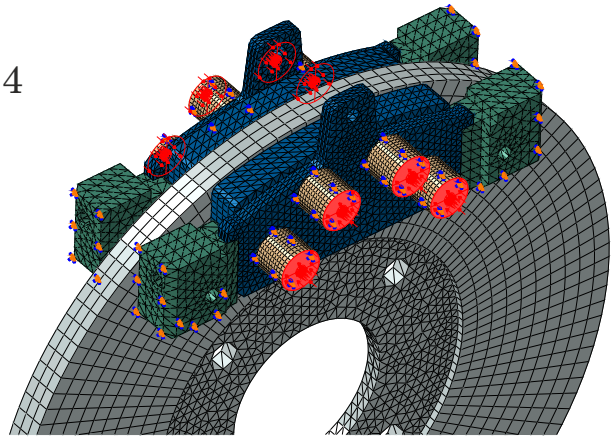

Figure 5.10: A view of the boundary conditions and the loads acting on the pistons.

5.2.5 Comparison of New 3D Analytical Model with Equivalent Finite-Element Model

The CoP position calculated using the new 3D analytical model was compared with a CoP value resulting from a FE analysis. A simple FE model of a disc brake with eight opposed pistons was therefore developed in ABAQUS® as shown in Figure 5.9. This model consists of a disc, brake pads, abutments and eight opposed pistons, allowing the user to generate a variety of different CoP positions over the major part of the pad surface. The caliper was not included in the model because influence of its geometry was not important for this study. The brake disc does not include the top-hat geometry and the flange is mounted symmetrically in the disc section to avoid small differences in CoP positions between the inboard and outboard side of the brake as shown later in this chapter. The disc was given a rotational speed of 50 rev/min for a duration of 1 s. For the sake of simplicity, isothermal conditions were assumed. Table 5.4 summarises the material properties used in the simulation.

The brake pad consists of two components, friction material and backplate, both being

Table 5.4: Material data used in the simulation model.

Part	Material	Density ($kg.m^{-3}$)	Young's Modulus (GPa)	Poisson's ratio (-)
Brake disc	Cast iron	7200	125	0.24
Pad friction material	Friction material	2700	3	0.25
Backplate	Steel	7850	210	0.3
Abutments	Steel	7850	210	0.3
Pistons	Steel	7850	210	0.3

connected together with a tie constraint. The abutments are modelled as deformable bodies and constrain the pad movement with a surface-to-surface contact and small sliding formulation at the backplate/abutment interface (Figure 5.11).

The interaction between the friction material and the brake disc was modelled with the surface-to-surface algorithm and a small sliding formulation was set to reduce the calculation time. Also, the piston/backplate interface was defined by a surface-to-surface contact, but here a finite sliding formulation was used to avoid convergence problems during the simulation. The friction coefficients at the brake pad/disc, backplate/pistons and the backplate/abutment interface were set to typical values of 0.4, 0.2 and 0.15, respectively. The friction coefficient at the pad/disc interface was ramped from zero to the steady state value at the beginning of the rotation to avoid any discontinuities and convergence problems (Abaqus, 2012), whereas the friction coefficient at all other surfaces remains constant during the whole simulation. The CoP position can be calculated from the pressure values at each node using the following formulas:

$$y_{CoP} = \frac{\sum_{i=1}^{n} p_i(y_i) \times y_i}{\sum_{i=1}^{n} p_i(y_i)} \tag{5.30}$$

$$z_{CoP} = \frac{\sum_{i=1}^{n} p_i(z_i) \times z_i}{\sum_{i=1}^{n} p_i(z_i)} \tag{5.31}$$

The quality of the mesh was verified using a mesh sensitivity analysis as shown in Table 5.5. The disc was meshed again with a coarse and a finer mesh. The calculated

Table 5.5: Mesh sensitivity analysis of the 8-piston brake model provided for a coarse, medium and fine mesh of the disc. The highlighted mesh was chosen for further analysis. Rel.Diff. = Relative difference, Long. = Longitudinal, Rad. = Radial.

Mesh (Number of Disc Elements)	Coarse (5843)	Medium (14362)	Rel. Diff.	Fine (64714)	Rel. Diff.
CoP Inboard Long. (mm)	-7.724	-7.726	-0.03%	-7.725	+0.01%
CoP Inboard Rad. (mm)	98.06	98.05	+0.01%	98.05	0.0%
CoP Outboard Long. (mm)	-7.713	-7.712	+0.01%	-7.712	0.0%
CoP Outboard Rad. (mm)	98.04	98.03	+0.01%	98.03	0.0%
Calculation time (mm:ss)	04:17	06:20	+47.9%	13:49	+118.2%

CoP values were compared resulting in differences of the positions $< 0.05\%$, which is well within acceptable limits. The refinement of the current mesh resulted in almost identical values of the CoP but doubled the calculation time.

Table 5.6 defines piston loads to simulate six different CoP positions across the pad/disc interface. These positions can be visualised using *CalBrakes* as shown in Figure 5.12. A comparison of CoP positions calculated using the 2D, 3D and FE model is shown in Figure 5.13. It can be seen that the differences in the CoP positions between all approaches are small but vary with the load settings. *CalBrakes* allows the user to plot a comparison of the CoP positions determined by the 3D analytical and numerical models as can be seen in Figure 5.14. Due to symmetry of the disc geometry, the CoP positions

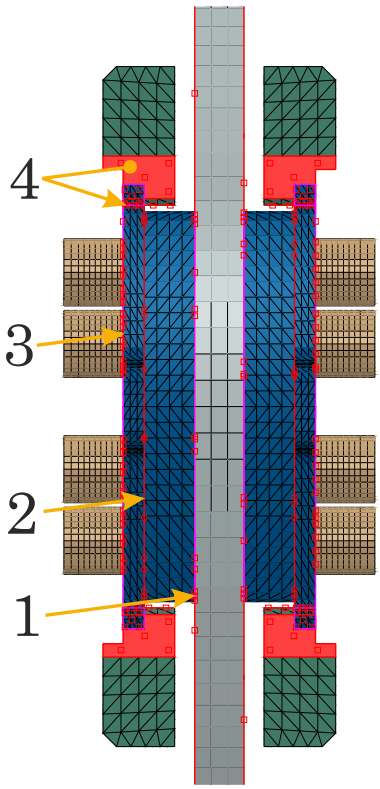

Figure 5.11: A detail of the interactions between the components: 1) surface-to-surface contact, small sliding formulation between the disc and the pad friction material, 2) tie constraint between the backplate and the friction material, 3) surface-to-surface contact, finite sliding formulation between the piston and the backplate, 4) surface-to-surface contact, small sliding formulation between the backplate and the abutments.

for the inboard and outboard side of the brake are identical, therefore only one pad/disc interface is illustrated. The CoP position calculated using the 3D analytical model and the FE model are plotted with the marker (o) and (+), respectively.

The absolute position error e_{abs} between estimated x_{est}, y_{est}, and actual (reference) x_{ref}, y_{ref} points can be determined using a method based on computing the Euclidean distance (Stephan et al., 2009) between two points as following:

$$e_{abs} = \sqrt{(x_{est} - x_{ref})^2 + (y_{est} - y_{ref})^2} \tag{5.32}$$

Table 5.6: Piston loads to compare the CoP positions using an analytical and FE model.

Load	Pressure (bar)			
No.	p_1	p_2	p_3	p_4
1	50	0	0	0
2	5	45	0	0
3	0	0	0	50
4	0	0	5	45
5	12.5	12.5	12.5	12.5
6	20	5	20	5

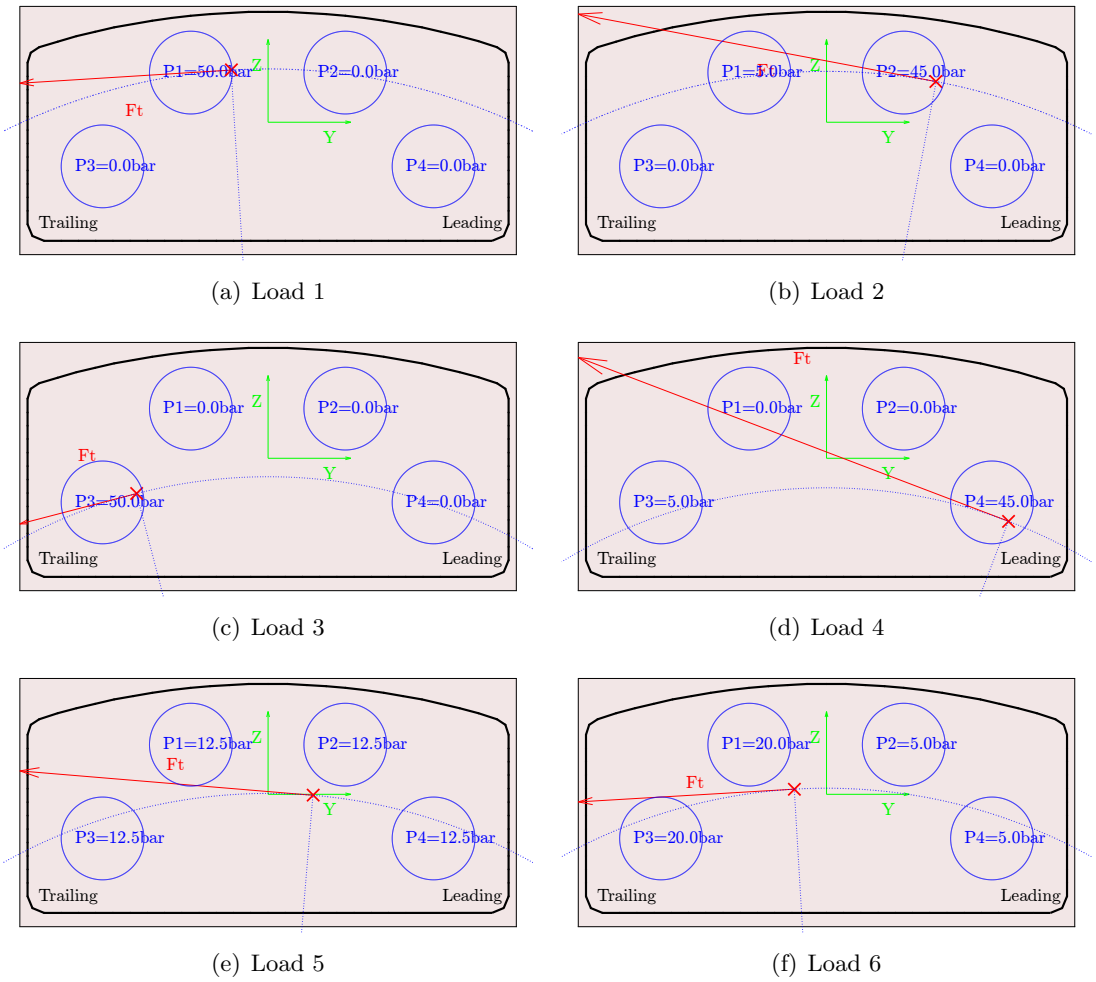

Figure 5.12: Six different piston load scenarios to generate a variety of CoP positions over the pad.

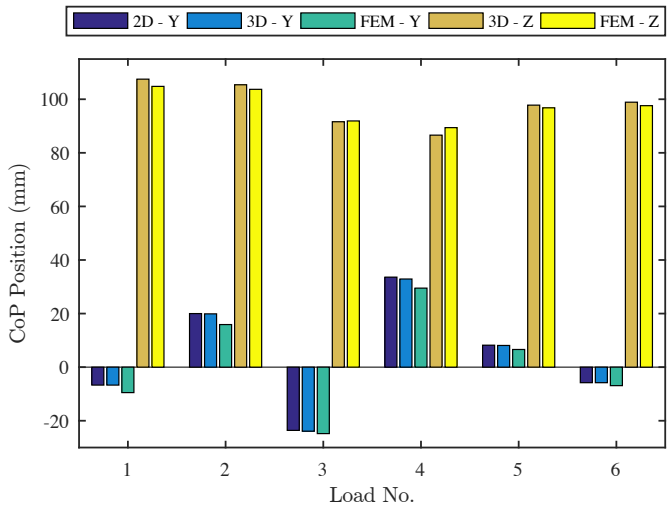

Figure 5.13: Comparison of CoP positions calculated using the 2D, new 3D and FE model for six different piston loads.

In the disc brake context, the relative position error e_{rel} between two points can be calculated as:

$$e_{rel} = \frac{e_{abs}}{r_e} \times 100\,\% \tag{5.33}$$

where r_e is the effective radius.

Table 5.7 summarises the aboslute and relative errors of the CoP calculated for comparison of the CoP positions determined by the new 3D model and the reference 2D analytical and FE models. By comparing the 3D and FE model, the absolute position errors of the CoP greater than 2 mm (highlighted) are for the load cases 1, 2 and 4. The biggest discrepancy between the 2D and 3D model is for the load case 4 (highlighted). It can be noticed that the largest differences tend to be for the CoP positions close to the leading edge and radially outward from the disc centre, where the influence of the reaction force at the leading abutment seems to be more significant. However, all relative errors are smaller than 5 %, which shows a good agreement between the models.

Table 5.8 shows calculated values of the pad/disc normal reaction R (clamp force)

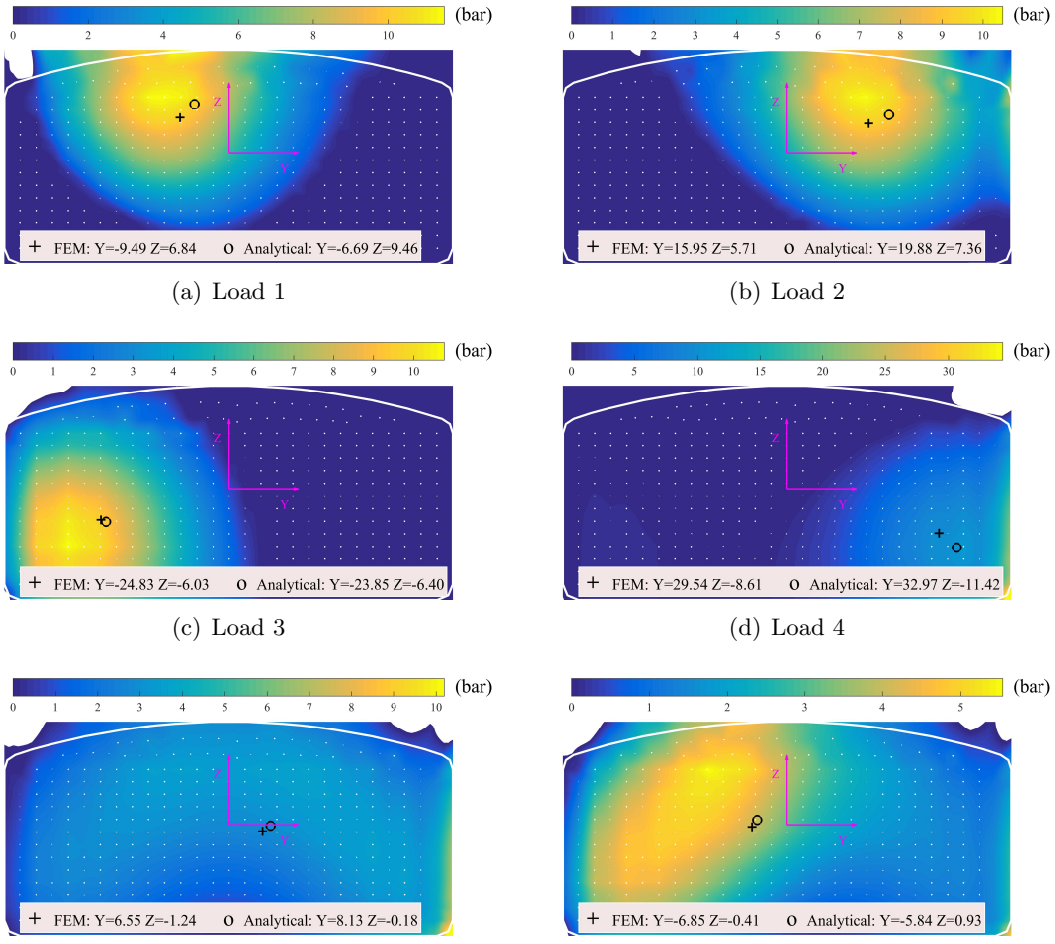

(a) Load 1 (b) Load 2

(c) Load 3 (d) Load 4

(e) Load 5 (f) Load 6

Figure 5.14: Comparison of the numerical and analytical calculation of the CoP for pressure loads 1 - 6 defined in Table 5.6.

Table 5.7: Absolute (Eq. 5.32) and relative position errors (Eq. 5.33) calculated for comparison of the CoP positions determined by the 3D analytical and the reference 2D analytical and FE models. Highlighted are absolute errors larger than 2 mm. For calculation of the relative errors, r_e=97.75 mm was assumed.

Load No.	Absolute (mm) and relative position error (in brackets)	
	3D vs. 2D Model (Ref.)	3D vs. FE Model (Ref.)
1	0.0 (0.0 %)	3.9 (4.0 %)
2	0.1 (0.1 %)	4.3 (4.4 %)
3	0.3 (0.3 %)	0.9 (0.9 %)
4	0.7 (0.7 %)	4.4 (4.5 %)
5	0.1 (0.1 %)	1.8 (1.8 %)
6	0.0 (0.0 %)	1.7 (1.7 %)

and friction force F_t using the new 3D analytical model, 2D analytical model and FE model for loads 1 - 6. The friction force F_t differs only slightly across all methods whereas the normal reaction force R determined from the FE model exhibits more significant difference. This may be due to a different characterisation of the abutment surface contacts for both approaches. Also, the flexural effects of the pad in the FE model may contribute to the larger discrepancy between the results.

Table 5.8: Calculated friction F_t and normal reaction R force values at the pad/disc interface for pressure loads 1 - 6 defined in Table 5.6.

Load No.	Piston Pressure (bar)				Force (N)					
					3D Analytical Model		2D Analytical Model		FE Model	
	p_1	p_2	p_3	p_4	F_t	R	F_t	R	F_t	R
1	50	0	0	0	333.5	833.7	333.4	833.6	350.5	885.4
2	5	45	0	0	333.8	834.4	333.4	833.6	346.8	883.4
3	0	0	50	0	334.0	835.1	333.4	833.6	330.8	860.7
4	0	0	5	45	334.7	836.7	333.4	833.6	330.6	875.1
5	12.5	12.5	12.5	12.5	333.5	833.7	333.4	833.6	338.7	874.6
6	20	5	20	5	333.5	833.6	333.4	833.6	339.3	872.4

5.3 Friction Coefficient Calculation

5.3.1 Traditional Approach to Friction Coefficient Calculation

Assuming two rubbing surfaces and the piston actuation force equal to the clamping force, the brake torque at the wheel T_W can be calculated using the following formula (Day, 2014):

$$T_W = 2\mu(p - p_t)A_a\eta r_e \tag{5.34}$$

where μ is the friction coefficient, p is the actuation pressure, p_t is the threshold pressure,

A_a is the total piston area, η is the efficiency of the hydraulic system and r_e denotes the effective radius. Neglecting the threshold pressure p_t and the efficiency η of the hydraulic system, Eq. 5.34 can be written as:

$$T_W = 2\mu p A_a r_e \tag{5.35}$$

Typically, the effective radius r_e is assumed to be equal to the mean pad radius r_m according to:

$$r_e = r_m = \frac{r_o + r_i}{2} \tag{5.36}$$

where r_o and r_i are the outer and inner radii of the rubbing area, respectively.
The effective radius r_e of the Fiat Punto disc can be calculated using Eq. 5.36:

$$r_e = r_m = \frac{118.5 + 77}{2} = 97.75\,\text{mm} \tag{5.37}$$

To calculate friction coefficient μ from the given torque T_W and piston pressure p value, Eq. 5.35 can be rearranged and used in the following form:

$$\mu = \frac{T_W}{2pA_a r_e} \tag{5.38}$$

5.3.2 Friction Coefficient Calculation Using 3D Analytical Model

If the brake torque is known, Eq. 5.19 for the 3D CoP position calculation and Eq. 5.24 for torque calculation can be also used to determine the friction coefficient μ. Because the calculation of μ cannot be expressed explicitly, these equations need to be evaluated in an iterative loop for a range of the μ values as illustrated in the program flowchart in Figure 5.15. When the difference between the calculated brake torque and measured brake torque is less than an acceptable error value, the loop is terminated and the value of μ is stored. The friction coefficient calculation was implemented in the program *CalBrakes*.

5.3.3 Comparison of Friction Coefficient Calculation Methods

The friction coefficient calculation using the 3D analytical model described above was compared with the traditional calculation of the friction coefficient by means of Eq. 5.38. All parameters used in the following calculations are displayed in Table 5.9. In the traditional approach the effective radius $r_e = r_m$ and this radius was calculated using Eq. 5.37, whereas the new method suggests that the effective radius $r_e = r$ as derived in Eq. 5.19.

Table 5.10 shows a comparison of the mean rotor radius r_m and the radial distance r of the CoP calculated using the new 3D analytical model for the friction coefficient $\mu = 0.4$. It is clear that both methods are independent of the actuation pressure assuming that a uniform piston load is used.

The Fiat Punto disc arrangement shown in Figure 5.16 was used to conduct drag brake tests for a range of piston pressure values. A constant rotational speed of 155 rpm was

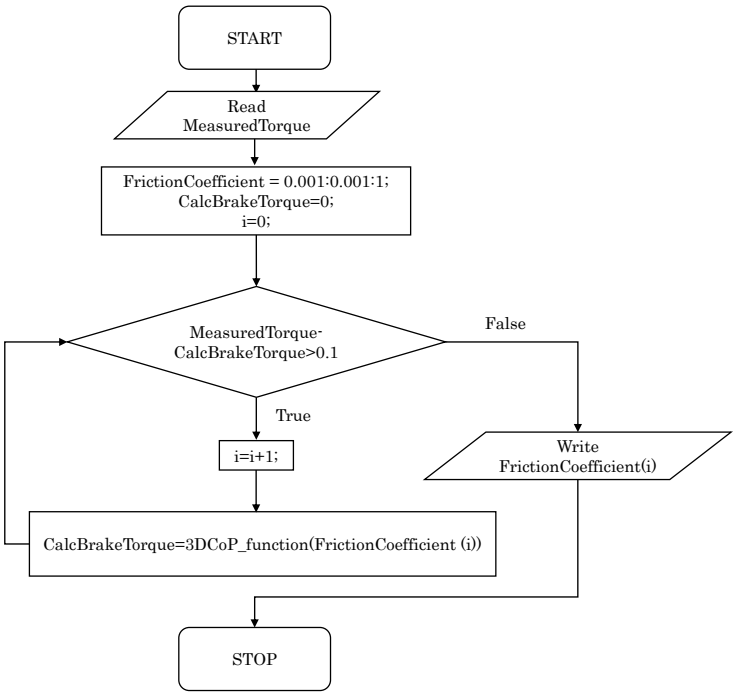

Figure 5.15: Flowchart of the friction coefficient evaluation using the 3D analytical model.

Table 5.9: Data used for the friction coefficient calculation.

Traditional Approach		3D Analytical Model	
A_a	$1266.94\times10^{-6}\,\mathrm{m}^2$	A_a	$1266.94\times10^{-6}\,\mathrm{m}^2$
r_e	97.75 mm	n_1	20 mm
		n_2	20 mm
		r_{pad}	98 mm
		μ_A	0.15
		t_{fm}	11.3 mm
		t_{bp}	4.7 mm
		y_A	45 mm

Table 5.10: Comparison of the effective radii calculated the traditional way and using the 3D analytical model.

No.	Actuation pressure p (bar)	Calculated r_m using Eq. 5.37 (mm)	Calculated radial distance of the CoP r using the 3D analytical model for $\mu = 0.4$ (mm)
1	2.5	97.75	97.66
2	5.0		
3	7.5		
4	10.0		

set for all testing procedures. During the braking event, the brake torque was monitored using a torque sensor mounted in the input shaft and a pressure transducer was used to collect the brake line pressure data. The rotor surface temperature was recorded using a sliding thermocouple. For all brake line pressure values, special care was taken to collect all data within a certain temperature range, in this case a range of 100 - 120 °C was

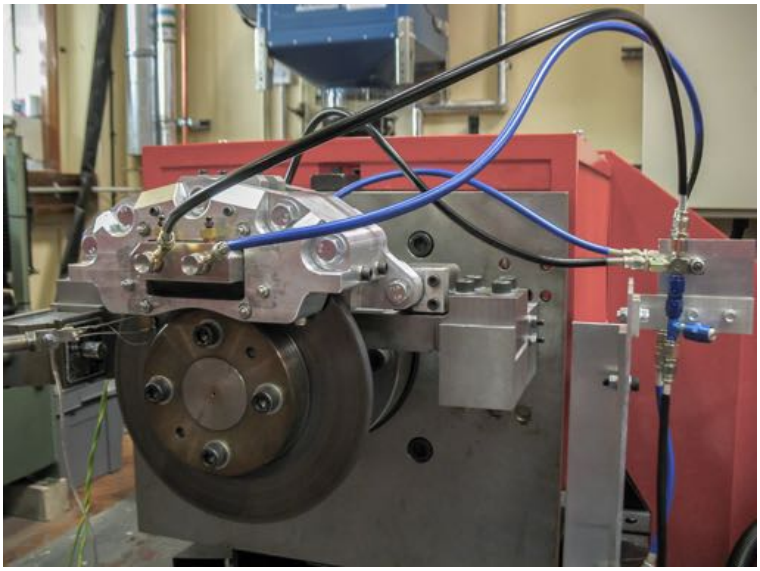

Figure 5.16: Fiat Punto brake disc arrangement for friction coefficient evaluation.

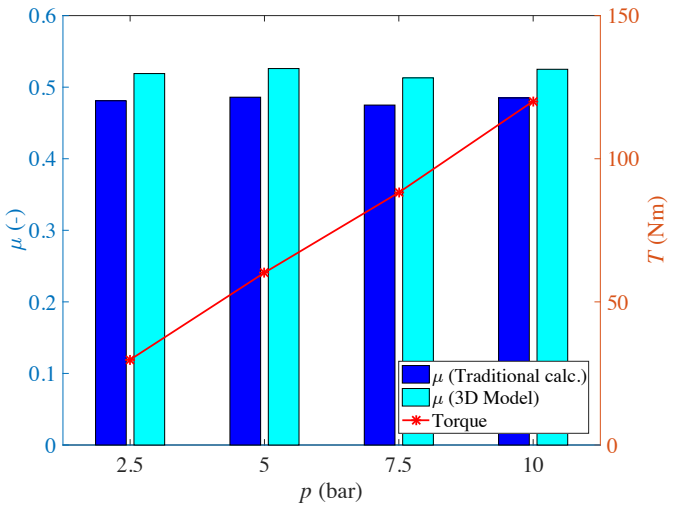

Figure 5.17: Comparison of the friction coefficient values calculated using the traditional method and the new 3D model.

chosen, to avoid differences in brake torque values that might otherwise arise due to the friction coefficient dependency on temperature.

Figure 5.17 displays a comparison of the friction coefficient values calculated using both methods for four different brake line pressures: 2.5, 5, 7.5 and 10 bar. The new 3D model gives an approximately 8% greater value of the friction coefficient than the value determined using the traditional method. The difference is due to the greater complexity and accuracy of the new 3D model which is included in the proposed calculation method. Although both methods give similar values of the effective radius r_e, the higher value of the friction coefficient stems predominantly from differences in the reaction force R calculation which, for the 3D approach, depends on the refined relation defined in Eq. 5.16.

5.4 Brake Disc Top-Hat Geometry Analysis

This section is concerned with investigation of the influence of the disc top-hat geometry on the centre of pressure and squeal propensity as a useful case study (Budinsky et al., 2017).

5.4.1 Finite-Element Model

A reduced isothermal FE model of a four-piston opposed brake system was developed in ABAQUS® as shown in Figure 5.18.

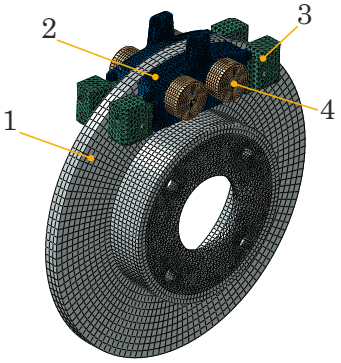

Figure 5.18: FE model of the brake system consisting of a: 1) Fiat Punto brake disc, 2) a Mintex brake pad, 3) pad abutments, 4) pistons.

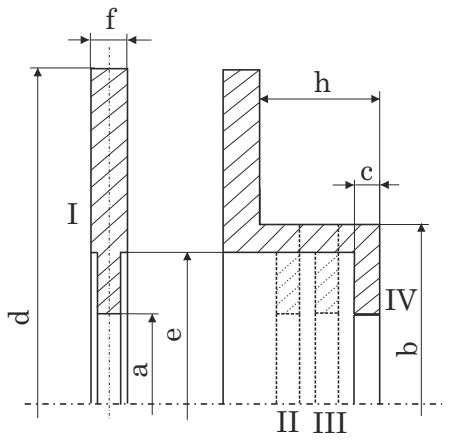

Figure 5.19: Structural modifications of the solid disc brake rotor: a=59 mm, b=136 mm, c=6 mm, d=240 mm, e=122 mm, f=11 mm. Model I is a baseline model for a top-hat height comparison (models I-IV) with a flange designed symmetrically to the disc central plane, while models II, III and IV differ in the value of the top-hat height parameter h = 9, 29 and 49 mm, respectively.

This model consists of a Fiat Punto brake disc, Mintex MDB 1189 brake pads, pistons and abutments. Since the influence of the caliper geometry was not important for this study, the caliper was not included in the model. In simple FE models of a brake, it is common to exclude the pistons from the simulation model and apply the load directly on designated areas on the backplate. For this particular model of the brake, the absence of the pistons would induce an error in the CoP position due to the rotation of the pad with the loads. In order to fix the positions of the piston loads during the braking, the pistons were allowed axial movement only. The interactions between the parts are analogous to the setting for the opposed eight-piston FE model presented above in Section 5.2.

In order to evaluate the influence of the disc top-hat height on the CoP position and squeal propensity, in total four models of a solid brake disc with a different top-hat height parameter h were developed as shown in Figure 5.19. Model I is the baseline model with a flange integrated symmetrically in the disc part, while the models II to IV differ only in the top-hat section, where the top-hat height parameter h = 9, 29 and

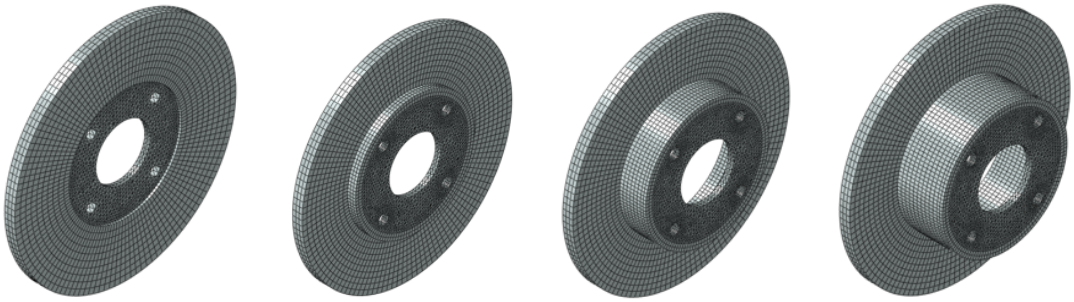

(a) Model I (b) Model II (c) Model III (d) Model IV

Figure 5.20: FE model of the disc with varying top-hat height parameter.

49 mm, respectively. The type of element used for the disc and neck part meshing is an eight-node linear brick with reduced integration (type C3D8R), while the flange with mounting holes is meshed with a four-node linear tetrahedron (type C3D4). Figure 5.20 shows meshed models for all disc top-hat variations. The material properties used in the simulation were analogous to those in Table 5.4.

5.4.2 Influence of Disc Top-Hat Geometry on CoP Position

Figure 5.21 shows a plot of CoP positions of the models I-IV for three different brake-line pressure settings: 5 bar (black solid line), 30 bar (blue dashed line), and 60 bar (red dash-dot line). It can be seen that the differences between the CoP positions for different top-hat heights are very small, but a clear trend can be observed. The Z-axis, representing the radial outward/inward position is zoomed compared with the Y-axis that shows the trailing/leading shift of the CoP, hence in reality the difference in the radial position is not as significant as indicated in the plot. Moreover, the variation of the radial position is significantly smaller than the mesh element size, so the results might not be precisely correct. Still, it is interesting that for the higher brake-line pressure the CoP position of the baseline model is located slightly radially inward.

On the other hand, the shift of the CoP in the trailing/leading direction is more significant. Generally, for a given model variant the CoP of the both inboard and outboard side tends to shift towards the leading side with increasing pressure. This was also observed from dynamic measurements of the CoP by (Kim et al., 2015). Also, with increasing pressure the outboard CoP for 5 bar is located radially more inward but for 30 and 60 bar, this changes and the outboard CoP is positioned radially more outward than the inboard CoP. Moreover, the inboard CoP position tends to move towards the trailing edge and the outboard CoP towards the leading end for the increasing top-hat height parameter. As a result, having a disc with a high top-hat causes a significant difference between the inboard and outboard CoP position during braking.

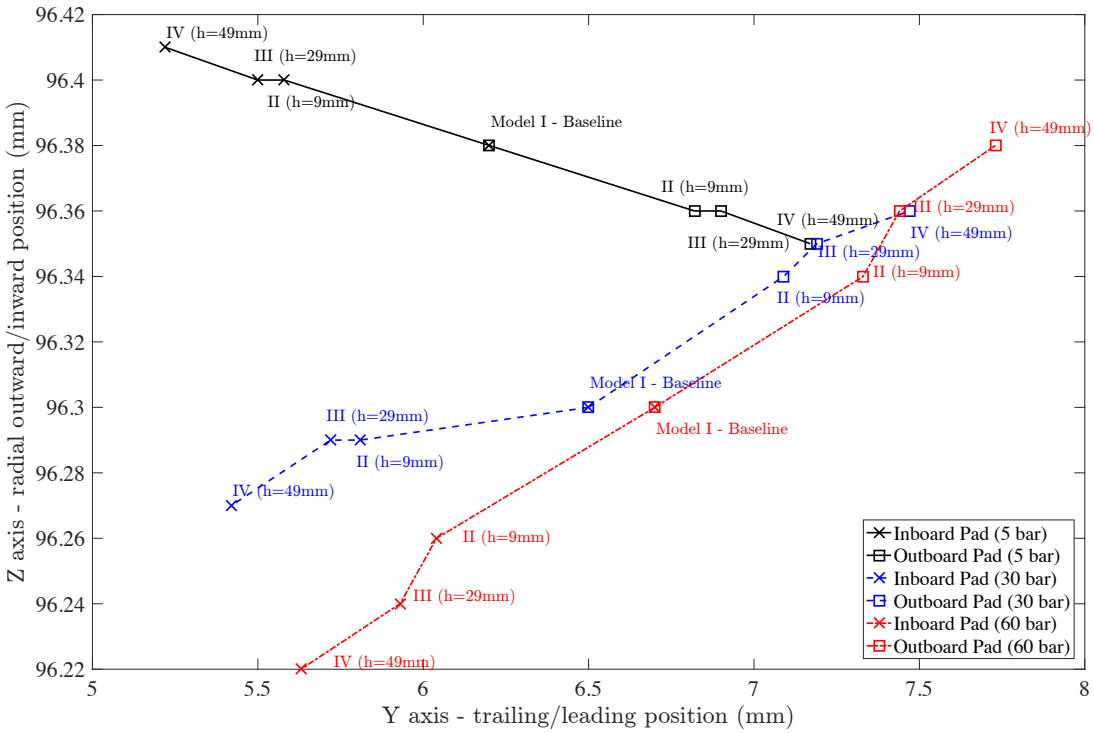

Figure 5.21: Plot of the CoP positions for four different modifications of the disc top-hat height: model I is a baseline model with a symmetrically positioned flange, and models II - IV having the disc top-hat parameter h=9, 29 and 49 mm, respectively.

5.4.3 Influence of Disc Top-Hat Geometry on Squeal Propensity

The final step of the simulation includes a complex eigenvalue analysis (CEA) that was performed on all brake models with the same braking conditions as described above for frequency range 0 - 10 kHz. (Bakar, 2012) found that inclusion of friction damping improves the squeal prediction, therefore this option was added in the model description. As an indicator of unstable modes of vibration the negative damping ratio was used. The frequencies of unstable vibration resulted from the CEA performed on all disc variants are shown in Table 5.11. These frequencies represent possible unstable modes of vibration that may give rise to squeal.

Since the FE models of the brake used in this study are simplified, the simulation results yield only a limited number of possible unstable modes. If an unstable doublet mode was present, only one of the doublet is shown here. It can be seen that with the increasing top-hat height parameter h the number and modes of unstable frequencies of vibration remained similar. All unstable modes resulted in an out-of-plane or coupled out-of-plane and in-plane type of vibration (e.g. modes 58-60) of the brake rotor. Any clear distinction between the particular modes is difficult due to the presence of the disc top-hat structure and other components in the assembly that contribute to the coupling of the vibration. The unstable rotor mode shapes for pressure setting 5 bar from Table 5.11 are displayed in Figure 5.22. A deformation scaling factor was applied to the plots to emphasise the shape of the modes. This can induce visible spikes of the position of some

Table 5.11: Unstable frequencies of vibration in the frequency range 0 - 10 kHz for different brake disc top-hat height parameters. The mode number is indicated in the brackets ( ).

	Pressure (bar)	Unstable frequencies of vibration (Hz)		
Model I Baseline	5	**8162** (53)	**8330** (58)	**8646** (66)
	30		**8336** (57)	
	60		**8449** (57)	
Model II h=9 mm	5	**8163** (53)	**8328** (60)	**8644** (68)
	30		**8332** (60)	
	60		**8444** (60)	
Model III h=29 mm	5	**8163** (56)	**8328** (60)	**8647** (70)
	30		**8335** (60)	
	60		**8447** (61)	
Model IV h=49 mm	5	**8163** (55)	**8328** (60)	**8647** (70)
	30		**8336** (59)	
	60		**8448** (61)	

of the nodes at the contact of more components, such as the brake pad/disc interface. However, this seems to be only a graphical problem and should not have impact on the actual results.

The CEA performed on the current brake model in the frequency range 0 - 10 kHz did not show any distinct change of the unstable vibration for different disc top-hat height parameters. Therefore, the findings made by (Bae and Wickert, 2000) on disc models with a different top-hat height using a free vibration analysis could not be confirmed. The present study did not indicate that a certain design value of the top-hat height exists that could minimise the existence of unstable modes of the vibration. Also, due to the almost invariant character of the unstable modes of the vibration over the whole parameter range it is not possible to infer any conclusion with respect to the effect of the CoP position as predicted in the previous section.

5.4.4 Summary

The points below summarise the major findings of this section:

1. The analysis of pressure distribution on all disc variants during braking showed

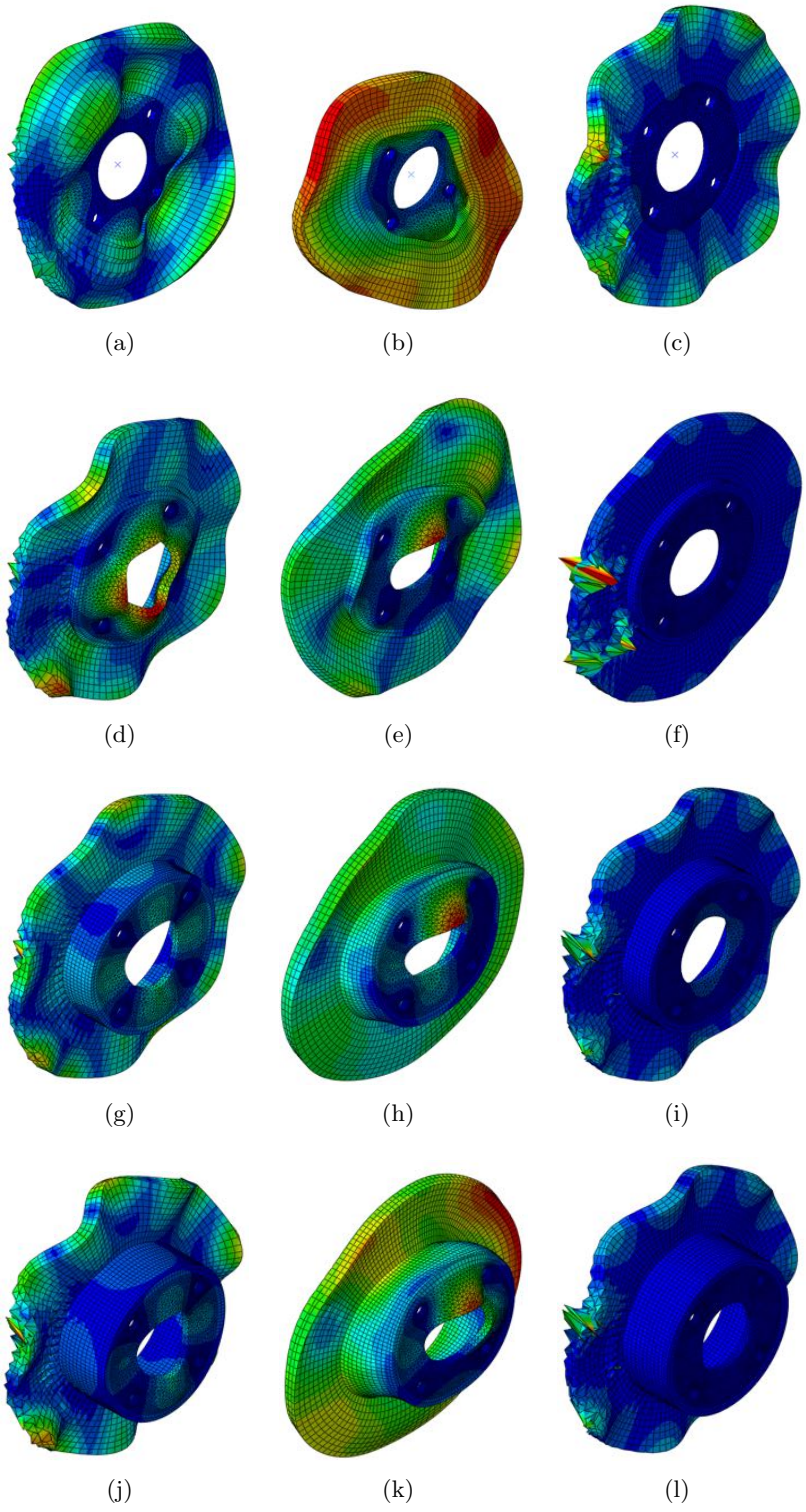

Figure 5.22: Illustrations of the vibration modes of the brake disc for all model variants. The brake line pressure is 5 bar. A deformation scaling factor is applied to the plots to emphasise the shape of the modes.

that a small difference in CoP positions for the outboard and inboard pad exists, which is dependent on the top-hat geometry.

2. The CoP on the both inboard and outboard side tends to shift towards the leading side with increasing pressure.

3. The outboard CoP is located radially more outward than the inboard CoP above a certain value of applied pressure.

4. The inboard CoP position tends to move towards the trailing edge and the outboard CoP towards the leading end for the increasing top-hat height parameter. This effect is most probably due to the bending of the top-hat structure.

5. The CEA showed that the number of unstable modes and their frequency remains nearly identical across all disc model variants. An ideal top-hat height parameter that would show a reduced propensity to squeal was not found.

6. Due to the almost invariant results of the CEA over the disc model range, any correlation between the vibrational behavior and the CoP position for the top-hat height parameter could not be found.

5.5 Finite-Element Model of Rover Disc Brake

As the Rover disc was predominantly used for squeal investigations, a reduced FE model of this configuration was developed in ABAQUS®. The model consists of a disc, pair of pads, abutments and pistons as can be seen in Figure 5.23. To simplify the complexity

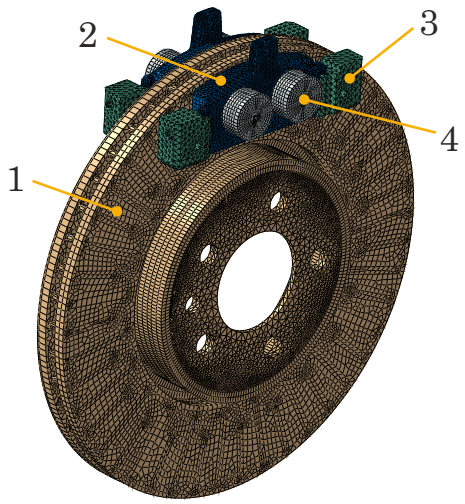

Figure 5.23: FE model of the Rover disc brake assembly: 1) brake disc, 2) brake pad, 3) abutment, 4) piston.

of the model and reduce the calculation time, the caliper was not included in the assembly. Simple geometries such as the disc and piston were created in the FE software, whereas the more complex components such as the backplate, the friction material and the abutments were designed in SOLIDWORKS® and imported to ABAQUS® using a STEP format.

Figure 5.24 illustrates the interactions between the components. All bodies were

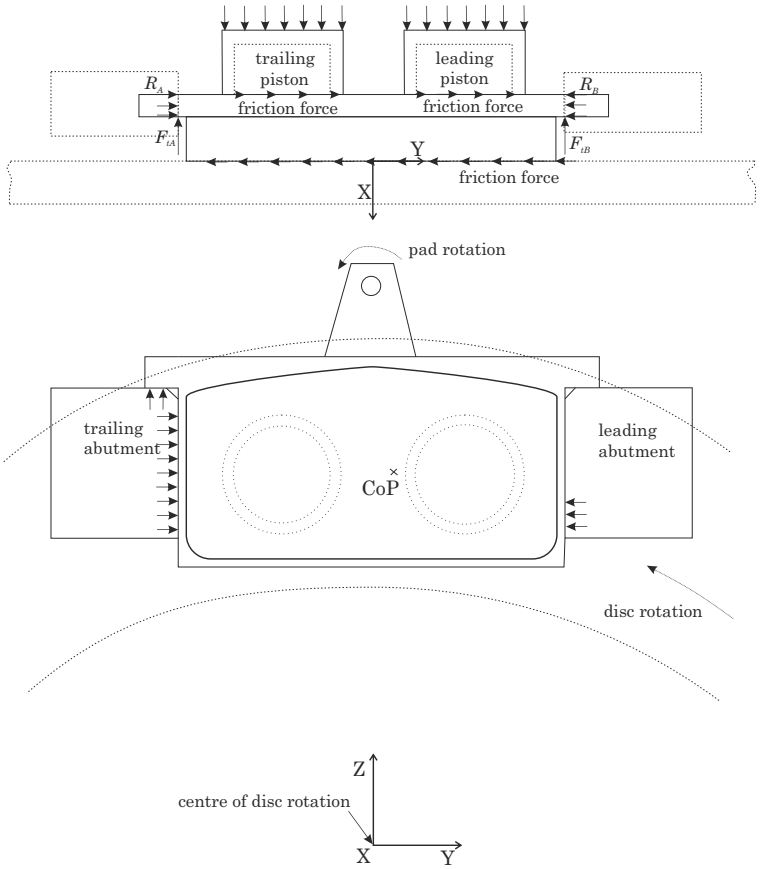

Figure 5.24: Loads and boundaries defined in the FE model.

modelled as flexible bodies having the material and interaction properties analogous to those for the opposed 8-piston brake model presented in Table 5.4 and Figures 5.10 - 5.11, respectively.

5.5.1 Mesh Analysis

Generally, the mesh density determines the size of an element. In a detailed FE model, large elements might lead to a greater aspect ratio, which is the ratio of the longest to the shortest edge in an element (Abaqus, 2012). Ideally, this ratio should be close to 1 to achieve good results. However, a finer mesh causes increase of the computational time, so a trade-off between the mesh density and calculation time needs to be found.

Figures 5.25 - 5.26(a) show meshed components used in the brake model. The mesh type and number of elements of each component are given in Table 5.12.

The friction ring (Figure 5.26(b)) and top-hat section of the brake disc (Figure 5.26(c)) were meshed using a linear hexahedral element of type C3D8I that includes an incompatible modes option. This element gives a better accuracy/calculation time ratio when compared to the common element types of C3D8 or C3D8R with reduced integration (Elguezabal et al., 2015). The flange was meshed using a linear tetrahedral element of type C3D4.

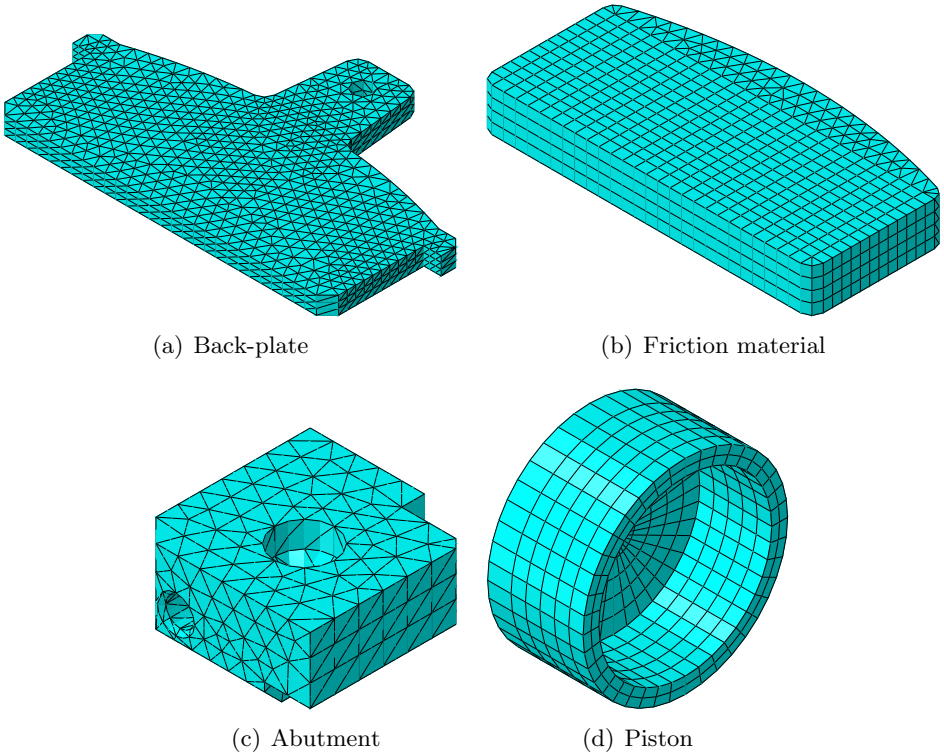

(a) Back-plate (b) Friction material

(c) Abutment (d) Piston

Figure 5.25: Meshed brake components.

Table 5.12: Type and number of the mesh elements used in the FE model.

Part	FEM element type	Number of elements
Disc	C3D4 (Tet)	15345
	C3D8I (Hex)	45423
Friction material	C3D4 (Tet)	1754
	C3D8R (Hex)	1448
	C3D6 (Wedge)	16
Backplate	C3D4 (Tet)	8607
Abutment	C3D4 (Tet)	2671
Piston	C3D8I (Hex)	640
	C3D6 (Wedge)	40

To find an optimal number of elements for the disc, a mesh refinement technique was performed for four levels of mesh density: ultra coarse (Figure 5.27(a)), coarse (Figure 5.27(b)), medium (Figure 5.27(c)) and fine (Figure 5.27(d)) mesh. For these meshes, a modal analysis was conducted to extract natural frequencies. The results of the first three meaningful frequencies are plotted against number of mesh elements in Figure 5.28.

It can be seen that the natural frequencies tend to converge to a certain value with increasing number of elements. The natural frequency of the model with the medium number of elements does not change significantly with further mesh refinement and the relative frequency difference between the medium and coarse mesh density is 1.1% for the 10th mode as can be seen in Table 5.13.

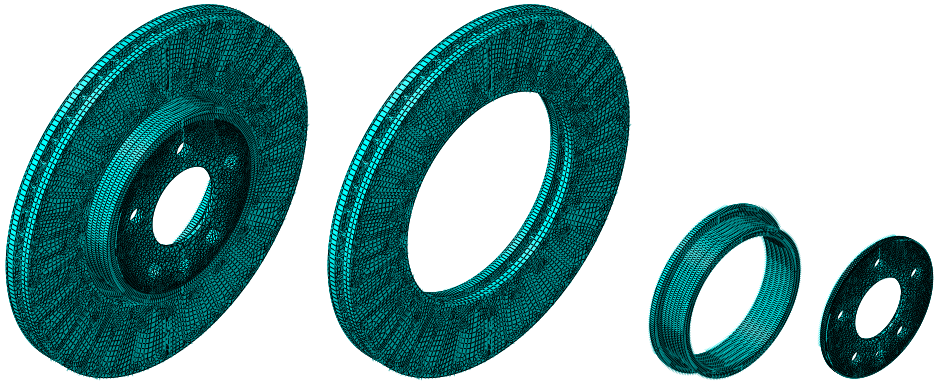

(a) Meshed disc (b) Friction ring (c) Top-hat (d) Flange

Figure 5.26: Meshed brake disc.

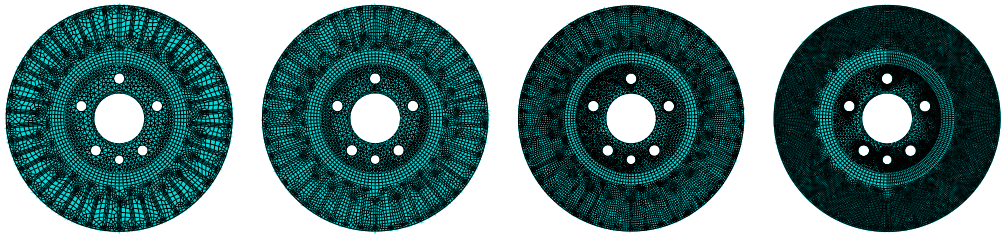

(a) Ultra coarse (b) Coarse (c) Medium (d) Fine

Figure 5.27: Variety of mesh densities for mesh sensitivity analysis.

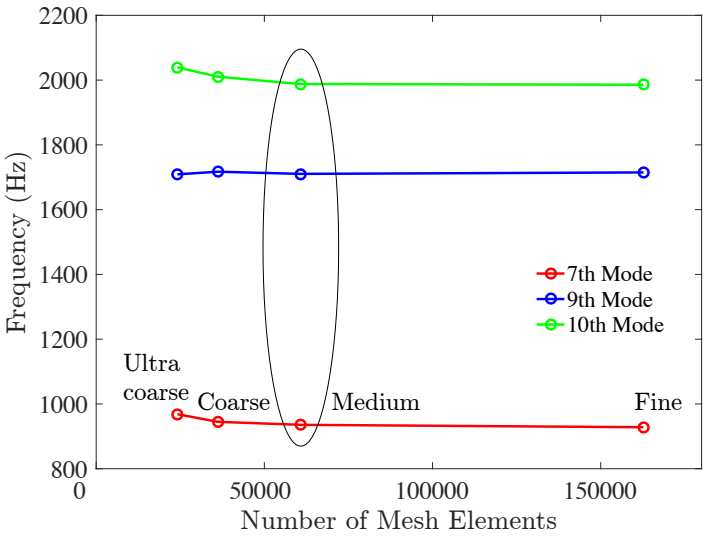

Figure 5.28: Mesh refinement technique showing the convergence of the natural frequency values for increasing number of elements.

Maximum natural frequency differences less than 2% are considered to be within satisfactory limits (Rabia et al., 2013). The calculation time of the mesh having the medium number of elements is 3 min 49 s (see bottom row in Table 5.13) which is an

Table 5.13: Natural frequency values for increasing number of mesh elements (Ultra coarse, Coarse, Medium, and Fine). Rel.Diff. = Absolute value of the relative difference.

	Natural frequency (Hz)						
Mesh density/ Mode	Ultra coarse	Coarse	Rel. Diff.	Medium	Rel. Diff.	Fine	Rel. Diff.
7th	968.3	944.8	-2.4%	935.6	-1.0%	928.1	-0.8%
9th	1709.1	1717.1	+0.5%	1710.4	-0.4%	1714.9	+0.3%
10th	2039.3	2010.4	-1.4%	1987.8	-1.1%	1985.7	-0.1%
Calculation time (mm:ss)	01:37	02:14		03:49		23:40	

acceptable value, therefore this mesh was used in all subsequent analyses.

The mesh density of the friction material (Figure 5.25(b)) and backing plate (Figure 5.25(a)) were chosen to provide an appropriate mesh for the CoP position calculation. The mesh densities of the abutments and pistons were reasonably estimated as these have smaller influence on the accuracy of the brake modal analysis.

5.5.2 Comparison of Finite-Element Model with Other Models

The performance of the Rover disc brake FE model was compared with: 1) the results from a previous experimental modal analysis (EMA) of the disc, 2) CoP predictions calculated by the 3D analytical model.

1. **Modal Analysis**

   Instrumentation for the EMA was not available in the UoL laboratory during this research. However, EMA of the same Rover disc was performed by (Hassan, 2009), hence his results were used for the new model validation. The material properties of the disc were varied to achieve a maximum relative error of the natural frequencies lower than 2.5%. Table 5.14 shows the absolute and relative error of the disc natural frequencies for the FE model and the real disc using EMA.

Table 5.14: Comparison of natural frequencies between the FE model and measurements on real disc provided by (Hassan, 2009).

Natural frequency (Hz)			
FE model	Real disc	Absolute error	Relative error (%)
935	918	17	-1.85
1710	1703	7	-0.41
2175	2187	12	+0.55
3563	3629	66	+1.82
5383	5502	119	+2.16
7015	7001	14	-0.20
8257	8238	19	-0.23
9809	9801	8	-0.08

2. **Centre of Pressure Position**

   The CoP predictions resulting from the FE simulation were compared with the CoP positions calculated by the 3D analytical model for LTPR = 1/9 to 9. All CoP positions and their calculated absolute and relative position errors are summarised in Table 5.15. For all LTPRs, the relative position error is less than 5 %, which shows a good agreement between the models.

Table 5.15: Comparison of CoP positions between the FE model and the reference 3D analytical model (blue cells) on inboard (Inb.) and outboard (Outb.) side. The differences are quantified as the absolute position error (orange cells) defined by Eq. 5.32 and the relative position error (green cells) calculated by Eq. 5.33. Anal. = Analytical 3D model (Reference model).

LTPR	CoP (mm)						Abs. Error		Rel. Error (%)	
	Y			Z						
	Anal. (Ref.)	Inb.	Outb.	Anal. (Ref.)	Inb.	Outb.	Inb.	Outb.	Inb.	Outb.
1/9	-8.2	-10.3	-9.7	0.5	-0.4	-0.6	2.3	1.9	1.9	1.6
1/4	-3.9	-5.7	-5.0	0.3	-0.6	-0.8	2.0	1.6	1.7	1.4
1/3	-1.7	-3.6	-2.9	0.1	-0.7	-0.8	2.1	1.5	1.8	1.3
1/2	1.9	-0.4	0.3	-0.1	-0.9	-1.0	2.4	1.8	2.0	1.5
1	9.0	5.9	6.6	-0.7	-1.2	-1.2	3.1	2.5	2.6	2.1
2	16.2	12.0	12.7	-1.3	-1.5	-1.4	4.2	3.5	3.6	2.9
3	19.7	15.1	15.8	-1.6	-1.6	-1.5	4.6	3.9	3.9	3.3
4	21.8	17.0	17.7	-1.9	-1.7	-1.6	4.8	4.1	4.1	3.5
9	26.1	20.9	21.5	-2.3	-1.8	-1.8	5.2	4.6	4.4	3.9

5.5.3 Complex Eigenvalue Analysis of Rover Disc Brake

The complex eigenvalue analysis (CEA) was employed to examine squeal propensity of the Rover disc brake assembly. The ABAQUS® input file for the Rover disc assembly followed the recommended practice presented in Chapter 2. Its basic structure is shown in Appendix C. In the current model, the friction coefficient was assumed to be constant and the friction damping option was activated for the simulation. The piston pressures were set to uniform pressure where p_1, p_2, p_3, p_4 = 30 bar, the friction coefficient μ = 0.4 and a rotational speed of 50 rpm was imposed on the disc. As a predictor of unstable modes of vibrations the negative damping ratio was used as shown in Figure 5.29. The unstable modes with a significant positive real part of the eigenvalue are shown in Figure 5.30.

In the next numerical experiment, the LTPR was varied from 1/9 to 9 and three different friction coefficients were investigated μ = 0.4, 0.5 and 0.6. For this parametric study, the disc speed was set to 30 rpm. The results of unstable mode predictions are plotted in Figure 5.31. The results clearly show that the high-frequency squeal is relatively insensitive to the LTPR range, whereas for instance when μ = 0.5, the low-frequency squeal (1785 Hz) was suppressed for LTPR = 1/9, 1/4, 1/3, 1/2 and 9. This might suggest

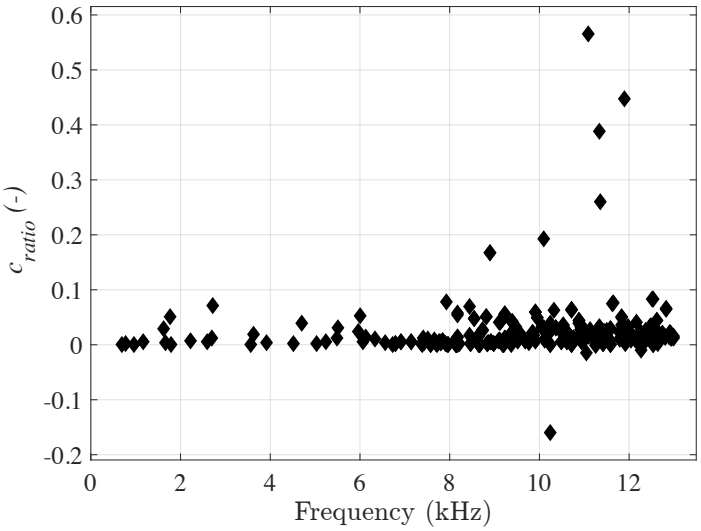

Figure 5.29: Effective damping ratio showing potential unstable modes of vibration.

that the high-frequency squeal is not influenced by different geometric constraints induced by variation of LTPR, but a different generation mechanism takes place, for instance mode coupling. It can also be noticed that for the LTPR values when low-frequency squeal was suppressed, the high-frequency squeal showed a small increase of occurrences. This indicates that by varying the LTPR different frequencies are emphasised. It is also worth mentioning that the higher friction coefficient of 0.6 resulted in higher squeal propensity as expected.

The squeal predictions determined using the CEA were compared with squeal monitored on the UoL brake dynamometer for equivalent test conditions: constant speed of 30 rpm and constant pressure setting during the squeal monitoring. The LTPR was varied from 1/9 to 9 and the brake torque was kept constant (approximately 75 Nm). The data were logged when the initial temperature of the disc surface was 160°C and gradually decreased to 120°C. The CEA and experimental results are compared in Figure 5.32. It can be seen that the low-frequency squeal of 1785 Hz was predicted well for most cases of the LTPR, however due to the simplicity of the FE model some squeal frequencies such as 2.1 kHz, 4.0 - 4.5 kHz, 5.5 - 6.2 kHz were not determined. Also, the model seems to overpredict squeal frequencies, in particular in the range of 9.5 - 13 kHz. A good match of an predicted squeal frequency and squeal monitored during experiment is labelled with a black circle.

In Figure 5.33, squeal predictions from the CEA (constant speed 30 rpm and torque 75 Nm) are plotted with the relative squeal occurrence observed on the dynamometer when the modified SAE J2521 (constant speed 30 rpm and 100 rpm, variable torque) test procedure was used. This comparison does not represent equivalent testing conditions but shows a spectrum of detected squeal frequencies over a longer time period. It can be seen that the existence of the low-frequency squeal of 1785 Hz is predicted quite well for specific LTPRs (labelled with a black circle). Also, the high-frequency squeal measured

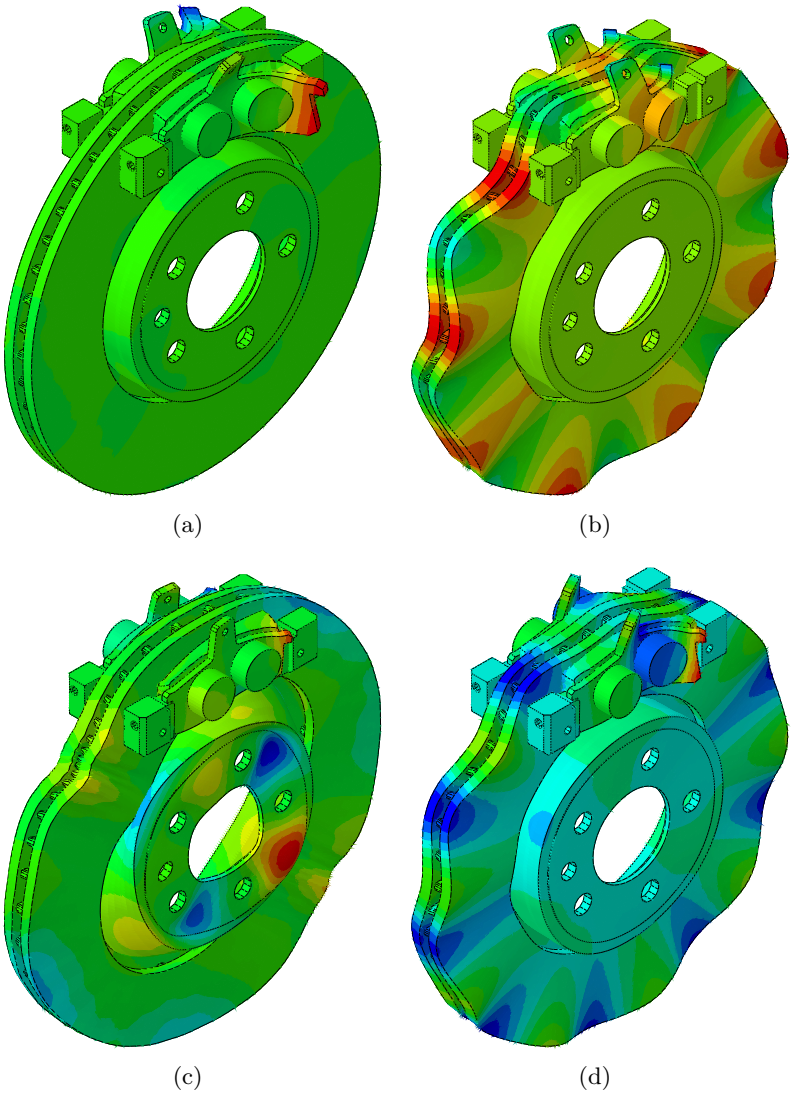

Figure 5.30: Unstable modes of vibration of the Rover disc assembly for $p1$, $p2$, $p3$, $p4$ = 30 bar, μ = 0.4, ω = 50 rpm: a) Mode 153, 10.2 kHz, Real part +5131.5 b) Mode 190, 11.0 kHz, Real part +503.8, c) Mode 197, 11.2 kHz, Real part +56.2, d) Mode 253, 12.3 kHz, Real part +403.4.

in the range 8 - 9.5 kHz seems to be in a good agreement with the predicted values.

5.6 Summary

This chapter has presented development of a new 3D analytical model of the pad/disc interface that predicts the position of the normal and friction force acting at a point (which can be related to the CoP) in the circumferential and radial directions. An existing 2D analytical model served as a reference for comparison of the CoP offset calculated by both methods. Also, a FE model of a corresponding brake, with a symmetrical flange of the disc to avoid differences between the inboard and outboard side, was used to verify the performance of the analytical model. It was shown that the CoP predictions

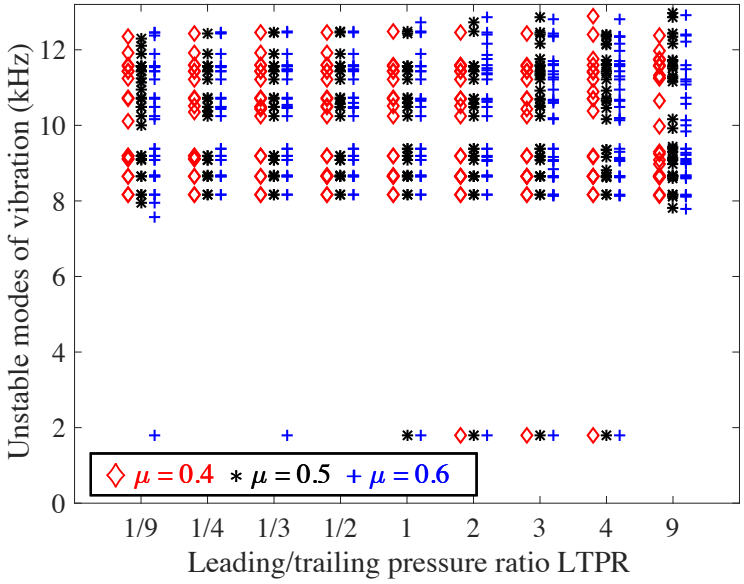

Figure 5.31: Unstable frequencies for a variation of LTPR and different friction coefficient values.

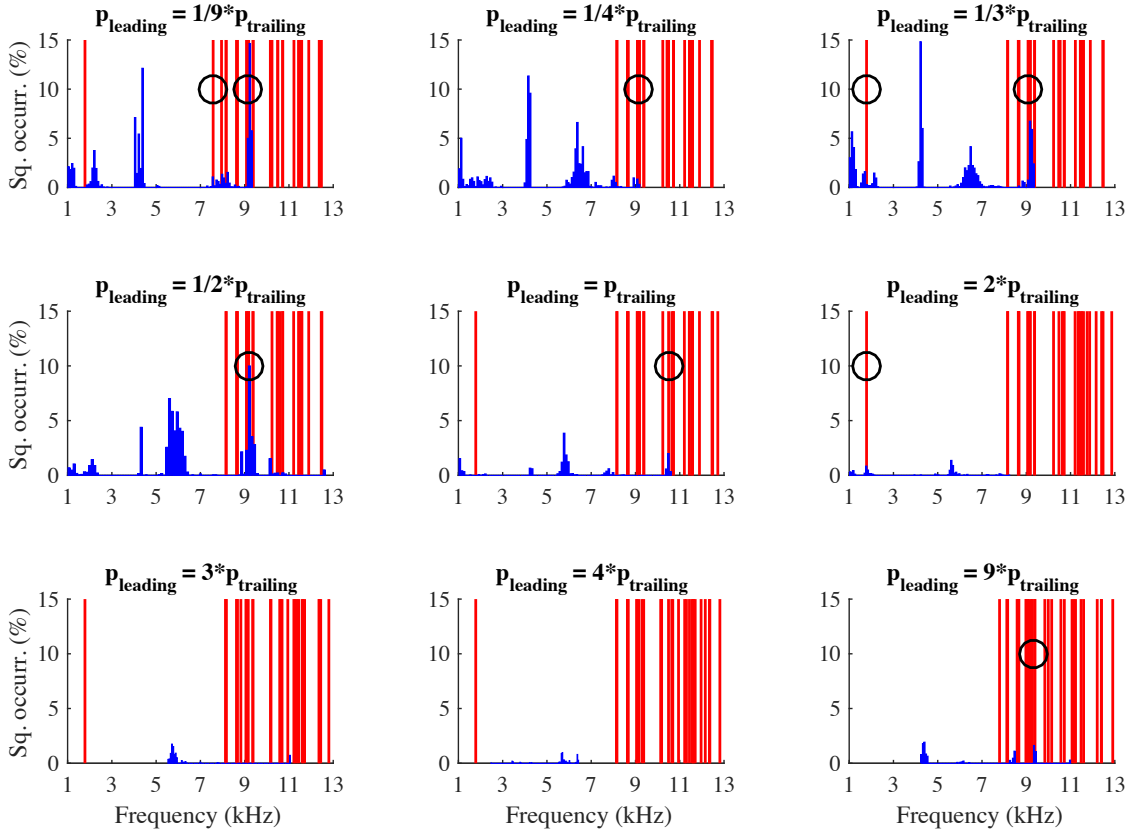

Figure 5.32: Plot of CEA squeal predictions (red) and squeal relative occurrence detected on the brake dynamometer (blue) for constant speed and pressure setting. A black circle shows a good match between the simulation model and experiment.

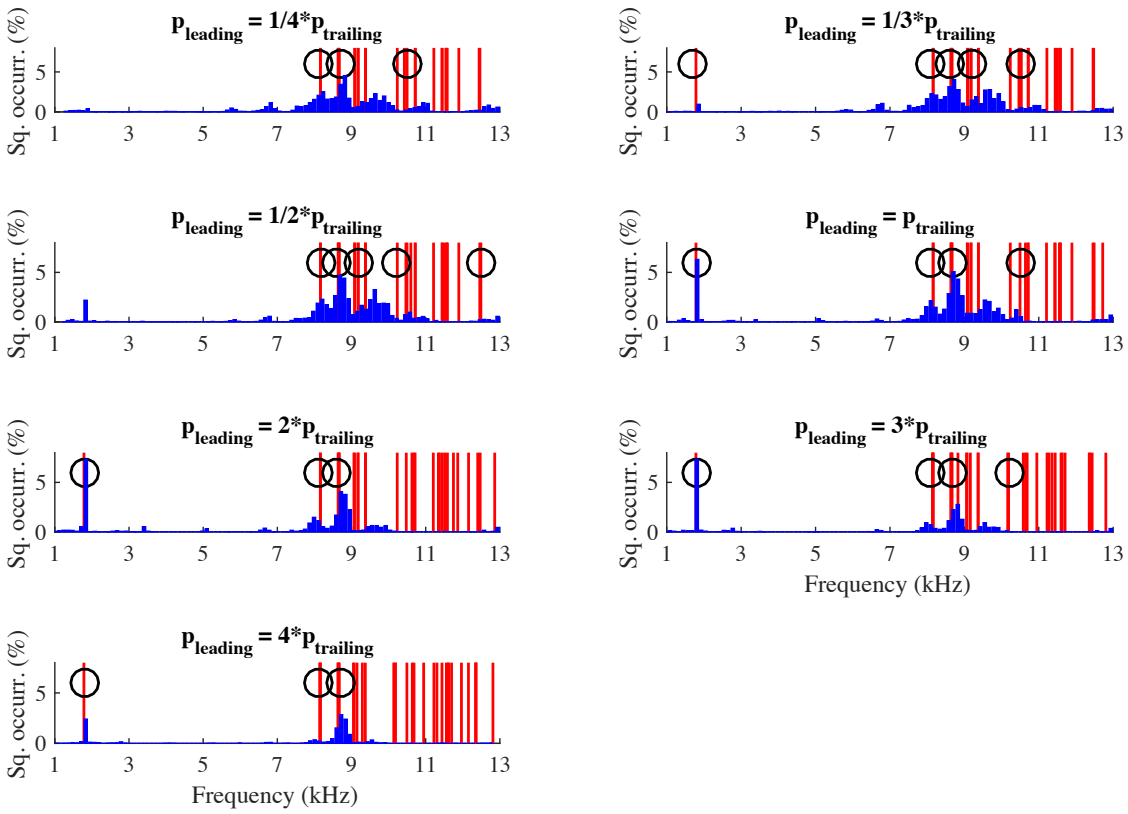

Figure 5.33: Plot of CEA squeal predictions (red) with constant speed of 30 rpm and torque and squeal relative occurrence detected on the brake dynamometer (blue) following a modified SAE J2521 drag brake test (constant speed 30 rpm and 100 rpm, variable torque). A black circle shows a good match between the simulation model and experiment.

determined by the analytical model correlated well for the most area of the pad with those determined by the FE model. The current analytical model with two piston forces was also derived for the case when four pistons act on each pad.

Also in this chapter, a reduced FE model of the current brake setup including the Rover disc was developed to predict the squeal performance for a variety of the LTPRs. As described above, the FE solver uses Eq. 2.11 to extract the complex eigenvalues of a given problem. In the current context, each LTPR determines new geometric constraints for the brake assembly resulting eventually in the formation of a specific stiffness K and damping C matrix. The mass matrix M is not affected. Solution of the modified characteristic equation results in prediction of unstable modes that are specific to each LTPR. It would be interesting to demonstrate the formation of LTPR-specific stiffness and damping matrices using an analytical model of a disc brake, for instance similar to a model developed by (Flint and Hulten, 2002).

The disc mesh size was optimised using a mesh sensitivity analysis and the performance of the model was compared with other models on two levels: experimental modal analysis of the disc and CoP prediction. The FE model could be further improved in multiple aspects. As was presented in the literature review in Chapter 2, by adding other brake

or chassis components into the assembly as well as by introducing other effects, such as heat transfer, wear or real pad topography, the squeal prediction of the model could be further enhanced. Moreover, a more thorough characterisation of the materials (elastic constants, density, etc.) would contribute to better squeal prediction. A good example of a complex FE modelling methodology that could be adopted here is presented in (Tirovic et al., 2018).

Finally, a CEA was performed for a variation of LTPR showing a potential when the low-frequency squeal can be reduced. The simulation results were compared with experiments performed on the brake dynamometer. Having equivalent braking conditions, the low-frequency squeal of about 1785 Hz was predicted well for most LTPRs, however some squeal frequencies between 2.1 and 6.2 kHz were not predicted at all. Contrarily, the FE model overpredicted squeal in particular between 9.5 - 13 kHz. Comparing the FE squeal predictions with longer experiments utilising the modified SAE J2521 procedure showed a better agreement of the squeal frequencies across the whole range.

6 Development of Embedded Brake Pad Sensor

"Innovation is moving at a scarily fast pace."
Bill Gates

6.1 Introduction

For many years there has been endeavour in the brake community to dynamically monitor pressure distribution, reaction forces and temperature at the pad/disc contact interface during actual braking. Such a system would speed up the development phase of new brake components, for instance development of modified brake calipers or pads. In the future, an intelligent brake pad monitoring system could also directly interface with a vehicle's electronic control unit, providing real-time information on brake performance. Although embedded thermocouples have become a common tool in brake laboratories to monitor temperature close to the contact surface, the monitoring of the pressure distribution and contact forces were for many years challenging. High temperatures and pressures, as well as limited space are the factors that make any design attempts very difficult. However, some solutions have been found to employ embedded force or pressure sensors between the friction material and the backplate (Degenstein and Winner, 2006), (Fieldhouse et al., 2009), (Kim et al., 2015).

In this chapter a new embedded brake pad sensor is presented which enables the user to monitor the centre of the pressure (CoP) position and magnitude of the normal reaction force acting at the pad/disc contact surface. The CoP position is calculated in real-time from the moment equilibrium equation in which the normal force values are determined at pre-defined positions using high-temperature piezoresistive force sensors. First, the design requirements for the new pad sensor are listed below, followed by a detailed description of the mechanical and electronic components. The calibration procedure of the sensors, as well as some testing results are then presented. The chapter concludes with a discussion of the outcome and a brief summary.

6.2 Design Requirements

The design requirements for the new embedded brake pad sensor and their relative importance are listed in Table 6.1.

Table 6.1: Design requirements for the new embedded brake pad sensor and their relative importance.

Design Requirement	Essential	Desired
Real-time monitoring of the CoP position during a braking event.	X	
Real-time monitoring of the normal reaction force during a braking event.		X
Backplate shape and dimensions should be identical to the Mintex MDB 1189 brake pad to enable the sensor to be used on the current 4-piston opposed brake caliper.	X	
The mechanical properties (friction coefficient, stiffness) of the friction material should be similar to those of a typical conventional brake pad.		X
The material of the backplate should be preferrably steel to achieve similar mechanical properties to the Mintex MDB 1189 brake pad, e.g. stiffness.		X
Embedding the low-cost high temperature Tekscan^{TM} force sensors HT201.	X	
Monitoring of the force sensor temperature.	X	
Plug and play data acquisition to facilitate use and portability of the system.		X

6.3 Overview of Components

Based on the above design requirements, an embedded brake pad sensor was designed as shown in Figure 6.1. The static part of the sensor is represented by a stainless steel backplate, featuring a recess, in which a friction material (lining) plug with a small clearance can freely move. The tangential movement of the plug is abuted at the trailing side of the backplate. The bottom surface of the backplate contains five protrusions at pre-defined positions, on which sensors are fixed using a special high-temperature tape

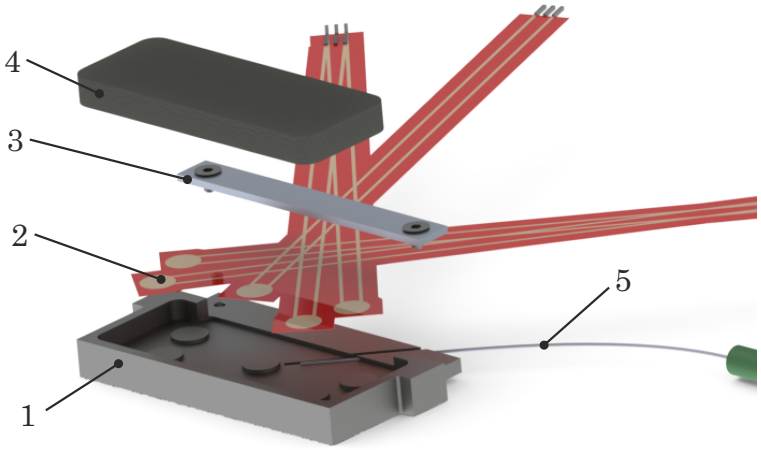

Figure 6.1: Embedded brake pad sensor: 1) backplate, 2) FlexiForce^{TM} HT201 force sensor, 3) sensor holder, 4) friction material (lining) plug, 5) thermocouple.

and secured with a holder that is bolted to the backplate. The sensors can monitor the force resulting from the contact between the protrusions and the friction material plug. Their positions are determined to allow CoP position calculation across the major part of the pad and to prevent overlapping of the sensors. Since the sensors have fixed position, the CoP position can be calculated by applying static moment equilibrium relations. The sensor employed in this configuration is a FlexiForce^{TM} HT201 piezoresistive force sensor developed by Tekscan^{TM}. It is an ultra-thin flexible high-temperature sensor capable of measuring force and pressure in environments with temperatures not exceeding 204°C (400°F) and is ideal for prototyping and embedded electronics. This sensor enables, depending on the employed circuit, measurement of force up to 2224 N (500 lb). The average linearity error up to 204°C is specified to be below 3% of the full scale value (here the full scale represents 889 N (200 lb)). The pad features four force sensors located approximately in the corners of the friction material and one in the centre to capture the component of the force resulting from the plug deflection. The temperature of the sensors is monitored by a K-type thermocouple inserted in a groove leading from the edge of the backplate to the center protrusion.

To achieve a high portability of the brake pad sensor, the overall device was developed as a plug-and-play system as shown in Figure 6.2. The main components of the system include: 1) USB cable, 2) USB 6003 DAQ system, 3) electronic circuit box, 4)

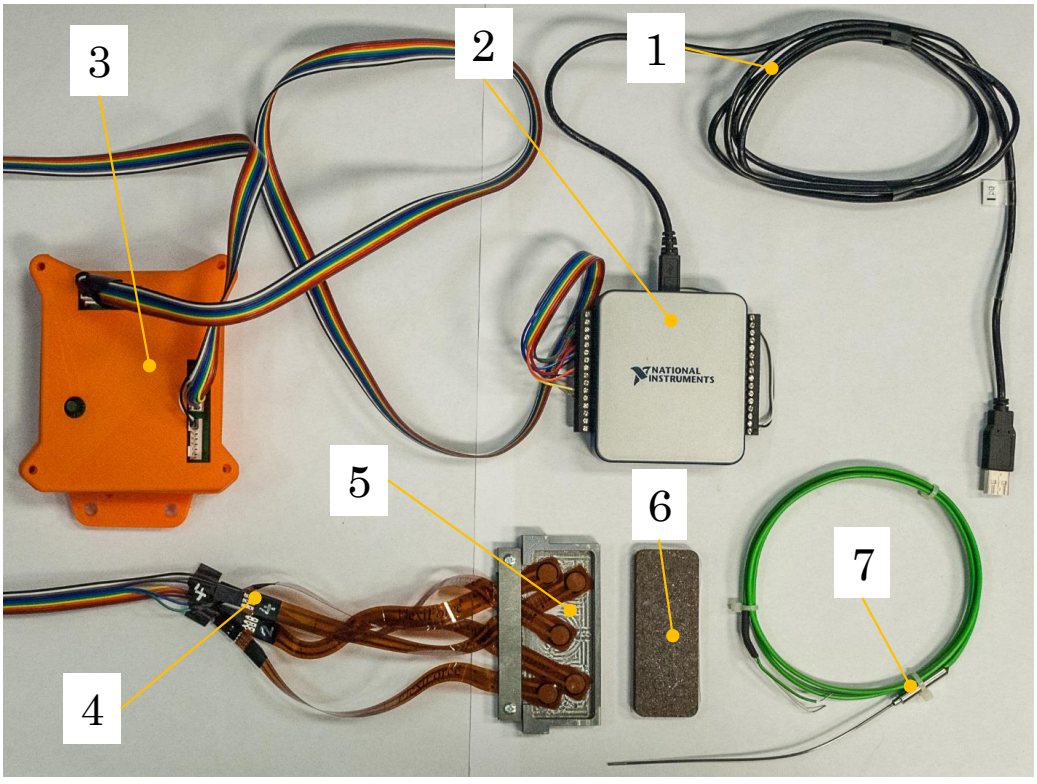

Figure 6.2: Pad sensor assembly: 1) USB cable, 2) National Instruments^{TM} USB 6003 DAQ system, 3) electronic circuit case, 4) Tekscan^{TM} HT201 force sensors, 5) backplate, 6) friction material (lining) plug, 7) thermocouple.

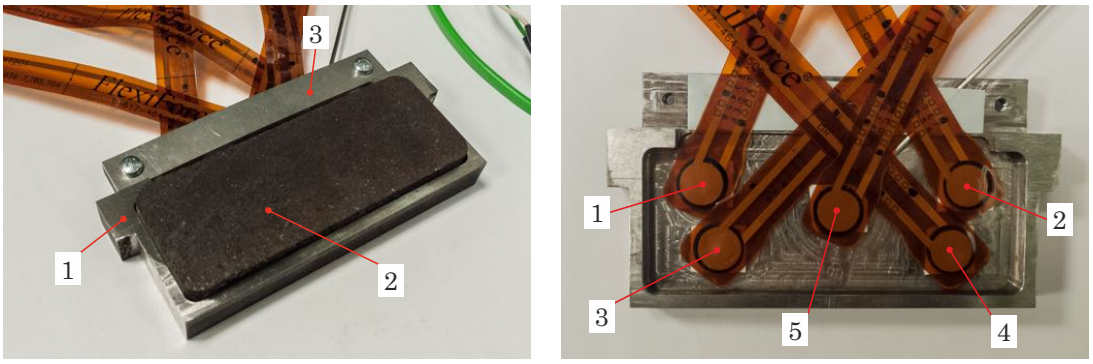

(a) (b)

Figure 6.3: Brake pad embedded sensor: a) 1 - backplate, 2 - friction material (lining) plug, 3 - sensor holder, b) positions of the force sensors: 1 - sensor 1, 2 - sensor 2, 3 - sensor 3, 4 - sensor 4, 5 - sensor 5.

Tekscan^{TM} HT201 force sensors, 5) backplate with a recess, 6) friction material (lining) plug, 7) thermocouple.

A realistic view of the assembled pad sensor is shown in Figure 6.3(a), including main components such as the recessed backplate, the friction material plug and the sensor holder. It is assumed that the backplate is stiffer than a conventional brake pad due to protruding rim existing around the backplate to embed the plug, which cannot be avoided. The plug is fabricated from a block of friction material (Figure 6.4) that yields for the friction pair with the Rover disc an average friction coefficient of 0.56. The thickness of the friction material is limited to 8 mm due to the maximum cutting capacity of the Synova® MCS 300 laser cutter. With the friction plug removed, the positions of the force sensors on the protrusions can be seen in Figure 6.3(b).

Figure 6.4: Fabrication of the friction material plug using a laser cutting technology.

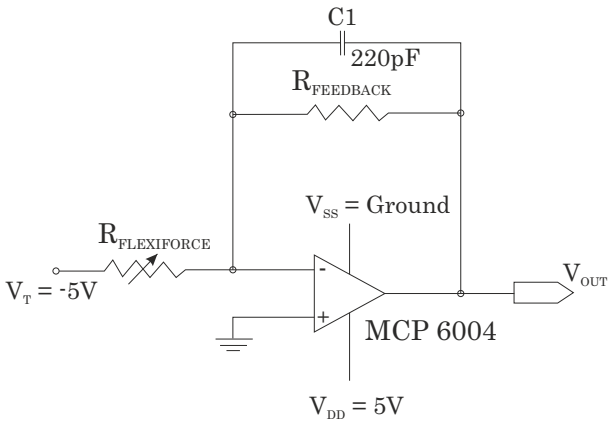

Figure 6.5: Schematic of an inverting operational amplifier (dual source) circuit (According to materials from Tekscan^{TM}).

6.4 Electronic Circuitry of Pad Sensor

Based on the desired load range and degree of linearity, Tekscan™ offers a variety of electronic circuits that can be used for their FlexiForce™ force sensors. Generally, these circuits include an operational amplifier (op-amp) to achieve a linear voltage/load output. In this work, an inverting op-amp (or also referred as a dual source) circuit recommended by Tekscan™ as shown in Figure 6.5 was used. Although this circuit is more complex (requires two power sources with opposite voltages), it provides the most versatility in terms of force range adjustment and also a good linearity. Figure 6.7 shows a single channel circuit that was first assembled to test the functionality of the FlexiForce™ HT201 force sensors. This circuit consists of a prototype solderless

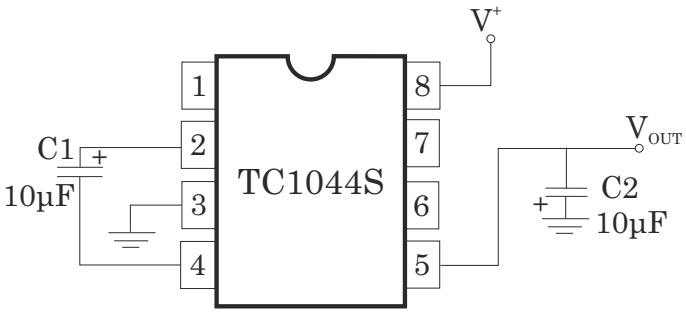

Figure 6.6: Schematic illustrating realisation of inverted voltage using a TC1044S microchip.

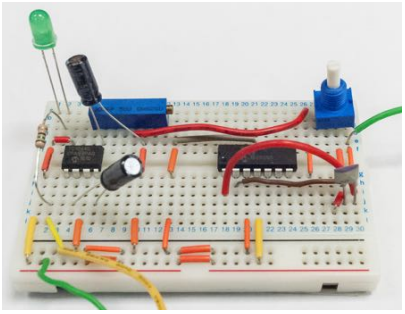

Figure 6.7: First prototype circuitry developed for the force sensor.

breadboard allowing quick connecting of the components with jumping wires. The whole circuitry is powered by 5 V output of the USB 6003 DAQ system. The output voltage was analysed in LabVIEW showing a stable waveform pattern and resulting in an average value of 5.01 V, which is well within acceptable limits for this application. The inverted voltage (-5 V) at the sensor input was realised using a TC1044S microchip (see Figure 6.6) that can convert an input in the range of 1.5 - 12 V to a corresponding negative voltage output.

After successul testing of the prototype circuit, an eight channel system was developed using EAGLE commercial software as shown in Figure D-2 in Appendix D. The circuit contains 2x MPC6004 microchips, 1x TC1044S microchip, 9x Bourns 3310Y series potentiometers, 8x 220 pF capacitors, 2x 10 μF capacitors, 1x light diode, 1x 150 Ω resistor, 1x 10-way Molex KK 6401 Series connector, and 2x 8-way Molex KK 6401 Series connectors. From the schematic, EAGLE enables the user to generate a layout of a printed circuit board (PCB) as can be seen in Figure D-1. It is a double-sided PCB design, allowing the wires to be routed on both sides of the board. A glass-reinforced epoxy laminate material FP-4 was chosen as an isolation substrate between the copper layers. The PCB was fabricated at UoL premises.

The complete pad sensor electronics was mounted in a housing (1) as shown in Figure 6.8. Its shape was designed in SOLIDWORKS® and printed using a 3D printer. The housing allows for mounting the electronics on the rig as well as preventing access to the

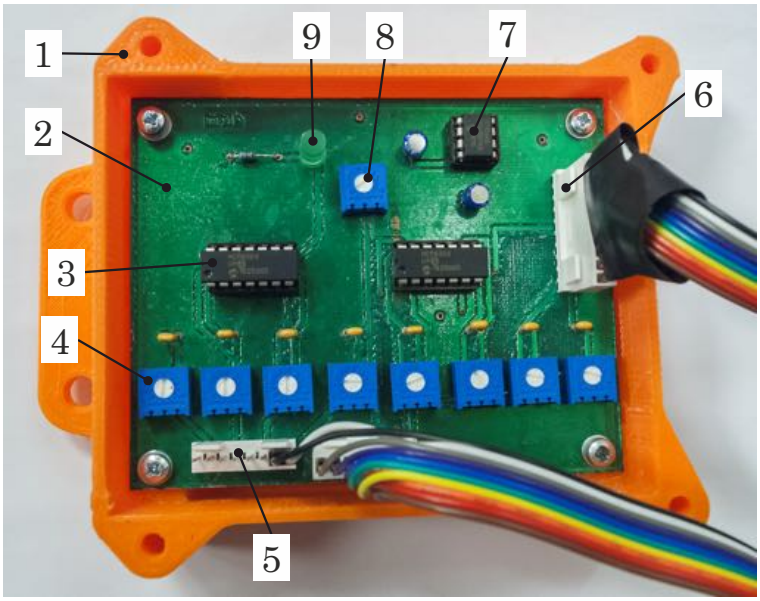

Figure 6.8: Electronics of the pad sensor: 1) case, 2) PCB, 3) MPC6004 microchip, 4) Bourns 3310Y series potentiometer, 5) sensor input connector, 6) signal output connector, 7) TC1044S microchip, 8) Bourns 3310Y series potentiometer, 9) light diode.

adjustable electronic components. All electronic parts were soldered to the PCB, except for the more expensive microchips used for mounting corresponding Integrated Circuit (IC) sockets. Each sensor range can be adjusted using one of eight variable potentiometers. The magnitude of the negative reference voltage V_T (see the schematic in Figure 6.5 for reference) for all eight channels can be adjusted by means of a variable potentiometer. This allows the system to monitor a wide range of forces.

6.5 Calibration

6.5.1 Force Sensor

The working principle of the piezoresistive force sensor is based on the fact that with increasing load the conductance of the sensor increases. Since each sensor output can be a function of many variables, including interface materials, Tekscan™ recommends that each sensor is individually calibrated. The calibration setup is shown in Figure 6.9. An Instron® testing system was used, allowing the application of compressive forces up to 5 kN when a smaller sensor cell is installed. This system can be controlled using the Bluehill® software where a calibration routine can be programmed. A second computer was used to provide logging of the sensor data. Figure 6.10 shows a detail of the calibration setup. The calibration forces are applied to the sensor by a small puck adapter to limit the force application only to the loading area of the sensor.

To facilitate the calibration procedure for all five sensors, a program routine (3) was developed in MATLAB® as can be seen in Figure 6.9. This program records data during the calibration procedure and calculates the coefficients of fitting curves. Despite the use

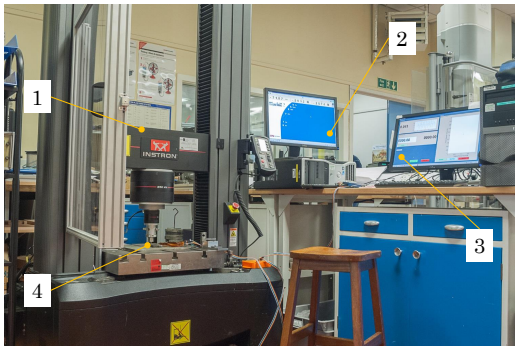

Figure 6.9: Overview of the calibration setup: 1) Instron testing system, 2) Bluehill software, 3) MATLAB program to log and process the sensor data, 4) pad sensor.

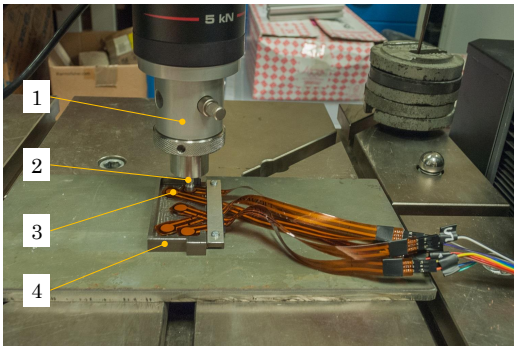

Figure 6.10: Detail of the calibration setup: 1) 5 kN load cell with an adaptor, 2) puck to concentrate force over the sensing area, 3) force sensor, 4) backplate.

of recommended electronic circuitry for sensors, the calibration curve in the load range up to 1 kN exhibits a relatively significant degree of nonlinearity as shown in Figure 6.11(a). Comparison of different regression methods shows that a nonlinear fit better represents

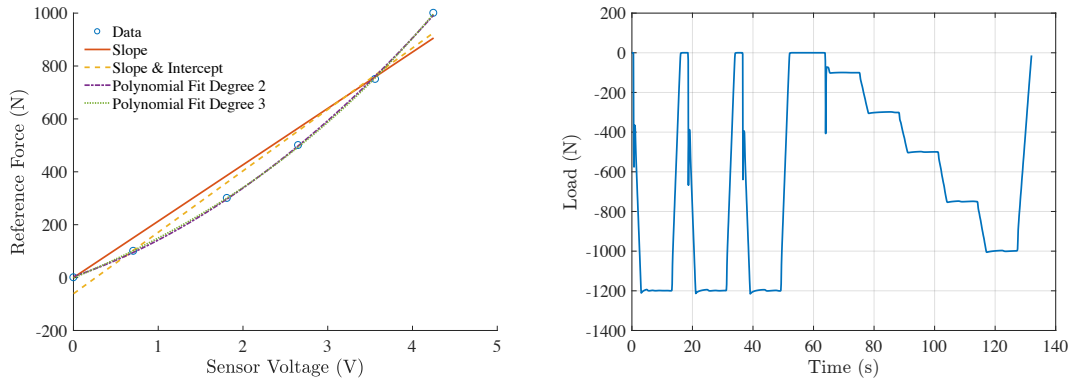

(a) (b)

Figure 6.11: Calibration of the force sensors: a) comparison of linear and nonlinear regression methods in the loading range 0 to 1 kN: linear, linear with intercept, polynomial fit of degree 2, and polynomial fit of degree 3, b) automated routine of the applied compressive force.

the voltage/force dependency. Therefore, to ensure a good accuracy in the load range up to 1 kN, the polynomial fit of degree 3 was employed. The reference voltage V_T was set to -41 mV. The calibration fitting curves and their parameters for sensors 1 to 5 are shown in Figures D-3(a) - D-3(e), respectively.

The calibration procedure was adopted from the recommended practice defined by Tekscan™. Two measurement points at 30% and 75% of maximum load were added to allow a better approximation of the nonlinear fit. Figure 6.11(b) shows a timeline of the whole calibration process that was programmed using the Bluehill® software. The

sequence is described in Section D.1.

To examine hysteresis of the force sensor, the load is increasingly applied to 1 kN and back to 0 kN as shown in Figure 6.12.

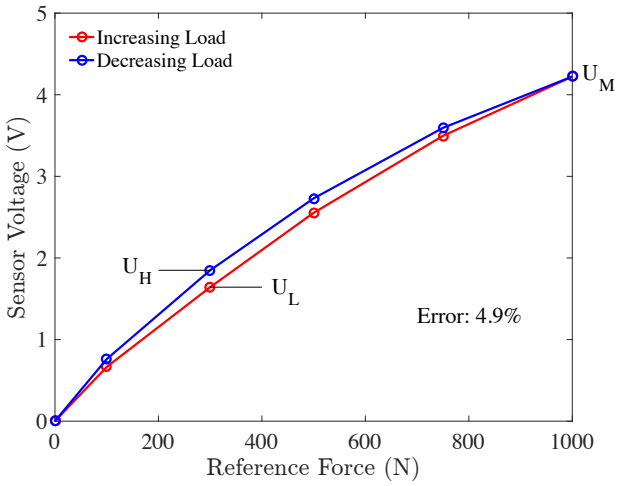

Figure 6.12: Plot showing a hysteresis property of the force sensor. The evaluated maximum hysteresis error is 4.9%.

where the sensor voltages U_H and U_L were collected when the $U_H - U_L$ was maximal. U_M represents the voltage of the maximum load. Evaluation of the maximum hysteresis error using Eq. 6.2 yields 4.9%, which correlates well with the error of 4.2% determined by (Matute et al., 2017) for this family of force sensors. The hysteresis error can be significant for dynamic loading.

Another important parameter of the force sensors is the drift error that can be defined as a relative increase or decrease of the output voltage signal for a constant load during a specific time period and can be calculated as following:

$$DE = 100\% \times \frac{U_F - U_I}{U_I} \tag{6.1}$$

where U_I and U_F represent the initial and final voltage during a specific time period, respectively.

The drift error was evaluated by applying 1 kN to the force sensor for a duration of 20 min while monitoring the output voltage as shown in Figure 6.13. The hysteresis error can be calculated as follows:

$$HE = 100\% \times \frac{U_H - U_L}{U_M} \tag{6.2}$$

The resulted error is 4.2%, which is similar to the value of 4.3% calculated by (Matute et al., 2017). Since both static and dynamic loading is present during CoP measurements, the hysteresis as well as the drift error contribute to a lower measurement quality.

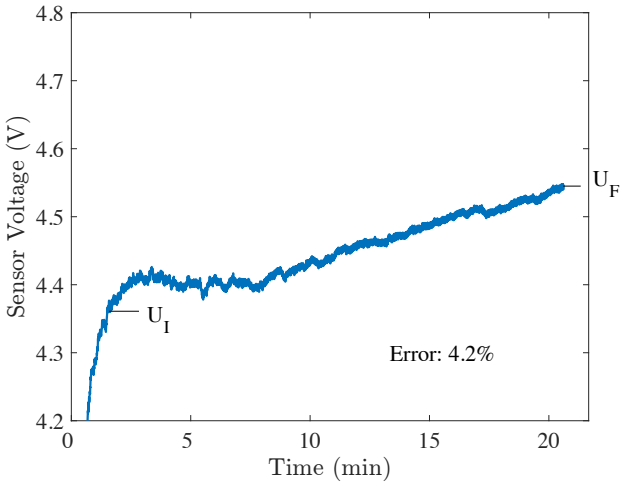

Figure 6.13: Plot showing a drift error of the force sensor for a constant load of 1 kN. The load was applied in duration of 20 min. The resulting drift error is 4.2%.

6.5.2 Thermocouple

In order to monitor temperature in the sensor area between the plug and the backplate, the sensor is equipped with a thermocouple positioned in a groove of the backplate with its tip reaching the centre protrusion of the sensor 5. The output from the thermocouple is connected to the T4 input port of the signal amplifier, thereby replacing the T4 sliding thermocouple. The thermocouple is of the K type (stainless steel probe) and can be used in the range of temperatures -100 up to 1100°C. It was calibrated using the same procedure as for sliding thermocouples explained in Chapter 4. The resulted calibration curve is plotted in Figure D-3(f).

6.6 Pad Sensor DAQ

To monitor and log the pad sensor data, a LabVIEW program shown in Figure 6.14 was developed and included in the main test program as described in Chapter 4. The program uses the nonlinear fit coefficients from the calibration described above to convert the output voltage from each sensor to a corresponding force value. From the force values and predefined positions of the sensors, the CoP position can be calculated using the static force equilibrium condition. To compare the CoP position determined using the pad sensor with the CoP position calculated by means of the 3D analytical model, this model originally programmed for the MATLAB® was translated to the LabVIEW graphical language and implemented in the pad sensor logging program.

6.6.1 CoP Position Calculation

Static force equilibrium equations (Eqs. 6.3 - 6.4) can be employed to calculate the coordinates of the point of action y_{Res} and z_{Res} of the resultant force when individual force values F_i and their coordinates y_i, z_i are known. The number of forces is represented

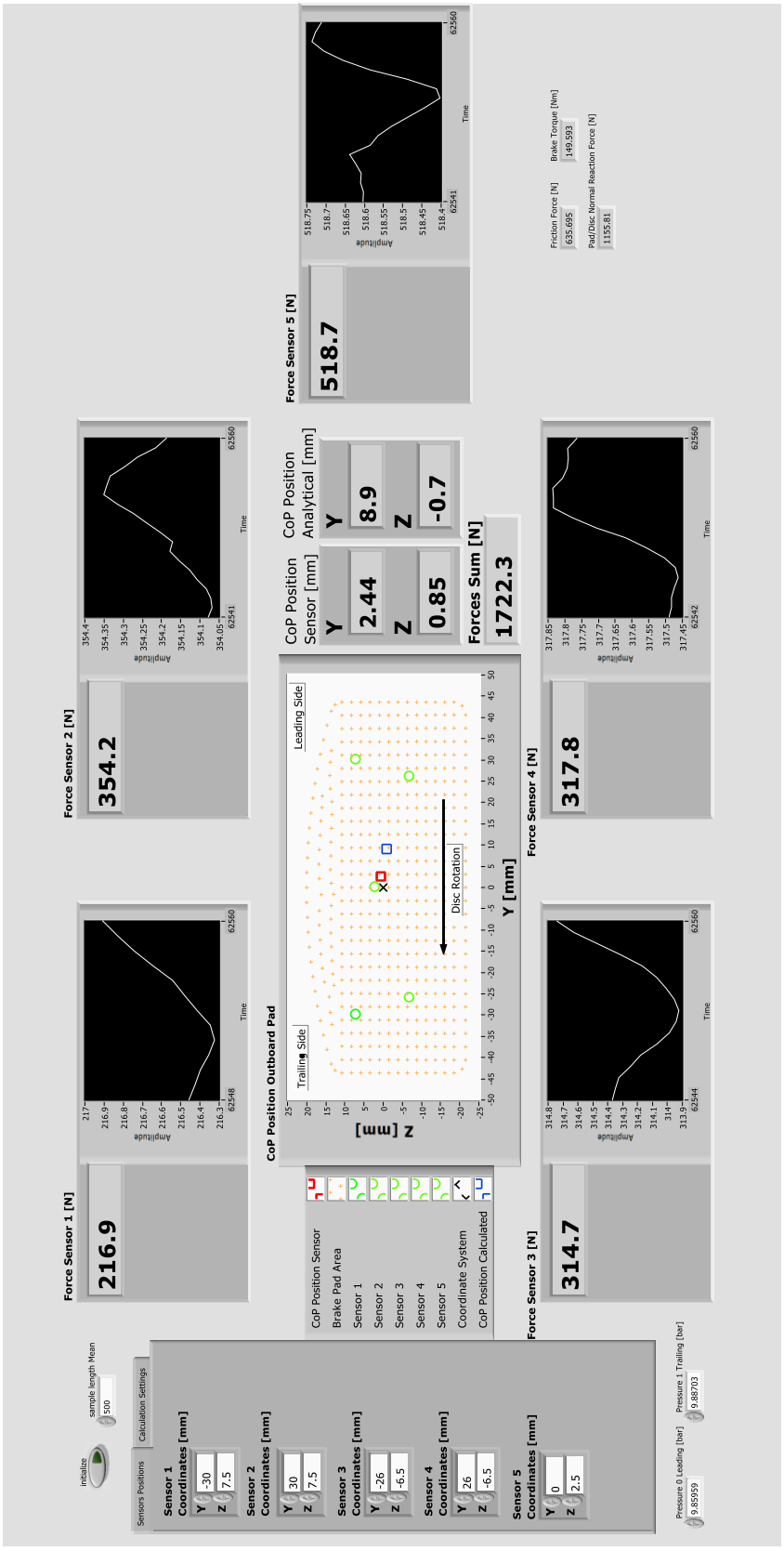

Figure 6.14: LabView program to display and log the pad sensor data.

by n.

$$y_{Res} = \frac{\sum_{i=1}^{n} F_i \times y_i}{\sum_{i=1}^{n} F_i} \tag{6.3}$$

$$z_{Res} = \frac{\sum_{i=1}^{n} F_i \times z_i}{\sum_{i=1}^{n} F_i} \tag{6.4}$$

This calculation is provided online in the LabVIEW program and allows the user to monitor the current CoP positions (see Figure 6.14).

The position error (Eq. 5.32) of the CoP predictions was evaluated for a predefined pattern of test positions (Figure 6.15). These form a 3x9 pattern of circles with 5.5 mm

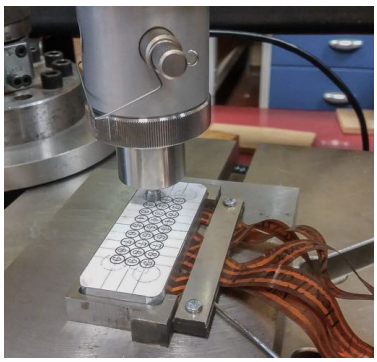

Figure 6.15: Procedure to test the predefined load positions.

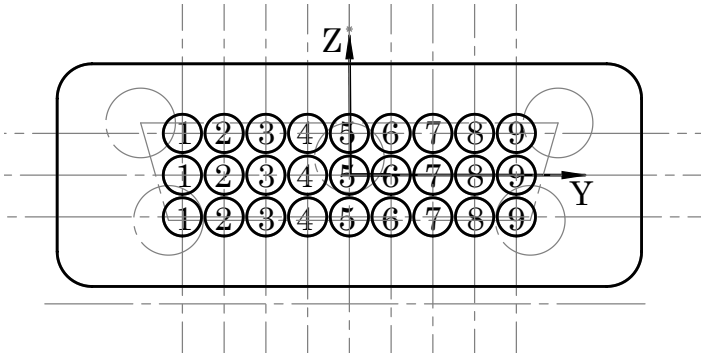

Figure 6.16: Illustration of a predefined pattern for testing load positions.

diameter to fit the size of a puck applying the force (Figure 6.16). The pattern was printed on sticking paper and attached to a dummy friction material plug made of stainless steel. This plug allows the application of larger forces than the original friction material would be able to withstand. To demonstrate the position dependancy on the applied force, two different loads 0.5 and 1 kN were tested.

Table 6.2 summarises results from the testing procedure, showing the positions of the test points pattern in the top rows as well as the calculated positions and relative and absolute position errors for both applied loads in the remaining part of the table. The relative errors larger than 2 % are highlighted, which helps to indicate areas of greater position discrepancy. This is located between the sensors 1 and 2, which may suggest that these sensors have larger calibration error. It can be also noticed that the relative errors are slightly larger for 0.5 kN, yielding the maximum value of 2.4 %, whereas for 1 kN the maximum error is 2.2 %.

6.6.2 Temperature Dependancy

Raising the temperature of the force sensors increases the force value determined by the sensor. This behaviour is demonstrated in Figure 6.17 where the total force indicated by the pad sensor, as well as the sensor temperature are plotted when increasing the disc temperature between 70 - 200°C over a time period of 10 minutes. Since all force sensors depend on the temperature with similar rate, this should not significantly influence the

Table 6.2: Measured positions and absolute (Eq. 5.32) and relative position errors (Eq. 5.33) for the test matrix given in Figure 6.16, and two applied forces 0.5 and 1 kN. For calculation of the relative position error, $r_e = 118$ mm was used. The highlighted cells represent errors larger than 2 %.

		Row		Column 1	2	3	4	5	6	7	8	9
	Test Points (mm)	1	Y	-24	-18	-12	-6	0	6	12	18	24
			Z	6	6	6	6	6	6	6	6	6
		2	Y	-24	-18	-12	-6	0	6	12	18	24
			Z	0	0	0	0	0	0	0	0	0
		3	Y	-24	-18	-12	-6	0	6	12	18	24
			Z	-6	-6	-6	-6	-6	-6	-6	-6	-6
0.5 kN	Measurement (mm)	1	Y	-21.7	-16.0	-10.5	-4.3	1.9	7.4	13.2	18.4	24.0
			Z	4.3	4.1	3.9	4.1	4.0	4.1	4.1	4.1	4.1
		2	Y	-21.6	-16.6	-11.3	-6.0	0.1	5.8	11.9	18.4	23.7
			Z	-1.3	-1.4	-1.2	-1.3	-0.8	-0.8	-1.2	-1.5	-1.3
		3	Y	-22.1	-17.5	-12.5	-6.0	-0.4	5.7	12.1	19.0	24.1
			Z	-5.8	-5.9	-5.9	-5.7	-5.7	-5.7	-6.0	-6.0	-6.1
	Abs. Error (mm)	1		2.9	2.8	2.6	2.5	2.8	2.4	2.2	1.9	1.9
		2		2.7	2.0	1.4	1.3	0.8	0.8	1.2	1.6	1.3
		3		1.9	0.5	0.5	0.3	0.5	0.4	0.1	1.0	0.1
	Rel. Error (%)	1		2.4	2.3	2.2	2.2	2.3	2.0	1.9	1.6	1.6
		2		2.3	1.7	1.2	1.1	0.7	0.7	1.0	1.3	1.1
		3		1.6	0.4	0.4	0.3	0.4	0.4	0.1	0.8	0.1
1 kN	Measurement (mm)	1	Y	-22.6	-17.2	-11.4	-4.6	1.7	7.9	13.6	19.3	24.7
			Z	4.6	4.4	4.1	4.3	4.2	4.3	4.2	4.2	4.3
		2	Y	-21.6	-16.7	-11.6	-5.9	0.2	6.7	13.0	19.3	24.2
			Z	-1.0	-1.3	-1.0	-1.1	-0.6	-0.6	-1.0	-1.4	-1.4
		3	Y	-22.6	-18.2	-12.8	-6.0	0.6	7.3	13.8	20.5	24.5
			Z	-5.7	-5.7	-5.8	-5.4	-5.6	-5.6	-5.9	-6.1	-6.0
	Abs. Error (mm)	1		2.0	1.8	2.0	2.2	2.5	2.5	2.4	2.2	1.8
		2		2.6	1.8	1.1	1.1	0.6	0.9	1.4	1.9	1.4
		3		1.4	0.4	0.8	0.6	0.7	1.4	1.8	2.5	0.5
	Rel. Error (%)	1		1.7	1.5	1.7	1.9	2.1	2.2	2.0	1.9	1.6
		2		2.2	1.6	0.9	0.9	0.5	0.8	1.2	1.6	1.2
		3		1.2	0.3	0.7	0.5	0.6	1.2	1.5	2.1	0.4

CoP position, however the temperature dependancy should be considered when evaluating the total force.

6.7 Pad Sensor Tests

Figures 6.18(a) - 6.18(b) show the implementation of the pad sensor in the new caliper. Using this setup, a simple drag braking procedure was performed to demonstrate the functionality of the pad sensor. The pad sensor was tested for a range of leading/trailing pressure ratios (LTPR) between 1/9 and 9, two different speeds 30 and 100 rpm, two different braking torques 75 and 150 Nm and for both inboard and outboard positions.

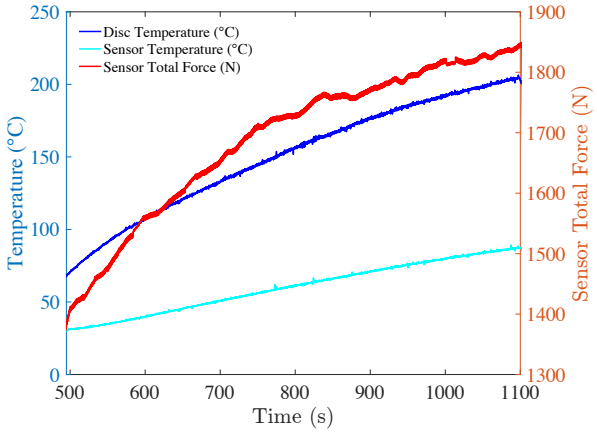

Figure 6.17: Dependency of the total force value on sensor temperature.

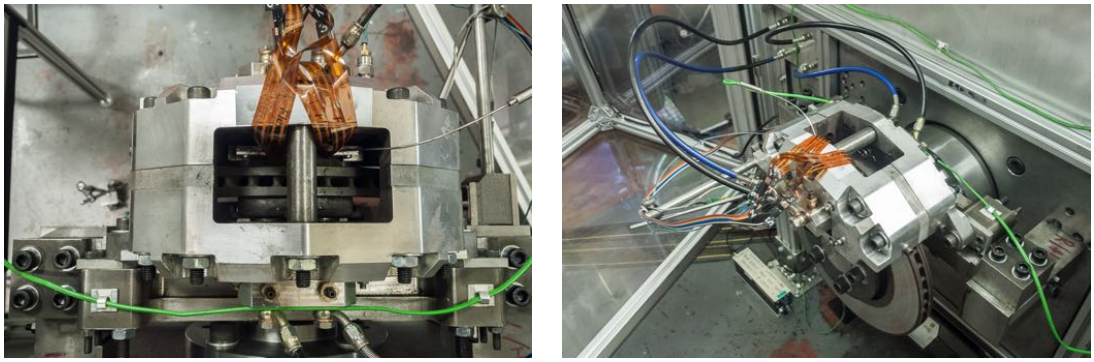

(a) (b)

Figure 6.18: Brake pad embedded sensor installed on the caliper: a) top view, b) side view.

Table 6.3 shows the particular piston pressure settings for each LTPR. The measured temperatures of the disc surface and pad sensor inner area for each test are listed in Table 6.4. During data logging the temperature of the disc surface is maintained in a thermal equilibrium state.

The CoP positions for all tests measured by the pad sensor are displayed in Figures 6.19(a) - 6.19(b). It can be seen that by increasing LTPR, the general trend of the monitored CoP position is movement, as expecting, towards the leading side, and slightly radially inward. The latter is not very intuitive, but a similar trend was also predicted

Table 6.3: Piston pressure values used for 75 and 150 Nm brake torque and for a variety of LTPR values.

LTPR			1/9	1/4	1/3	1/2	1	2	3	4	9
Piston Pressure (bar)	80 Nm Brake Torque	Lead.	1	2	2.5	3.3	5	6.7	7.5	8	9
		Trail.	9	8	7.5	6.7	5	3.3	2.5	2	1
	140 Nm Brake Torque	Lead.	2	4	5	6.7	10	13.3	15	16	18
		Trail.	18	16	15	13.3	10	6.7	5	4	2

Table 6.4: Test conditions for comparison of CoP predictions determined from the analytical model and brake pad sensor.

		Inboard				Outboard			
Brake Torque (Nm)		75		150		75		150	
Disc Speed (rpm)		30	100	30	100	30	100	30	100
Average Temperature (°C)	Disc Surface	70	125	97.5	217.5	70	125	100	212.5
	Pad Sensor	40	72	63.5	121	46	82	67	140

by the FE and analytical model in Chapter 5.

6.8 Comparison with 3D Analytical Model

The monitored CoP data shown in Figures 6.19(a) - 6.19(b) were used to validate the 3D analytical model of the pad/disc interface presented in Chapter 5. For a given range of LTPRs, the CoP positions were evaluated by the model and the results were added to the plots (black line). Since the 3D analytical model does not differentiate between the inboard/outboard side and is not dependent on the absolute pressure values or speed of the disc, the average of the positions determined by the pad sensor for a given LTPR was calculated and used as a reference to determine the relative error of the model (given in brackets). It can be seen that all errors are $< 10\,\%$ with maximum error of $9.2\,\%$ for LTPR = 9 in circumferential direction. Generally, the larger errors were calculated when LTPR >1, which indicates that the model seems to be less accurate for these LTPRs due to a possible missing reaction force at the leading abutment. A similar trend was observed when the analytical model was compared with the FE model in Chapter 5. Generally, the pad sensor circumferential inboard CoP positions better correlated with the analytical model than the outboard positions. This can be due to a higher rigidity of the brake assembly closer to the caliper mounting points and higher influence of disc and caliper deformations on the CoP positions at the outboard position.

The differences of the CoP positions between the analytical model and pad sensor can be explained by the relative simplicity of the analytical model that ignores flexural effects of the pad, the real surface topology of the friction material, uncertainities of the model values such as the friction coefficients, and thermal effects. On the other hand, the position difference of the pad sensor can be affected by several factors. The contact of the friction material plug with the side wall of the backplate as well as with the sensing area of the sensors may account for a certain error of the measured force value. The aforementioned hysteresis and drift error also contribute to the overall position deviation.

6.9 Discussion

The tests on the brake dynamometer showed that the new pad sensor was reacting to the changes of LTPR as predicted in the previous modelling work. To the researcher's knowledge, the concept of a brake pad sensor that features multiple ultra-thin high-

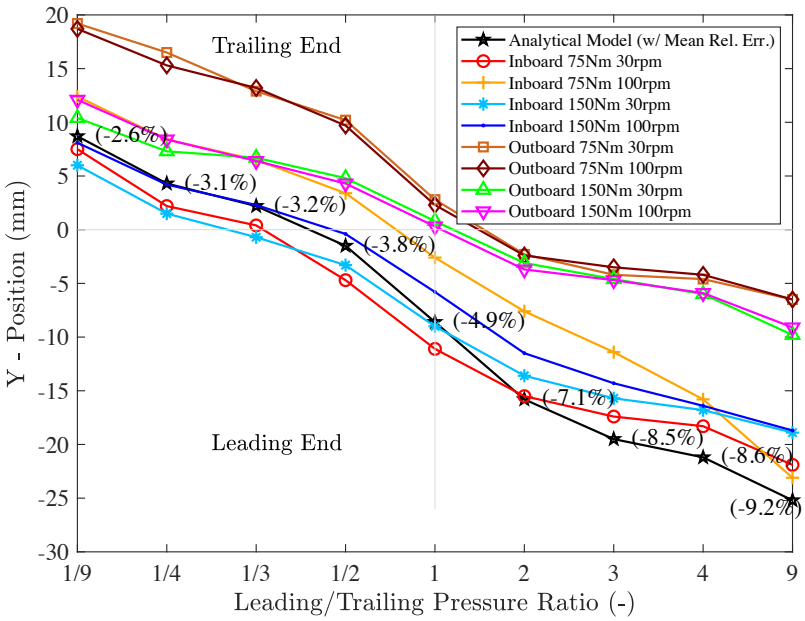

(a)

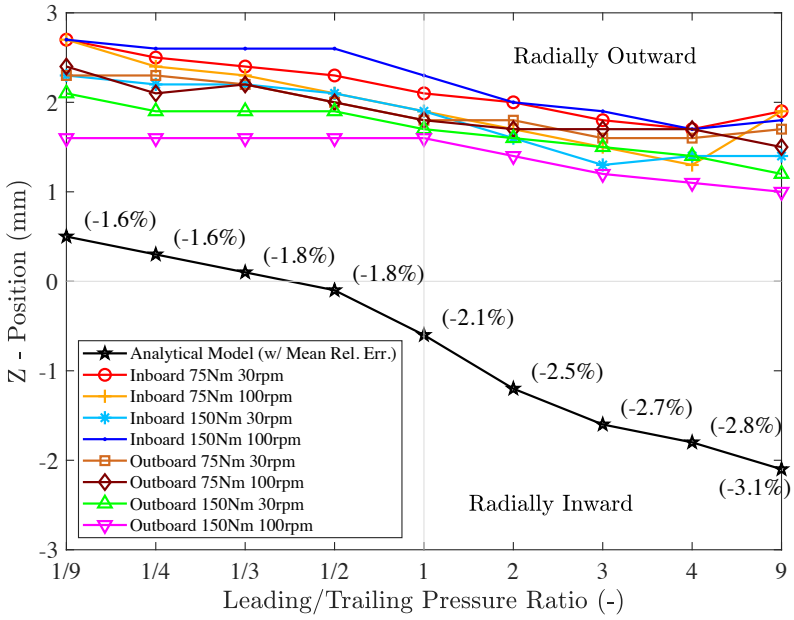

(b)

Figure 6.19: Plot of the CoP predictions determined using the pad sensor: a) Y - Position (circumferential), b) Z - Position (radial). The predictions of CoP positions determined by the 3D analytical model are added to the plot for comparison. The data in brackets represents the relative error to the mean value of all measurements for a given LTPR.

temperature FlexiForce^{TM} sensors has not been yet used in the brake community for dynamic monitoring of the CoP. This design therefore represents an alternative to other existing pad sensors reviewed in Chapter 2.

The pad lining is made of a relatively soft and brittle material, so when applying a calibration force using a small puck, the force must be limited to a certain value, e.g.

200 N, otherwise it can cause cracks in the friction material. To avoid this completely, as already mentioned above, a dummy friction material plug made of steel should be used for evaluation of the static CoP.

It was observed that during braking the existing runout of the Rover disc causes significant changes of the CoP position per one revolution of the disc. Therefore, a mean function was applied to the final CoP position value in order to stabilise its rapid oscillations.

Some improvements of the pad sensor design could be suggested, e.g. replacement of the piezoresistive force sensors for load cells that exhibit generally higher repeatability of measurement (Matute et al., 2017). The drift error could be also reduced by measuring capacitance instead of the currently measured conductance (Kim et al., 2015). This, however, leads to a more complicated circuitry (Matute et al., 2017). It is also assumed that some errors may arise from the friction contacts between the lining plug and the backplate, which cannot be fully avoided but could be potentially minimised by application of grease at the contact areas.

6.10 Summary

This chapter has presented the main work packages leading to the development of a new brake pad sensor. Starting with the overall assembly, all mechanical parts of the pad sensor have been introduced, and their design and fabrication process explained. The complex electronic circuitry of the pad sensor has been then presented, followed by the calibration procedure for the force sensors. Even if an electronic circuitry recommended by the sensor manufacturer to achieve a linear load/voltage output was used, it was shown that in the load range up to 1 kN a nonlinear fit better represents the load/voltage relation. The ability of the sensor to evaluate CoP positions was tested statically for a matrix of test points defined on the friction lining. The maximum relative position error was $< 3\,\%$.

Both hysteresis and drift are inherited properties of the piezoresistive sensors and contribute to the overall error of the measurement and were therefore evaluated. Also, the force sensor dependency on temperature was shown to be important. Increase of the sensor temperature resulted in rise of the force value given by the sensor, however it is assumed that all force sensors experience the same rise of temperature, therefore the CoP position should not be significantly influenced.

Finally, the new 3D analytical model of the pad/disc interface was validated with pad sensor measurements during experimental tests, which showed a good correlation between these approaches resulting in a maximum relative error $< 10\,\%$. The position errors were attributed to the fundamental differences of both methods, in particular it can be due to the actual mechanical design of the pad sensor, the type of piezoresistive force sensors and circuitry, as well as calibration method used. On the other hand the analytical model makes no allowance for the flexibility of the pad and surrounding parts or any temperature effects.

7 Experimental Brake Squeal Investigation

"Experience is the best teacher"
Cicero

7.1 Introduction

This chapter combines all previously described elements of work to demonstrate the performance of the new automatic squeal reduction (ASQR) system during brake dynamometer squeal tests. In the first part, a series of constant speed and constant brake torque tests for varying leading/trailing pressure ratio (LTPR) are presented to show how the squeal occurrence depends on the LTPR. This demonstrates what LTPR settings can lead to a reduction or even complete suppression of certain squeal frequencies. A conversion table between the LTPR and absolute values of the CoP demonstrates the possibility to assign a particular CoP value for each LTPR. Then, duty cycle tests provided for varying LTPR are used to indicate the squeal reduction ability for a specific LTPR during more realistic braking conditions. From these tests, a control strategy presented in Chapter 4 is developed to effectively reduce or suppress the squeal occurence.

The second part of the chapter focuses on the demonstration of the squeal reduction system. First, the effects of the LTPR variation on other parameters as well as the constant brake torque tracking ability are presented. This may show limitations of the suggested ASQR system, in particular, due to the fugitive property of squeal. By introducing squeal filtering methods certain of these limitations can be minimised. Finally, the semi-automatic and fully automatic reduction mode developed in Chapter 4 is used to demonstrate the ability of the ASQR system to suppress squeal during braking tests. The chapter concludes with discussion points that may serve as a good source of information for further development of the ASQR system.

7.2 Brake Squeal Experiments

The new brake test rig described in Chapter 3 and Chapter 4 was used to perform a series of experiments to investigate the relation between the leading/trailing pressure ratio (LTPR) and the squeal propensity. These tests paved the way to the development of the automatic squeal reduction (ASQR) system presented in Chapter 4. Because the Rover disc assembly as shown in Figure 3.13(c) most frequently and consistently exhibited a

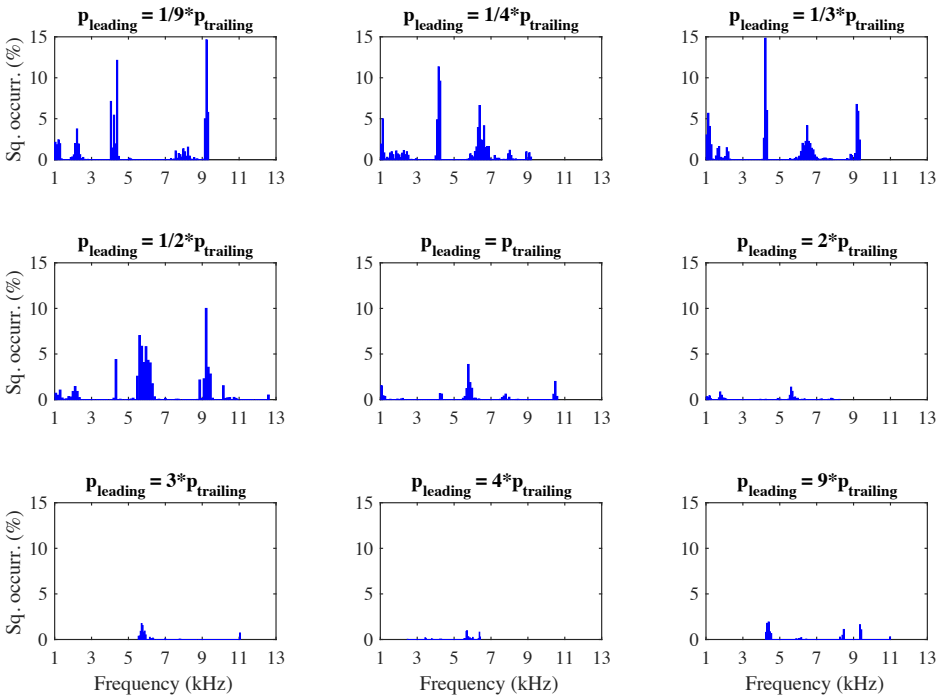

(a)

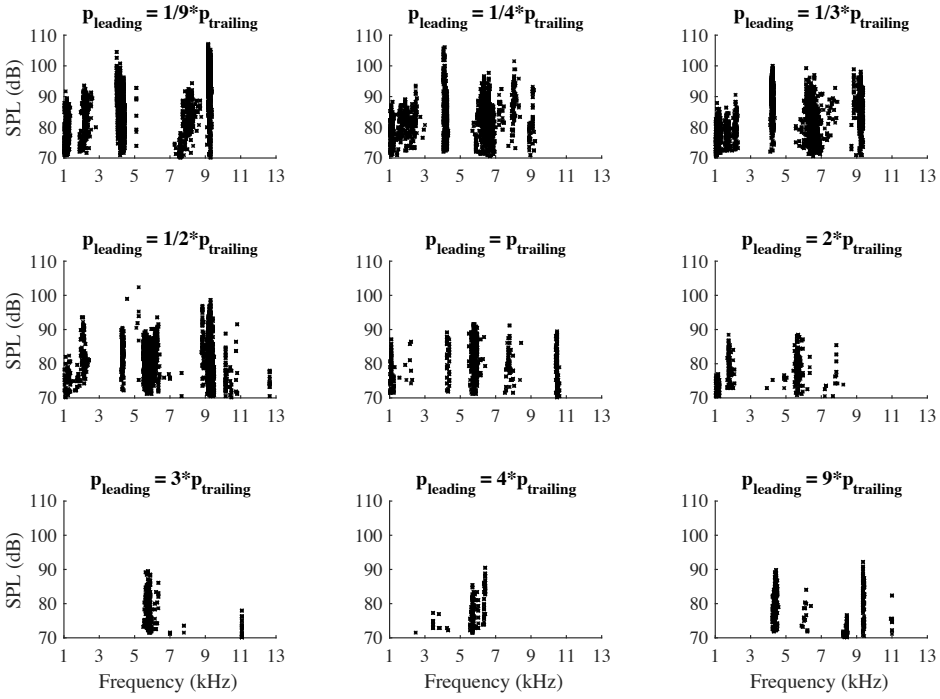

(b)

Figure 7.1: Squeal occurrences as a function of frequency (kHz) - Test 1: a) relative squeal occurrence, b) SPL - Sound Pressure Level (dB(A)).

low-frequency squeal (around 1.8 kHz) compared with the Fiat Punto disc, this assembly was used for all the subsequent experimental work.

7.2.1 Nonuniform Pressure Tests

In total, four braking procedures (Test 1, Test 2, Test 3, and Test 4) were performed to find potential minima of the squeal occurrence for specific LTPRs. For Tests 1, 2 and 4, the LTPR was set to 1/9, 1/4, 1/3, 1/2, 1, 2, 3, 4, and 9, whereas for Test 3 the order was reversed to show the possible impact of pad conditioning on the results. The disc speed was set to 30 rpm for the first three tests, whereas for the fourth test the speed was 100 rpm. Prior the tests, the disc was heated up to a surface temperature above 170°C and the squeal was monitored during the cooling down phase between 150 - 120°C. This should ensure similar thermal conditions of the disc for each test. Brake noise was monitored by a microphone, while the squeal filter was set to 900 - 13000 Hz and the minimum amplitude threshold to 70 dB(A). Figures 7.1(a) - 7.1(b) show the squeal indices of Test 1 as a relative occurrence as well as their sound pressure levels (SPL) plotted against frequency, respectively. The plots clearly mark the unstable frequencies of vibration within the spectrum and demonstrate the influence of the LTPR on the squeal occurrence. It can be observed that for LTPR $>$ 2, the squeal was less frequent. Similar plots for Tests 2, 3 and 4 are shown in Figures E-1 - E-3 in Appendix E.

The total squeal occurrence as a function of LTPR for all four tests is plotted in Figure 7.2. All four tests exhibited a similar trend despite the reversed order for Test 3. A pad conditioning due to increasing LTPR was not observed in this case. For increasing LTPR, the squeal occurrence decreases, having a global minimum for LTPR in the range

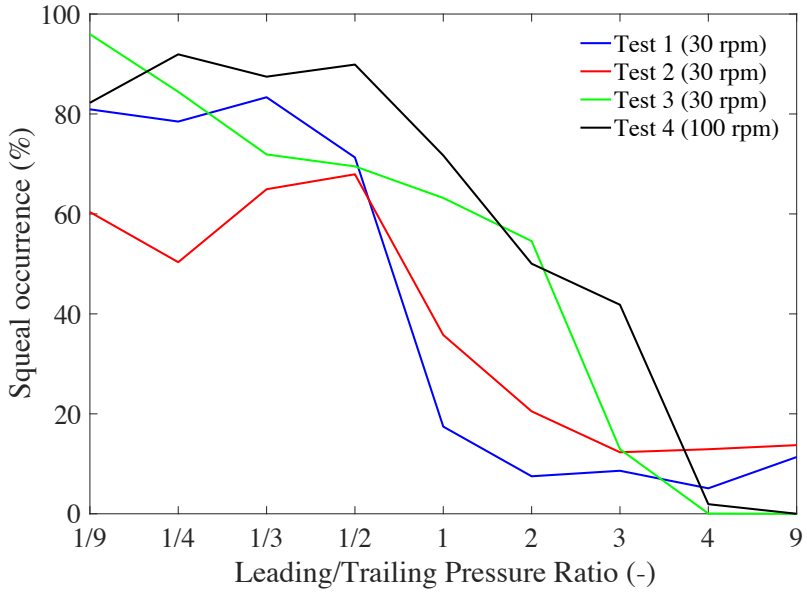

Figure 7.2: Plot showing relative squeal occurrence for Test 1, 2, and 3 with the disc speed of 30 rpm and Test 4 when the disc speed was set to 100 rpm. The LTPR = 1/9, 1/4, 1/3, 1/2, 1, 2, 3, 4, and 9.

3 to 9.

As described in Chapter 5, a specific CoP position can be determined for each LTPR. Table E-1 in Appendix E shows a conversion between the LTPR and CoP position for all LTPR values from 1/9 to 9 using the analytical and FE modelling techniques. The analyses were carried out for three different pad/disc friction coefficients $\mu = 0.4$, $\mu = 0.5$, and $\mu = 0.6$. Table E-1 can help to identify quiet areas of pad where a specific LTPR reduced squeal.

7.2.2 Nonuniform Pressure Tests - Test Cycle

In these experiments, the drag braking procedure from the SAE J2521 standard was modified to meet the UoL brake dynamometer torque limitation. The original maximum brake pressure ramp value 30 bar was lowered to 22.5 bar as shown in Figure 7.3. The disc speeds of 30 and 100 rpm correspond to vehicle velocities of 3 and 10 km/h recommended in the standard. In order to investigate squeal occurrence as a function of the LTPR variations, where LTPR = 1/4, 1/3, 1/2, 1, 2, 3, and 4, the test cycle was designed for each of the leading and trailing channels separately as shown in Figure 7.4. The pressure ramps were calculated so that the leading/trailing mean pressure at every operational point is the same for all LTPR values. This should prevent significant brake torque variation across all LTPRs and allow a direct comparison of the results. As described in the original SAE J2521, the test cycle was repeated for temperatures from 50°C up to 300°C and from 300°C down to 50°C with increments of 25°C, whereby the whole cycle lasted about 1 hour. As a system pre-heat phase, half of the whole cycle (up to 300°C) was carried out, followed by cooling period down to the first measured temperature of 50°C. The experiment was conducted twice (Test 1 and Test 2), and each experiment was performed during a single day to minimise the influence of varying environmental

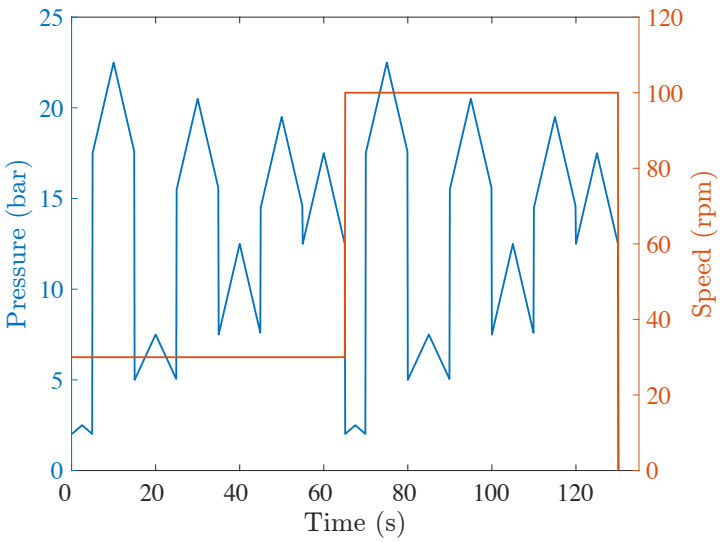

Figure 7.3: Modified SAE J2521 drag brake cycle to meet the brake dynamometer maximum torque limitation.

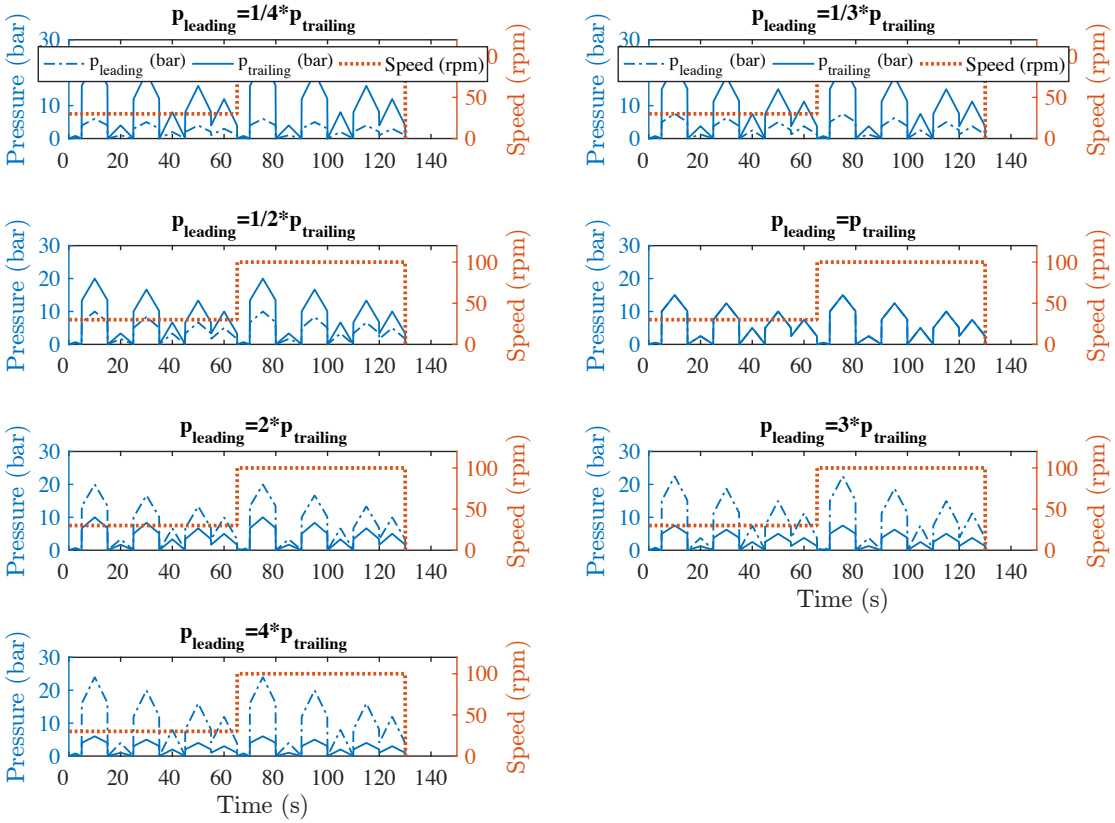

Figure 7.4: Test cycles to investigate the squeal occurrence for LTPR = 1/4, 1/3, 1/2, 1, 2, 3, and 4.

conditions on results. Moreover, Test 1 was performed for increasing LTPRs from 1/4 to 4, whereas Test 2 was performed for decreasing LTPRs to study the effects of pad conditioning on the results.

Figures 7.5(a) - 7.5(b) show histograms of total squeal occurrence as a percentage of total test time plotted against frequency spectrum at each LTPR for Tests 1 and 2, respectively. It is clear that the LTPR influences the occurrence of specific frequencies, e.g. a low-frequency squeal event of about 1.8 kHz was almost completely eliminated for LTPR = 1/4 and significantly minimised for LTPR = 1/3 and 4. It was also shown that some squeal frequencies remain present even if the LTPR was varied, such as the broad band of squeal frequencies around 8 kHz. The results imply a good potential to suppress certain squeal frequencies if an appropriate LTPR as well as suitable noise filtering algorithms are used.

Figure 7.6 depicts the total squeal time in minutes plotted against LTPR for both tests (Test 1 and 2). Although there are small differences in results for the two tests, a general trend can be observed, such as the maximum squeal time occured in the range of LTPR from 1/3 to 1/2. These curves also demonstrate that the brake tends to be quieter when LTPR $>$ 2, which is in accordance with experiments found in the literature indicating that, besides a trailing offset, a relatively large leading CoP offset tends to produce a stable brake.

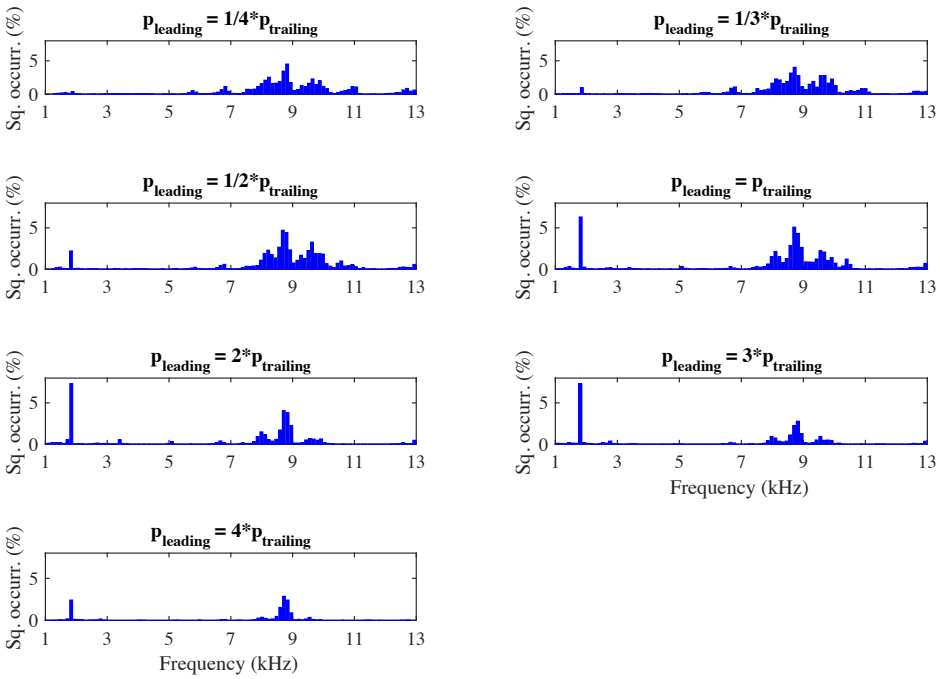

(a)

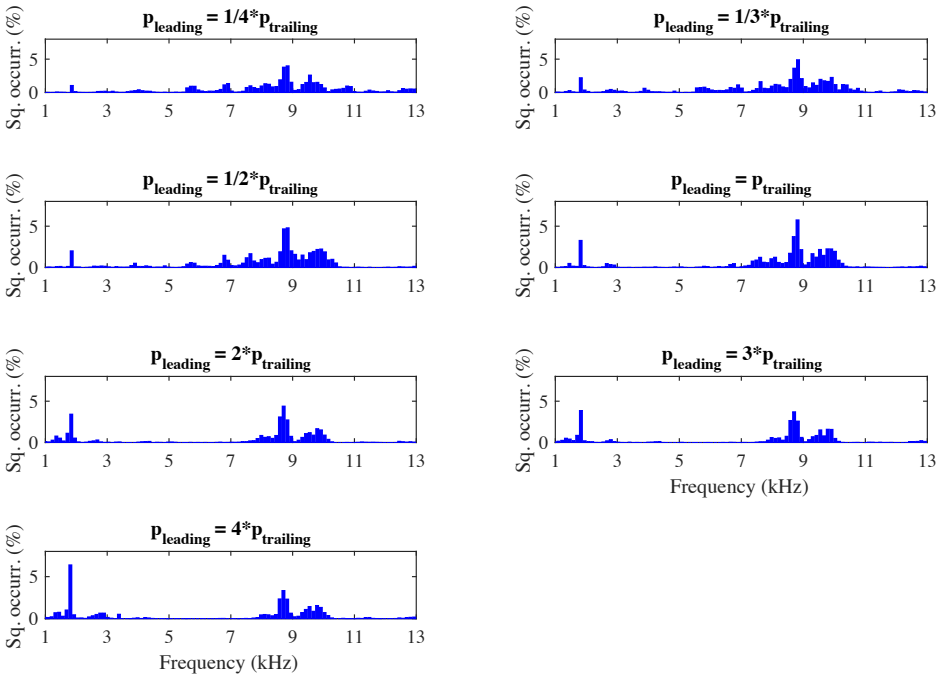

(b)

Figure 7.5: Squeal occurrences as percentage of test time plotted against frequency (kHz) for a modified SAE J2521 drag brake procdure: a) Test 1, b) Test 2.

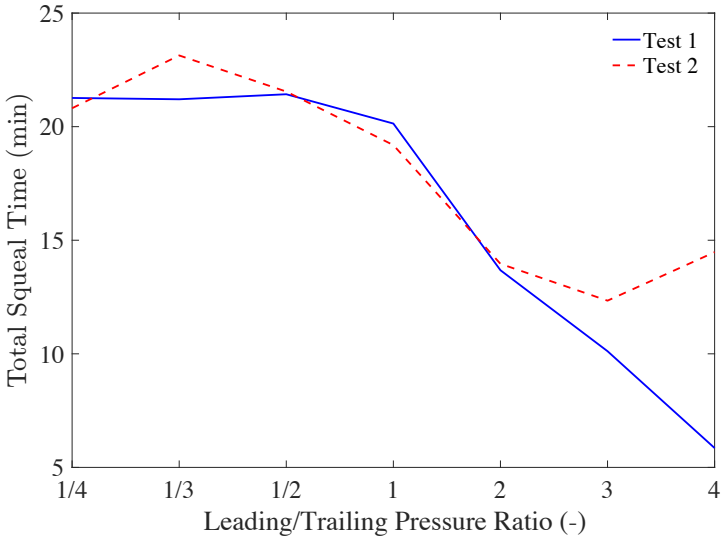

Figure 7.6: Total squeal time [min] vs. leading/trailing pressure ratio (LTPR) for Tests 1 and 2.

7.2.3 LTPR Variation

Figure 7.7 shows an example of how the squeal frequencies were influenced during a slow variation of the LTPR and continuous control of the brake torque. First a squeal noise at about 12.8 kHz emerges, which gradually fades by varying LTPR, but this generates new squeal events in the range 9 to 10 kHz that are insensitive to further variation of the LTPR. This clearly shows that during LTPR change other squeal frequencies can be randomly triggered, however as described in Chapter 2, typically lower squeal frequencies (<5 kHz) are more annoying and represent burden on vehicle occupants and environment. As can be seen in Figure 7.7, by focusing on a specific squeal frequency bandwith e.g. 12 - 13 kHz or 8 - 10 kHz, a certain LTPR can be identified that can completely eliminate squeal occurrences within the frequency bandwith.

7.2.4 Automatic Squeal Suppression

The following test shows an application of the ASQR system in a semi-automatic mode, i.e. the user activates the action of automatic squeal reduction. As an example, Figure 7.8 depicts an intermittent squeal occurrence of 1.8 kHz that was found for a specific LTPR (in this case LTPR $<$ 1) represented by the blue line (leading pressure) and the red line (trailing pressure), respectively. The green line indicates activation of the ASQR mode. In this mode the very first squeal occurrence triggers alteration of the LTPR causing the squeal to disappear. It can be observed that after the automatic mode was deactivated and the initial LTPR was recreated in manual mode, the squeal appeared again.

In order to demonstrate the functionality of the squeal reduction system during a duty cycle, a simple test schedule containing brake torque ramps of 75, 150, 125 and 100 Nm was designed as shown in Figure 7.9. Overall, the cycle was repeated for temperatures

from 75°C up to 175°C and back down to 75°C, in increments of 25°C. Prior to the test, the brake disc surface was heated to 300°C and cooled down to 75°C. The brake torque, rotational speed and temperature range of the cycle were appropriately chosen to easily recreate squeal events, such as the one at 1.8 kHz.

In the following experiment the braking torque cycle was used to demonstrate the

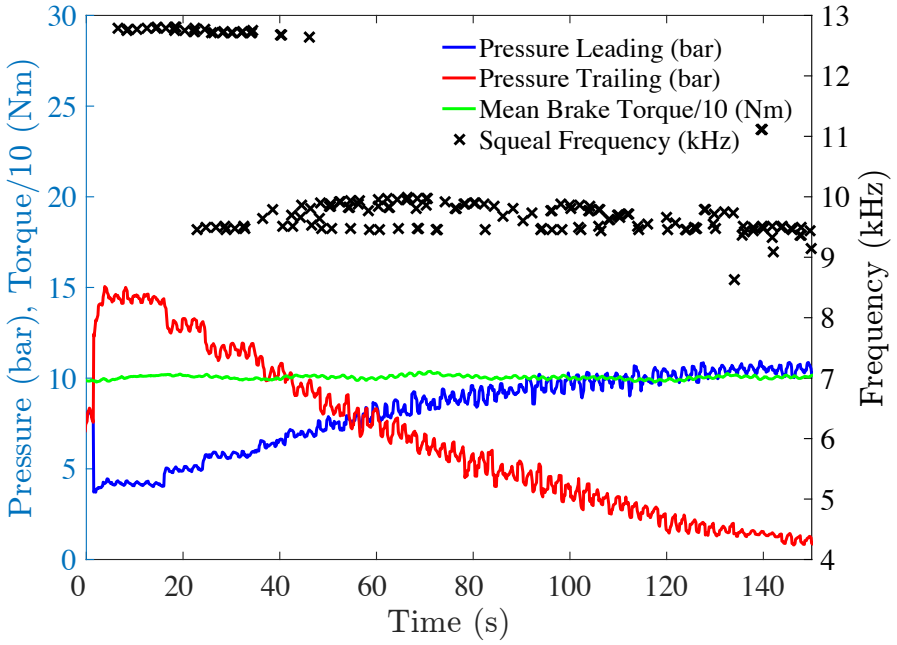

Figure 7.7: Squeal frequency occurrences (Hz) during variation of the LTPR.

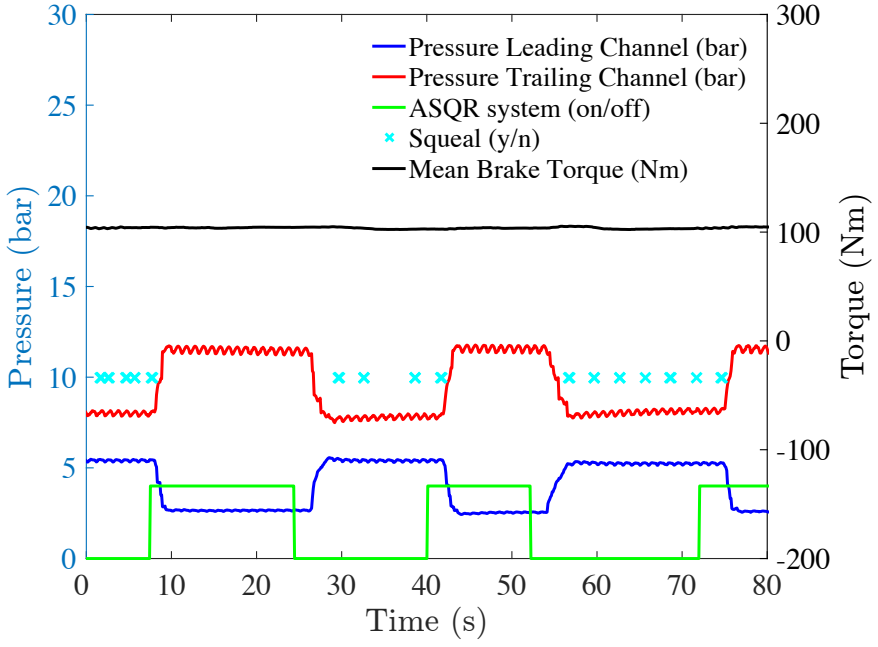

Figure 7.8: Test demonstrating ability of the ASQR to suppress squeal occurrences in a semi-automatic mode.

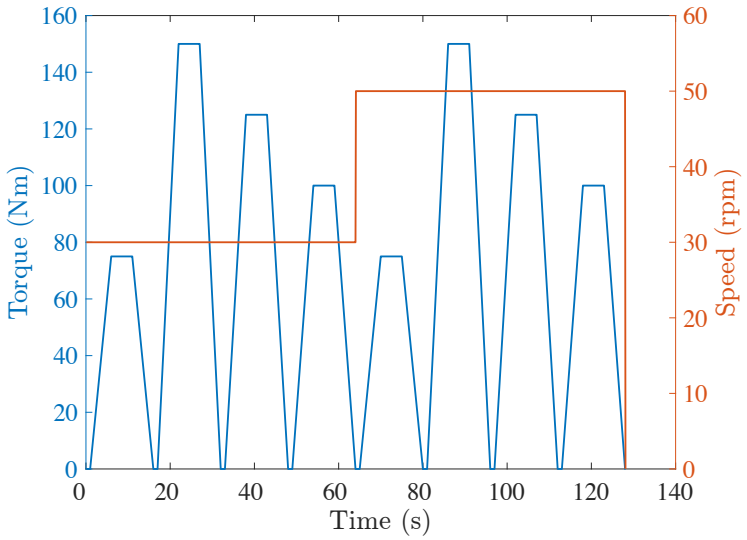

Figure 7.9: Test cycle for brake torque tracking experiments.

fully-automatic mode of the ASQR system. As explained above, certain squeal frequencies occur at every LTPR to some extent. Therefore to simplify the problem, the sound spectrum was filtered to detect only low-frequency squeals in the range 900 to 5000 Hz. Moreover, only SPL higher than 90 dB(A) was considered as a squeal occurrence. If the brake torque command equals zero, which represents a fully released brake pedal, the value of the LTPR was reset to the initial value LTPR = 1. This ensures that the next torque ramp starts with LTPR = 1, which represents the standard braking mode with equal pressure acting at all pistons.

An illustrative time sequence of squeal suppression is shown in Figure 7.10, where a squeal noise at about 1.8 kHz emerged (indicated with the black cross symbol). This was readily suppressed by changing the LTPR so that it did not occur until the end of the brake torque ramp, when the LTPR was reset again to the initial value. A comparison of squeal occurrence histograms plotted versus the frequency spectrum for a test both without (Standard Mode) and with activated ASQR (Auto Squeal Reduction Mode) is shown in Figure 7.11. The total squeal time for the standard and activated ASQR mode was 71.1 s and 26.1 s, respectively, representing a significant reduction of about 63% in favor of activated ASQR mode.

7.3 Summary

This chapter has focused on demonstrating the performance of a new automatic squeal reduction (ASQR) system. For the squeal experiments, the Rover disc setup was employed to perform a series of tests. Squeal was observed mainly for disc speeds below 100 rpm, within the temperature range 75 to 175°C, and when medium hydraulic pressure of 5 to 20 bar was applied. In order to generate squeal, it was found beneficial to first warm up the disc surface temperature above 250°C and then let it to cool down to the

squeal temperature zone.

The variation of the LTPR during constant speed and brake torque tests, as well as during duty cycles, showed what LTPR can be set to minimise or completely eliminate the squeal occurrence. Reduced squeal propensity was observed for large leading or trailing CoP offsets. However, for a large leading offset, when LTPR was in the range from 3 to 9, the squeal was minimised. This result was adopted in the control logic of the ASQR system, where the LTPR of 4 (leading) and 1/4 (trailing) were used to suppress squeal.

It was observed that by changing LTPR to suppress the more annoying low-frequency squeal, some high-frequency squeal can be randomly triggered, which would induce instability for the squeal controller. In order to provide a robust squeal control algorithm, the whole monitored frequency spectrum was band-filtered and a minimum SPL threshold was applied for squeal detection algorithm. The control algorithm can then continuously monitor squeal occurrence and provide LTPR change when squeal occurs. In the semi-automatic mode the user decides when LTPR change should happen, whereas in the fully-automatic mode the computer triggers the action once squeal is detected.

To demonstrate the ASQR mode, a new simple brake torque tracking test cycle containing four different torque ramps and two disc rotational speeds was developed. During this cycle with activated ASQR mode, the occurrence of squeal frequencies filtered in the range 900 to 5000 Hz and with amplitudes above 90 dB(A) was successfully reduced by 63%.

The current squeal control algorithm is based on simple event-based logical control, in which the LTPR alteration is triggered by a detected squeal event. This control type is considered as appropriate for the currently easily generated intermittent squeal, which

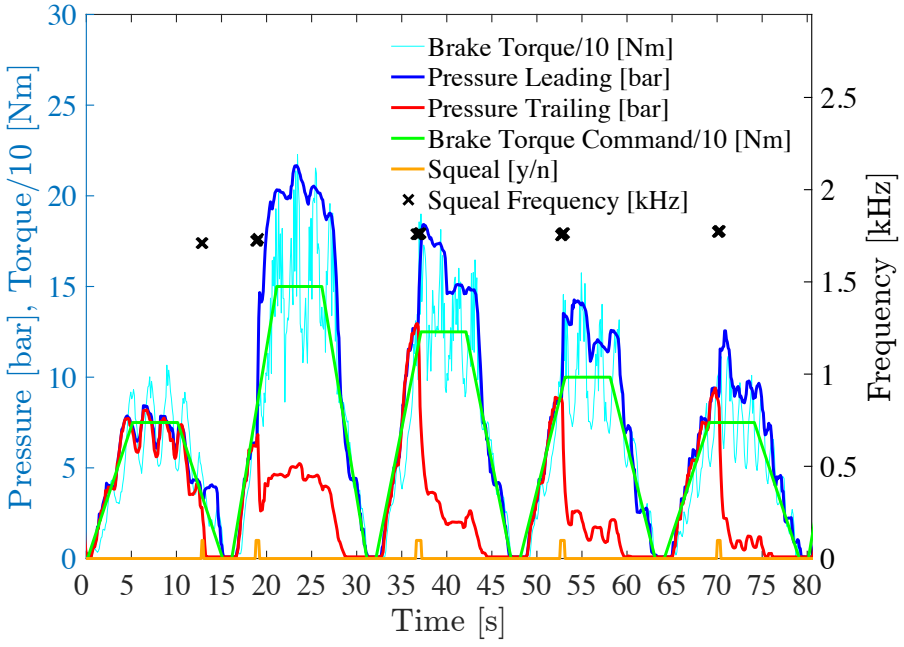

Figure 7.10: Example of activated fully-automatic ASQR mode during a typical braking torque cycle.

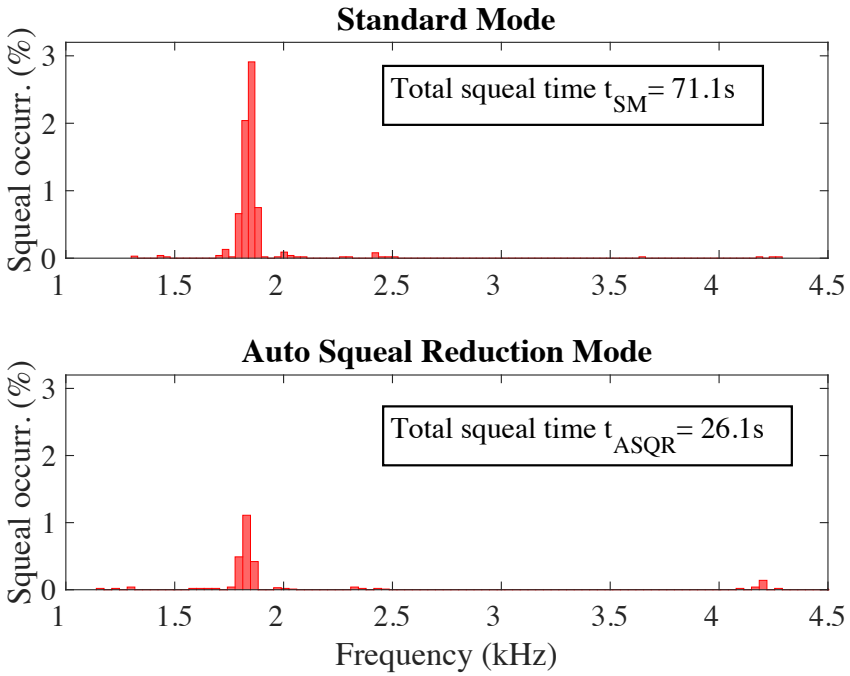

Figure 7.11: Comparison of squeal occurrence histogram as a percentage of total time vs. frequency for deactivated (Standard Mode) and activated ASQR (Auto Squeal Reduction Mode) mode.

is very likely caused by the significant runout of the disc. Therefore, for the future experiments, the aim should be to minimise the runout of the disc. Possible solutions might include a shorter and stiffer shaft adaptor, supported end of the shaft or use of brand new discs. A more sophisticated control technique, for instance based on monitoring and minimising the sound pressure level of the squeal could then be developed.

Tests also showed how the squeal changes over time with the condition of the pad. This can be explained by gradual changes of the surface topography of the pad, as well as by thermochemical alterations of the friction material surface. Each pad condition might give a rise to a different squeal frequency. Therefore, due to the resulting fugitive nature of brake squeal, it is often difficult to replicate certain experiments with a particular pad/disc combination.

8 Conclusions and Future Work

"If I have seen further it is by standing on the shoulders of giants."
Isaac Newton

8.1 Discussion

It was demonstrated via brake dynamometer experiments that variation of the leading/trailing pressure ratio (LTPR) influences the squeal frequency spectrum; some low-frequency squeals occured less frequently or disappeared completely for a specific LTPR. The tests showed that LTPR >4 (large leading offset of the CoP) better minimised the squeal than LTPR <1 (zero or trailing offset of the CoP), which might be in contradiction with some previous experiments found in the literature. The tests on LTPR variation were also performed by following a modified SAE J2521 cycle, where LTPR was varied from 1/4 to 4. Here also, the relative occurrence of unstable modes of vibration differed for specific LTPRs. Overall, the minimum total squeal times were found for LTPRs of 3 to 4. Since for each LTPR a specific position of the CoP can be calculated, this method showed the potential to determine quieter zones of the CoP for a given pad/disc combination.

It was shown that a simple single-input two-output (SITO) control scheme is appropriate for controlling leading and trailing piston pressures, and thereby the CoP position. The scheme allows for controlling the process variables and setting the ratio between the two output values. In this work, the process variable is the brake torque and the ratio of the output values is represented by the LTPR. The main disadvantage of the SITO control system in its simple form is that it does not allow feedback control of the ratio between the outputs so its value can differ from a set value by a small error. Also, due to the complexity of the current actuation system, the set value of the LTPR can be generally different from the real LTPR calculated from the hydraulic pressure values by a certain gain. Despite these minor drawbacks, the SITO control system showed a satisfactory performance as a part of the ASQR system.

It was demonstrated that the ASQR system in a fully automatic mode suppressed successfully squeal in most cases if a relatively narrow squeal bandwith of interest was defined, such as 1 to 5 kHz, and the LTPR was set to 4. At the same time the brake torque was held constant. The LTPR that leads to a quieter brake was evaluated through the experiments mentioned above.

Squeal experiments did not show a continuous relation between the LTPR and squeal

sound pressure level, and often the squeal within the frequency bandwith of interest rapidly appeared and disappeared when the LTPR was changed. This implies that for a specific frequency bandwith, the boundaries for the CoP positions between the quiet and loud zones over the pad area can be confined by sharp boundaries rather than smooth transitions. This could be explained by the squeal generation mechanism of the sprag/slip theory in which the system instability can be triggered when a specific geometric condition of the assembly is formed, and this either exists or it does not. Therefore, the currently used discontinuous control of the squeal based on placing the CoP position within a pre-defined zone, which was realised by setting a specific LTPR, seems to be appropriate.

A new three-dimensional (3D) rigid body model of the brake pad/disc interface was developed which can be used to calculate CoP position in both circumferential and radial directions during braking. A comparison with a finite element (FE) model of an equivalent brake showed a close correlation between these two approaches, giving the new analytical model a potential use in applications where an instantaneous value of the CoP with good accuracy is required. In the present work, the new 3D model was used in real time to predict the CoP position for the current LTPR. Another application example was shown with respect to calculation of the friction coefficient using data acquired from drag brake tests on a brake dynamometer. A comparison of the results collected from the brake dynamometer tests showed that the new 3D model gives an approximately 8% larger value of the friction coefficient than the friction coefficient calculated in the traditional way. It is proposed that the new model yields more accurate values of the effective friction radius compared to the mean radius used in the traditional approach.

A new computation method of CoP determination and complex eigenvalue analysis (CEA) was proposed that links the ABAQUS® and MATLAB® environments for a rapid simulation and data post-processing of numerous brake models in which input data, such as material, geometry, interaction properties or loads can be varied. This technique was demonstrated in a case study analysis on the influence of the disc top-hat geometry on the CoP position and squeal propensity. The analysis of pressure distribution on all disc variants during braking showed that a small difference in CoP positions for the outboard and inboard pad exists, which is dependent on the top-hat geometry. The CoP on both the inboard and outboard side tends to shift towards the leading side with increasing pressure. The outboard CoP is located radially more outward than the inboard CoP above a certain value of applied pressure. The inboard CoP position tends to move towards the trailing edge and the outboard CoP towards the leading end for the increasing top-hat height parameter. This effect is most probably due to the bending of the top-hat structure.

The CEA performed on discs with varying top-hat height parameter showed that the number of unstable modes and their frequency remains nearly identical across all disc model variants. An ideal top-hat height that would show a reduced propensity to squeal was not found. Due to the almost invariant results of the CEA over the disc model range, any correlation between the vibrational behaviour and the CoP position for the different top-hat height parameters could not be found.

The reduced FE model of the current brake setup showed that the CEA can predict unstable modes of vibration and some of these modes were also experimentally monitored on the brake dynamometer. As with most CEA, there is a certain squeal overprediction, in particular, for high-frequency squeal. On the other hand, some of the unstable modes in the range 3 to 7 kHz, which were monitored on the dynamometer, were not predicted by the model. A CEA performed on a variation of LTPR showed potential settings when the low-frequency squeal can be reduced. Assuming $\mu = 0.5$, the low-frequency squeal (1.8 kHz) was suppressed for LTPR = 1/9, 1/4, 1/3, 1/2 and 9. Interestingly, the high-frequency squeal was shown to be insensitive to the variation of LTPR indicating that this frequency bandwith can be related to a different squeal generation mechanism, for instance mode coupling.

A comparison of the CoP predictions determined by the new pad sensor and the analytical model showed a good general correlation but a relatively large discrepancy in the absolute values of the CoP positions. This was attributed to the fundamental differences of both methods, in particular it could be due to the actual mechanical design of the pad sensor, the type of piezoresistive force sensors and the type of currently measured variable. On the other hand the analytical model makes no allowance for the flexibility of the pad and surrounding parts or any temperature effects. It was observed that the inboard pad sensor position better correlated with the analytical model than the outboard position. The reason for this could be that the inboard side is not affected by large caliper deformations during braking as the outboard side and better corresponds with the analytical model.

During the present work, only an intermittent type of squeal was able to be generated. This intermittency could be caused by the significant axial runout of the current dynamometer setup. Numerous tests performed on the brake dynamometer showed that squeal predominantly occurs for rotor speeds below 100 rpm, within the temperature range 75 to 175°C, and when medium pressures 5 to 20 bar are applied. To recreate squeal it is a good practice to warm up the brake to a temperature above 250°C and gradually allow it to cool down to the squeal temperature zone. Referring to the elusive nature of squeal mentioned in the literature, it was found that squeal experiments are frequently difficult to replicate because the squeal behaviour of a certain pad/disc combination evolves over time, i.e. different unstable modes of vibration are emphasized leading to audible squeal. This may be explained by modifications of the pad material composition (burnishing), and gradual changes of the pad/disc interface geometry due to wear.

8.2 Conclusions

Overall it was concluded that the unstable modes of brake vibration which lead to audible squeal can be suppressed by changing the position of the centre of pressure (CoP) at the pad/disc interface. It was shown that LTPR values less than 1/4 and greater than 4 lead to quiter brake, whereby the latter could reduce the squeal occurrence more frequently. It was successfully demonstrated that by implementing these values in the

control algorithm of the new automatic squeal reduction (ASQR) system, squeal can be suppressed automatically after its detection. Due to a sophisticated control architecture the brake torque was only minimally influenced during this process. The performance of the ASQR system was demonstrated for a newly developed test cycle where it minimised the total time of low-frequency squeal occurrence by 63%.

Therefore, the principal novelty of this research and contribution to science is, that it shows the potential of the proposed ASQR system to be used for active suppression of disc brake squeal by setting specific LTPR values when squeal is detected. Moreover, the newly developed pad sensor along with analytical and FE models demonstrate the possibility to evaluate CoP positions at the pad/disc interface. The CoP position has been shown to be an important parameter having impact on squeal occurrence.

The present work paves the way for possible active suppression of disc brake squeal and can serve as a good source of information in this field. The design processes, analytical procedures and experimental techniques presented here can be useful methods for engineers in the automotive and related fields to make further progress in research studies of disc brake squeal.

8.3 Suggestions for Future Work

Some improvements that can follow upon the current work are summarised as follows:

- In the present work a four-piston opposed prototype caliper was developed that was connected to a two channel actuation system capable of varying the CoP only in the direction of sliding. It is suggested to develop a four channel actuation system and explore the possibility of squeal reduction when actuating each piston independently or in a different coupled formations (e.g. cross-coupling). The modularity of the prototype caliper enables the replacement of the piston module for a module with a different number of pistons. A concept of a module with four pistons is already presented in this thesis. For future research, it is suggested to complete the design and fabricate and test such a prototype. However, at least a four-channel actuation system would need to be developed so that opposite pistons can be coupled.

- In order to further improve the squeal prediction, the validation methodology of the model should be enhanced by determining more accurate material properties of the components, validating the model at the component and assembly level, as well as including thermal effects into the model. There is currently no equipment available at the UoL brake laboratory for experimental modal analysis (EMA), which represents a significant limitation for validation of the brake models. For future work, it is suggested to acquire a system that can be readily used for this type of analysis.

- Several improvements can be suggested for improvement of the pad sensor. First, it needs to be investigated if the number of the force sensors between the plug

and the backplate could be reduced as a number higher than three implies a statically indeterminate case and may be a source of measurement error. The drift and hysteresis error could be also reduced by measuring capacitance instead of the currently measured conductance. This, however, leads to more complicated circuitry. Instead of piezoresistive force sensors, it is suggested to use slim piezoelectric quartz sensors that usually exhibit higher repeatability of measurement (lower drift). Disadvantages of this type of sensor are generally larger dimensions and higher costs.

- The current actuation design is based on a laboratory electro-pneumatic actuation system. For future work, it is suggested to implement the ASQR system presented here in a brake system that is currently commonly used on vehicles which includes an electro-hydraulic ABS unit integrated with a master cylinder. For a four-piston opposed caliper, the ABS module should contain four channels, whereby the pressure of each channel can be independently modulated. The brake pedal actuation can be provided by a medium-stroke pneumatic cylinder with appropriate pressure regulator.

- Due to memory limitation of the current Field-Programmable Gate Array (FPGA), the parallel use of an accelerometer and a microphone to detect squeal could not be implemented. It is suggested to acquire a larger memory size of FPGA that can be used to develop an algorithm for parallel evaluation of both signals in order to increase robustness of the squeal measurement.

- The current ASQR system features a simple state-machine control that uses a discontinuous control algorithm to change LTPR based on pre-defined values. This type of control was shown as appropriate for the intermittent squeal generated using the current setup. For a continuous type of squeal, it is worth exploring other types of control algorithm, such as continuous control based on minimising the sound pressure level.

- The basic function of the squeal reduction system used in the present work is based on changing the pressure distribution at the pad/disc interface in order to minimise squeal occurrence. This simple function itself could be used in the brake industry for instance as a tool for development of quiet calipers. A more sophisticated ASQR system may not be attractive for industry to implement on actual vehicles mainly due to its higher costs. However, if squeal reduction could be combined with controlling other aspects connected with the pressure distributions at the pad/disc interface, such as wear of the pad, the system could gain more attention.

8.4 Epilogue

Investigation of brake squeal remains a fascinating field of modern automotive science, and it seems that, despite a great effort devoted to resolving this undesired effect, the

squeal problem will continue to be discussed in the brake research community in the following decades. This work contributed to the author's knowledge about design and modelling of brake systems, as well as on how to develop and commission a brake actuation and control system. Due to the interdisciplinary character of brake squeal research, it was necessary to study a vast number of published literature related to this topic, along with learning and mastering of numerous software packages, such as SOLIDWORKS®, ABAQUS®, MATLAB®, or LabVIEW. The laboratory work improved the author's practical skills in measurements of physical phenomena, classical machinery, electronics, and brake testing. The findings of this research, in the author's view, make a valuable contribution to knowledge and understanding in the important and demanding area of automotive brake squeal.

References

Abaqus (2012). *Abaqus 6.12, Example Problems Manual, Volume I: Static and Dynamic Analyses*. Retrieved from `https://things.maths.cam.ac.uk/computing/software/abaqus_docs/docs/v6.12/pdf_books/EXAMPLES_1.pdf`.

Abaqus-2 (2018). Abaqus 6.10, abaqus theory manual, 2.5.1 eigenvalue extraction. Retrieved from `https://www.sharcnet.ca/Software/Abaqus610/Documentation/docs/v6.10/books/stm/default.htm?startat=ch02s05ath24.html`.

Abdelhamid, M. K. (1995). Structural instability test/analysis of brake squeal. In *SAE Noise and Vibration Conference and Exposition, SAE Technical Paper 951281*. SAE International, Warrendale, Pennsylvania, USA.

Abendroth, H. and Wernitz, B. (2000). The integrated test concept: Dyno-vehicle, performance-noise. *SAE Technical Paper 2000-01-2774*. SAE International, Warrendale, Pennsylvania, USA.

Agudelo, C., Deacon, P., Tiwari, A., Hortet, A., Anderson, R., Markiewicz, R., and Marschall, M. (2017). Systematic assessment of the influence of test setup, test procedure, and friction material on brake emissions during inertia dynamometer tests. In *Proceedings of EuroBrake 2017*. FISITA, 2017. ISBN: 978-0-9572076-8-4.

Akay, A. (2002). Acoustics of friction. *The Journal of the Acoustical Society of America*, 111(4):1525--1548.

Alemani, M. (2017). *Particle emissions from car brakes: the influence of contact conditions on the pad-to-rotor interface*. PhD thesis, KTH Royal Institute of Technology, Stockholm, Sweden.

Alemani, M., Perricone, G., Olofsson, U., Saederberg, A., Wahlstroem, J., and Ciotti, A. (2014). A proposed dyno bench test cycle to study particle emissions from disc brakes. In *Proceedings of EuroBrake 2014*. FISITA, 2014. ISBN: 978-0-9572076-4-6.

Alnaqi, A. A. (2014). *Characterisation of coated lightweight brake rotors*. PhD thesis, University of Leeds, Leeds, United Kingdom.

Anwana, O. D., Cai, H., and Chang, H. (2002). Analysis of brake caliper seal-groove design. *SAE Technical Paper 2002-01-0927*. SAE International, Warrendale, Pennsylvania, USA.

Ashraf, N. (2013). *An investigation into the influence of the contact pressure distribution at the friction pair interface on disc brake squeal*. PhD thesis, University of Huddersfield, Huddersfield, United Kingdom.

Augsburg, K., Hesse, D., Wenzel, F., and Eichner, G. (2017). Measuring and characterization of brake dust particles. In *Proceedings of EuroBrake 2017*. FISITA, 2017. ISBN: 978-0-9572076-8-4.

Badertscher, J. and Cunefare, K. A. (2003). Experimental investigation of dither control on effective braking torque. In *SAE 2003 Noise and Vibration Conference and Exhibition, SAE Technical Paper 2003-01-1617*. SAE International, Warrendale, Pennsylvania, USA.

Bae, J.-C. and Wickert, J. (2000). Free vibration of coupled disk-hat structures. *Journal of sound and vibration*, 235(1):117--132.

Bajer, A., Belsky, V., and Kung, S.-W. (2004). The influence of friction-induced damping and nonlinear effects on brake squeal analysis. *SAE Technical Paper 2004-01-2794*. SAE International, Warrendale, Pennsylvania, USA.

Bakar, A. (2012). *Disc Brake Squeal A Prediction Methodology*. AV Akademikerverlag, Saarbruecken. ISBN 978-3-639-45271-6.

Baker, A. K. (1986). *Vehicle braking*. Pentech Press, London. ISBN 0727322028.

Bao, H. and Panahi, I. (2013). A perceptually motivated active noise control design and its psychoacoustic analysis. *ETRI Journal*, 35(5):859--868.

Barron, R. (2003). *Industrial noise control and acoustics*. Marcel Dekker, New York. ISBN 0-8247-0701-X.

Belhocine, A. and Bouchetara, M. (2012). Simulation of fully coupled thermo mechanical analysis of disc brake rotor. *Wseas Transactions on Applied and Theoretical Mechanics*, 7(3).

Blaschke, P., Mallareddy, T. T., Paeschke, R., and Torsten, S. (2015). Pressure load influence on modal parameters of a brake pad/disc assembly and their characterization for brake squeal. In *Proceedings of EuroBrake 2015*. FISITA, 2015. ISBN: 978-0-9572076-6-0.

Blaschke, P. and Rumold, W. (1999). Global nvh matrix for brake noise - a bosch proposal. In *Annual Brake Colloquium And Engineering Display, SAE Technical Paper 1999-01-3405*. SAE International, Warrendale, Pennsylvania, USA.

Blauert, J. (2008). *Acoustics for engineers Troy lectures*. Springer, Berlin London. ISBN 978-3-642-03392-6.

Brooks, P., Crolla, D., Lang, A., and Schafer, D. (1993). Eigenvalue sensitivity analysis applied to disc brake squeal. In *Proceedings of The Institution of Mechanical Engineers, Braking of Road Vehicles*. London, United Kingdom.

Budinsky, T., Brooks, P., and Barton, D. (2017). The influence of disc geometry on the centre of pressure and squeal propensity for an automotive disc brake. In *EuroBrake 2017 Conference Proceedings*. FISITA, 2017. ISBN: 978-0-9572076-8-4.

Bugatti (2018). Weltpremiere: Bremssattel aus dem Drucker [web log post]. Retrieved from `https://www.bugatti.com/de/media/news/2018/bugatti-weltpremiere-bremssattel-aus-dem-3d-drucker/`.

Chen, F. (2006). *Disc brake squeal : mechanism, analysis, evaluation, and reduction/prevention*. SAE International, Warrendale, Pennsylvania, USA. ISBN 0-7680-1248-1.

Chen, F., Chern, J., and Swayze, J. (2002). Modal coupling and its effect on brake squeal. In *SAE 2002 World Congress and Exhibition, SAE Technical Paper 2002-01-0922*. SAE International, Warrendale, Pennsylvania, USA.

Chu, Z., Zheng, F., Liang, L., Yan, H., and Kang, R. (2018). Parameter determination of a minimal model for brake squeal. *Applied Sciences*, 8(1):37.

Cunefare, K., Montbrun, N., Rastelli, V., Aller, J., and Dizrasa, M. (2001). Burst mode dither control of automotive brake squeal. *Signal*, 50:100.

Davis, S. C., Diegel, S. W., and Boundy, R. G. (2014). Transportation energy data book: Edition 33. Retrieved from `https://info.ornl.gov/sites/publications/files/pub50854.pdf`.

Day, A. (2014). *Braking of road vehicles*. Butterworth-Heinemann, Oxford. ISBN 0123973147.

Degenstein, T. and Winner, H. (2006). Dynamic measurement of the forces in the friction area of a disc brake during a braking process. In *Proceedings of FISITA World Automotive Congress, Yokohama*.

Dihua, G. and Dongying, J. (1998). A study on disc brake squeal using finite element methods. In *International Congress and Exposition, SAE Technical Paper 980597*. SAE International, Warrendale, Pennsylvania, USA.

Dunlap, K. B., Riehle, M. A., and Longhouse, R. E. (1999a). An investigative overview of automotive disc brake noise. *SAE Technical Paper 1999-01-0142*. SAE International, Warrendale, Pennsylvania, USA.

Dunlap, K. B., Riehle, M. A., and Longhouse, R. E. (1999b). An investigative overview of automotive disc brake noise. In *International Congress and Exposition, SAE Technical Paper 1999-01-0142*. SAE International, Warrendale, Pennsylvania, USA.

Earles, S. (1977). A mechanism of disc-brake squeal. *SAE Technical Paper 770181*. SAE International, Warrendale, Pennsylvania, USA.

Elguezabal, J., Zarraga, O., Erana, I., Abete, J. M., and Ulacia, I. (2015). Comparison between different complex eigenvalue strategies to reduce brake squeal overprediction. In *Proceedings of EuroBrake 2015*. FISITA, 2015. ISBN: 978-0-9572076-6-0.

Erjavec, J. (2004). *TechOne: Automotive Brakes*. Thomson/Delmar Learning, Clifton Park, NY. ISBN 1401835260.

Erjavec, J. and Thompson, R. (2014). *Automotive technology: a systems approach*. Cengage Learning, USA. ISBN 978-1-133-61231-5.

EU (2010). Regulation no 90 of the economic commission for europe of the united nations (un/ece) uniform provisions concerning the approval of replacement brake lining assemblies and drum brake linings for power-driven vehicles and their trailers. *Official Journal of the European Union*, 53(L 130). ISSN 1725-2555.

Faria, M. I. S. T., Robin, A., Prisco, L. P., Puccini, M. C., Gonalves, D. C., and Loureno, J. C. (2013). Corrosion of al 7075 alloy during the production of aeronautic components: Influence of process parameters at the deburring stage. *Materials and Corrosion*, 64(12):1114--1120.

Felske, A., Hoppe, G., and Matthi, H. (1978). Oscillations in squealing disk brakes - analysis of vibration modes by holographic lnterferometry. In *1978 Automotive Engineering Congress and Exposition, SAE Technical Paper 780333*. SAE International, Warrendale, Pennsylvania, USA.

Fieldhouse, J. D., Ashraf, N., Talbot, C., Pasquet, T., Franck, P., and Gabriel, R. (2006). Measurement of the dynamic center of pressure of a brake pad during a braking operation. *SAE Technical Paper 2006-01-3208*. SAE International, Warrendale, Pennsylvania, USA.

Fieldhouse, J. D., Ashraf, N., and Talbot, C. J. (2009). The measurement and analysis of the disc/pad interface dynamic centre of pressure and its influence on brake noise. *SAE International Journal of Passenger Cars-Mechanical Systems, SAE Technical Paper 2008-01-0826*, 1(1):736--745. SAE International, Warrendale, Pennsylvania, USA.

Fieldhouse, J. D. and Newcomb, P. (1993). The application of holographic interferometry to the study of disc brake noise. In *International Congress and Exposition, SAE Technical Paper 930805*. SAE International, Warrendale, Pennsylvania, USA.

Fieldhouse, J. D. and Steel, W. P. (2003). A study of brake noise and the influence of the centre of pressure at the disc/pad interface, the coefficient of friction and calliper mounting geometry. *Proceedings of the Institution of Mechanical Engineers, Part D: Journal of Automobile Engineering*, 217(11):957--973.

Fleet Parts Ltd (2018). Fleet Parts Ltd - Brake calipers. Retrieved from `http://www.fleetparts.co.uk/components/disc-brake-calipers/`.

Flint, J. and Hulten, J. (2002). Lining-deformation-induced modal coupling as squeal generator in a distributed parameter disc brake model. *Journal of sound and vibration*, 254(1):1--21.

Formula1 (2018). Formula 1: Brake system - technical regulations. Retrieved from `https://www.formula1.com/content/fom-website/en/championship/inside-f1/rules-regs/Brake_system.html/`.

Fosberry, R. and Holubecki, Z. (1959). *Interim report on disc brake squeal*. Motor Industry Research Association.

Gilles, T. (2016). *Automotive service: inspection, maintenance, repair*. Cengage Learning. ISBN 978-1-3051-1059-5.

Gramstat, S., Cserhati, A., Lugovyy, D., and Schrder, M. (2017). Investigations of brake particle emissions testing method, vehicle peculiarities and friction material influence. In *Proceedings of EuroBrake 2017*. FISITA, 2017. ISBN: 978-0-9572076-8-4.

Grigoratos, T. and Martini, G. (2015). Brake wear particle emissions: a review. *Environmental Science and Pollution Research*, 22(4):2491--2504.

Harding, P. and Wintle, B. (1978). Flexural effects in disc brake pads. *Proceedings of the Institution of Mechanical Engineers*, 192(1):1--7.

Hashemi-Dehkordi, S., Mailah, M., Abu-Bakar, A., and Harith, H. (2008). Brake squeal suppression using active force control. *Engineering Postgraduate Conference*.

Hassan, M. Z. (2009). *Thermal Deformation Analysis Of Automotive Disc Brake Squeal*. PhD thesis, University of Leeds, Leeds, United Kingdom.

Hedge, A. (2016). *Ergonomic Workplace Design for Health, Wellness, and Productivity*. CRC Press. ISBN-13 978-1-4665-9843-0.

Hess, D. and Soom, A. (1991). Normal vibrations and friction under harmonic loads: Part ihertzian contacts. *Journal of Tribology*, 113(1):80--86.

Hill, W. and K.D., S. (1961). Elevated temperature elastic dynamic moduli of various metallic materials. *Wadd Technical report*.

Hochlenert, D. (2006). *Selbsterregte Schwingungen in Scheibenbremsen : mathematische Modellbildung und aktive Unterdrueckung von Bremsenquietschen*. Shaker, Aachen. ISBN 3-8322-5684-9.

Hoffmann, N., Fischer, M., Allgaier, R., and Gaul, L. (2002). A minimal model for studying properties of the mode-coupling type instability in friction induced oscillations. *Mechanics Research Communications*, 29(4):197--205.

Jang, H., Ko, K., Kim, S., Basch, R., and Fash, J. (2004). The effect of metal fibers on the friction performance of automotive brake friction materials. *Wear*, 256(3-4):406--414.

Jarnestrom, P. A., Eliasson, M., Ahlex, M., Fumi, D., and Axelsson, R. (2015). The effect on brake noise using ptfe coated brake shims with low friction surface. In *Proceedings of EuroBrake 2015*. FISITA, 2015. ISBN: 978-0-9572076-6-0.

Jarvis, R., Mills, B., et al. (1963). Vibrations induced by dry friction. *Proceedings of the Institution of Mechanical Engineers*, 178(1):847--857.

Kao, T.-K., Richmond, J. W., and Moore, M. W. (1994). The application of predictive techniques to study thermo-elastic instability of brakes. *SAE Technical Paper 942087*. SAE International, Warrendale, Pennsylvania, USA.

Kaufman, J. G. (2008). *Properties of aluminum alloys fatigue data and the effects of temperature, product form, and processing*. ASM International, Materials Park, Ohio. ISBN 978-0-87170-839-7.

Kim, J. Y., Kim, J., Kim, Y. M., Jeong, W., and Cho, H. (2015). An improvement of brake squeal cae model considering dynamic contact pressure distribution. *SAE International Journal of Passenger Cars - Mechanical Systems, SAE Technical Paper 2015-01-2691*, 8(4):1188--1195. SAE International, Warrendale, Pennsylvania, USA.

Kim, M., Moon, J., and Wickert, J. A. (2000). Spatial modulation of repeated vibration modes in rotationally periodic structures. *Journal of vibration and acoustics*, 122(1):62--68.

Kinkaid, N., O'Reilly, O., and Papadopoulos, P. (2003). Automotive disc brake squeal. *Journal of sound and vibration*, 267(1):105--166.

Kinkaid, N., O'Reilly, O., and Papadopoulos, P. (2005). On the transient dynamics of a multi-degree-of-freedom friction oscillator: a new mechanism for disc brake noise. *Journal of Sound and Vibration*, 287(4):901--917.

Knorr Bremse (2018). Bendix - Installation Instructions. Retrieved from `http://www.knorr-bremsecvs.com/en/activeservices/downloadservices/downloaddocumentation_1/downloaddocumentation_1.jsp`.

Lee, K. (2007). Vented disc brake rotor. US Patent App. 11/711,194.

Liles, G. D. (1989). Analysis of disc brake squeal using finite element methods. In *SAE Noise and Vibration Conference and Exposition, SAE Technical Paper 891150*. SAE International, Warrendale, Pennsylvania, USA.

Limpert, R. (2011). *Brake design and safety*. SAE International, Warrendale, Pennsylvania, USA. ISBN 0768034388.

Macknight, N. (2002). *Technology of the F1 car*. Hazleton Pub. Distributors in North America, Motorbooks International, Richmond Osceola, Wis. ISBN 1874557683.

Mahajan, S. K., Hu, Y.-K., and Zhang, K. (1999). Vehicle disc brake squeal simulations and experiences. *SAE Technical Paper 1999-01-1738*. SAE International, Warrendale, Pennsylvania, USA.

Malmassari, C., Cucchi, F., Yuhas, D. E., Vorres, C. L., and Jacek, R. (2015). Evolution of brake noise performance and its relation to variations in friction material elastic properties. In *Proceedings of EuroBrake 2015*. FISITA, 2015. ISBN: 978-0-9572076-6-0.

Mastinu, G. (2013). *Road and off-road vehicle system dynamics handbook*. CRC Press, Boca Raton. ISBN 978-0-8493-3322-4.

Matsui, H., Murakami, H., Nakanishi, H., and Tsuda, Y. (1992). Analysis of disc brake squeal, 1992. In *International Congress and Exposition, SAE Technical Paper 920553*. SAE International, Warrendale, Pennsylvania, USA.

Matsuzaki, M. and Izumihara, T. (1993). Brake noise caused by longitudinal vibration of the disc rotor. In *International Congress and Exposition, SAE Technical Paper 930804*. SAE International, Warrendale, Pennsylvania, USA.

Matute, A., Paredes-Madrid, L., Gutierrez, E., and Vargas, C. A. P. (2017). Characterization of drift and hysteresis errors in force sensing resistors considering their piezocapacitive effect. In *SENSORS, 2017 IEEE*, pages 1--3. IEEE.

Millner, N. (1978). An analysis of disc brake squeal. In *1978 Automotive Engineering Congress and Exposition, SAE Technical Paper 780332*. SAE International, Warrendale, Pennsylvania, USA.

Mills, H. (1938). Brake squeak: first interim report. *Report N9000B, Institution of Automobile Engineers, Automobile Research Committee*.

Moeser, M. (2009). *Engineering acoustics an introduction to noise control*. Springer, Berlin London. ISBN 978-3-540-92722-8.

Morello, L., Rossini, L. R., Pia, G., and Tonoli, A. (2011). *The Automotive Body: Volume II: System Design*. Springer Science & Business Media.

Murakami, H., Tsunada, N., and Kitamura, T. (1984). A study concerned with a mechanism of disc-brake squeal. In *Passenger Car Meeting and Exposition, SAE Technical Paper 841233*. SAE International, Warrendale, Pennsylvania, USA.

Nack, W. V. (1999). Brake squeal analysis by finite elements. In *Noise and Vibration Conference and Exposition, SAE Technical Paper 1999-01-1736*. SAE International, Warrendale, Pennsylvania, USA.

Naunheimer, H. (2011). *Automotive transmissions fundamentals, selection, design and application*. Springer, Berlin London. ISBN: 978-3-642-16213-8.

Nishiwaki, M., Harada, H., Okamura, H., and Ikeuchi, T. (1989). Study on disc brake squeal. In *SAE International Congress and Exposition, SAE Technical Paper 890864*. SAE International, Warrendale, Pennsylvania, USA.

North, M. (1972). *Disc brake squeal: a theoretical model*. Hillington Press.

Ostermeyer, G. P., Raczek, S., Abendroth, H., Wernitz, B., Koelsch, C., and Giese, A. (2015). On the correlation of friction behaviour and brake squeal. In *Proceedings of EuroBrake 2015*. FISITA, 2015. ISBN: 978-0-9572076-6-0.

Owen, C. E. (2003). *Classroom Manual for Automotive Brake Systems*. Cengage Learning. ISBN 1-4018-3890-1.

Papinniemi, A., Lai, J. C., Zhao, J., and Loader, L. (2002). Brake squeal: a literature review. *Applied acoustics*, 63(4):391--400.

Park, J. S., Han, M. G., and Oh, S. Y. (2016). A study of the relationship between leading offset and squeal noise. *SAE International Journal of Passenger Cars - Mechanical Systems, SAE Technical Paper 2016-01-1919*, 9(3):1144--1150. SAE International, Warrendale, Pennsylvania, USA.

Perricone, G., Wahlström, J., and Olofsson, U. (2016). Towards a test stand for standardized measurements of the brake emissions. *Proceedings of the Institution of Mechanical Engineers, Part D: Journal of Automobile Engineering*, 230(11):1521--1528.

PPS Inc. (2017). Pressure Profile Systems, Inc. Retrieved from `http://www.pressureprofile.com/brake-pad-sensors`.

Rabia, A. M., Ghazaly, N. M., Salem, M., and Abd-El-Tawwab, A. M. (2013). Finite element analysis of disc brake vibration considering surface roughness. *Minia Journal of Engineering and Technology*, 32(1):226--235.

Racecar engineering (2018). F1 2014 explained: Brake systems [Web log post]. Retrieved from `http://www.racecar-engineering.com/technology-explained/f1-2014-explained-brake-systems/`.

Rajaram, L. and Sudharsan, S. (2005). Optimization of caliper housing using fem. *SAE Technical Paper 2005-26-060*. SAE International, Warrendale, Pennsylvania, USA.

Reibenschuh, M., Oder, G., Cus, F., and Potrc, I. (2009). Modelling and analysis of thermal and stress loads in train disc brakes-braking from 250 km/h to standstill. *Strojniški vestnik*, 55(7-8):494--502.

Reif, K. (2014). *Brakes, brake control and driver assistance systems : function, regulation and components*. Springer Gabler, Wiesbaden. ISBN 3658039779.

Rhee, S., Tsang, P., and Wang, Y. (1989). Friction-induced noise and vibration of disc brakes. *Wear*, 133(1):39 -- 45.

Ripin, M. B. Z. (1995). *Analysis of disc brake squeal using the finite element method*. PhD thesis, University of Leeds, Leeds, United Kingdom.

Rotora Brakes (2018). Rotora Brakes - High Performance Brake Systems and Braking Components. Retrieved from `http://www.brakewarehouse.com/rotora-brakes.wws`.

Samie, F. and Sheridan, D. C. (1990). Contact analysis for a passenger car disc brake. In *International Congress and Exposition, SAE Technical Paper 900005*. SAE International, Warrendale, Pennsylvania, USA.

Savaresi, S. M. and Tanelli, M. (2010). *Active braking control systems design for vehicles*. Springer Science & Business Media.

Scraba, W. (2014). *How to build a winning drag race chassis and suspensionhp1462*. HP Books, New York. ISBN 1101097833.

Shackelford, J. F., Han, Y.-H., Kim, S., and Kwon, S.-H. (2016). *CRC materials science and engineering handbook*. CRC press. ISBN 978-1-4822-1656-1.

Shimizu, H., Oura, Y., Suzuki, T., and Sano, Y. (2014). The effect of grease on brake squeal. *SAE Technical Paper 2014-01-2512*. SAE International, Warrendale, Pennsylvania, USA.

Shin, K., Brennan, M., Oh, J.-E., and Harris, C. (2002). Analysis of disc brake noise using a two-degree-of-freedom-model. *Journal of Sound and Vibration*, 254(5):837--848.

Soh, H. and Yoo, J. (2010). Optimal shape design of a brake calliper for squeal noise reduction considering system instability. *Proceedings of the Institution of Mechanical Engineers, Part D: Journal of Automobile Engineering*, 224(7):909--925.

Spurr, R. T. (1961). A theory of brake squeal. *Proceedings of the Institution of Mechanical Engineers: Automobile Division*, 15(1):33--52.

Stan, C. (2005). *Development trends of motorcycles II*, volume 2. expert verlag.

Stegmann, P., Kruse, S., and Augsburg, K. (2015). Robustness of disc brake systems regarding squeal. In *Proceedings of EuroBrake 2015*. FISITA, 2015. ISBN: 978-0-9572076-6-0.

Stenberg, T. R. (1935). *Brake Linings*. University of Michigan, Akron, Ohio, USA.

Stephan, P., Heck, I., Krau, P., and Frey, G. (2009). Evaluation of indoor positioning technologies under industrial application conditions in the smartfactorykl based on en iso 9283. *IFAC Proceedings Volumes*, 42(4):870--875.

Supachai, L., Suwantaroj, K., Puangcharoenchai, P., Mongkonlerdmanee, S., and Koetniyom, S. (2013). Study of heat transfer on front and back-vented brake discs. *Songklanakarin Journal of Science and Technology*, 35:671--681.

TBM Brakes (2018). Brake piston count does not matter! [web log post]. Retrieved from https://www.tbmbrakes.com/brake-piston-count-not-matter/.

The Brake Report (2017). ITT Smart Pad Development Tool Unveiled at EuroBrake 2017 [Web log post]. Retrieved from https://thebrakereport.com/itt-smart-pad-development-tool-unveiled-eurobrake-2017/.

Thompson, J. and Fudge, C. (2002). One year's experience utilizing the SAE J2521 brake noise test procedure. In *Braking 2002. From the driver to the road. Papers from the international conference.*

Thorpe, A. and Harrison, R. M. (2008). Sources and properties of non-exhaust particulate matter from road traffic: a review. *Science of the total environment*, 400(1):270--282.

Tirovic, M. and Day, A. (1991). Disc brake interface pressure distributions. *Proceedings of the Institution of Mechanical Engineers, Part D: Journal of Automobile Engineering*, 205(2):137--146.

Tirovic, M., Vianello, M., and Bannister, P. (2018). Methodology for predicting brake squeal propensity using complex eigenvalue analysis, including thermo-mechanical effects. *Proceedings of the Institution of Mechanical Engineers, Part D: Journal of Automobile Engineering*, pages 1 -- 26.

Triches, M., Gerges, S. N. Y., and Jordan, R. (2004). Reduction of squeal noise from disc brake systems using constrained layer damping. *Journal of the Brazilian Society of Mechanical Sciences and Engineering*, 26(3):340--348.

Tumbrink, H. J. (1989). Measurement of load distribution on disc brake pads and optimization of disc brakes using the ball pressure methods. In *SAE International Congress and Exposition, SAE Technical Paper 890863*. SAE International, Warrendale, Pennsylvania, USA.

Twiflex Ltd (2018). Twiflex Ltd - Direct acting caliper brakes. Retrieved from https://www.twiflex.com/products/Disc-Braking-Systems/Direct-Acting-Calipers.

Vermot des Roches, G., Chiello, O., Balmes, E., and Lorang, X. (2015). Squeal complex eigenvalue analysis, advanced damping models and error control. In *Proceedings of EuroBrake 2015*. FISITA, 2015. ISBN: 978-0-9572076-6-0.

Wagh, N. P. (2005). Design and analysis of modular caliper assembly. Master's thesis, Wichita State University, College of Engineering, Dept. of Mechanical Engineering. Retrieved from https://soar.wichita.edu/bitstream/handle/10057/750/t05037.pdf?sequence=3.

Wagner, U., Hochlenert, D., and Hagedorn, P. (2007). Minimal models for disk brake squeal. *Journal of Sound and Vibration*, 302(3):527--539.

Wagner, U., Hochlenert, D., Jearsiripongkul, T., and Hagedorn, P. (2004). Active control of brake squeal via smart pads. In *22nd Annual Brake Colloquium and Exhibition, SAE Technical Paper 2004-01-2773*. SAE International, Warrendale, Pennsylvania, USA.

White, J. H. (1985). *The American railroad passenger car*. JHU Press. ISBN 0-8018-2747-7.

Whittington, J., Ye, H., Kamalakannan, K., Vu, N., Mason, M., Kleinschmidt, T., and Sridharan, S. (2010). Low-cost hardware speech enhancement for improved speech recognition in automotive environments. In *24th ARRB Conference Proceedings, ARRB Group Ltd., Australia, Victoria, Melbourne.*

Wirth, X. (1987). Shaft braking disc for rail vehicle disc brake. US Patent 4,638,891.

Xie, M. S., Zhang, G. R., Li, J. H., and Fritsch, R. (2014). Brake pad taper wear on brake moan noise. *International Journal of Automotive Technology*, 15(4):565--571.

Yang, M., Afaneh, A.-H., and Blaschke, P. (2003). A study of disc brake high frequency squeals and disc in-plane/out-of-plane modes. In *SAE 2003 Noise and Vibration Conference and Exhibition, SAE Technical Paper 2003-01-1621*. SAE International, Warrendale, Pennsylvania, USA.

Yue, Y. and Zhang, L. (2009). A study of effects of brake contact interfaces on brake squeal. *SAE International Journal of Passenger Cars - Mechanical Systems, SAE Technical Paper 2009-01-2100*, 2(1):1406--1413. SAE International, Warrendale, Pennsylvania, USA.

Appendix A

A.1 Drawings

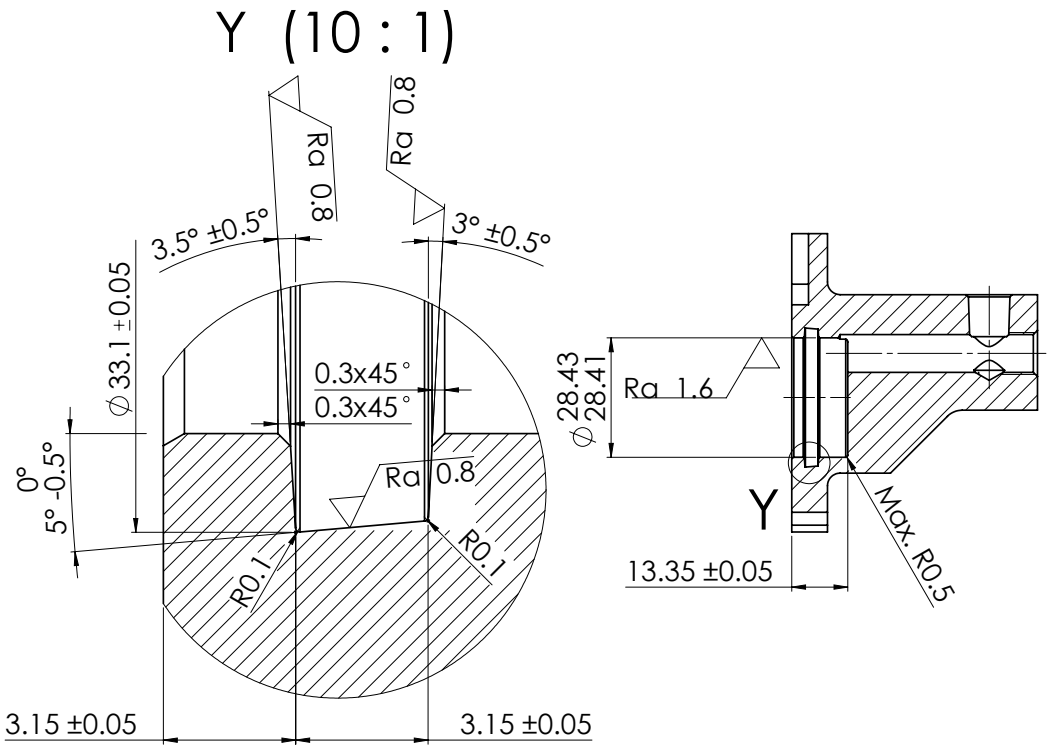

Figure A-1: Drawing of the piston seal groove that was used to order the particular machining tool.

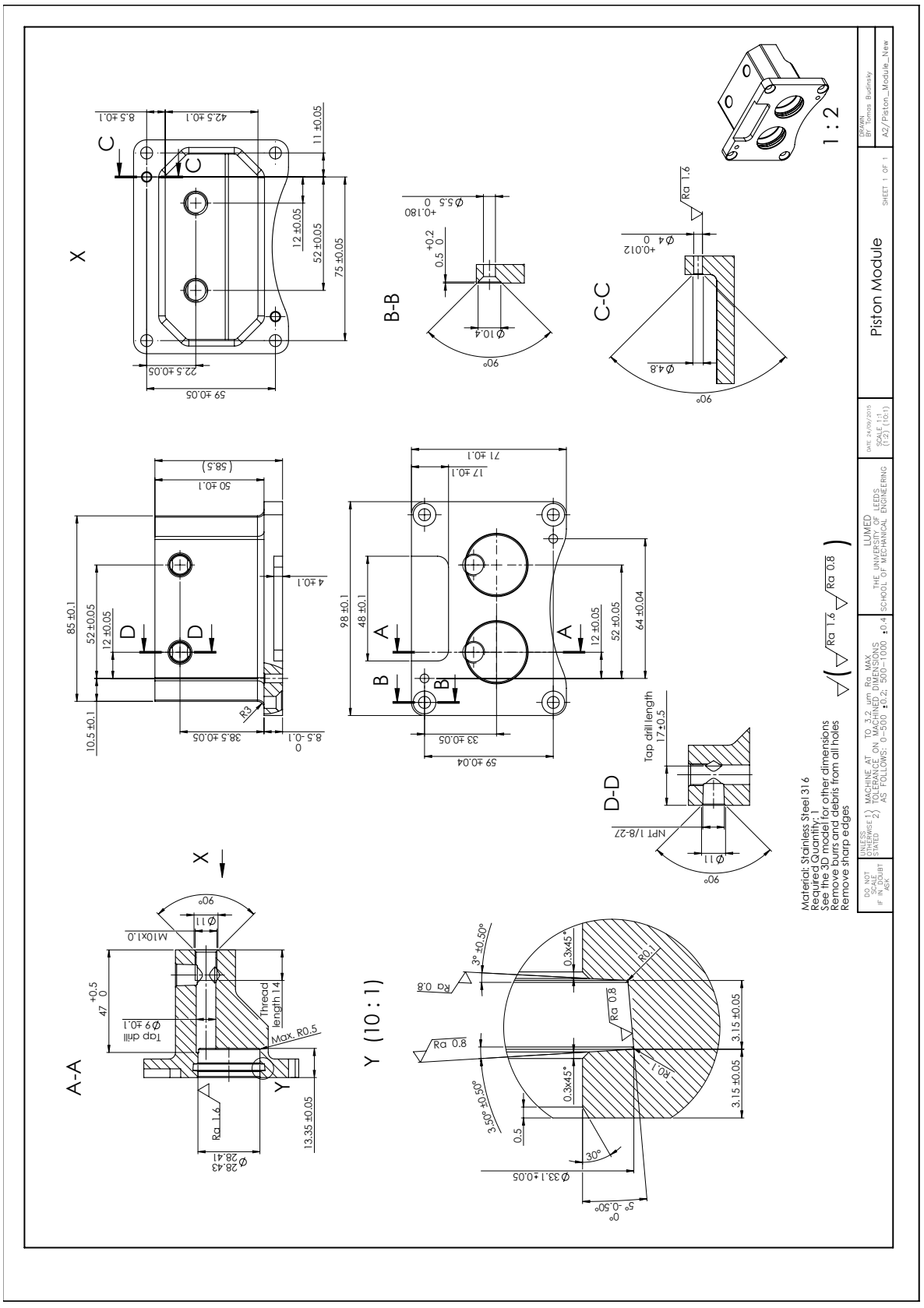

Figure A-2: Drawing of the two-piston module.

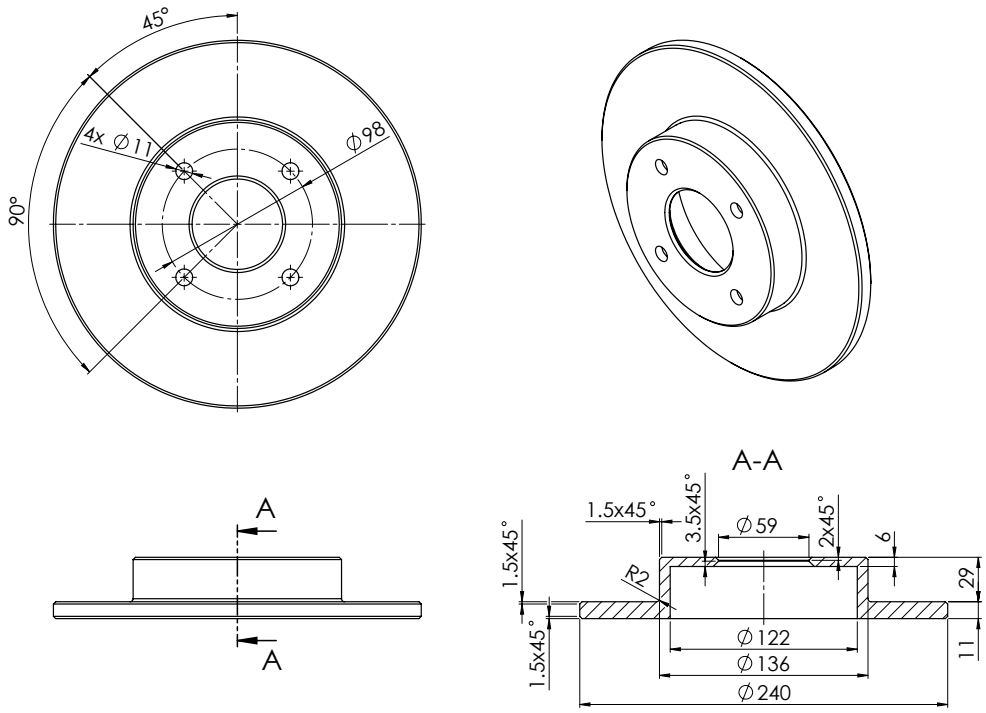

Figure A-3: Drawing of the Fiat Punto disc showing the nominal dimensions.

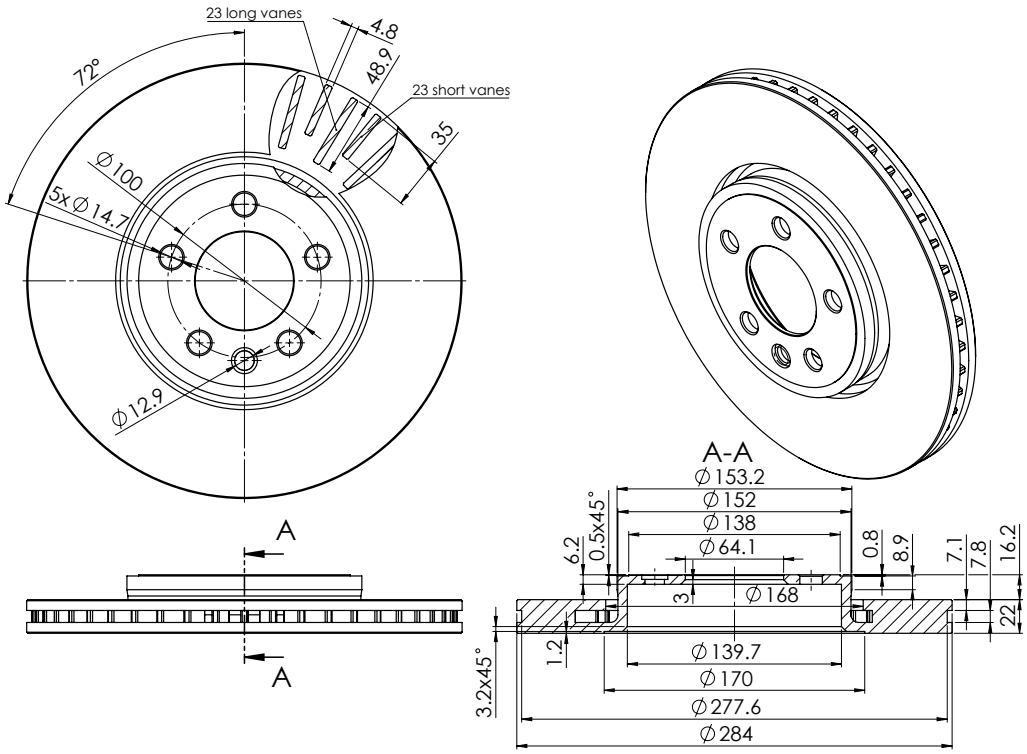

Figure A-4: Drawing of the Rover 75 disc showing the nominal dimensions.

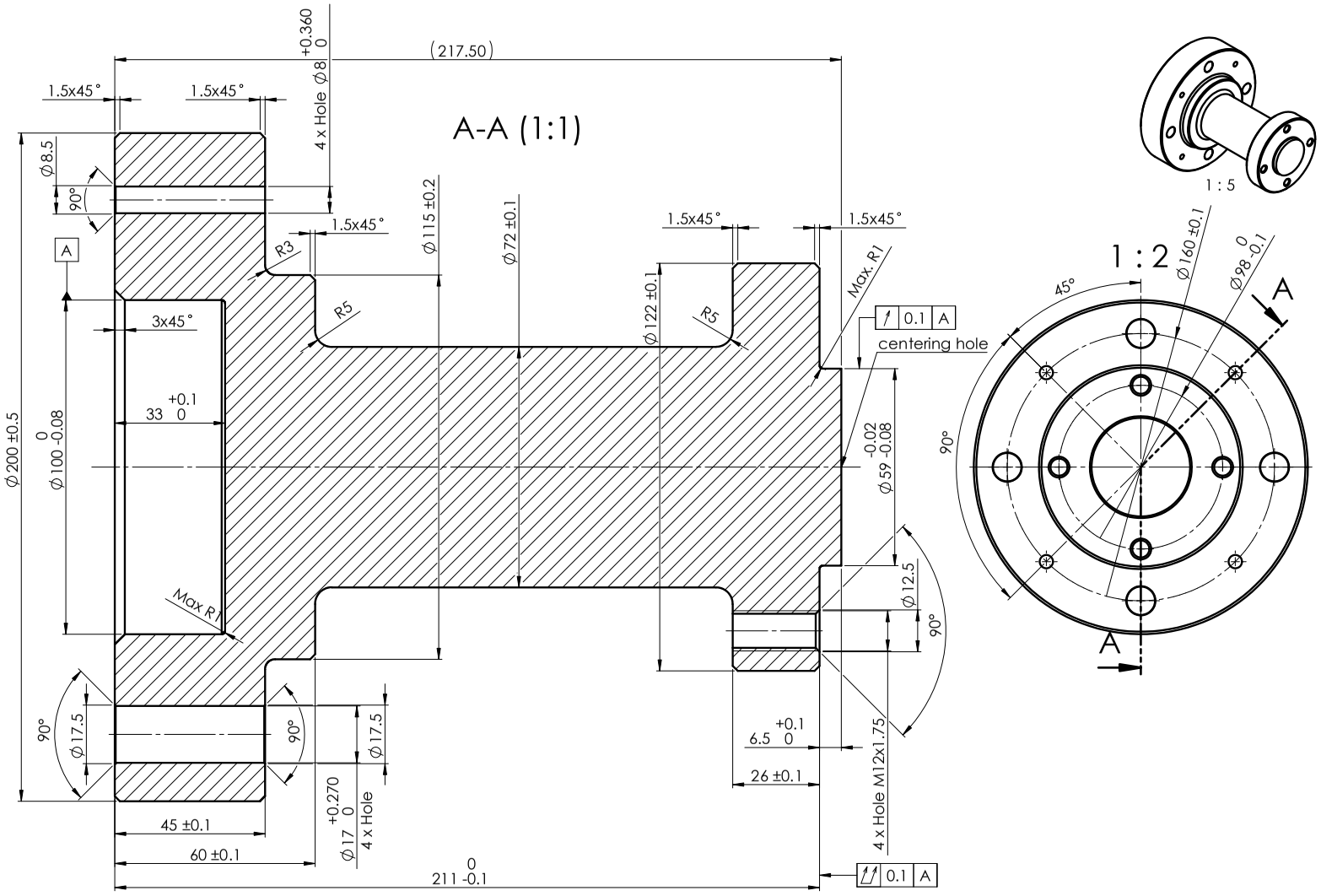

Figure A-5: Drawing showing all dimensions used to manufacture the adaptor for the Fiat Punto disc.

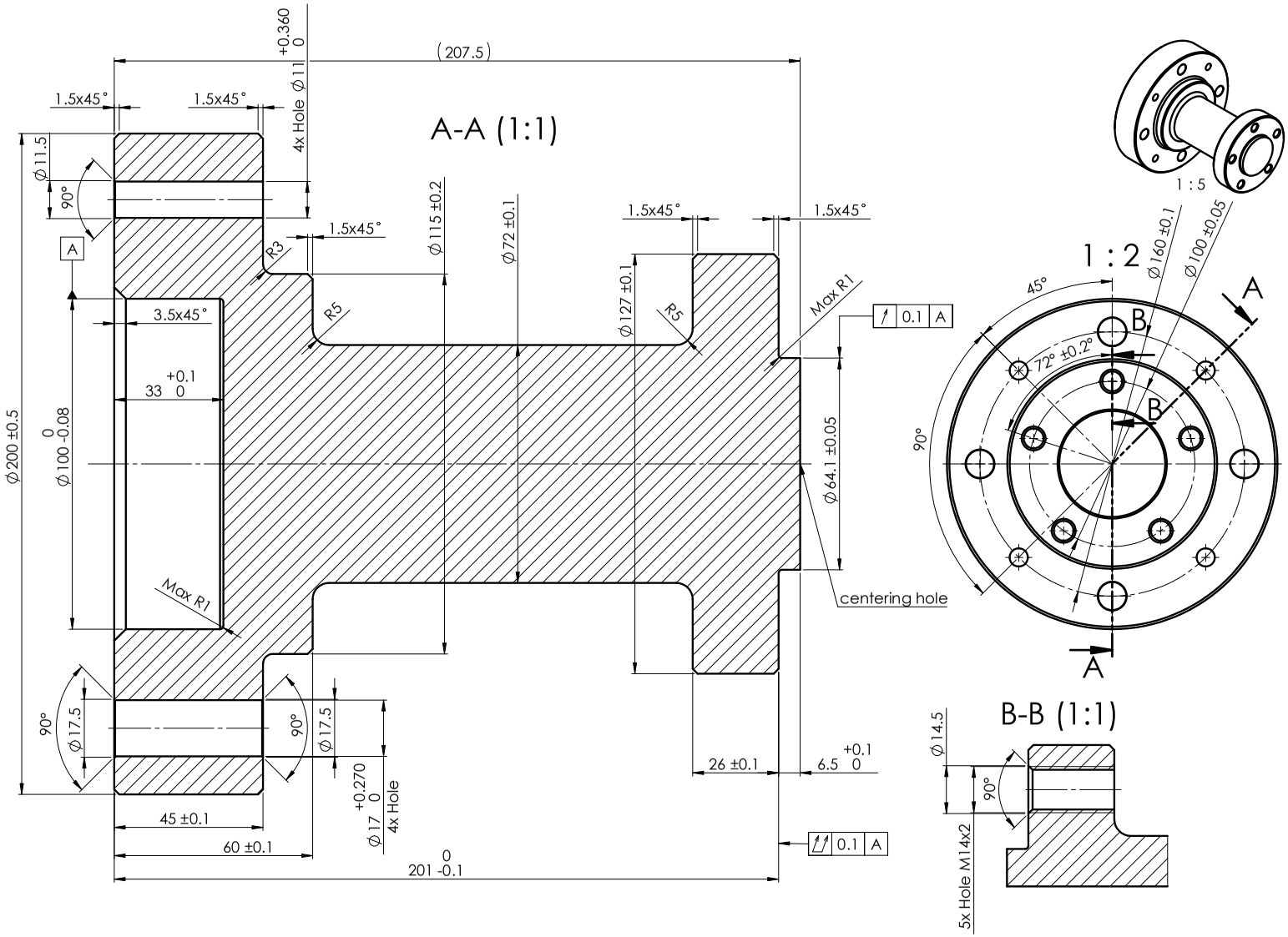

Figure A-6: Drawing showing all dimensions used to manufacture the adaptor for the Rover 75 disc.

A.2 Caliper Installation and Maintanence

a) All piston seals and the outer surfaces of the pistons should be lightly lubricated in a clean brake fluid. Make sure that the seal seats fully in the groove (Knorr Bremse, 2018).

b) All components should be properly mounted and all bolts appropriately tightened.

c) The caliper bolts clamping the inboard and outboard part should be tightened to a torque of 40 Nm.

d) The wheel bolts of Fiat Punto brake disc should be tightened to a torque of 86 Nm (according to the Fiat Punto repair manual).

e) When changing the brake pads, the recommended position of the caliper is shown in Figure A-7. In this position, the pads can be replaced from the bottom side of the caliper. However, make sure that the M10 bolt connection holding the caliper is properly tightened. If worn pads are replaced for new ones, it may be necessary to gently push back pistons in order to increase the space between them to accommodate the pad. During this operation, make sure that the bleed screws are loosened to allow the excess of the brake fluid to be pushed out from the hydraulic system. This procedure might be also necessary when changing a thiner disc for a wider one.

f) Make sure that the brake hydraulic system is properly bled before commencing braking tests. Brake bleeding removes the air or other gases trapped in the brake fluid and ensures correct operation of the hydraulic system (Gilles, 2016). The bleeding procedure of the current brake system can be carried out without a helper and has these sequences:

   1) Make sure the level of the brake fluid in the master cylinder container is between the indicated limits.
   2) In LabVIEW version 2015, open the actuation system project file .lvproj. From the project tree open the FPGA Main.vi and run the program. On the front panel, switch the safe mode to the manual mode.
   3) Set a low pressure value (up to 3 bar) of the first channel in the manual mode subpanel.
   4) Attach the bleeder hose to a bleed screw of the first channel as shown in Figure A-8.
   5) Loosen the bleed screw by approximately half turn. Observe the air bubbles in the brake fluid, while the brake fluid flows through the bleeder hose to the plastic container.
   6) After the brake fluid stops flowing, tighten the bleed screw.
   7) Repeat the procedures 3 - 6 until no bubbles are visible.

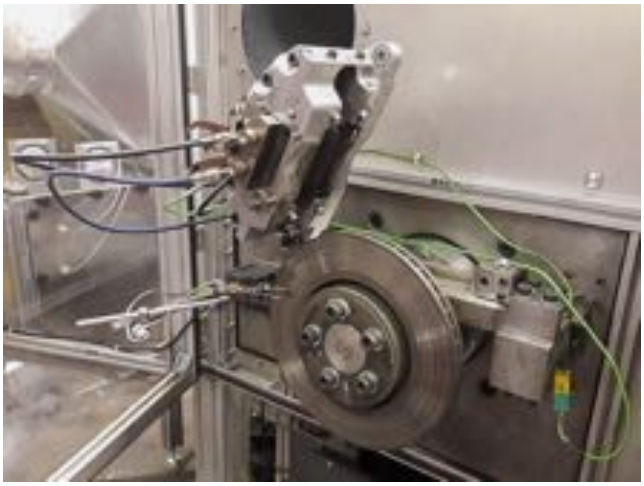

Figure A-7: Recommended caliper position during brake pads replacement.

Figure A-8: Brake bleeding procedure.

8) Repeat the procedures 3 - 7 for the second bleed screw of this channel.

9) Repeat the procedures 3 - 8 for the second channel until all four bleed screws are bled.

Appendix B

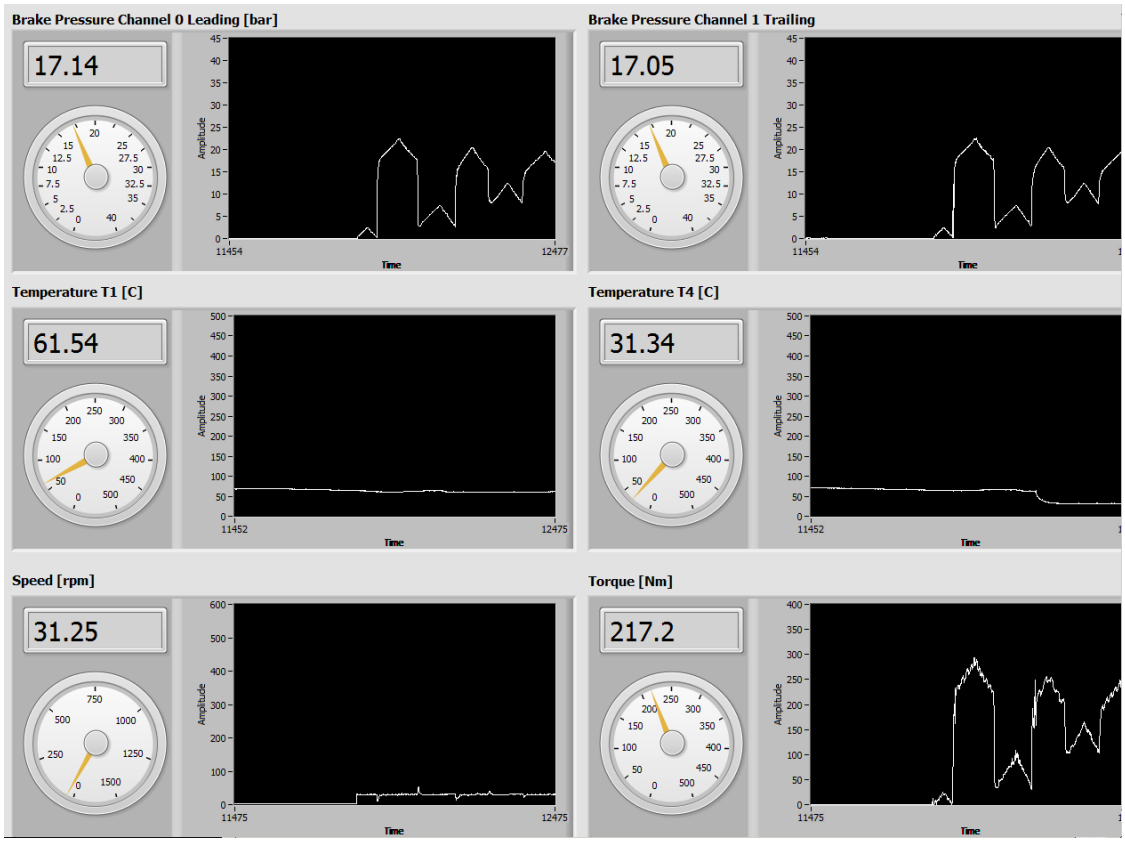

Figure B-1: A dettached UI panel showing the brake operating parameters.

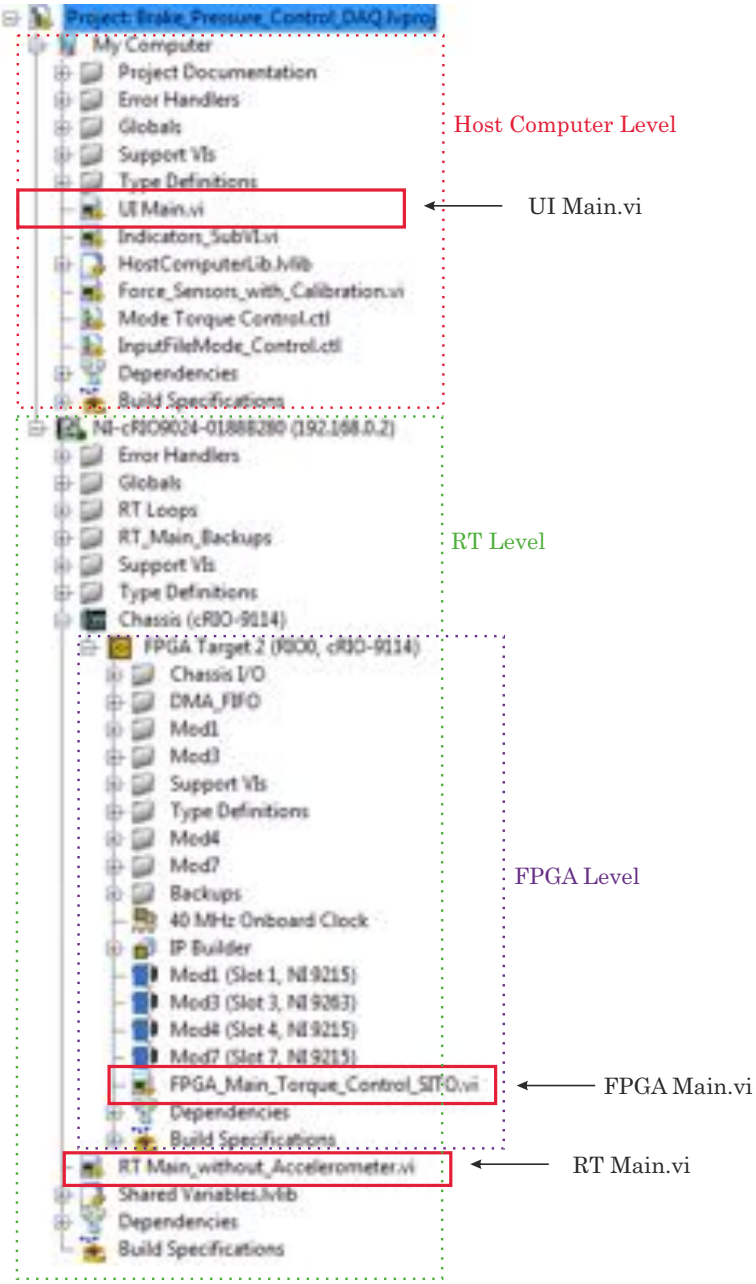

Figure B-2: Complete CompactRIO project structure containing the host computer level, RT level, and FPGA level.

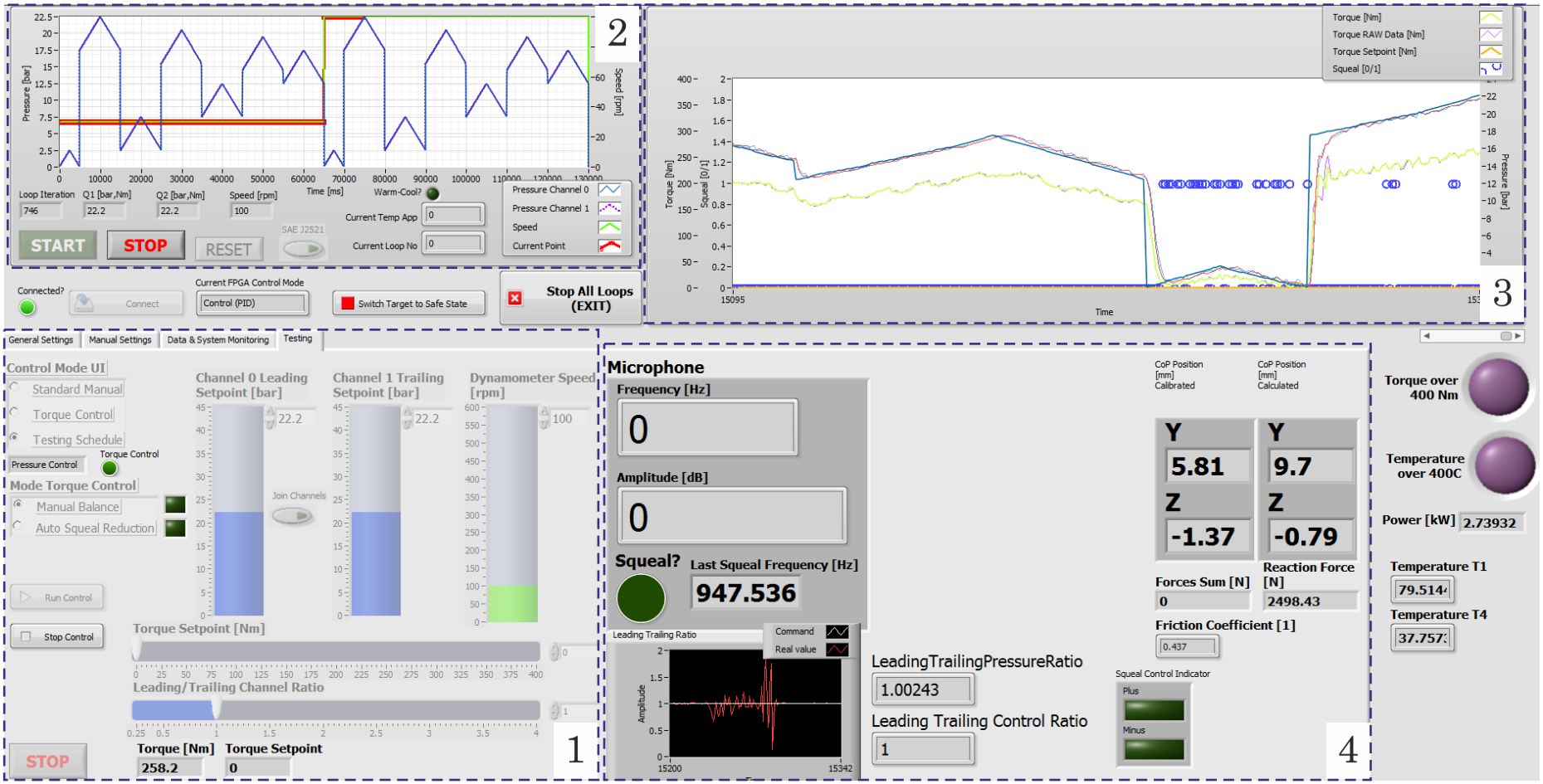

Figure B-3: Front panel of the UI Main.vi: setting the operational parameters of the brake test rig (Area 1), test cycles management (Area 2), time plots of the main operational parameters (Area 3), squeal, CoP and LTPR indicators (Area 4).

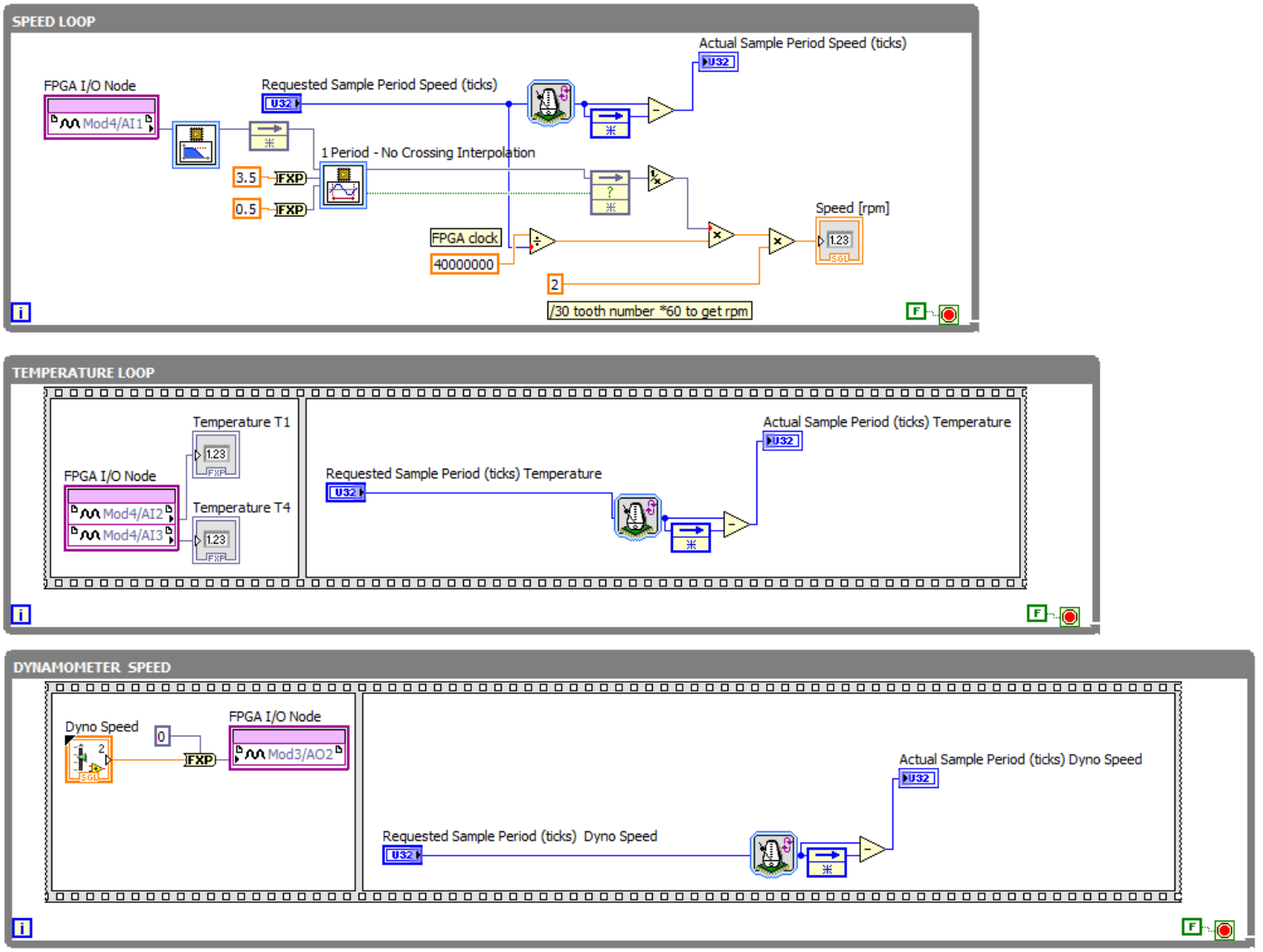

Figure B-4: DAQ loops programmed in LabVIEW.

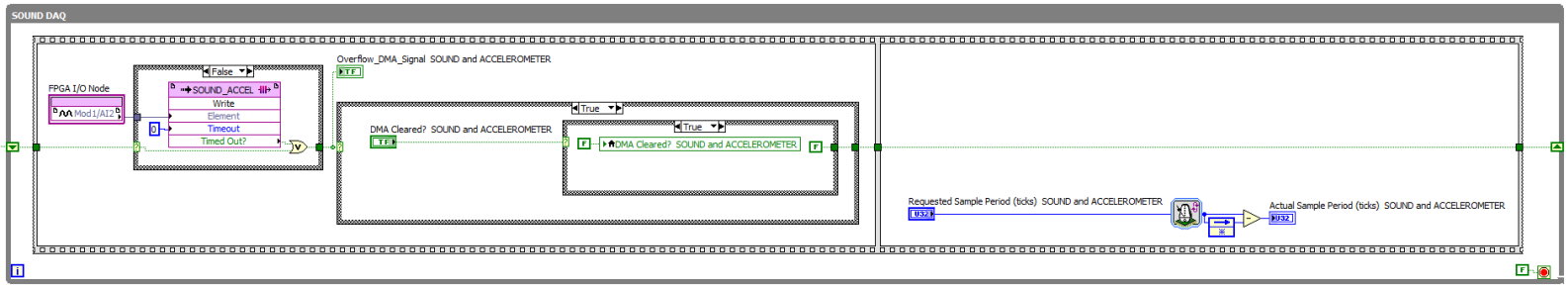

Figure B-5: DMA for sound data transfer programmed in LabVIEW.

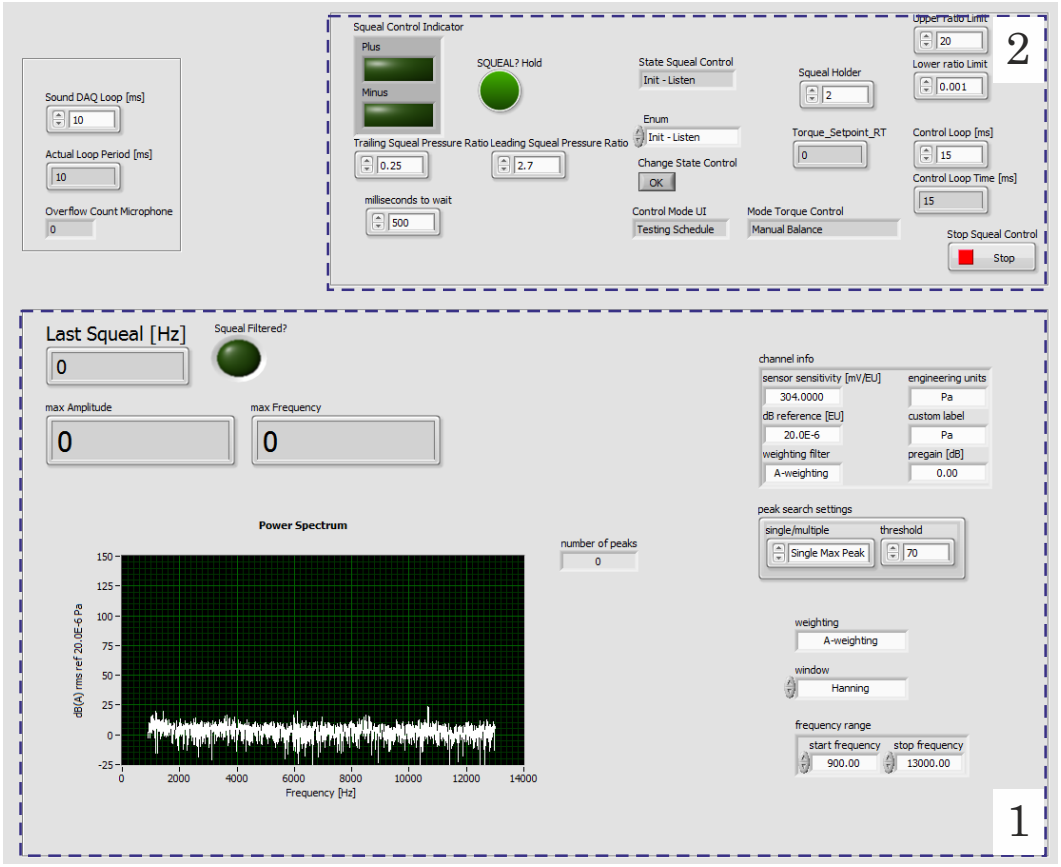

Figure B-6: Front panel of the RT Main.vi: setting the squeal filter parameters (Area 1), ASQR control management (Area 2).

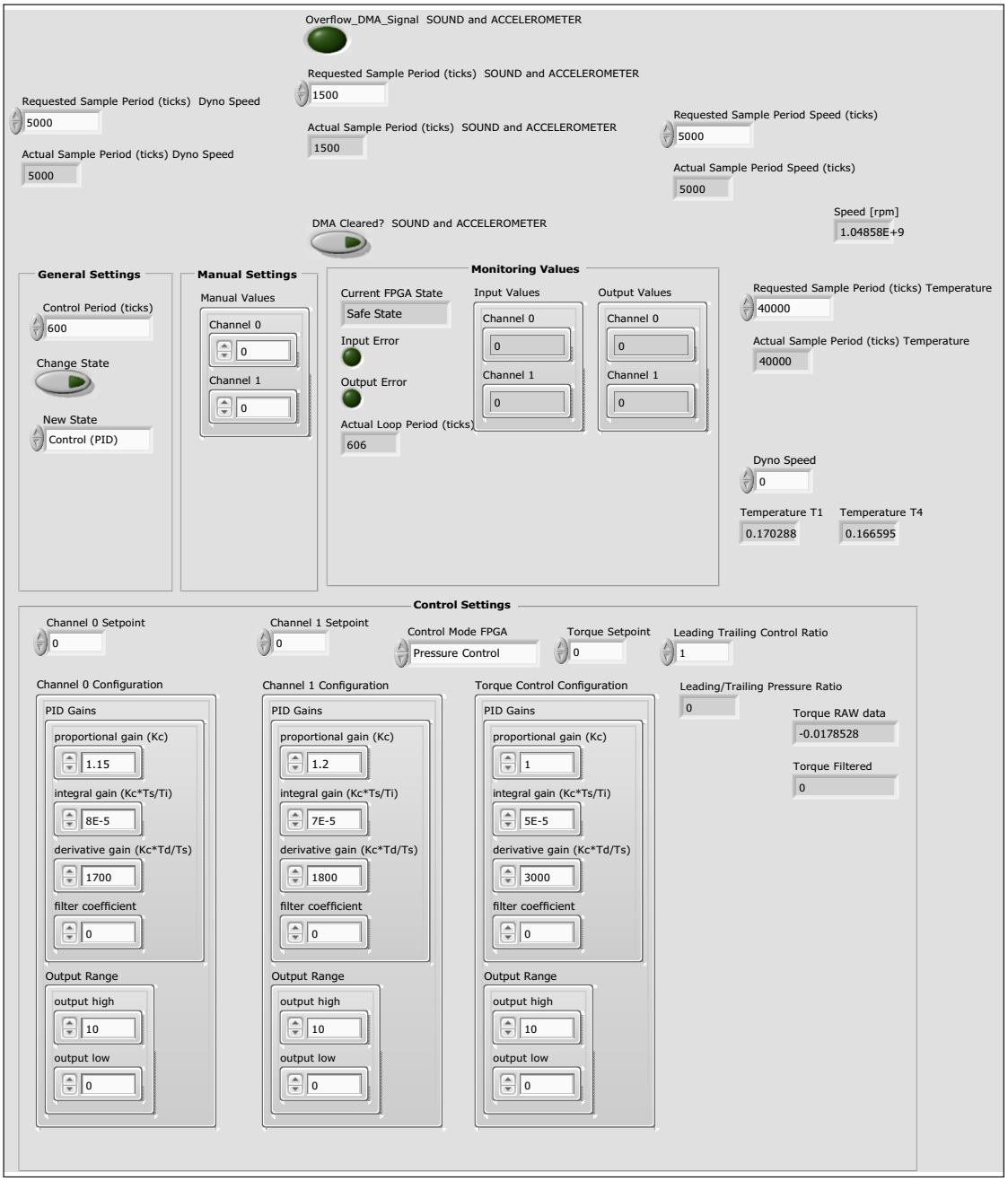

Figure B-7: Front panel of the FPGA level.

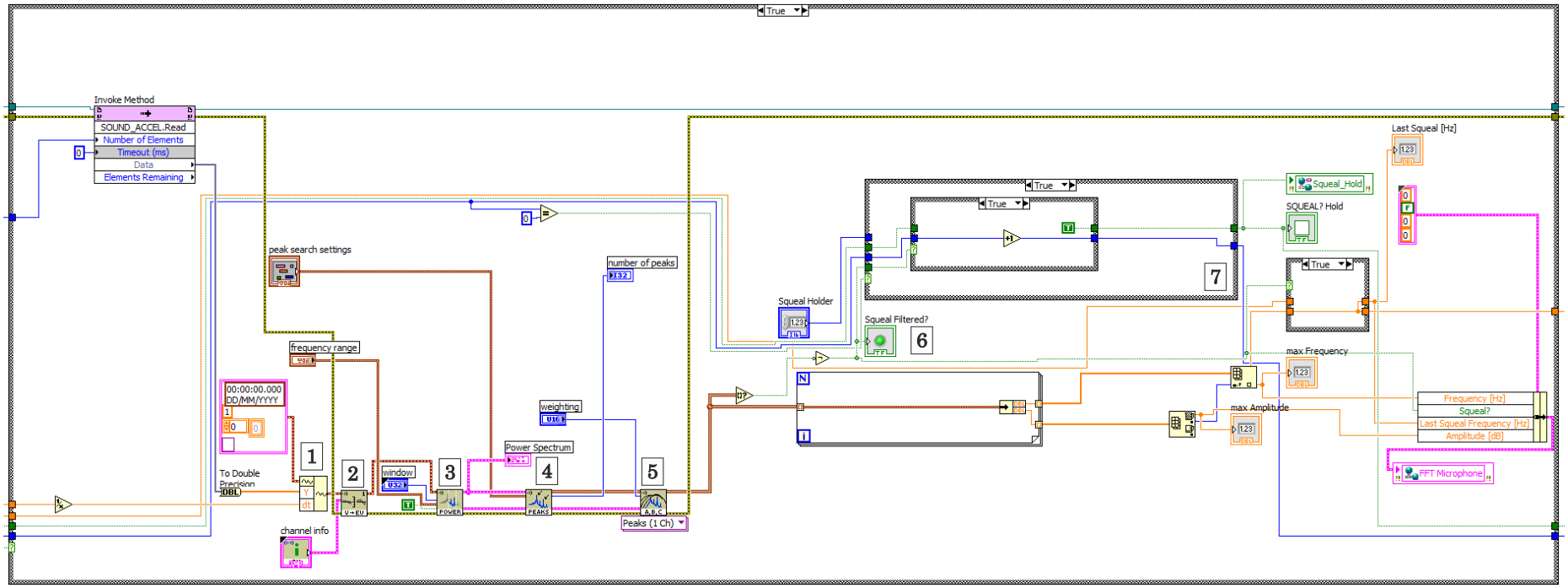

Figure B-8: Algorithm implemented at RT host to post-process the microphone signal and extract squeal frequencies: 1) conversion to a waveform signal, 2) scaling from voltage to decibels (V → EU VI), 3) power spectrum density calculation (POWER VI), 4) searching for amplitude peaks (PEAKS VI), 5) weighting of the amplitude values using an A-filtering (A, B, C VI), 6) setting the boolean operator to 0 (no squeal) or 1 (squeal), 7) squeal hold algorithm keeping the last value for a specific time period.

B.1 Dynamometer Control

To activate the brake dynamometer, it is necessary to switch on the power supply for the torque transducer electronic unit and set voltages 5 and 25 V as shown in Figure 4.22. Then, the electric motor fan (1) and electric motor drive mode (2) need to be activated on the dynamometer electric panel shown in Figure B-9. After closing the protection cage shown in Figure 4.1, the shaft can be set to motion by pressing the START (green) button on the motor controller (see Figure B-10), whereas the STOP (red) and EMERGENCY STOP (red) buttons serve to terminate the shaft rotation. After use of the emergency stop button, it needs to be reset by twisting it to enable the next run.

Figure B-9: Brake dynamometer electric panel: 1) electric motor fan, 2) electric motor drive mode.

Figure B-10: Close-up of the brake dynamometer speed controller: START - activate shaft rotation, STOP - stop shaft rotation, EMERGENCY STOP - fast push-down button to stop shaft rotation (after use twist it to reset).

B.2 Extraction System Control

The extraction system can be run via a rotary knob (1) positioned on the electric panel shown in Figure B-11. This activates the exterior fan unit, which creates an airflow within the system. The airflow can be controlled using a rotary controller (2) that sets the rotational speed of the fan. To measure the speed of the air or to collect particle emissions, the extraction tube leading from the enclosure has outlets as shown in Figure B-12. The outlets are positioned at a certain distance from the enclosure, where the airflow is expected to have a laminar character allowing the connection of measurement devices.

Figure B-11: Electric panel of the extraction system: 1) on/off rotary knob, 2) airflow rotary controller.

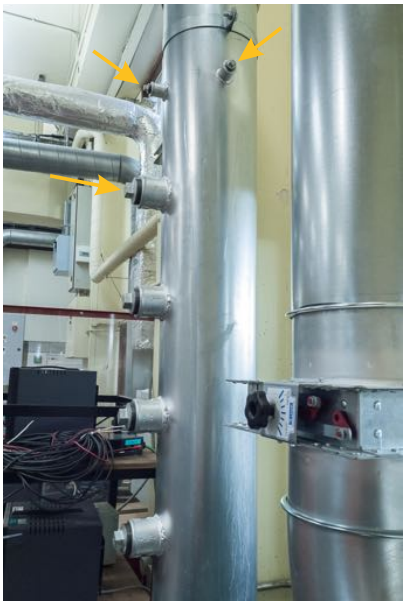

Figure B-12: Sample collection tube with variety of accessible outlets (see arrows).

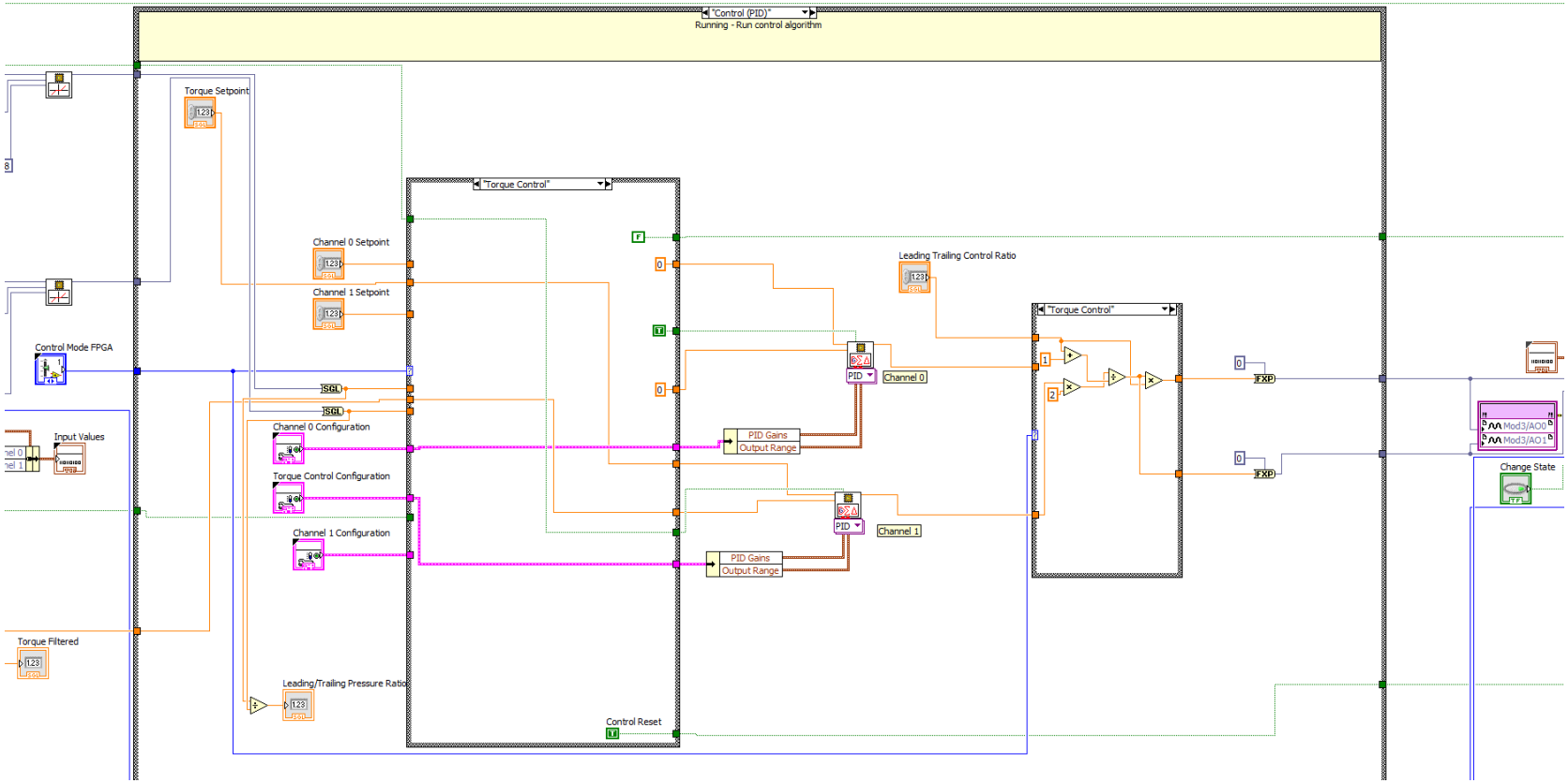

Figure B-13: LabView block diagram showing the torque mode.

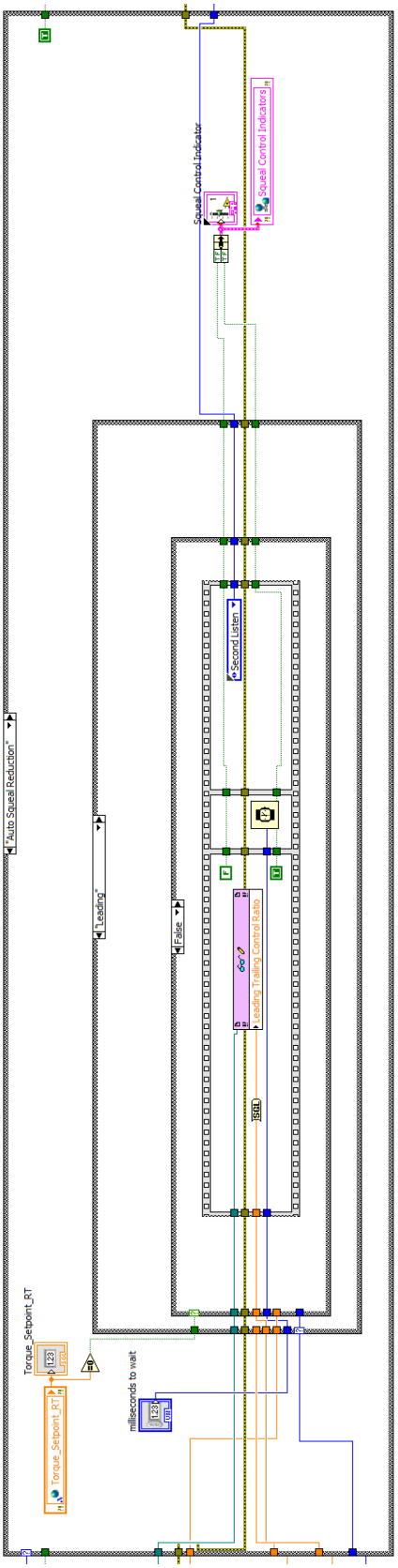

Figure B-14: LabVIEW code to control the LTPR change towards the leading side.

Appendix C

```
*Heading
...
*INCLUDE, INPUT=Reduced_Model_Rover_e.inp
**
** MATERIALS
...
**
** INTERACTION PROPERTIES
**
...
**
** BOUNDARY CONDITIONS
**
...
**
** INTERACTIONS
**
...
**
** STEP: Static_Brake_Pressure
**
*Step, name=Static_Brake_Pressure, nlgeom=YES, inc=10000000, unsymm=YES
*Static, direct
0.25, 1.,
*Boundary
Rotor_constr,1,3,0.
**
** LOADS
**
** Name: Piston_1   Type: Pressure
*Dsload
Piston_1, P,  1.00
** Name: Piston_2   Type: Pressure
```

```
*Dsload
Piston_2, P,  1.00
** Name: Piston_3   Type: Pressure
*Dsload
Piston_3, P,  1.00
** Name: Piston_4   Type: Pressure
*Dsload
Piston_4, P,  1.00
**
** OUTPUT REQUESTS
**
...
*End Step
**
** STEP: Static_Rotation
**
*Step, name=Static_Rotation, nlgeom=YES, inc=1000, unsymm=YES
*Static, direct
0.25, 1.,
**
*MOTION, ROTATION, type=velocity
ROTOR,   3.14,0.0,0.0,0.0,1.0,0.0,0.0
*Change Friction, interaction=Disc_Pad_Friction
*Friction, slip tolerance=0.005
 0.50,
**
** OUTPUT REQUESTS
...
*End Step
**
** STEP: Static_Frequency_Analysis_with_loads
**
*Step, name=Static_Frequency_Analysis_with_loads
*Frequency
, , 13000., , ,
**
** OUTPUT REQUESTS
...
*End Step
**
** STEP: Complex_Frequency
**
```

```
*Step, name=Complex_Frequency
*Complex Frequency, friction damping=YES
,,13000.,
**
** OUTPUT REQUESTS
**
...
*End Step
```

Appendix D

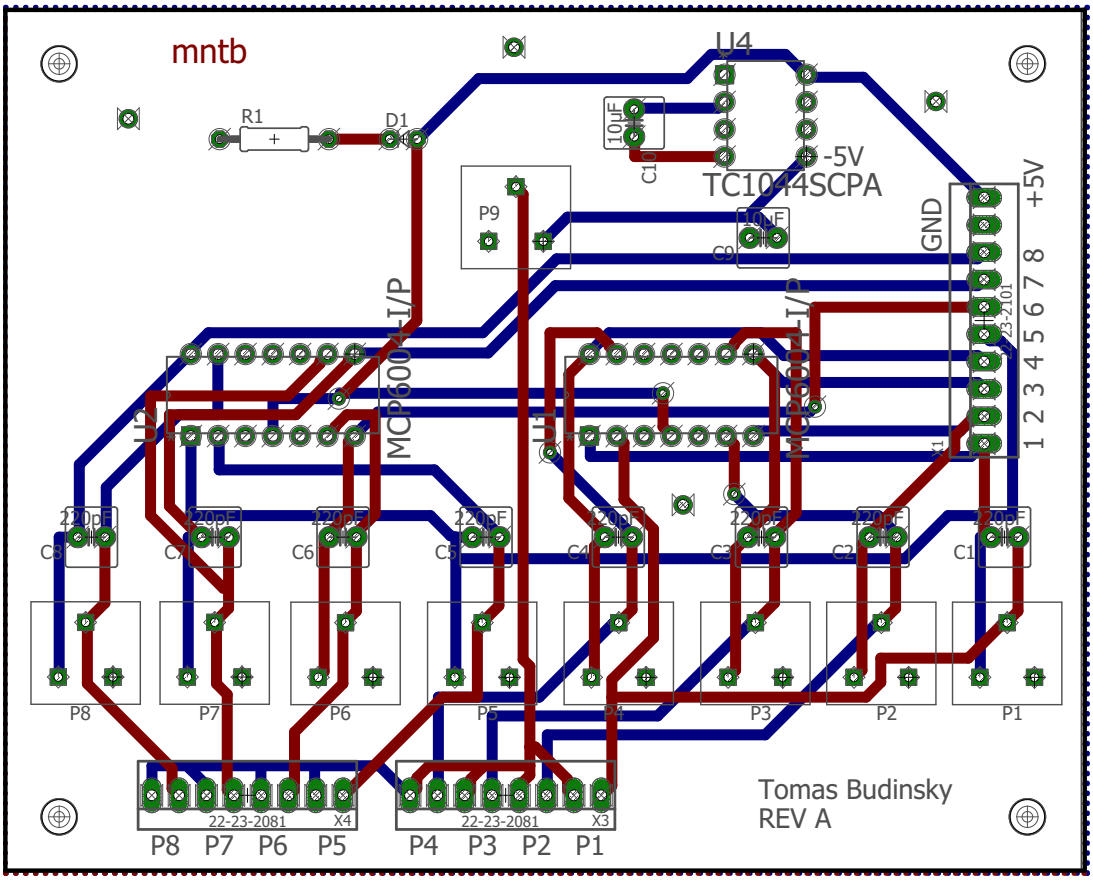

Figure D-1: Layout of the printed circuit board of the pad sensor developed in EAGLE software.

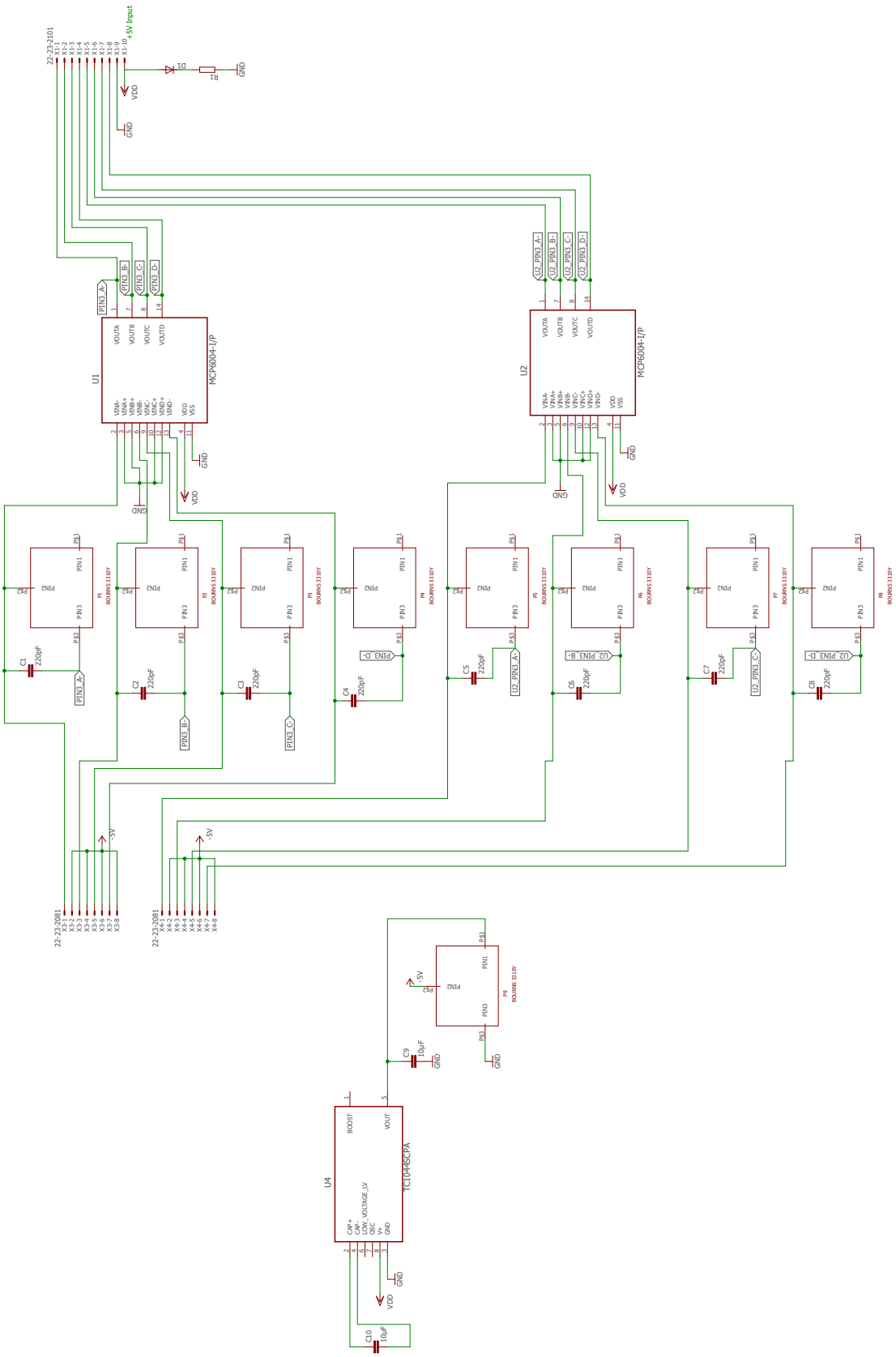

Figure D-2: Schematic of the electronic circuit of the pad sensor developed in EAGLE software.

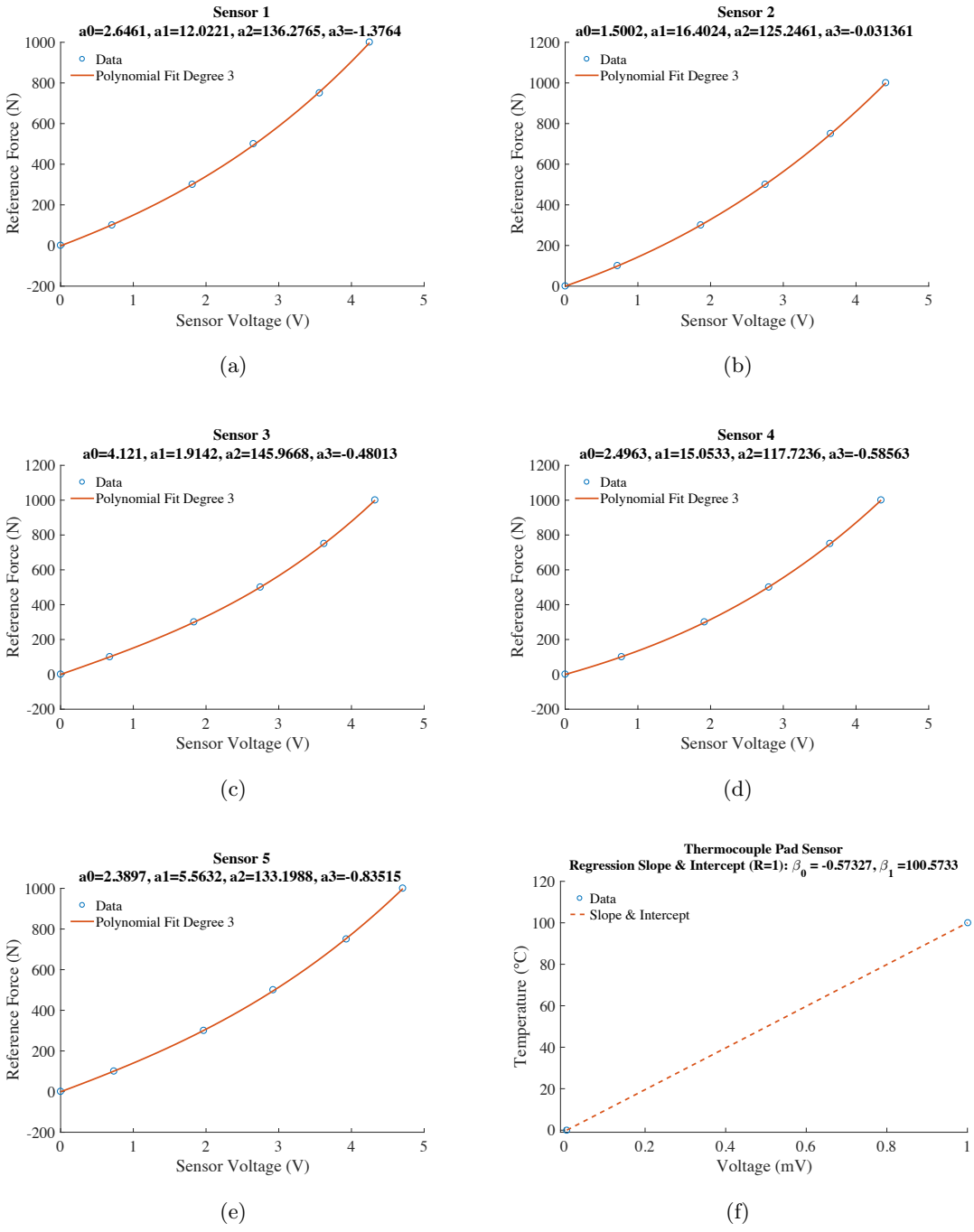

Figure D-3: Calibration curves: a) sensor 1, b) sensor 2, c) sensor 3, d) sensor 4, e) sensor 5, f) thermocouple.

D.1 Force Sensor Calibration Procedure

1) Sensor conditioning

    i) Apply and remove force at 120% of the expected maximum force 3 times for 10 s.

2) Circuit sensitivity adjustment

    i) Apply maximum force and adjust the potentiometer so that output is 90% of the circuit's maximum output.

3) Plotting force versus recorded output

    i) Record the circuit output with the sensor unloaded.

    ii) Apply a low calibration point at 10% of maximum load.

    iii) Apply a calibration point at 30% of maximum load.

    iv) Apply a middle calibration point at 50% of maximum load.

    v) Apply a calibration point at 75% of maximum load.

    vi) Apply a high calibration point at 100% of maximum load.

Appendix E

Table E-1: Conversion table between the LTPR and CoP positions using the new 3D analytical model and a FE model of the disc brake.

LTPR	$\mu = 0.4$					
	Y (mm)			Z (mm)		
	Analytical	Inboard	Outboard	Analytical	Inboard	Outboard
1/9	-8.2	-10.3	-9.7	0.5	-0.4	-0.6
1/4	-3.9	-5.7	-5.0	0.3	-0.6	-0.8
1/3	-1.7	-3.6	-2.9	0.1	-0.7	-0.8
1/2	1.9	-0.4	0.3	-0.1	-0.9	-1.0
1	9.0	5.9	6.6	-0.7	-1.2	-1.2
2	16.2	12.0	12.7	-1.3	-1.5	-1.4
3	19.7	15.1	15.8	-1.6	-1.6	-1.5
4	21.8	17.0	17.7	-1.9	-1.7	-1.6
9	26.1	20.9	21.5	-2.3	-1.8	-1.8
LTPR	$\mu = 0.5$					
	Y (mm)			Z (mm)		
	Analytical	Inboard	Outboard	Analytical	Inboard	Outboard
1/9	-6.3	-8.9	-8.1	0.5	-0.4	-0.6
1/4	-1.9	-4.2	-3.4	0.2	-0.7	-0.8
1/3	0.3	-2.2	-1.3	0.0	-0.8	-0.9
1/2	4.0	1.1	2.0	-0.4	-1.0	-1.1
1	11.3	7.4	8.3	-1.1	-1.3	-1.4
2	18.5	13.6	14.4	-1.9	-1.7	-1.7
3	22.1	16.6	17.5	-2.3	-1.9	-1.8
4	24.3	18.5	19.3	-2.6	-2.0	-1.9
9	28.5	22.3	23.1	-3.1	-2.2	-2.1
LTPR	$\mu = 0.6$					
	Y (mm)			Z (mm)		
	Analytical	Inboard	Outboard	Analytical	Inboard	Outboard
1/9	-4.3	-7.5	-6.5	0.4	-0.4	-0.6
1/4	0.1	-2.8	-1.7	0.0	-0.7	-0.9
1/3	2.4	-0.7	0.4	-0.3	-0.9	-1.1
1/2	6.1	2.6	3.7	-0.7	-1.1	-1.2
1	13.5	9.0	10.1	-1.6	-1.6	-1.6
2	20.8	15.1	16.2	-2.6	-2.0	-1.9
3	24.5	18.1	19.2	-3.1	-2.2	-2.1
4	26.6	20.0	21.0	-3.4	-2.3	-2.2
9	31.0	23.8	24.6	-4.1	-2.6	-2.5

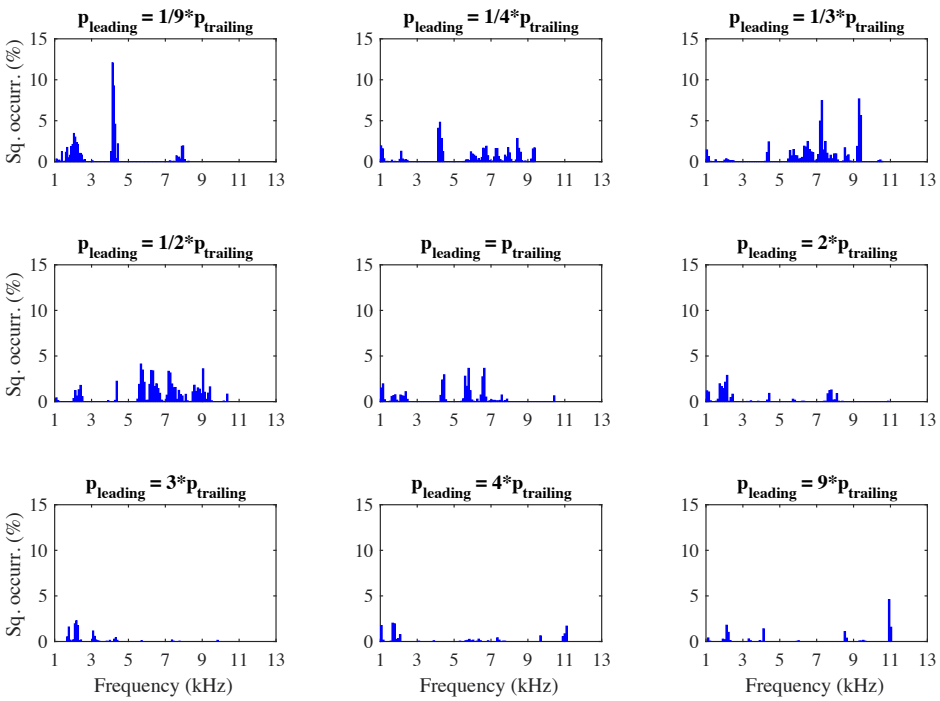

(a)

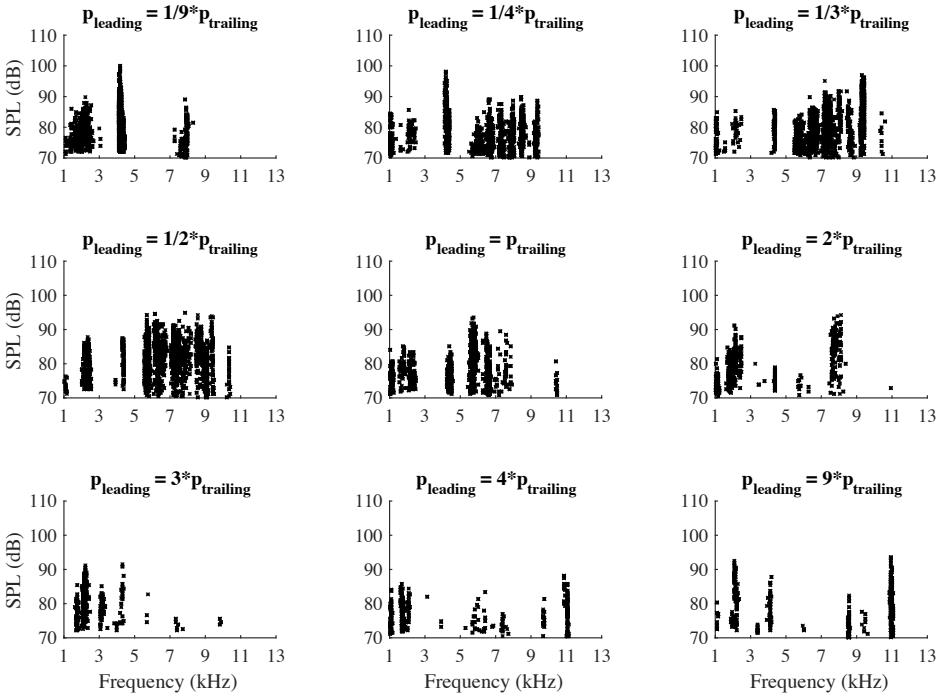

(b)

Figure E-1: Squeal occurrences as a function of frequency (kHz) - Test 2: a) relative squeal occurrence, b) SPL - Sound Pressure Level (dB(A)).

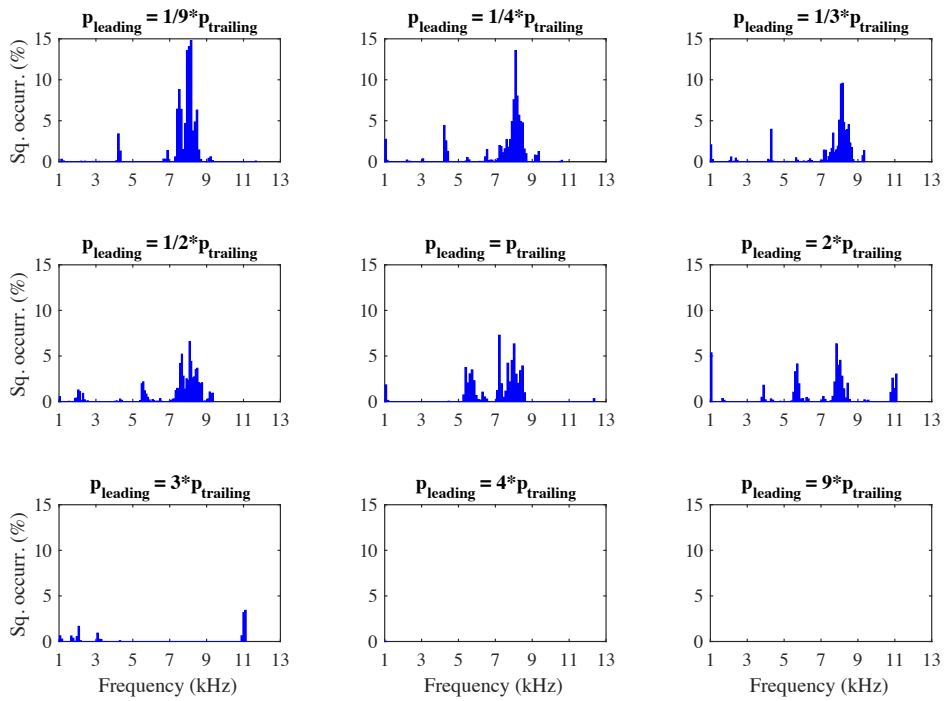

(a)

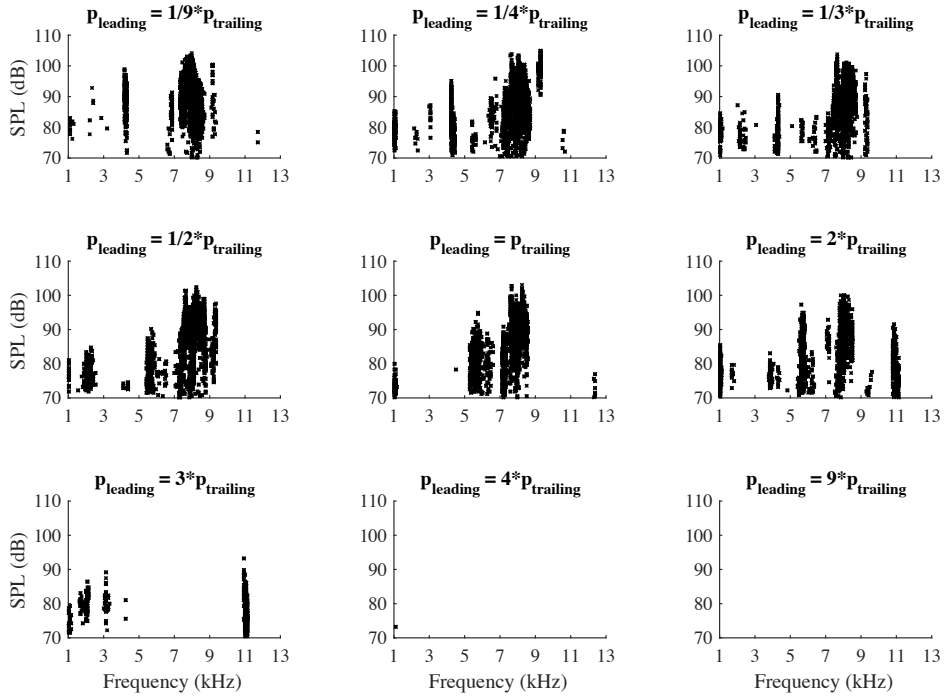

(b)

Figure E-2: Squeal occurrences as a function of frequency (kHz) - Test 3: a) relative squeal occurrence, b) SPL - Sound Pressure Level (dB(A)).

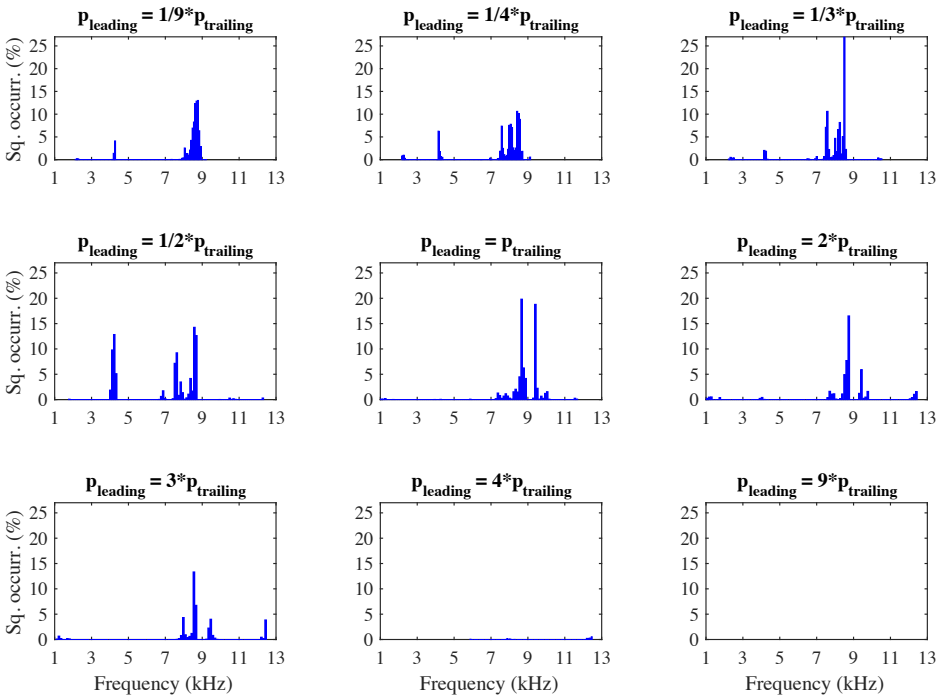

(a)

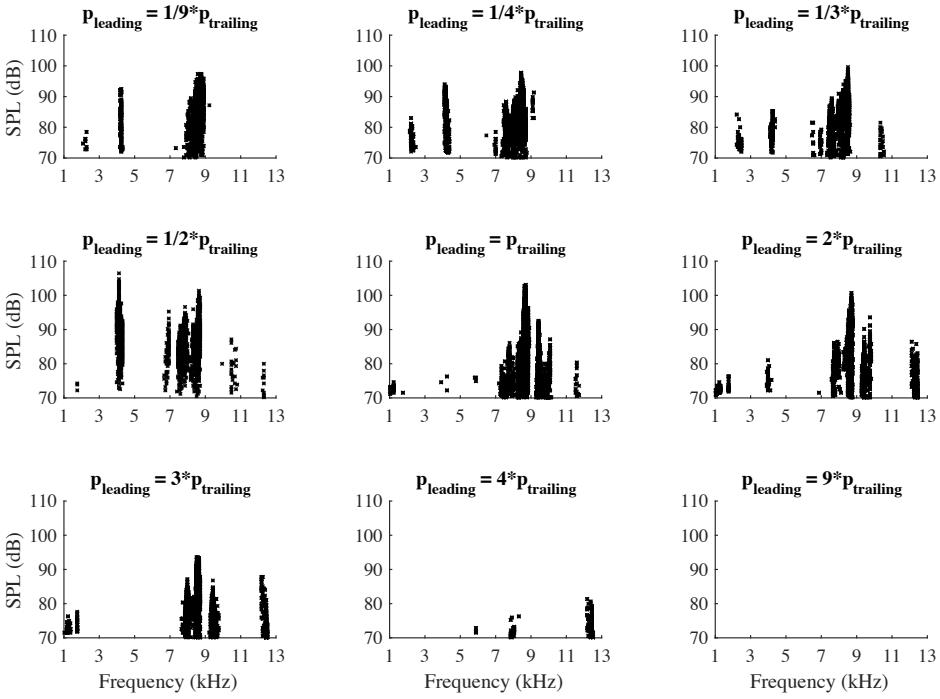

(b)

Figure E-3: Squeal occurrences as a function of frequency (kHz) - Test 4: a) relative squeal occurrence, b) SPL - Sound Pressure Level (dB(A)).